

# Biogeochemical and microbial controls on manganese-driven oxidation of methane in coastal sediments

Robin Klomp

Institute for Biological and  
Environmental Sciences

**RADBOUD  
UNIVERSITY  
PRESS**

Radboud  
Dissertation  
Series

# **Biogeochemical and microbial controls on manganese-driven oxidation of methane in coastal sediments**

Robin Klomp

The research of this thesis was financially supported by the OCW/NOW NESSC [024002001] and ERC Synergy Grant MARIX [854088].

**Biogeochemical and microbial controls on manganese-driven oxidation of methane in coastal sediments**

Robin Klomp

**Radboud Dissertation Series**

ISSN: 2950-2772 (Online); 2950-2780 (Print)

Published by RADBOUD UNIVERSITY PRESS  
Postbus 9100, 6500 HA Nijmegen, The Netherlands  
[www.radbouduniversitypress.nl](http://www.radbouduniversitypress.nl)

Design: Proefschrift AIO | Annelies Lips

Cover: Robin Klomp

Printing: DPN Rikken/Pumbo

ISBN: 9789465151922

DOI: 10.54195/9789465151922

Free download at: <https://doi.org/10.54195/9789465151922>

© 2026 Robin Klomp

**RADBOUD  
UNIVERSITY  
PRESS**

This is an Open Access book published under the terms of Creative Commons Attribution-Noncommercial-NoDerivatives International license (CC BY-NC-ND 4.0). This license allows reusers to copy and distribute the material in any medium or format in unadapted form only, for noncommercial purposes only, and only so long as attribution is given to the creator, see <http://creativecommons.org/licenses/by-nc-nd/4.0/>.

# **Biogeochemical and microbial controls on manganese-driven oxidation of methane in coastal sediments**

Proefschrift ter verkrijging van de graad van doctor  
aan de Radboud Universiteit Nijmegen  
op gezag van de rector magnificus prof. dr. J.M. Sanders,  
volgens besluit van het college voor promoties  
in het openbaar te verdedigen op

woensdag 15 april 2026

om 14.30 uur precies

door

**Robin Klomp**

geboren op 29 december 1997

te Arnhem

**Promotoren:**

Prof. dr. ir. Caroline P. Slomp

Prof. dr. ir. Mike S.M. Jetten

**Copromotor:**

Dr. Wytze K. Lenstra

**Manuscriptcommissie:**

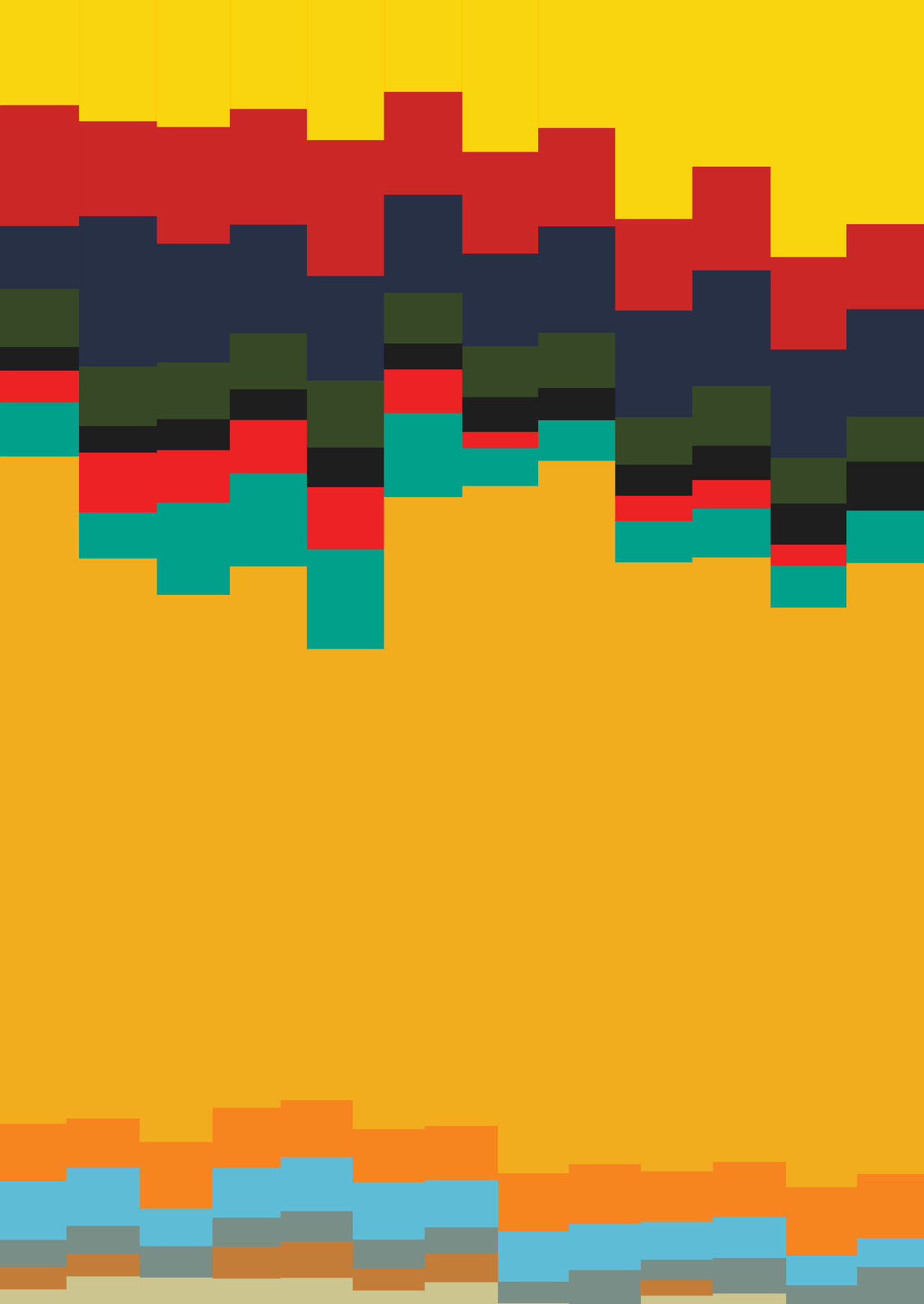
Prof. dr. Cornelia U. Welte

Prof. dr. Christian März (Universität Bonn, Duitsland)

Prof. dr. Christof Meile (University of Georgia, Verenigde Staten)

## Table of contents

	Summary	9
	Samenvatting	11
<b>Chapter 1</b>	General introduction and thesis outline	15
<b>Chapter 2</b>	A sequential extraction procedure for particulate manganese and its application to coastal marine sediments	29
<b>Chapter 3</b>	Dissolved Mn(III) is a key redox intermediate in sediment of a seasonally euxinic coastal basin	55
<b>Chapter 4</b>	Eutrophication threatens the ANME methane filter in coastal sediments by sulfide inhibition	105
<b>Chapter 5</b>	Potential for manganese oxide driven anaerobic methane oxidation in sediments of a seasonally euxinic coastal basin	131
<b>Chapter 6</b>	ANME-2ab driven methane oxidation in brackish coastal sediments via multiple pathways	159
<b>Chapter 7</b>	Anaerobic oxidation of methane coupled to manganese oxide reduction by ANME-2ab in brackish coastal sediments	191
<b>Chapter 8</b>	Synthesis and outlook	237
<b>Appendices</b>	References	250
	Data management	275
	Acknowledgements/Dankwoord	276
	List of publications	278
	Curriculum Vitae	280



# Summary

# Samenvatting

---

R.Klomp<sup>1</sup>

<sup>1</sup>Department of Microbiology, Radboud Institute for Biological and Environmental Sciences,  
Radboud University, Heyendaalseweg 135, 6525AJ Nijmegen, the Netherlands



## Summary

Atmospheric concentrations of methane ( $\text{CH}_4$ ), a key greenhouse gas, are steadily increasing, and are linked to anthropogenic and natural sources. Coastal systems account for the majority of marine  $\text{CH}_4$  emissions. In such systems, the rate of  $\text{CH}_4$  production in the sediment often exceeds its removal via aerobic and anaerobic oxidation, highlighting the need to understand the pathways of  $\text{CH}_4$  oxidation.

Sulfate ( $\text{SO}_4^{2-}$ ) is the major electron acceptor for anaerobic  $\text{CH}_4$  oxidation (AOM) in marine systems. Other electron acceptors, such as metal oxides, may also be used. However, definitive proof for AOM coupled to Mn oxide reduction (Mn-AOM) in brackish and marine coastal sediments is still lacking. Furthermore, it is unknown what microbes perform Mn-AOM in such environments. In this thesis, we studied the potential for Mn-AOM and the microbes involved in two coastal systems, marine Lake Grevelingen and the brackish Bothnian Sea.

A sequential extraction method for Mn mineral forms in sediment is presented in **chapter 2**. This method provides a straightforward and effective method to separate Mn oxides, Mn carbonates and Mn bound to pyrites and is demonstrated to be very useful when studying sedimentary Mn cycling.

In marine Lake Grevelingen, at Scharendijke basin, temperature-induced stratification in combination with a high organic matter input lead to euxinic bottom waters in summer. We find in **chapter 3** that dissolved Mn(III) bound to organic ligands is a key component of the sedimentary Mn cycle. Reactive transport modelling shows a strong interaction between the sedimentary Mn and iron (Fe) cycles. The model results also point towards a benthic flux of Mn(III) both when bottom waters are oxic and euxinic. Benthic release of Mn(III) likely contributes to increased lateral transport of Mn in the lake, because Mn(III) is relatively stable and therefore more mobile than dissolved Mn(II).

The impact of seasonal euxinia on the microbial  $\text{CH}_4$  filter in the sediment at Scharendijke basin is studied in **chapter 4**. Intense  $\text{SO}_4^{2-}$  reduction leads to high sulfide ( $\text{H}_2\text{S}$ ) production in the sediment in summer. In the sediment layer deposited in winter, high Fe oxide concentrations buffer the produced  $\text{H}_2\text{S}$  via the formation of FeS minerals. This allows the development of a  $\text{H}_2\text{S}$  free sediment layer which provides a niche for anaerobic methanotrophic archaea ANME of the clades ANME-2ab and ANME-3. Toxicity of  $\text{H}_2\text{S}$  most likely explains the strong anti-correlation between  $\text{H}_2\text{S}$  in the porewater and the abundance of ANME in the sediment.

Sediment incubations show that the Mn oxides birnessite, pyrolusite and manganite enhance AOM in Scharendijke basin sediments in **chapter 5**. However, the addition of dissolved Mn(III) bound to organic ligands did not stimulate AOM. A cryptic sulfur cycle likely contributed to AOM in the incubations with birnessite and pyrolusite. Based on 16S rRNA amplicon sequencing, ANME-2ab and ANME-3 were identified as key organisms for Mn-AOM, where ANME-2ab were likely involved in AOM directly coupled to Mn oxide reduction, whereas ANME-3 primarily benefitted from a cryptic sulfur cycle driven by Mn oxide reduction.

Bothnian Sea sediments are rich in Fe and Mn oxides. In this environment, eutrophication has led to an increased input of organic matter input into the sediment, which has resulted in increased  $\text{SO}_4^{2-}$  reduction rates and a shoaling of the sulfate-methane transition zone (SMTZ). We find in **chapter 6** that most AOM occurs in the SMTZ of location US2 and is performed by ANME-2ab. Metatranscriptomic analyses show that ANME-2ab are also active below the SMTZ. Sediment incubations reveal that ANME-2ab can couple AOM to the reduction of  $\text{SO}_4^{2-}$ , Mn oxide, Fe oxide and graphene oxide (an organic matter analogue), although a cryptic sulfur cycle could not always be excluded. The range of electron acceptors used by ANME-2ab for AOM likely contributes to the resilience of the microbial  $\text{CH}_4$  filter in brackish coastal sediments.

Sediment incubations provide evidence for a direct coupling between  $\text{CH}_4$  oxidation and reduction of the Mn oxides birnessite and pyrolusite in the brackish coastal sediments of the Bothnian Sea location US5B in **chapter 7**. The addition of molybdate as an inhibitor for  $\text{SO}_4^{2-}$  reduction in the incubations with birnessite allowed us to exclude the role of a cryptic sulfur cycle. ANME-2ab were identified as the key organism performing these reactions. Metagenomic sequencing suggests that ANME-2ab use extracellular electron transfer to perform Mn-AOM.

In this thesis we discovered direct, Mn oxide coupled  $\text{CH}_4$  oxidation that can contribute to a more resilient microbial  $\text{CH}_4$  filter, fundamentally altering our understanding of how coastal ecosystems will regulate greenhouse gas emissions in a future of changing climate and ocean chemistry.

## Samenvatting

De concentraties van methaan ( $\text{CH}_4$ ), een belangrijk broeikasgas, nemen gestaag toe in de atmosfeer en zijn gekoppeld aan antropogene en natuurlijke bronnen. Kustsystemen zijn verantwoordelijk voor het grootste deel van de mariene  $\text{CH}_4$ -emissies. In dergelijke systemen overtreft de snelheid van  $\text{CH}_4$ -productie in het sediment vaak de verwijdering van  $\text{CH}_4$  via aerobe en anaerobe oxidatie. Deze disbalans benadrukt het belang van inzicht in de oxidatieprocessen van  $\text{CH}_4$ .

Sulfaat ( $\text{SO}_4^{2-}$ ) is de belangrijkste elektronenacceptor voor anaerobe oxidatie van  $\text{CH}_4$  (AOM) in mariene systemen. Andere elektronenacceptoren, zoals metaaloxiden, kunnen ook worden gebruikt. Definitief bewijs voor AOM gekoppeld aan Mn-oxide reductie (Mn-AOM) in brakke en mariene kustsedimenten ontbreekt echter nog steeds. Bovendien is het onbekend welke microben Mn-AOM in deze milieus uitvoeren. In dit proefschrift onderzochten we de potentie voor Mn-AOM en de betrokken microben in twee kustsystemen: het mariene Grevelingenmeer en de brakke Botnische Zee.

In **hoofdstuk 2** wordt een sequentiële extractiemethode voor Mn-mineraalvormen in sediment gepresenteerd. Deze methode biedt een eenvoudige en effectieve manier om Mn-oxiden, Mn-carbonaten en aan pyriet gebonden Mn te scheiden en blijkt zeer nuttig te zijn bij het bestuderen van de sedimentaire Mn-kringloop.

In het mariene Grevelingenmeer, in het Scharendijke-bekken, leiden temperatuur gedreven stratificatie in combinatie met een hoge aanvoer van organisch materiaal tot euxinische bodemwateren in de zomer. In **hoofdstuk 3** vinden we dat opgelost Mn(III) gebonden aan organische liganden een sleutelcomponent is van de sedimentaire Mn-kringloop. Reactief transportmodellering toont een sterke interactie tussen de sedimentaire Mn en ijzer (Fe) kringloop. De modelresultaten wijzen ook op een benthische flux van Mn(III) zowel wanneer er zuurstof aanwezig is in het bodemwater als wanneer het bodemwater euxinisch is. Een benthische flux van Mn(III) naar de waterkolom draagt waarschijnlijk bij aan een verhoogd lateraal transport van Mn in het meer, omdat Mn(III) relatief stabiel en daardoor mobieler is dan opgelost Mn(II).

In **hoofdstuk 4** wordt de impact van seizoensgebonden euxinische omstandigheden op het microbiële  $\text{CH}_4$ -filter in het sediment van het Scharendijke-bekken bestudeerd. Intense  $\text{SO}_4^{2-}$  reductie leidt in de zomer tot een hoge sulfide ( $\text{H}_2\text{S}$ ) productie in het sediment. In de sedimentlaag die is afgezet in de winter bufferen

hoge concentraties Fe oxide de geproduceerde  $H_2S$  door de vorming van FeS-mineralen. Als gevolg hiervan vormt er een  $H_2S$ -vrije sedimentlaag die een niche biedt voor anaërobe methanotrofe archaea ANME van de clades ANME-2ab en ANME-3. De toxiciteit van  $H_2S$  verklaart waarschijnlijk de sterke anticorrelatie tussen  $H_2S$  in het poriewater en de abundantie van ANME in het sediment.

Sediment incubaties tonen aan dat de Mn oxiden birnessiet, pyrolusiet en manganiet bevorderend zijn voor AOM in de sedimenten van het Scharendijke-bekken (**hoofdstuk 5**). De toevoeging van opgelost Mn(III) gebonden aan organische liganden stimuleerde de AOM echter niet. Een verborgen zwavelcyclus droeg waarschijnlijk bij aan AOM in de incubaties met birnessiet en pyrolusiet. Op basis van 16S rRNA-ampliconsequencing werden ANME-2ab en ANME-3 geïdentificeerd als sleutelorganismen voor Mn-AOM, waarbij ANME-2ab waarschijnlijk direct betrokken was bij AOM gekoppeld aan de reductie van mangaanoxiden, terwijl ANME-3 voornamelijk profiteerde van een verborgen zwavelcyclus aangedreven door de reductie van mangaanoxiden.

De sedimenten van de Botnische Zee zijn rijk aan Fe en Mn oxiden. In dit milieu heeft eutrofiëring geleid tot een verhoogde aanvoer van organisch materiaal in het sediment, wat heeft geresulteerd in verhoogde  $SO_4^{2-}$ -reductiesnelheden en een ondieper wordende sulfaat-methaanovergangszone (SMTZ). In **hoofdstuk 6** stellen we vast dat op locatie US2 de meeste AOM plaatsvindt in de SMTZ en wordt uitgevoerd door ANME-2ab. Metatranscriptoom analyses tonen aan dat ANME-2ab ook actief zijn onder de SMTZ. Sedimentincubaties tonen aan dat ANME-2ab AOM kan koppelen aan de reductie van  $SO_4^{2-}$ , Mn oxide, Fe oxide en grafeenoxide (een analoog van organisch materiaal), hoewel een verborgen zwavelcyclus niet altijd kon worden uitgesloten. Het scala aan elektronenacceptoren dat ANME-2ab gebruiken voor AOM draagt waarschijnlijk bij aan de veerkracht van het microbiële  $CH_4$ -filter in brakke kustsedimenten.

Sediment incubaties leveren bewijs voor een directe koppeling tussen  $CH_4$ -oxidatie en reductie van de Mn oxiden birnessiet en pyrolusiet in de brakke kustsedimenten van de Botnische Zee, locatie US5B in **hoofdstuk 7**. De toevoeging van molybdaat als remmer van  $SO_4^{2-}$ -reductie in de incubaties met birnessiet stelde ons in staat de rol van een verborgen zwavelcyclus uit te sluiten. ANME-2ab werd geïdentificeerd als het belangrijkste organisme dat deze reacties uitvoert. Metagenomische sequencing suggereert dat ANME-2ab extracellulaire elektronentransfer gebruikt om Mn-AOM uit te voeren.

In dit proefschrift ontdekten we directe, aan Mn oxide gekoppelde CH<sub>4</sub>-oxidatie die kan bijdragen aan een veerkrachtiger microbieel CH<sub>4</sub>-filter. Dit verandert fundamenteel ons begrip van hoe kustecosystemen de uitstoot van broeikasgassen zullen reguleren in een toekomst met een veranderend klimaat en veranderende oceanchemie.



## Chapter 1

# General introduction and thesis outline

---

R.Klomp<sup>1</sup>

<sup>1</sup>Department of Microbiology, Radboud Institute for Biological and Environmental Sciences,  
Radboud University, Heyendaalseweg 135, 6525AJ Nijmegen, the Netherlands

## Methane as a greenhouse gas

Earth's long-term habitability is strongly related to the presence of the greenhouse gases methane ( $\text{CH}_4$ ) and carbon dioxide ( $\text{CO}_2$ ) in the atmosphere (Lacis et al., 2010). These gases regulate the temperature at the Earth's surface by trapping heat from solar radiation (Lacis et al., 2010). Since the start of the industrial era, anthropogenic emissions of these greenhouse gases have strongly increased, resulting in elevated concentrations in the atmosphere (Keeling, 1960; Etheridge et al., 1992; Saunio et al., 2025; Fig. 1). Consequently, the average temperature at the Earth's surface is increasing rapidly, leading to global climate change (Lee et al., 2023). Detailed insight into the sources and sinks of  $\text{CH}_4$  and  $\text{CO}_2$  and the processes controlling them is critical for projections of future global warming and climate change (Saunio et al., 2025).

Methane has 86 times more warming potential than  $\text{CO}_2$  on a 20 year time scale (Myhre et al., 2013). The concentration of  $\text{CH}_4$  in the atmosphere has increased from 808 ppb in pre-industrial times to a concentration of 1934 ppb in May 2025 (Meinshausen et al., 2017; Lan et al., 2025; Fig. 1). The contribution of  $\text{CH}_4$  to global warming is estimated to be 16 - 23 % since the onset of industrialization (Etminan et al., 2016; Meinshausen et al., 2017). The relatively short residence time of around 9 years in the atmosphere (Prather et al., 2012; Szopa et al., 2021) enables the advantage that a reduction in  $\text{CH}_4$  emissions can decrease global warming within a decadal time span (Ocko et al., 2021).

Atmospheric  $\text{CH}_4$  originates from anthropogenic sources, like agriculture, fossil fuel combustion and biomass burning, and natural sources, like wetlands, inland waters and oceans (Ciais et al., 2013). About 46% of the  $\text{CH}_4$  in the atmosphere originates from natural sources, which are expected to increase further due to climate change (Saunio et al., 2025). Marine emissions compose a small fraction of the natural sources, despite the large  $\text{CH}_4$  production in marine sediments (Regnier et al., 2011). Most of the  $\text{CH}_4$  that forms in marine sediments is oxidized via microbially mediated aerobic or anaerobic  $\text{CH}_4$  oxidation before it reaches the atmosphere (Knittel & Boetius, 2009). The marine  $\text{CH}_4$  flux is especially high in coastal regions (Weber et al., 2019). We currently lack a comprehensive understanding of the possible  $\text{CH}_4$  oxidation pathways in coastal sediments, the biogeochemical controls and the microbes involved in these processes (Wallenius et al., 2021).

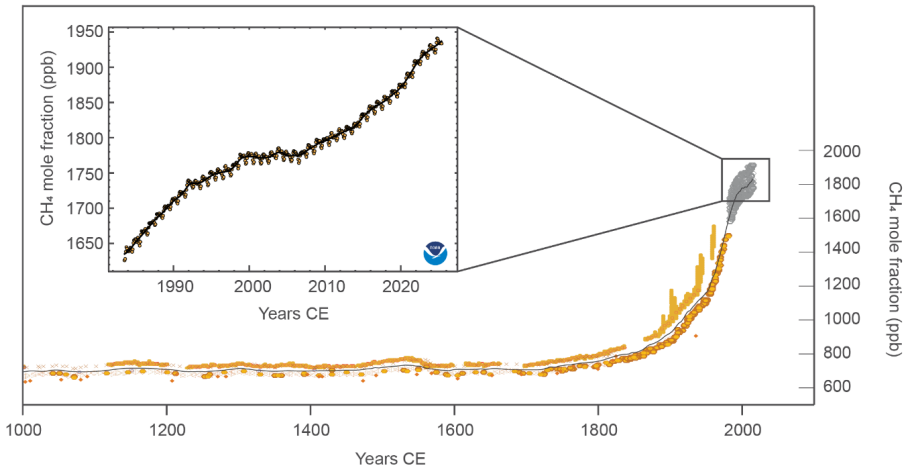


**Fig. 1.** Atmospheric methane concentrations over the past 1000 years from ice core records (adapted from Meinshausen et al. (2017)), with a zoom of the averaged concentrations from 1983 - 2025 measured at a globally distributed network of air sampling sites (adapted from Lan et al. (2025)).

## Microbial pathways for methane production and removal

Methane production in the sediment occurs mainly via anaerobic degradation of organic matter and is primarily mediated by methanogenic archaea (Whiticar, 1999; Welte, 2018). Methanogenesis is possible with various substrates, which are  $H_2/CO_2$  and formate (hydrogenotrophic methanogenesis), acetate (acetoclastic methanogenesis), methylated substrates, such as methanol (methylotrophic methanogenesis), and methoxylated compounds (Liu & Whitman, 2008; Kurth et al., 2020). Generally, methanogenesis starts after the depletion of inorganic electron acceptors for organic matter degradation, which in order of decreasing energy yield are oxygen ( $O_2$ ), nitrate ( $NO_3^-$ ) / nitrite ( $NO_2^-$ ), Mn oxides, Fe oxides and sulfate ( $SO_4^{2-}$ ) (Froelich et al., 1979). Typically, a large fraction of the  $CH_4$  that forms in sediments is removed via aerobic and anaerobic oxidation (Knittel & Boetius, 2009).

Anaerobic oxidation of  $CH_4$  (AOM) can be coupled to reduction of  $SO_4^{2-}$  (Jørgensen et al., 2001; Knittel & Boetius, 2009),  $NO_x$  (Raghoebarsing et al., 2006), Fe and Mn oxides (Beal et al., 2009; Segarra et al., 2013; Egger et al., 2015; Lenstra et al., 2023), and natural organic matter (Valenzuela et al., 2017; Pelsma et al., 2023; Fig. 2a; Table 1). In brackish and marine coastal sediments,  $SO_4^{2-}$ -AOM is the major removal pathway for methane in the so-called sulfate-methane transition zone (SMTZ; Egger

et al., 2018; Fig. 2b). Typically,  $\text{SO}_4^{2-}$ -AOM is performed by a consortium of ANME and sulfate reducing bacteria (SRB) (Boetius et al., 2000). When, under non-steady state conditions, metal oxides are buried into the methanic zone of the sediment, an opportunity for Fe- and Mn-AOM is created (Soyol-Erdene & Huh, 2013; Riedinger et al., 2014; Egger et al., 2017; Lenstra et al., 2023). The stimulation of AOM by metal oxides can also be indirect, when metal oxides produce  $\text{SO}_4^{2-}$  via the oxidation of reduced sulfur in a cryptic sulfur cycle (Holmkvist et al., 2011). Metal AOM is predicted to contribute from 3 % up to 10 % of  $\text{CH}_4$  oxidation in metal-rich brackish and marine sediments (Lenstra et al., 2023; Xiao et al., 2023), yet direct evidence for *in-situ* Mn-AOM in these environments is still lacking.

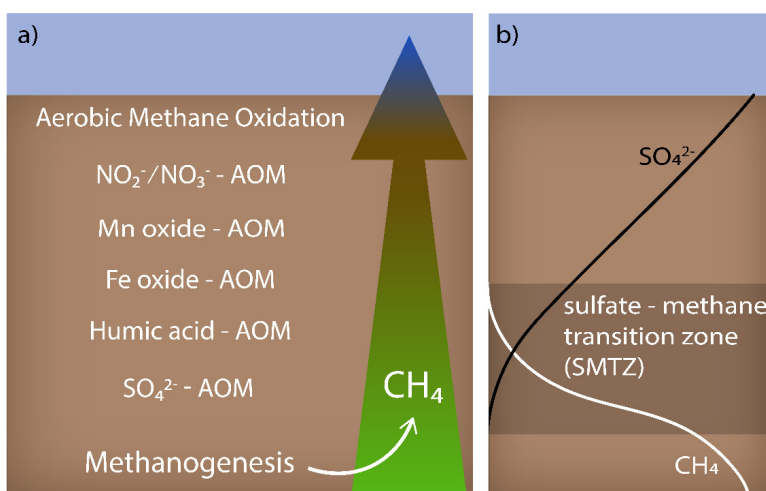


**Fig. 2.** a) Schematic overview of the possible pathways of methane oxidation in sediments (adapted from Wallenius et al., 2021). b) Typical profiles of sulfate and methane when a sulfate-methane transition zone (SMTZ) is present in the sediment.

The focus of research into Mn-AOM has mainly been on freshwater systems, where the process is generally associated with ANME-2d (*Candidatus* Methanoperedens; Ettwig et al., 2016; Leu et al., 2020; Su et al., 2020). ANME-2d can directly couple  $\text{CH}_4$  oxidation to the reduction of metal oxides, independent of a bacterial partner, as shown for Fe oxides (Cai et al., 2018) and Mn oxides (Leu et al., 2020) in a bioreactor enrichment started with a freshwater inoculum. Furthermore, ANME-2d appear to benefit from a Mn oxide driven cryptic sulfur cycle in  $\text{SO}_4^{2-}$  rich lake Cadagno (Su et al., 2020). In brackish and marine sediments, ANME-2d typically have low abundances, however, which makes it unlikely that this is a key organism for Mn-AOM in such environments (Aromokeye et al., 2020; Rasigraf et al., 2020;

Wallenius et al., 2021). A more common methanotroph in brackish and marine sediments is ANME-2ab, now classified as *Candidatus* Methanocomedenaceae (Chadwick et al., 2022). ANME-2a have been linked to Fe-AOM in incubations with marine sediment from the North Sea (Aromokeye et al., 2020). A similar depth trend of ANME-2a and total Fe contents (Rasigraf et al., 2020) in sediments from the brackish Bothnian Sea in which incubations indicate Fe-AOM activity (Egger et al., 2015), also point towards a potential role for ANME-2a in Fe-AOM. Furthermore, ANME-2ab were present in brackish sediments, where incubations showed that CH<sub>4</sub> oxidation could be coupled to a humic acid analogue (Pelsma et al., 2023). Although ANME-2ab were present in marine sediments on the continental slope of South China Sea where Mn-AOM was demonstrated via incubations (Xu et al., 2021), it has never been shown that they can couple CH<sub>4</sub> oxidation and Mn reduction. Therefore details on the key microorganisms involved in Mn-AOM in brackish and marine sediments are still elusive (Wallenius et al., 2021; Xue et al., 2025). A prerequisite for microbes to perform Mn-AOM *in-situ* is that CH<sub>4</sub> and Mn oxides co-occur in the sediment.

**Table 1** The chemical reaction and Gibbs free energy ( $\Delta G^\circ$ ) for the main CH<sub>4</sub> removal pathways.

CH <sub>4</sub> removal pathway	Chemical reaction	$\Delta G^\circ$ [kJ mol <sup>-1</sup> CH <sub>4</sub> ]
Aerobic methane oxidation	$\text{CH}_4 + 2 \text{O}_2 \rightarrow \text{CO}_2 + 2 \text{H}_2\text{O}$	-859 <sup>a</sup>
NO <sub>2</sub> <sup>-</sup> - AOM	$\text{CH}_4 + 8 \text{NO}_2^- + 8 \text{H}^+ \rightarrow 3 \text{CO}_2 + 4 \text{N}_2 + 10 \text{H}_2\text{O}$	-928 <sup>b</sup>
NO <sub>3</sub> <sup>-</sup> - AOM	$\text{CH}_4 + 4 \text{NO}_3^- \rightarrow \text{CO}_2 + 4 \text{NO}_2^- + 2 \text{H}_2\text{O}$	-503 <sup>b</sup>
Mn - AOM	$\text{CH}_4 + \text{MnO}_2 + 7 \text{H}^+ \rightarrow \text{HCO}_3^- + 4 \text{Mn}^{2+} + 5 \text{H}_2\text{O}$	-790 <sup>c</sup>
Fe - AOM	$\text{CH}_4 + 8 \text{Fe}(\text{OH})_3 + 15 \text{H}^+ \rightarrow \text{HCO}_3^- + 8 \text{Fe}^{2+} + 21 \text{H}_2\text{O}$	-572 <sup>c</sup>
NOM - AOM*	$\text{CH}_4 + 4 \text{Q} \cdot \text{NOM}_{\text{ox}} + 2 \text{H}_2\text{O} \rightarrow \text{CO}_2 + 4 \text{QH}_2 \cdot \text{NOM}_{\text{red}}$	-30 to -417 <sup>d</sup>
S - AOM	$\text{CH}_4 + \text{SO}_4^{2-} \rightarrow \text{HCO}_3^- + \text{HS}^- + \text{H}_2\text{O}$	-16.6 <sup>e</sup>

<sup>a</sup> Regnier et al. (2011); <sup>b</sup> In 't Zandt et al. (2020); <sup>c</sup> Sturm et al. (2019); <sup>d</sup> Valenzuela et al. (2022); <sup>e</sup> Meulepas et al. (2010). \*Q · NOM<sub>ox</sub> refers to the oxidizing equivalents which are stored as quinones in oxidized natural organic matter (NOM). QH<sub>2</sub> · NOM<sub>red</sub> refers to reducing equivalents stored as hydroquinones in reduced NOM.

## Manganese cycling in coastal sediments

Manganese is one of the most abundant transition metals in natural environments and an essential micronutrient for phytoplankton (Raven, 1990; Neretin et al., 2003). Furthermore, the Mn cycle interacts with, and hence can impact, other elemental cycles such as those of C, Fe, phosphorus (P), cobalt (Co) and molybdenum (Mo)

(e.g. Van Cappellen & Wang, 1996; Jilbert & Slomp, 2013; Sulu-Gambari et al., 2017). Therefore, a detailed understanding of the Mn cycle is important.

Manganese is mainly supplied to sediments in the form of solid phase Mn oxides, which can include birnessite, pyrolusite and manganite (Burdige et al., 1992; Sulu-Gambari et al., 2016; Luo et al., 2018). Typically, these Mn oxides are thought to be reductively dissolved upon burial into anoxic sediments (Burdige, 1993; Fig. 3). The dissolved Mn that forms can be present as Mn(II) and Mn(III) (Luther, 2010; Madison et al., 2013). Dissolved Mn(III) can form a metastable complex when bound to organic ligands (Kostka et al., 1995; Madison et al., 2011). This dissolved Mn(III)-ligand complex can make up for a significant part of the dissolved Mn in sediment pore water (Madison et al., 2013; Oldham et al., 2019). A part of the dissolved Mn may leave the sediment via a benthic flux (Lenstra et al., 2020). In the water column, dissolved Mn(III) is expected to be more mobile than dissolved Mn(II), because of a lower reactivity (Oldham et al., 2017a). The reactivity of the dissolved Mn(III)-ligand complex is controlled by the strength of the bond between Mn(III) and the organic ligand (Luther et al., 2015; Oldham et al., 2015, 2017a) and may affect the interaction between the Mn cycle and other elemental cycles. While reactive transport models describing organic matter degradation and associated reactions in sediments typically include Mn cycling (e.g. Van Cappellen & Wang, 1996; Lenstra et al., 2018), they so far do not include the dynamics of dissolved Mn(III).

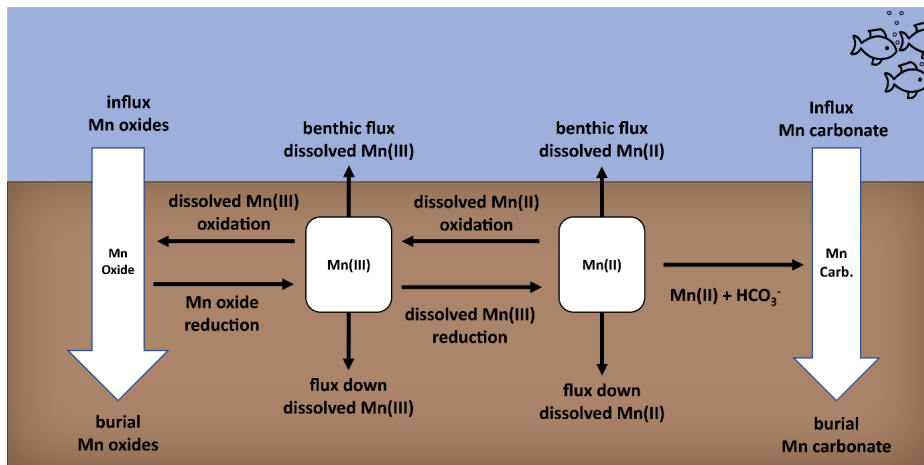


**Fig. 3.** A conceptual model of the manganese redox cycle in coastal sediments.

Diffusion of dissolved Mn into the oxygenated zone of the sediment may lead to re-oxygenation and formation of Mn oxides (Adelson et al., 2001; Slomp et al., 2013). Manganese can go through many reduction-oxidation cycles before either being buried or released to the water column (Canfield et al., 1993). The form in which Mn is buried depends on the redox conditions in the sediment and water column and is therefore indicative of the environmental history. For example, when concentrations of dissolved Mn(II) and alkalinity are high, Mn carbonates can precipitate (Lenz et al., 2014). In coastal sediments with a low salinity, and hence low  $\text{SO}_4^{2-}$  reduction rates, Mn can be buried in vivianite-type minerals  $((\text{Fe, Mn})_3(\text{PO}_4)_2 \cdot 4 \text{H}_2\text{O})$  (Nakano, 1992; Lenstra et al., 2018; Kubeneck et al., 2023). When sulfide ( $\text{H}_2\text{S}$ ) is present in the sediment, authigenic Mn sulfide may form, or Mn can be incorporated in pyrite (Huerta-Diaz and Morse, 1992; Lepland and Stevens, 1998; Lenstra et al., 2020). While various analytical techniques are available to determine forms of Mn in sediments, especially for sediments that are relatively enriched in Mn (e.g. XRD, synchrotron-based X-ray spectroscopy; e.g. Lenz et al., 2014; Lenstra et al., 2018; Hermans et al., 2019), a well-calibrated extraction procedure for sediment Mn is not yet available.

Under non-steady state conditions, sediment Mn oxides can also be buried into the methanic zone, potentially allowing for Mn-AOM (Kasten et al., 1998; März et al., 2008; Riedinger et al., 2014; Lenstra et al., 2023). This has been proposed to occur in marine sediments of the Argentine basin and the Bering Sea, based on the accumulation of dissolved Mn in the presence of  $\text{CH}_4$ , several meters below the sediment-water interface (Soyol-Erdene & Huh, 2013; Riedinger et al., 2014). Mn-AOM could also occur closer to the sediment-water interface in brackish and coastal marine sediments (e.g. Lenstra et al., 2023) and potentially contribute to  $\text{CH}_4$  removal, although direct evidence for this is still lacking.

## **Impact of climate and anthropogenic stresses on methane dynamics**

Over the past decades, coastal zones have changed rapidly due to climate change and anthropogenic stresses (Diaz & Rosenberg, 2008; Breitburg et al., 2018). Enhanced nutrient inputs from agricultural runoff and waste water have led to eutrophication of coastal seas (Doney, 2010). Primary productivity has accelerated and the input of organic matter to sediments has increased. Rising temperatures have led to a decrease in oxygen solubility and increased water column

stratification, which, with a higher oxygen demand from degrading organic matter, promote coastal deoxygenation (Diaz & Rosenberg, 2008).

The recent changes in coastal seas are strongly affecting  $\text{CH}_4$  dynamics in the sediment (Wallenius et al., 2021). Higher inputs of organic matter are promoting methanogenesis (Wallenius et al., 2025). Furthermore, the electron acceptors that can facilitate  $\text{CH}_4$  oxidation are depleted more rapidly. For example, an increased input of organic matter led to a shoaling of the  $\text{SO}_4^{2-}$  penetration depth in sediments of the Bothnian Sea over the past decades (Slomp et al., 2013; Egger et al., 2015; Rooze et al., 2016). As a result, Mn oxides may be exposed to  $\text{CH}_4$ , creating conditions that potentially allow for a role for Mn-AOM (Lenstra et al., 2023). At present, however, we lack insight into the actual occurrence of Mn-AOM in coastal sediments, including the Mn oxide minerals and key microbes potentially involved.

## Thesis outline

The research presented in this thesis focuses on the interaction between  $\text{CH}_4$  and Mn oxides in coastal sediments. This research was conducted as part of a larger project (ERC Synergy MARIX) combining geochemical and microbiological techniques to study  $\text{CH}_4$  and ammonium removal in redox transition zones. This multidisciplinary approach enabled us to study the geochemical context, microbial potential, key microorganisms involved and the environmental significance of Mn-AOM at sites in marine lake Grevelingen and the Bothnian Sea (Fig. 4).

Lake Grevelingen is a eutrophic marine lake in the southwest of the Netherlands (Fig. 4). The lake formed after damming of an estuary in the 1960's/70's (Hagens et al., 2015). Former tidal channels intersect the lake, forming several deeper basins in which temperature-driven stratification in combination with a high oxygen demand due to high organic matter input leads to anoxic or euxinic conditions in summer. One of these basins is the Scharendijke basin, which due to its geometry experiences extremely high sedimentation rates ( $\sim 13 \text{ cm yr}^{-1}$ ) and high input of organic matter ( $\sim 250 \text{ mmol C m}^{-2} \text{ d}^{-1}$ ; Egger et al., 2016). The methanogenic activity and concentrations of  $\text{CH}_4$  throughout the sediment are high (Egger et al., 2016; Wallenius et al., 2025). Furthermore, active Fe-S cycling with a strong seasonal variability is observed in the sediment (Egger et al., 2016), making active Mn cycling in the methanogenic sediments also likely. Hence, this site was considered suitable to study the potential for Mn-AOM.

The Bothnian Sea is a coastal high latitude sea in northern Europe (Fig. 4). The sea is relatively oligotrophic and has permanently oxygenated waters, but is increasingly affected by eutrophication (Kuliński et al., 2022). An associated enhanced organic matter supply to the sediment has led to a shoaling of the SMTZ over recent decades (Slomp et al., 2013; Egger et al., 2015; Rooze et al., 2016). Bothnian Sea sediments are characterized by high Mn oxide contents, and burial of metal oxides within and below the SMTZ at many sites (Slomp et al., 2013; Egger et al., 2015; Lenstra et al., 2023). In these sediments, Fe-AOM is possible (Egger et al., 2015), therefore the occurrence of Mn-AOM is also expected.

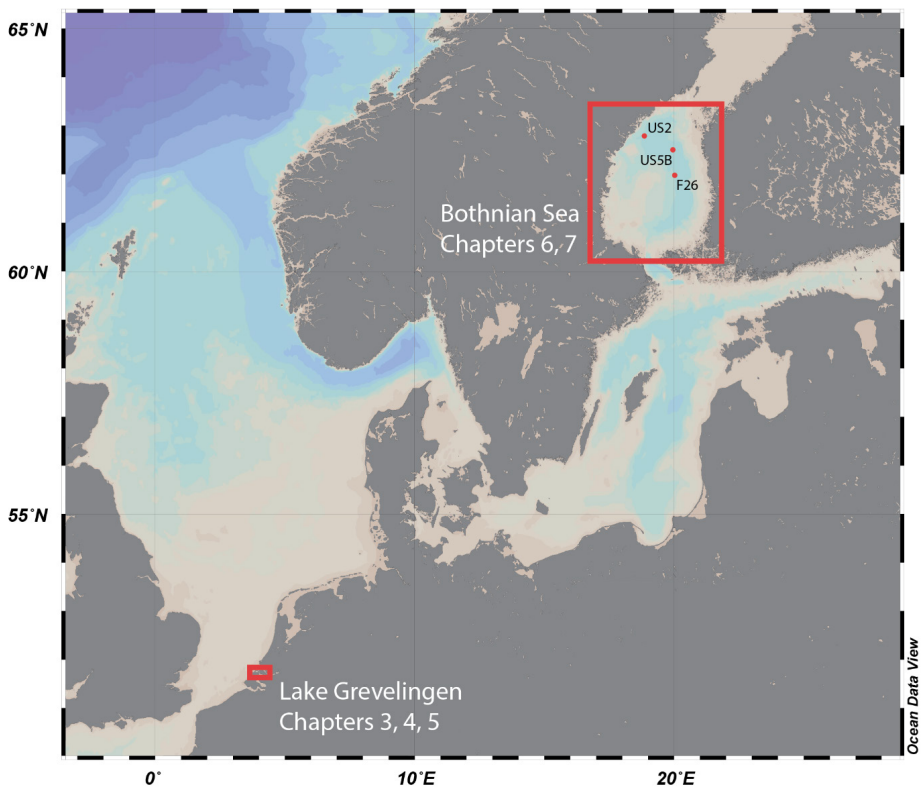


**Fig. 4.** A map showing the locations of the main study areas: Lake Grevelingen (The Netherlands) and the Bothnian Sea (northern Europe), including the locations of study sites US2, USSB and F26. Figure obtained with Ocean Data View (Schlitzer, 2023).

At both study sites, we combined geochemical and microbiological analyses to understand the factors that control the sedimentary microbial  $\text{CH}_4$  filter and to explore the role of Mn oxides in  $\text{CH}_4$  oxidation. The geochemical analyses

include analyses of the sediment via total sediment digestions, sequential extractions for the speciation of Mn, Fe and S, and synchrotron-based X-ray absorption spectroscopy to further specify Mn speciation. Porewater was analyzed via spectrophotometric assays to, amongst others, determine the redox state of dissolved Mn, ion chromatography for  $\text{SO}_4^{2-}$  concentrations, Inductively Coupled Plasma Optical Emission Spectroscopy (ICP-OES) for dissolved metal concentrations, gas chromatography to determine  $\text{CH}_4$  concentrations, continuous-flow isotope ratio mass spectrometry to determine the C and D isotopes of  $\text{CH}_4$  and gas chromatography coupled to a mass spectrometer to determine dissolved inorganic carbon concentrations and isotopic C composition. We also measured  $\text{SO}_4^{2-}$  reduction rates using radioactive tracer experiments and  $\text{CH}_4$  production and oxidation rates via sediment incubations. Reactive transport modelling was used to quantify reactions in the Mn cycle and evaluate the effect of environmental changes on the Mn cycle.

The microbiological analyses include 16S rRNA gene amplicon sequencing, qPCR, metagenomics and metatranscriptomics to determine the diversity and activity of the microbial community in the sediment. We performed incubation experiments with isotopically labelled  $^{13}\text{C}-\text{CH}_4$  to determine the potential for Mn-AOM, Fe-AOM,  $\text{SO}_4^{2-}$ -AOM and NOM-AOM in the sediment. We monitored changes in the  $\text{CO}_2$  isotopes via gas chromatography coupled to a mass spectrometer and in the concentrations of dissolved metals,  $\text{SO}_4^{2-}$  and  $\text{H}_2\text{S}$ . Changes in the microbial community composition were determined using 16S rRNA gene amplicon sequencing and metagenomic analyses to identify the key microbes involved.

In **chapter 2**, we calibrated a sequential extraction method to determine Mn mineral speciation in the sediment. The extraction method consists of 5 steps, which we validated using 16 different Mn standards and tested on coastal sediments from locations with bottom water redox conditions ranging from euxinic to oxic. The Mn standards show that the extraction steps separate (1) poorly ordered Mn oxides and Mn phosphates, (2) Mn carbonates and Mn sulfides, (3, 4), crystalline Mn oxides and (5) Mn associated with pyrites. The sediment samples show that the Mn mineral speciation depends on the bottom water redox conditions at the sites. When the bottom water is permanently anoxic or sulfidic, Mn carbonate, pyrite and non-reactive Mn occur in approximately equal amounts. When anoxia or euxinia is periodic, Mn carbonate is the dominant form of Mn, and small amounts of Mn oxide occur. Under oxic bottom waters, Mn oxides, Mn-rich vivianite-type minerals and Mn carbonates are the most common forms of Mn. This extraction procedure allows quantification of various Mn forms in marine sediment and can be applied

to large numbers of samples. This relatively easy separation of Mn mineral forms is very useful for studies of Mn cycling in sediments.

**Chapter 3** focuses on the role of dissolved Mn(III) bound to organic ligands in Mn dynamics in the sediment of Scharendijke basin in Lake Grevelingen. For this, the dynamics of dissolved Mn(III) were, for the first time, incorporated in a sediment reactive transport model, and the model results were verified with measured sediment and porewater profiles. Our study shows that dissolved Mn(III) is a key component in the sedimentary Mn cycle, not only under oxic, but also under euxinic bottom waters. Dissolved Mn(III) even coexists with high  $\text{H}_2\text{S}$  concentrations in the porewater. The results of the reactive transport modelling highlight strong interactions between the sedimentary Fe and Mn cycles. Modelled benthic fluxes reveal the highest release of dissolved Mn(III) when bottom waters are oxygenated, which partly persists throughout the euxinic months. The benthic release during bottom water euxinia is in line with the detection of dissolved Mn(III) in the euxinic part of the water column. Dissolved Mn(III) bound to organic matter is a relatively stable and mobile form of Mn, compared to dissolved Mn(II). Therefore, the release of dissolved Mn(III) may contribute to increased lateral transport of Mn throughout coastal waters and possibly also to open marine waters.

In **chapter 4** we follow the seasonal dynamics of the microbial  $\text{CH}_4$  filter in the sediment of Lake Grevelingen, where high input of organic matter during summer stratification drives intense  $\text{SO}_4^{2-}$  reduction and the development of bottom water euxinia. Buffering by Fe oxides maintains the sediment layer deposited during the prior winter and spring period free of  $\text{H}_2\text{S}$  throughout the year. This  $\text{H}_2\text{S}$ -free sediment provides a narrow niche where the abundance of ANME-2ab and ANME-3 increases during the summer. We find a strong anti-correlation between  $\text{H}_2\text{S}$  in the porewater and the abundance of ANME, in line with  $\text{H}_2\text{S}$  toxicity for the ANME. In contrast, the methanogenic community flourishes under sulfidic conditions. As a result, the sulfidic sediment is highly favorable for net  $\text{CH}_4$  production and the benthic release of  $\text{CH}_4$ .

**Chapter 5** explores the potential for Mn driven  $\text{CH}_4$  oxidation in the sediment of Lake Grevelingen via a combination of geochemical profiling and sediment incubations. Manganese oxides are buried below the SMTZ due to the high sedimentation rate and seasonality in bottom water redox conditions. We tested the potential for a coupling of  $\text{CH}_4$  oxidation in the sediment to reduction of the Mn oxides birnessite, pyrolusite and manganite and dissolved Mn(III) through incubations with  $^{13}\text{C}$ -labeled  $\text{CH}_4$ . Dissolved Mn(III) was tested when bound to either a strong or

a weak organic ligand. A clear signal of CH<sub>4</sub> oxidation was obtained with birnessite. Pyrolusite and manganite also enhanced CH<sub>4</sub> oxidation but at a lower rate. Organic-ligand bound dissolved Mn(III) did not impact CH<sub>4</sub> oxidation rates. A cryptic sulfur cycle likely contributed to CH<sub>4</sub> oxidation when birnessite and pyrolusite were the electron acceptors since SO<sub>4</sub><sup>2-</sup> emerged in the incubations. Based on 16S rRNA gene amplicon sequencing of the sediments from the incubations, we conclude that ANME-2ab were likely involved in CH<sub>4</sub> oxidation directly coupled to Mn oxide reduction, whereas ANME-3 likely primarily benefited from a cryptic sulfur cycle driven by Mn oxide reduction.

In **chapter 6** we unravel the functioning of the sedimentary microbial CH<sub>4</sub> filter in the Bothnian Sea (site US2) combining sediment and porewater profiles, 16S rRNA gene amplicon sequencing, metagenomics, metatranscriptomics and sediment incubations. We find that the strongest CH<sub>4</sub> removal occurred in the SMTZ performed by ANME-2ab. These ANME are also present and active below the SMTZ, where they depend on other electron acceptors than SO<sub>4</sub><sup>2-</sup>. We tested the potential for CH<sub>4</sub> oxidation with SO<sub>4</sub><sup>2-</sup>, Mn oxide, Fe oxide and a humic acid analogue via sediment incubations. We showed that both within and below the SMTZ, all tested electron acceptors could drive AOM by ANME-2ab, however the role of a cryptic sulfur cycle could not always be excluded. The variety of AOM pathways that are possible by ANME likely contribute to the resilience of the microbial CH<sub>4</sub> filter in brackish coastal sediments.

In **chapter 7** we provide evidence for a direct coupling between Mn oxide reduction and CH<sub>4</sub> oxidation in brackish coastal sediments, i.e. without a cryptic sulfur cycle involved, performed by ANME-2ab. Incubations with sediment from the Bothnian Sea (site US5B) showed that the Mn oxides birnessite and pyrolusite both enhanced CH<sub>4</sub> oxidation. Incubations where birnessite was added in combination with molybdate, an inhibitor for SO<sub>4</sub><sup>2-</sup> reduction, showed similar results as incubations with birnessite without molybdate, indicating that CH<sub>4</sub> oxidation with Mn oxides is independent of SO<sub>4</sub><sup>2-</sup> reduction. Analysis of 16S rRNA genes and metagenomic sequencing revealed that ANME-2ab are the responsible microorganisms and suggest that these organisms use extracellular electron transfer to perform Mn-AOM.

In **chapter 8**, the findings of **chapter 2 - 7** are summarized and integrated into a broader scientific context. Furthermore, we provide an outlook for future research.





## Chapter 2

# A sequential extraction procedure for particulate manganese and its application to coastal marine sediments

---

W.K. Lenstra<sup>1</sup>, R. Klomp<sup>1</sup>, F. Molema<sup>1</sup>, T. Behrends<sup>1</sup>, C.P. Slomp<sup>1</sup>

<sup>1</sup>Department of Earth Sciences - Geochemistry, Utrecht University, PO Box 80021, 3508 TA Utrecht,  
The Netherlands

This chapter was published in *Chemical Geology*:

Lenstra, W. K., Klomp, R., Molema, F., Behrends, T., & Slomp, C. P. (2021). A sequential extraction procedure for particulate manganese and its application to coastal marine sediments. *Chemical Geology*, 584(June), 120538. <https://doi.org/10.1016/j.chemgeo.2021.120538>

## Abstract

An existing sequential extraction scheme for particulate iron (Fe) is evaluated for manganese (Mn) using a range of Mn standards. The scheme consists of 5 steps and quantifies 5 operationally defined Mn pools (1) poorly ordered Mn oxides and Mn phosphates (ascorbic acid extractable); (2) Mn carbonates and Mn sulfides (1 M HCl extractable), (3 and 4) crystalline Mn oxides (citrate buffered dithionite and ammonium oxalate extractable, respectively) and (5) Mn associated with pyrite (concentrated HNO<sub>3</sub> extractable). Application of the extraction scheme to coastal sediments from six locations (Black Sea, Baltic Sea, Bothnian Sea, Gulf of Mexico and Chesapeake Bay) highlights the dependency of sediment Mn partitioning on bottom water redox conditions. In sediments deposited in anoxic and sulfidic (euxinic) bottom waters, Mn is mostly present in Mn carbonates, pyrite and in non-reactive Mn forms, in approximately equal amounts. We find that in sediments deposited in periodically euxinic and hypoxic (oxygen <63 μmol L<sup>-1</sup>) waters, Mn carbonates dominate over the two other fractions, and small amounts of Mn oxides are observed. In sediments deposited in oxygenated bottom waters, Mn oxides, Mn-rich vivianite-type minerals and Mn carbonates dominate and no pyrite-bound Mn is observed. A large advantage of the extraction scheme is that it quantifies sediment forms of Mn and Fe simultaneously. Given the role of Mn as a bottom water redox proxy, the separation of poorly ordered Mn oxides, carbonates and pyrite is of specific relevance.

## Keywords

Manganese, Sequential extraction, Sediments, Manganese standards

## Introduction

Manganese (Mn) is a key micro-nutrient in marine surface waters (Raven, 1990; Moore et al., 2013). The cycling of Mn in the marine environment interacts with that of iron (Fe), carbon, phosphorus, nitrogen, sulfur and various trace metals (Burdige, 1993; Canfield et al., 1993; Luther et al., 1997; Beal et al., 2009). For example, Mn oxides can act as an electron acceptor in the oxidation of organic matter and as a carrier for phosphorus, cobalt and nickel (Goldberg, 1954; Koschinsky and Hein, 2003; Jilbert and Slomp, 2013). In ancient sediments, Mn contents are frequently used as a proxy of bottom water oxygen concentrations (i.e. Calvert and Pedersen (1993), Johnson et al. (2016), Ostrander et al. (2019)). With the present-day expansion of low oxygen areas in the open and coastal ocean (Breitburg et al., 2018), detailed insight into the forms of Mn in sediments and the water column and their response to environmental changes is becoming increasingly important. In oxic waters and surface sediments, particulate Mn is mainly present in the form of Mn oxides (Fig. 1; Calvert and Pedersen (1993), Burdige (1993)). These Mn oxides can consist of minerals within the group of tecto- and phyllo-manganates such as birnessite and pyrolusite or crystalline forms such as manganite and bixbyite (Hem and Lind, 1983; Anschutz et al., 2005). Upon burial or downward mixing by macrofauna, Mn oxides can be reductively dissolved during the degradation of organic matter or through reactions with sulfide ( $\text{H}_2\text{S}$ ), dissolved Fe(II) or  $\text{CH}_4$  (Postma, 1985; Burdige, 1993; Beal et al., 2009). This leads to release of dissolved Mn to the porewater, either as Mn(II) or Mn(III) (Madison et al., 2013). Upward diffusing dissolved Mn(II) and Mn(III) can be re-oxidized in the oxic surface sediment and again form Mn oxides (Sundby and Silverberg, 1985; Learman et al., 2011). In anoxic sediments, where dissolved Mn(II) and carbonate ( $\text{CO}_2^-$ ) concentrations in porewaters are high, red  $\text{MnCO}_3$  or mixed Mn-Mg-Ca carbonate phases, such as rhodochrosite or pseudokutnahorite, may form (Middelburg et al., 1987; Mucci, 1988; Neumann et al., 2002). In coastal sediments with a low salinity, vivianite-type minerals rich in Mn ( $(\text{Fe}, \text{Mn})_3(\text{PO}_4)_2 \cdot 4 \text{H}_2\text{O}$ ) can contribute to burial of Mn (Nakano, 1992; Egger et al., 2015; Lenstra et al., 2018). In sulfidic sediments, part of the dissolved Mn can be incorporated in pyrite or in authigenic Mn sulfide minerals, such as alabandite and rambergite, (Suess, 1979; Lepland and Stevens, 1998; Huerta-Diaz and Morse, 1992; Lenstra et al., 2020). A small fraction of non-reactive Mn can be present in clays, such as smectites and primary Fe-Mg silicates.

Changes in particulate Mn forms with depth and time in sediments and the water column are frequently inferred from trends in total Mn contents (i.e. Lyons and Severmann (2006), Dellwig et al. (2007), Sulu-Gambari et al. (2017)). For example,

when oxic marine bottom waters transition into anoxia, surface sediments typically become depleted of Mn (Calvert and Pedersen, 1993; Brumsack, 2006). This is usually attributed to reductive dissolution of Mn oxides and escape of the dissolved Mn to the water column (Sulu-Gambari et al., 2017; Hermans et al., 2021). This dissolved Mn may then precipitate again as Mn oxide in the water column upon contact with oxygen in the redoxcline and the Mn oxide may then settle on the seafloor. Analyses of the chemical and mineral composition of particulate Mn from marine environments with XRD, synchrotron-based X-ray spectroscopy and SEM-EDS have confirmed such redox driven cycles. (Lenz et al., 2014; Lenstra et al., 2020; Lee et al., 2021). While these latter methods allow the identification and, in suspended matter, quantification of Mn minerals, these techniques are rather time-intensive (e.g. Lam et al. (2015)). Hence, they can typically only be carried out for a subset of samples and need to be complemented with bulk geochemical analyses by wet chemical techniques. Various single step and sequential procedures for the extraction of particulate Mn have been proposed (Tessier et al., 1979; Hyacinthe et al., 2001; Hyacinthe and Van Cappellen, 2004; Anschutz et al., 2005; Mouret et al., 2009). However, to date, these methods have not been applied in a sequential scheme, calibrated with standards for key Mn minerals.

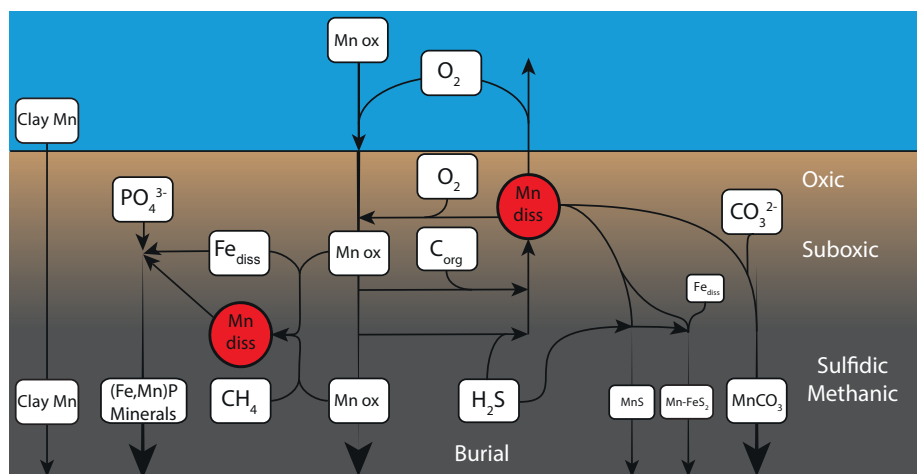


**Fig. 1.** Schematic overview of Mn dynamics in coastal sediments. Mn ox: Mn oxides, Clay Mn: Mn associated with clays, Mn<sub>diss</sub>: dissolved Mn, C<sub>org</sub>: organic carbon, Fe<sub>diss</sub>: dissolved Fe, Mn-FeS<sub>2</sub>: Mn associated with pyrite, MnS: Mn sulfides, MnCO<sub>3</sub>: Mn carbonates.

In this study, we present a 5-step sequential extraction procedure for Mn, which we apply to a total of sixteen standards that include various types of Mn oxides, Mn phosphates, Mn carbonate, Mn sulfide and clays. This procedure combines steps from

three sequential extraction schemes used for the partitioning of solid phase Fe (Poulton and Canfield, 2005; Claff et al., 2010; Raiswell et al., 2010) as presented by Lenstra et al. (2019) in a study of Black Sea sediments and suspended matter. We demonstrate that the method is particularly successful in separating poorly ordered Mn oxides, Mn carbonates and Mn in pyrite. By applying the method to a range of coastal sediments, we further demonstrate its suitability in distinguishing particulate Mn phases.

## Material and methods

### Mn extraction scheme

The 5-step sequential extraction procedure applied in this study (Table 1) employs (1) ascorbic acid (pH 7.5) to extract poorly ordered Mn oxides such as birnessite and pyrolusite (Raiswell et al., 2010; Hyacinthe and Van Cappellen, 2004); (2) 1 M HCl to dissolve metal carbonates (Claff et al., 2010); (3) citrate buffered dithionite and (4) ammonium oxalate to extract crystalline metal oxides (Poulton and Canfield, 2005) and (5) concentrated HNO<sub>3</sub> to extract Mn bound in pyrite (Huerta-Diaz and Morse, 1992; Claff et al., 2010). All solutions were deoxygenated before addition to the samples, except for the concentrated HNO<sub>3</sub> solution. All reagents used during the sequential extraction procedure were analytical grade and the solutions were prepared using deionised (Milli-Q) water.

**Table 1** Sequential extraction procedure based on Raiswell et al. (2010), Poulton and Canfield (2005) and Claff et al. (2010) as presented in Lenstra et al. (2019). All extraction steps were performed at room temperature.

Step	Extractant	Time (h)	Terminology	Reference
1	0.17 M sodium citrate, 0.6 M sodium bicarbonate and 0.057 M ascorbic acid (pH 7.5)	24	Mn Asc	Raiswell et al. (2010)
2	1 M HCl	4	Mn HCl	Huerta-Diaz and Morse (1990)
3	50 g L <sup>-1</sup> sodium dithionite solution buffered to pH 4.8 with 0.35 M acetic acid/ 0.2 M sodium citrate	4	Mn CDB	Poulton and Canfield (2005)
4	0.2 M ammonium oxalate/ 0.17 M oxalic acid (pH 3.2)	6	Mn Oxalate	Poulton and Canfield (2005)
5	65% HNO <sub>3</sub>	2	Mn HNO <sub>3</sub>	Lord (1982), Claff et al. (2010)

Aliquots of ca. 20 mg of each Mn standard (in triplicate) and 100 mg of each sediment sample were subjected to 10 ml of extractant in each step. During the extraction the samples were shaken on a shaker table. After extraction, all solutions

were centrifuged and subsequently passed through a 0.45  $\mu\text{m}$  nylon filter except for the concentrated  $\text{HNO}_3$  solution. Concentrations of Mn were analyzed by Inductively Coupled Plasma Optical Emission Spectroscopy (ICP-OES; Spectro Arcos).

To gain insight in the dissolution kinetics of Mn oxides and Mn phosphate during the 24 h extraction with ascorbic acid (Step 1; Table 1), experiments were performed using birnissite, manganite and Mn bearing vivianite (Mn/Fe ratio: 0.1) standard. All Mn experiments were carried out in triplicate on ca. 20 mg of the Mn standards using 10 ml of extractant. During this extraction 5 samples were taken with time at 0, 1.1, 2.55, 4.45, 6.35 and 24 h after the start.

### Mn standards

The sixteen Mn standards consist of six different types of Mn oxides, capturing various crystallinities and redox states, a range of six vivianite-type minerals ( $(\text{Fe}, \text{Mn})_3(\text{PO}_4)_2 \cdot 4 \text{H}_2\text{O}$ ) with varying ratios of Fe and Mn, a Mn carbonate (rhodochrosite), a Mn sulfide (alabanite) and two clay samples (two types of smectite; Table 2). One of the amorphous Mn oxide standards was obtained from a Mn nodule.

The vivianite-type minerals were synthesized by mixing a 0.2 M Mohr salt solution ( $(\text{NH}_4)_2\text{Fe}(\text{SO}_4)_2 \cdot 6 \text{H}_2\text{O}$ ) with a solution of 0.16 M ammonium acetate and 0.47 M disodium phosphate in an argon filled glovebox (1:1 volume ratio) following the procedure described by Rouzies and Millet (1993). To synthesize vivianite-type minerals with varying Mn concentrations, we added 0.6 M  $\text{MnCl}_2$  solution in various ratios to the solutions following Dijkstra et al. (2018a), and always kept the P:(Fe+Mn) ratio at 1:1. All chemical solutions were deoxygenated before mixing and prepared in sulfate-free artificial seawater with a salinity of 14, as in Dijkstra et al. (2018a). Artificial seawater was prepared according to Millero (1974) after Kester et al. (1967). After combining the Fe, Mn and phosphate containing solutions, these were shaken for 48 h under an argon atmosphere. Subsequently, the supernatant was removed by centrifuging and the minerals were washed twice with deoxygenated water and dried under an argon atmosphere for 7 days.

To determine the total elemental concentrations of the Mn standards, all standards were ground in an agate mortar and ca. 10 mg was digested in 2.5 ml mixed acid ( $\text{HNO}_3$ : $\text{HClO}_4$ ; 2:3) and 2.5 ml 40% HF at 90 °C. After fuming off the acids, the residue was redissolved in 2.5 ml concentrated  $\text{H}_2\text{O}_2$  and 2.5 ml concentrated HCl. After fuming off the  $\text{H}_2\text{O}_2$  and HCl, the residue was redissolved in 1 M  $\text{HNO}_3$ . The solutions were subsequently analyzed for total Al, Ca, Fe, Mn, P, S and Ti by ICP-OES. The average analytical uncertainty based on duplicates was 6% for Mn.

The mineralogy of all Mn standards was determined by X-ray diffraction (XRD) using a Bruker D2 diffractometer with Cobalt K $\alpha$  radiation over a 5–85  $2\theta$  range with a step size of 0.026°. The characterization of the Mn standards using XRD is described in Supplementary Information (Fig. A.1).

### **Sediment collection and analyses**

The sequential extraction scheme was applied to coastal sediments from six sites, which were selected to capture a range of bottom water redox conditions (Table 3). The sites are located in the euxinic Northern Gotland basin in the Baltic Sea (LL19), the seasonally hypoxic Gulf of Finland (GoF5), the oxic deep basin of the Bothnian Sea (US5B), the hypoxic shelf edge near the chemocline in the northwestern Black Sea (Black Sea 6), the seasonally hypoxic Louisiana shelf in the Gulf of Mexico (GoM1) and an oxic estuary in Chesapeake Bay (ET5.1).

Sediment depth profiles of organic carbon, total Mn, and pyrite, and porewater profiles of dissolved Mn and H<sub>2</sub>S determined for these sites were all previously published except for site GoM1 in the Gulf of Mexico (Table 3). We briefly summarize the methods here. At each site, a sediment core was collected and sliced under a nitrogen atmosphere. Porewater was extracted via centrifugation and sediments were subsequently freeze-dried and ground in an agate mortar under an argon atmosphere. Total Mn in the sediment was determined through dissolution with HF and HNO<sub>3</sub> and analyzed with an ICP-OES as described in Section 2.2. Organic carbon contents were determined on a NCS analyzer after decalcification. Pyrite was determined as chromium reducible sulfur. For further details on the procedures for site GoM1, we refer to Lenstra et al. (2019).

The bottom water salinity at the sites, as determined with a CTD system at the time of sampling, ranged from 5.2 at ET5.1 to 35.6 at GoM1 (Table 3). Organic carbon contents in the surface sediment ranged from 0.8 wt% at GoM1 to 10.4 wt% at GoF5 (Table 3). Sediments at all sites contained pyrite (Fig. A.2), with highest concentrations at the euxinic (LL19) and seasonally hypoxic site in the Baltic Sea (GoF5). Dissolved porewater Fe was lowest at the euxinic sites and highest at the oxic sites (Fig. A.2).

**Table 2** Source and total elemental concentrations of the manganese standards included in this study, bdl is below detection limit. The Mn minerals were characterized with XRD (Fig. A.1). The low amount of sample used (i.e. 10 mg) for the determination of the total element composition might lead to some uncertainties in these numbers.

Standard XRD characterization <sup>a</sup>	Source	Al μmol g <sup>-1</sup>	Ca μmol g <sup>-1</sup>	Fe μmol g <sup>-1</sup>	Mn μmol g <sup>-1</sup>	P μmol g <sup>-1</sup>	S μmol g <sup>-1</sup>	Ti μmol g <sup>-1</sup>
<i>Mn(IV) oxide</i>								
Mn nodule	In house collection	1349	303	2668	2238	71	147	135
Pyrolusite	Alfa Aesar	402	590	29	6994	72	bdl	bdl
<i>Mn(IV/III) oxide</i>								
Birnessite	LGIIT <sup>b</sup>	366	32	13	10.491	bdl	342	bdl
<i>Mn(III) oxide</i>								
Manganite	Ward	351	53	360	2125	bdl	bdl	bdl
Bixbyite	Alfa Aesar	352	35	13	12.231	bdl	bdl	bdl
<i>Mn(II/III) oxide</i>								
Hausmannite	Alfa Aesar	368	49	42	5921	bdl	bdl	bdl
<i>Mn(II) phosphate</i>								
Hureaulite	Alfa Aesar	115	307	9	5970	5768	382	bdl
Switzerite	Synthesis	401	67	27	5663	4403	bdl	bdl
Mn/Fe (6)	Synthesis	341	44	892	5369	3993	32	bdl
Mn/Fe (2)	Synthesis	68	117	2322	4558	4397	244	bdl
Mn/Fe (0.5)	Synthesis	353	21	3834	1976	3808	191	bdl
Mn/Fe (0.1)	Synthesis	403	20	5179	560	3603	427	bdl
<i>Mn carbonate</i>								
Rhodochrosite	Baker	401	41	25	9154	bdl	bdl	bdl

**Table 2** Continued

Standard XRD characterization <sup>a</sup>	Source	Al μmol g <sup>-1</sup>	Ca μmol g <sup>-1</sup>	Fe μmol g <sup>-1</sup>	Mn μmol g <sup>-1</sup>	P μmol g <sup>-1</sup>	S μmol g <sup>-1</sup>	Ti μmol g <sup>-1</sup>
<i>Mn(II) sulfide</i>								
Alabanite	Alfa Aesar	254	41	29	10.577	bdl	8235	bdl
<i>Clay</i>								
Smectite-1	Clay mineral society	3706	108	773	5	27	218	104
Smectite-2	Clay mineral society	2581	332	2287	3	38	490	84

<sup>a</sup> XRD characterization: main mineral observed by XRD, complete overview in given in the appendix and Fig. A.1

<sup>b</sup> Laboratoire de Géophysique Interne et Tectonophysique

**Table 3** Location and site characteristics of the six sites included in this study, BW is bottom water.

Basin	Label	Latitude N	Longitude	Depth mbss	Organic carbon <sup>a</sup> wt%	BW oxygen μmol L <sup>-1</sup>	BW salinity	Year of sampling	Reference
Baltic Sea	LL19	58°53.24'	20°19.5'E	173	9.6	0 (H <sub>2</sub> S: 6.3)	11.7	2016	a
Baltic Sea	Gof5	59°57.10'	25°11.02'E	65	10.4	11	9.4	2016	b
Black Sea	Black Sea 6	43°45.9'	30°05.1'E	114	0.9	27	20	2015	c
Gulf of Mexico*	GoM1	28°48.55'	91°20.12'W	16	0.8	56	35.6	2018	d
Bothnian Sea	US5B	62°35.17'	19°58.13'E	214	3.2	180	6	2013	e
Chesapeake Bay	ETS.1	38°48.36'	75°54.66'W	4	6.2	339	5.2	2017	f

<sup>a</sup> Lenstra et al. (2021)

<sup>b</sup> Hermans et al. (2021)

<sup>c</sup> Lenstra et al. (2020)

<sup>d</sup> Lenstra et al., (2022)

<sup>e</sup> Egger et al. (2015)

<sup>f</sup> Kubeneck et al. (2021)

## Results and discussion

### Sequential extraction of Mn standards

The application of the 5-step sequential extraction procedure (Table 1) to the sixteen Mn standards (Table 2) revealed distinct differences in the solubility of the various Mn forms (Fig. 2; Table A.1). The ascorbic acid solution (Step 1), efficiently extracted the tecto- and phyllo-manganates birnessite (99%) and pyrolusite (87%) and the amorphous Mn oxides in the nodule (88%), but only partially dissolved the crystalline Mn oxides manganite (49%), bixbyite (48%) and hausmannite (40%). This indicates that not all Mn oxides are necessarily dissolved during a 24 h extraction with ascorbic acid. This contrasts with the observations of Hyacinthe and Van Cappellen (2004) who reported efficient extraction of birnissite, bixyite, hausmannite and pyrolusite using this procedure. The difference might be related to differences in the composition of the Mn standards and/or differences in ageing (Eitel et al., 2018), which might especially affect the extraction of Mn minerals from older sediments and rocks.

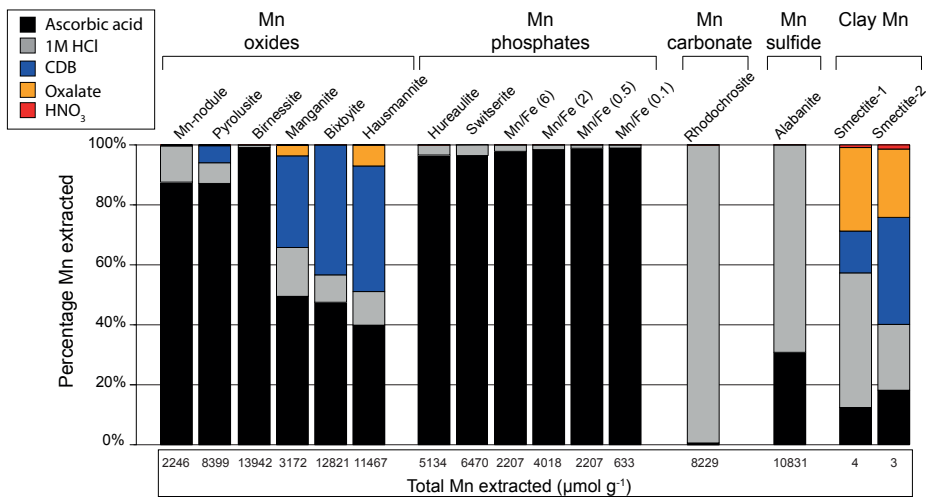


**Fig. 2.** Percentages of Mn extracted from sixteen standards (Table 2) during the 5-step sequential extraction procedure (Table 1). Total extracted Mn during the procedure for the different standards is given at the bottom of each bar in  $\mu\text{mol g}^{-1}$ . Percentages and values are means of triplicate analyses. Amounts of Mn extracted, including standard deviations for all extraction steps are presented in Table A.1.

Ascorbic acid was highly efficient in extracting all Mn phosphates and vivianite-type minerals (>95%; Fig. 2), besides Mn oxides. The dissolution of the vivianite-type minerals slightly decreased with increasing Mn content, from 99% (Mn/Fe ratio: 0.1) to 96% for switzerite (the Mn-rich end-member), which could indicate that the mineral

stability increases slightly when the Mn content in the minerals is high. The ascorbic acid solution did not dissolve Mn carbonates (<1%) but did dissolve some MnS (ca. 30%), as also observed by Hyacinthe and Van Cappellen (2004).

The 1 M HCl solution (Step 2) efficiently extracted Mn carbonate (99%) and Mn sulfide (70%; Fig. 2). A small amount of the crystalline Mn oxides, manganite (16%), bixbyite (9%) and hausmannite (11%), was extracted in 1 M HCl as well. This demonstrates that 1 M HCl mainly targets Mn carbonates and Mn sulfides and that these can be differentiated from the poorly ordered Mn oxides and Mn phosphates that are extracted in the first step of this method.

The CDB and ammonium oxalate solutions (Step 3 and 4) are widely used to extract crystalline Fe oxides, such as goethite, hematite and magnetite (Poulton and Canfield, 2005; Claff et al., 2010). We observed that the CDB and ammonium oxalate solutions extracted the remaining part of the crystalline Mn oxides (i.e. manganite, bixbyite and hausmannite; Fig. 2). However, because these Mn oxides were partly dissolved in the first two steps, poorly ordered and more crystalline Mn oxides cannot be fully separated via this procedure.

Concentrated HNO<sub>3</sub> (Step 5) is commonly used to extract pyrite and associated trace metals after the extraction of the other metal phases (Lord, 1982; Huerta-Diaz and Morse, 1992; Claff et al., 2010). Since no other Mn standards are extracted in the concentrated HNO<sub>3</sub> solution, this suggests that this step is indeed specific for Mn associated with pyrite. Part of the Mn in the smectites was extracted in all steps. However, the total extracted Mn concentrations were very low (<5 μmol g<sup>-1</sup>; Fig. 2; Table A.1).

The kinetic experiments with ascorbic acid were performed on two minerals that were nearly completely dissolved in this step (i.e. poorly ordered Mn oxide (birnessite) and Mn bearing vivianite (Mn/Fe ratio: 0.1)) and one mineral that was partly dissolved (crystalline Mn oxide (manganite); Fig. 3). Dissolved Mn concentrations in the birnessite and Mn bearing vivianite experiment both reach a plateau after ca. 2.5 h, which indicates that the complete dissolution of these minerals occurs relatively fast (Fig. 3A and C). Concentrations of dissolved Fe and Mn versus time in the ascorbic acid extraction of Mn bearing vivianite were nearly identical. This suggests that the mineral dissolved homogeneously and that there is no preferential release of either Mn or Fe. Manganite dissolution does not reach a plateau in the experiment (Fig. 3B), which is in accordance with our observation that ca. 50% of manganite dissolved in the ascorbic acid solution during the 24 h extraction. In future experiments, the effect of shortening the extraction time of the

ascorbic acid extraction might be assessed in more detail to improve the separation between poorly ordered Mn oxides, such as birnessite, and vivianite-type minerals and the crystalline Mn oxides, such as manganite.

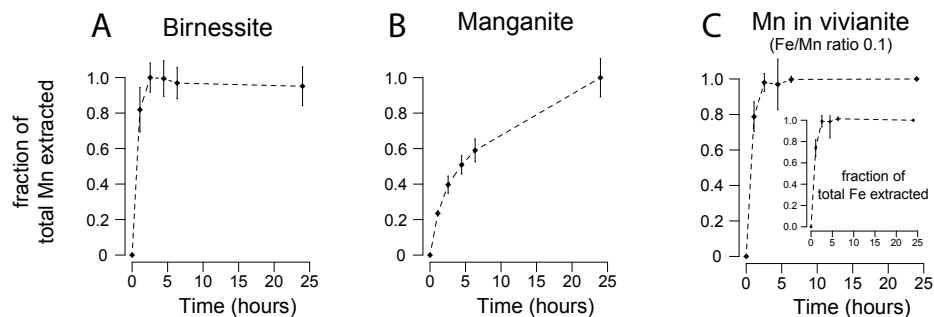


**Fig. 3.** Fraction of Mn (and Fe for the vivianite-type mineral) dissolved during the extraction of three Mn standards with ascorbic acid during 24 h (Step 1), A: birnessite, B: manganite and C: Mn bearing vivianite. Y axis represents the fraction of the Mn standard extracted in the 24 h ascorbic acid extraction. Data points represent the means of triplicate samples.

### Porewater Mn and Mn speciation in sediments

The sediments at the six study sites differ greatly in their porewater characteristics. The shape of the porewater profiles point towards production of dissolved Mn in the sediment at all locations (Burdige (2006); Fig. 4A). Porewater sulfide was present at all sites and either increases with depth (LL19, GoF5, Black Sea 6) or shows a subsurface maximum (GoM1, US5B, ET5.1). Concentrations are highest at the euxinic and seasonally hypoxic sites in the Baltic Sea (LL19, GoF5). These differences in sulfide availability are expected to impact both total Mn contents and the Mn speciation in the sediment (Burdige and Nealson, 1986).

Our total Mn analyses and the application of the sequential extraction procedure to the sediments from the six sites, ordered based on their bottom water redox conditions (euxinic to oxic; Table 3) confirm that there are large differences in sediment Mn contents and speciation (Figs. 4B and 5). Below, we discuss the Mn profiles for each site within the context of several key site characteristics, including what is known about the sediment forms of Mn based on previous studies (Table 4).

The porewaters at the euxinic site LL19 in the Baltic Sea are rich in both dissolved Mn and  $\text{H}_2\text{S}$  (maxima of  $\sim 70$  and  $250 \mu\text{mol L}^{-1}$ , respectively, Fig. 4A). The linear increase in dissolved Mn with depth points towards a Mn source below the sampled interval. Total sediment Mn contents (Fig. 4B) are mostly below  $10 \mu\text{mol g}^{-1}$

except for the depths between 7 and 10 cm where they increase to ca.  $100 \mu\text{mol g}^{-1}$  (Fig. 4B). At this site, only few Mn oxides are expected because of their rapid reduction with  $\text{H}_2\text{S}$ , either in the water column or sediment (Burdige, 1993). The subsurface maximum in total Mn at this site has previously been attributed to Mn carbonate precipitation linked to water column reoxygenation (Jilbert and Slomp, 2013; Lenz et al., 2015). The extraction data show that ascorbic acid extractable Mn contents are very low (Fig. 5A). A slight enrichment is observed near the sediment water interface, however, that may indicate that small amounts of poorly ordered Mn oxides can survive transport through a euxinic water column and be deposited at the sediment-water interface. At ca. 8 cm depth the majority of the Mn is extracted in the HCl step, which points towards the presence of Mn carbonate, in line with expectations. The CDB and ammonium oxalate extractable Mn is low and near constant with depth. The Mn extractable with  $\text{HNO}_3$  is a small but detectable fraction, pointing towards incorporation of small amounts of Mn during the formation of pyrite. Such incorporation has been reported previously for sediments in the region, based on Mn-XANES (Lenz et al., 2014).

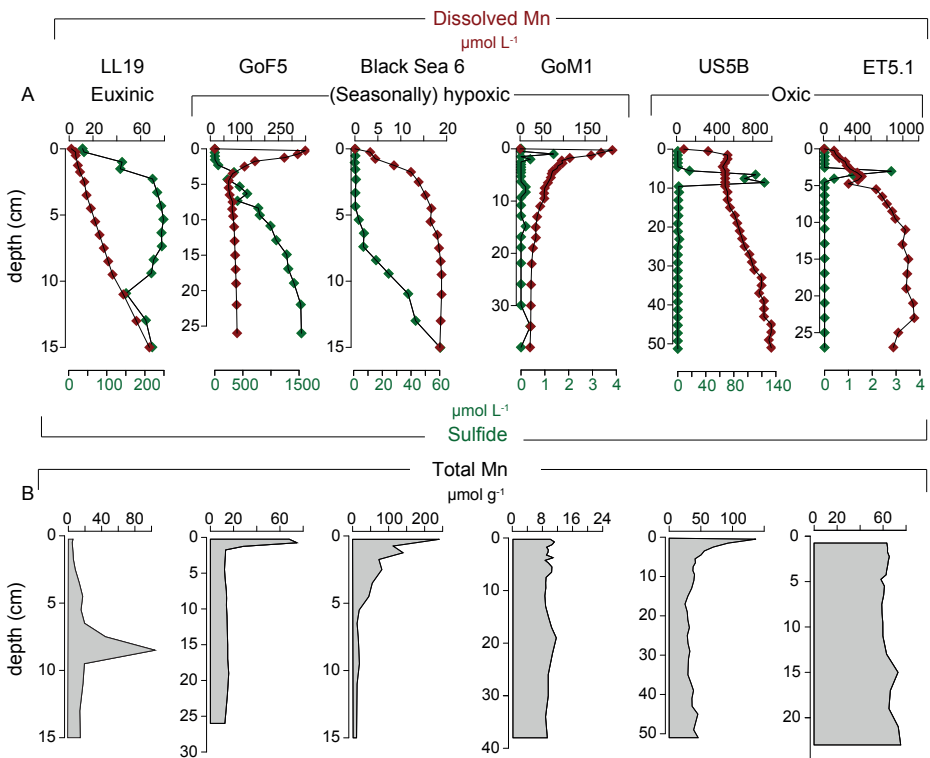


**Fig. 4.** Depth profiles for six sites investigated in this study. A: Porewater Mn and sulfide; B: solid phase Mn.

The porewaters at the (seasonally) hypoxic sites GoF5, Black Sea 6 and GoM1, located in the Baltic Sea, Black Sea and Gulf of Mexico, respectively, are all enriched in dissolved Mn and indicate mobilization of Mn from the solid phase in the upper 5 cm of the sediment. The observed maxima in porewater Mn at sites GoF5 and GoM1 are typically interpreted as indicators of Mn oxide dissolution near the sediment water interface and Mn carbonate formation at depth. At GoF5, a strong enrichment in ascorbic acid extractable Mn at the sediment-surface and the presence of HCl-extractable Mn at depth confirm this interpretation (Fig. 5). Ascorbic acid extractable Mn at site GoM1 is very low, which may be related to dilution because of the high sedimentation rate (ca. 2 cm yr<sup>-1</sup>; Canfield (1988)), rapid dissolution of Mn oxides upon deposition and subsequent benthic release of dissolved Mn (Lenstra et al., 2022). The Black Sea site is located near the chemocline at the shelf edge of the deep euxinic basin.

Here, the Mn enrichment, in the nearly sulfide-free surface sediment, was expected to either consist of Mn oxides or Mn carbonates (Table 4). Our extraction results suggest that the Mn was extracted by HCl and hence consists mostly of Mn carbonates. At all three sites, the CDB and ammonium oxalate extractable Mn account for an appreciable and constant fraction of Mn, pointing towards burial of less reactive/nonreactive Mn forms in the sediment. At sites GoF5 and GoM1, Mn is extracted in the HNO<sub>3</sub> step when pyrite concentrations are above 40 μmol g<sup>-1</sup> (Fig. A.2). This suggests that when pyrite contents and dissolved manganese concentrations are both sufficiently high, Mn can be incorporated in the pyrite structure.

**Table 4** Expected main Mn forms in the surface sediment (0 – 2 cm) and deeper sediment (below 5 cm) based on previous studies.

Site	Surface sediment	Deeper sediment	Method	Source
LL19	Small amount of Mn oxides	Mn carbonates	μXRF <sup>a</sup>	Lenz et al. (2015)
GoF5	Mn oxides and/or Mn phosphates	Non-reactive Mn	Mn-XANES & μXRF <sup>b</sup>	Hermans et al. (2021)
Black Sea 6	Mn oxides and/or Mn carbonates	Non-reactive Mn	Mn-XANES & Mn-EXAFS	Lenstra et al. (2021)
GoM1	Mn oxides	Mn carbonates	-	Lenstra et al. (2022)
US5B	Mn oxides	Mn oxides/Mn phosphates	SEM-EDS, μXRF <sup>a,b</sup> , Mn-XANES	Egger et al. (2015)
ET5.1	Mn oxides	Mn oxides/Mn phosphates	SEM-EDS & μXRF <sup>a</sup>	Kubeneck et al. (2021)

<sup>a</sup> Desktop μ X-Ray Fluorescence (μXRF)

<sup>b</sup> Synchrotron-based focused-beam μXRF,

SEM-EDS: Scanning Electron Microscopy – Energy Dispersive X-ray Spectroscopy

Mn-EXAFS: Extended X-ray Absorption Fine Structure

Mn-XANES: X-ray Absorption Near-Edge Structure

The porewaters at the sites with oxic bottom waters, US5B and ET5.1, located in the Bothnian Sea and Chesapeake Bay, are highly enriched in dissolved Mn ( $>1000 \mu\text{mol L}^{-1}$ ) with concentrations increasing with sediment depth. The subsurface maximum in dissolved  $\text{H}_2\text{S}$  at both sites is linked to methane oxidation with sulfate (Egger et al., 2015; Kubeneck et al., 2021). At both sites, sink-switching of Mn from Mn oxides to Mn bearing vivianite-type minerals has been proposed (Egger et al., 2015; Kubeneck et al., 2021). At both sites, Mn extractable with ascorbic acid was elevated near the sediment-water interface but also at depth (Fig. 5C). Because both Mn oxides and Mn phosphates are extracted in the ascorbic acid step, we cannot differentiate between Mn oxides and Mn in vivianite-type minerals. The slight increase in HCl-extractable Mn with depth suggests the formation of Mn carbonates. CDB and ammonium oxalate extractable Mn contribute an appreciable and constant fraction. Manganese associated with pyrite is below the detection limit at these sites, in line with the low pyrite content ( $<45 \mu\text{mol g}^{-1}$ ; Fig. A.2).

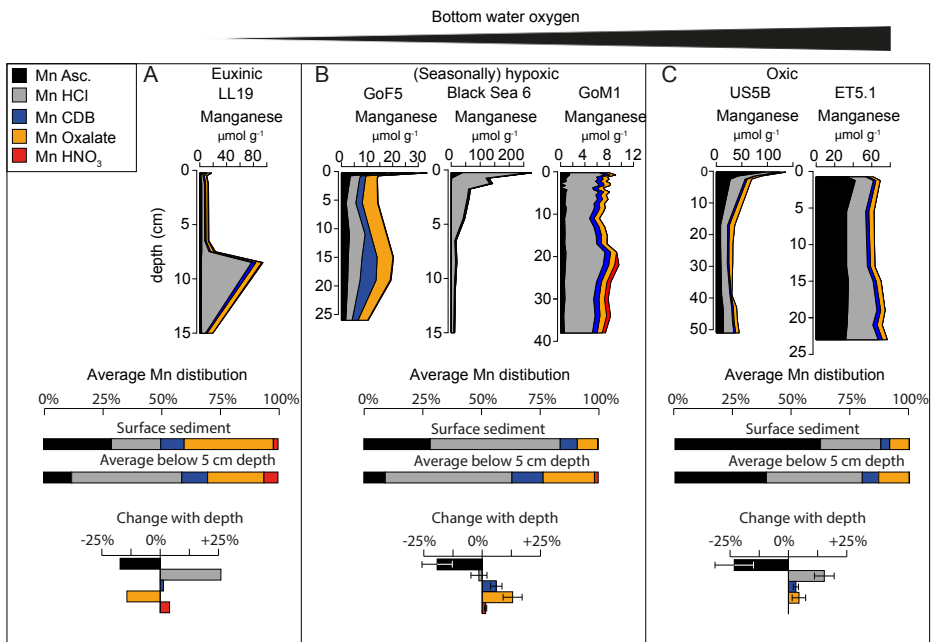


**Fig. 5.** Depth profiles of different forms of Mn at six sites as determined with the sequential extraction procedure, average distribution of Mn extracted in surface sediment and below 5 cm for non-sulfidic sites and change with depth of the different extracted Mn phases for A: euxinic site LL19; B: (seasonally) hypoxic sites GoF5, Black Sea 6 and GoM1; C: oxic sites US5B and ET5.1. The peak of Mn at ca. 8 cm depth at site LL19 is related to an inflow event of oxygen-rich water resulting in the deposition of high concentrations of Mn. The relatively low sample resolution at LL19 is the cause of the broad Mn peak in panel A (see Fig. 4 and the supplementary data).

## Implications and conclusions

In this study we applied an existing sequential extraction procedure for Fe on a range of Mn standards consisting of Mn oxides, Mn phosphates, Mn carbonate, Mn sulfide and Mn in clays (Table 1 and A.1). The ascorbic acid solution (Step 1) was efficient in extracting poorly ordered Mn oxides, such as birnessite and pyrolusite, and Mn phosphates. Additionally, ascorbic acid partly extracted crystalline Mn oxides, such as manganite and hausmannite. The 1 M HCl (Step 2) was highly efficient in extracting Mn carbonate and Mn sulfide. Since Mn sulfides are only observed in highly sulfidic systems (e.g. Suess (1979), Lepland and Stevens (1998)), we expect that 1 M HCl predominantly extracts Mn carbonates in marine systems. To detect the possible presence of Mn sulfides other techniques such as XRD, SEM-EDS or XANES/EXAFS, are required. The CDB and ammonium oxalate solutions (Step 3 and 4), extracted the remainder of the crystalline Mn oxides. These crystalline Mn oxides were partially extracted in the previous steps, therefore step 3 and 4 are not specific for Mn oxides with a high crystallinity. The concentrated HNO<sub>3</sub> solution (Step 5) extracted a negligible amount of the Mn standards (Fig. 2; Table A.1) but has been shown to be highly efficient in extracting pyrite in a sequential extraction procedure (Lord, 1982; Huerta-Diaz and Morse, 1992; Claff et al., 2010). Therefore this step is likely specific for Mn incorporated in pyrite.

Application of the extraction procedure to a range of coastal sediments shows how the results complement those of total Mn and X-ray analyses in allowing a quantification of the various sediment Mn forms for a large number of samples. Our extraction results also highlight a number of key aspects of Mn cycling in coastal systems. These are discussed one by one below.

In euxinic coastal marine basins, Mn oxides (or mixed Fe-Mn-P phases) formed in the redoxcline, are expected to be reductively dissolved by H<sub>2</sub>S before they reach the surface sediment (e.g. Dellwig et al., 2010; Dijkstra et al., 2018b). Any Mn detected in such sediments is thought to be associated with either pyrite or clays (Lyons and Severmann, 2006; Lenstra et al., 2020). We find, however, that at the euxinic site in the Baltic Sea, ascorbic acid extractable Mn accounts for ca. 30% of the total Mn pool in the surface sediment, with concentrations quickly decreasing with sediment depth (Fig. 5A). This suggests that some Mn oxides and/or mixed Fe-Mn-P phases survive transport through the euxinic water column and are deposited at the sediment water interface. This may be due to the shallow water euxinic column at our Baltic Sea study site (80 m versus 2000 m in the Black Sea), possibly augmented by rapid sinking and shuttling of Mn-rich particles upon their association with other inorganic or organic particles (e.g. Martin and Knauer (1980)).

At sites with (seasonally) hypoxic bottom waters, the Mn speciation of surface sediments will depend on a range of factors including bottom water oxygen concentrations, the input of Mn oxides from the water column, and the presence of reductants in the sediment, such as organic matter and porewater sulfide (Burdige, 1993). Given that our study sites in the Baltic Sea, Black Sea and Gulf of Mexico show large differences in such characteristics (Table 3; Fig. 4), it is not surprising that their Mn speciation in the surface sediment also differs. At site GoF5, rapid cycling of Mn between the surface sediment and the redoxcline in the water column likely explains the enrichment in Mn oxides near the sediment surface in these otherwise highly reducing sediments (Figs. 4 and 5) as discussed in detail by Hermans et al. (2021). At the Black Sea site near the redoxcline, in contrast, most Mn in the surface sediment is present as Mn carbonate, pointing towards conversion of Mn oxides to Mn carbonates in these sulfide-poor shelf sediments. Based on the shape of the total sediment Mn profile, this Mn could have been wrongly assigned to Mn oxides if no Mn speciation data were available. At site GoM1, very little Mn oxide is present in the surface sediment, likely due to rapid mobilization in the sediment and diffusive loss of dissolved Mn to the water column (Figs. 4 and 5), possibly followed by offshore transport of the Mn (Bianchi et al., 1997; Owings et al., 2021).

At our sites with oxic bottom waters, both the surface and deeper sediments contain quite some ascorbic acid extractable Mn. While in the surface sediment this Mn fraction likely consists of Mn oxides, at depth Mn-rich vivianite plays an additional role as deduced from a range of microscopic and X-ray analyses of the sediment at these sites (Egger et al., 2015; Kubeneck et al., 2021). Vivianite is frequently formed below the sulfate-methane-transition zone in marine sediments (Marz et al., 2008; Egger et al., 2015; Lenstra et al., 2018), and while its role as a sink for P is well-recognized, its contribution to Mn burial deserves further study. Further work is also needed to establish what types of Mn oxides may be buried in coastal sediments and their potential role in, for example, anaerobic methane oxidation (e.g. Beal et al. (2009)).

At all sites, the relative contribution of 1 M HCl extractable Mn to total Mn increased with sediment depth (Fig. 5). At the euxinic site, the sharp increase in Mn between 7 and 10 cm (Figs. 4 and 5) can be linked to an inflow of oxygenated North Sea water into the Gotland basin, subsequent deposition of newly formed Mn oxides at the sediment surface and their rapid conversion to Mn carbonate (Lenz et al., 2015). At many of the other sites, some sink-switching of Mn oxides to Mn carbonates likely also occurs, although this is much less pronounced. Importantly, our study sites are all characterized by either no macrofauna or low numbers thereof, and

hence, low rates of sediment mixing through bioturbation (Hermans et al., 2019; Lenstra et al., 2019; Egger et al., 2015; Kubeneck et al., 2021). The presence of Mn carbonate near the sediment water interface therefore suggests rapid formation of this mineral near the sediment water interface and/or input from the water column. We note that suspended matter in the Baltic Sea and Black Sea contains 1 M HCl extractable Mn (Lenstra et al., 2020, 2021), supporting the latter suggestion.

At all sites, CDB and ammonium oxalate extractable Mn accounted for a constant background concentration of Mn. This suggests that the associated Mn phases are non-reactive, and most likely involve recalcitrant Mn oxides or Mn in clays. Additionally, part of the Mn released in the ammonium oxalate step might be Mn that was re-adsorbed onto crystalline Fe oxides during previous extraction steps (Koschinsky et al., 2001). Finally, we show that  $\text{HNO}_3$  extractable Mn is a small but detectable fraction that increases slightly with depth at sites where pyrite concentrations are relatively high, in line with incorporation of Mn in pyrite.

With the use of this new sequential extraction procedure for particulate Mn, it is possible to determine key operationally defined Mn forms in sediments simultaneously with those of Fe. This has large benefits for the study of Mn and Fe dynamics in marine sediments, as illustrated here for Mn for six coastal sites with strongly contrasting bottom water redox conditions. We envisage that this procedure will also be of benefit when studying ancient marine sediments, by allowing a quick separation of Mn oxides and Mn carbonates. Sediments in the eastern Mediterranean Sea, for example, are characterized by an enrichment in total Mn at or near the top of the most recent sapropel. This enrichment usually consists of Mn oxides but, in some cases, the Mn oxides may convert to Mn carbonate. This was, for example, demonstrated for a highly Mn-enriched sediment in the Aegean Sea using X-ray diffraction (Mercone et al., 2001). Our procedure should allow such cases to be identified, also when sediment Mn contents are lower. Similarly, the extraction procedure could be used to assess the composition of Mn-rich layers in ancient Arctic Ocean sediments where, besides diagenetically formed Mn carbonates, buried Mn oxide layers are observed (e.g. Lowemark et al., (2014)). We note, however, that the current technique is not calibrated for the quantification of the widely used highly reactive Fe parameter in ancient sediments (Raiswell et al., 2018; Alcott et al., 2020). The value of the extraction procedure for the analysis of Fe and Mn in suspended matter was illustrated previously (Lenstra et al., 2020, 2021).

### **Data availability**

All data is available in the supplementary material of this publication.

### **Declaration of Competing Interest**

The authors declare no conflict of interest.

### **Acknowledgements**

We thank C. Mulder, H. de Waard, N. van Helmond and A. van Leeuwen-Tolboom for analytical assistance. This research was funded by the Netherlands Organisation for Scientific Research (NWO-Vici grant 865.13.005), Netherlands Earth System Science Centre (NESSC Gravitation grant 024.002.001) and ERC (ERC synergy MARIX grant 854088).

## Appendix A. Supplementary data

Supplementary data to this article can be found online at <https://doi.org/10.1016/j.chemgeo.2021.120538>.

### Supplements

The characterization of the Mn standards determined by X-ray diffraction (XRD) is given in figure A.1. Below we briefly discuss the XRD profiles for all minerals except for the synthesized minerals with varying Mn/Fe ratio's.

Mn-nodule: the sharp peaks in the diffractogram can be attributed to silicates including quartz and feldspars. A small peak around  $9.15^\circ$   $2\theta$  CuK $\alpha$  suggests the presence of phyllo-manganates with a d-spacing of 10 Å, such as todorokite. No other distinctive peaks of Fe or Mn minerals typical for Mn nodules (e.g. Glasby [1972]; Knaack et al. [2020]), could be identified. This implies that most of the Fe and Mn in the nodule is XRD amorphous and accounts for the broad peaks shaping the background signal in the diffractogram.

Pyrolusite: the peaks are in agreement with those from literature. Additional peaks can be explained by the presence of quartz in the sample.

Birnessite: the diffraction peaks at around  $12.5^\circ$   $2\theta$  CuK $\alpha$  are indicative for phyllo-manganates with a d-spacing of around 7 Å, such as birnessite. The position of diffraction peaks above  $35^\circ$   $2\theta$  CuK $\alpha$  are in agreement with those expected for H1 polytype birnessite according to Drits et al. [2007], i.e. a one layer hexagonal structure with vacant sites.

Manganite: the XRD profile confirms the presence of manganite together with some quartz.

Bixbyite: the peaks in the diffractogram agree with those expected for bixbyite. There are a few small diffraction peaks which indicate the presence of a minor component, which could not be identified.

Hausmannite: the peaks in the diffractogram point towards the presence of hausmannite together with minor amounts of quartz and feitknechtite.

Hureaulite: The position of the diffraction peaks agree with those expected for hureaulite.

Rhodochrosite: the major diffraction peaks can be attributed to rhodochrosite. Additional diffraction peaks agree with those reported for wellsite, a barium aluminum silicate, of which the presence is questionable, however. The humps around  $14^\circ$  and  $30^\circ$   $2\theta$  CuK $\alpha$  indicate the presence of some additional amorphous material.

Alabanite: the diffraction peaks can be explained by the presence of alabanite and some elemental sulfur.

Smectite-1 and Smectite-2: the major peaks at around  $6.15^\circ$   $2\theta$  CuK $\alpha$  are indicative for clay minerals with a d-spacing of around  $14 \text{ \AA}$ , which is also the case for the asymmetric peaks at around  $20^\circ$   $2\theta$  CuK $\alpha$  and supports the designation of these materials as smectite. The other sharp peaks can be explained by the presence of quartz.

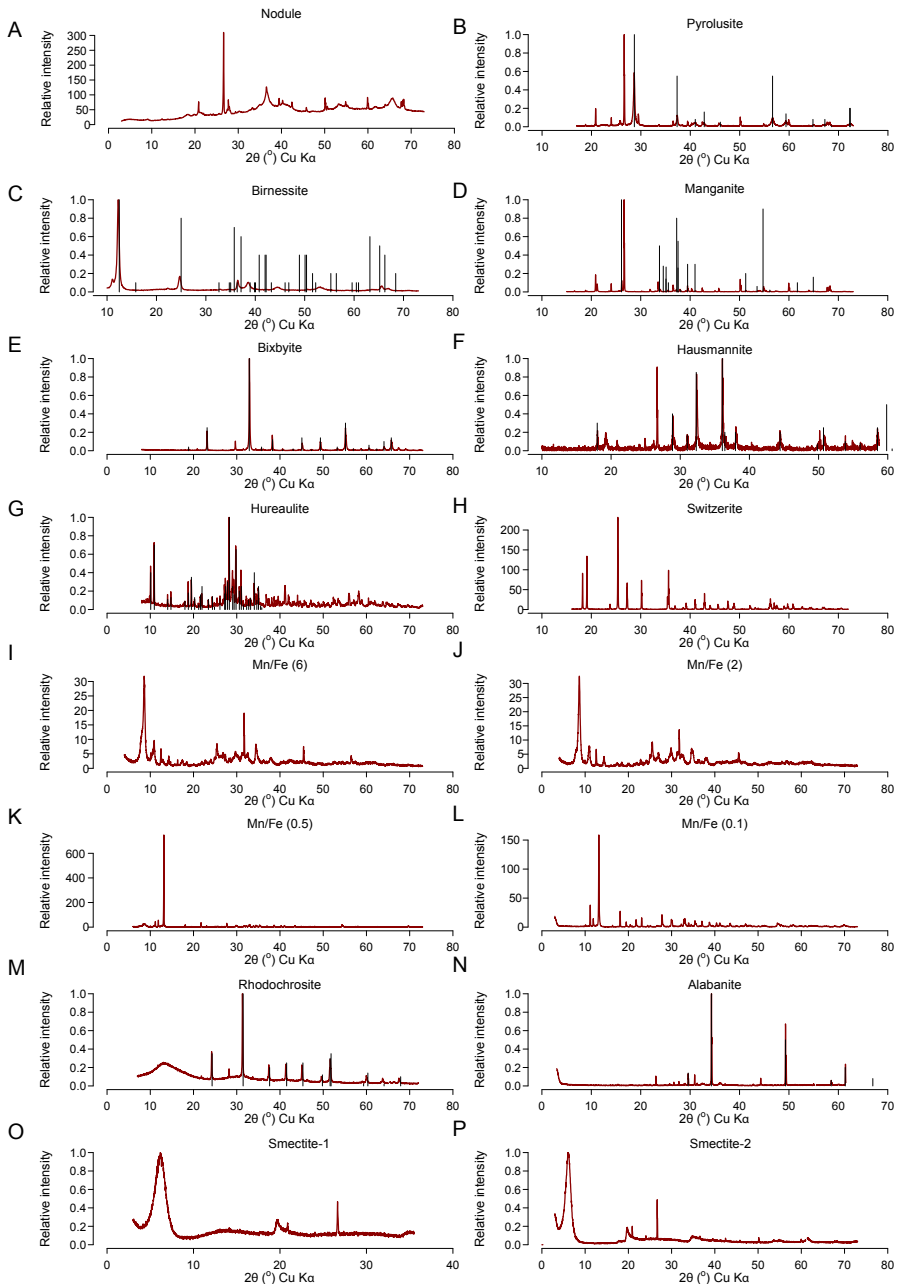


**Figure A.1** XRD spectra for all standards used in this study. Red lines are measured spectra, black vertical lines are theoretical peaks for the minerals. For synthesized minerals (I-L) and clay minerals (O-P), no black lines are included.

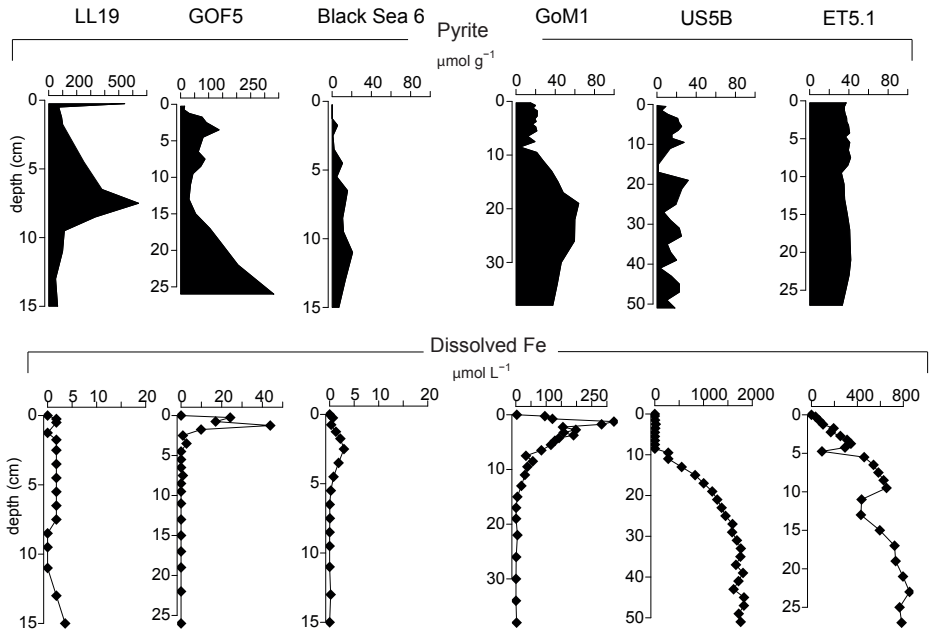


**Figure A.2** Depth profiles of pyrite and dissolved Fe for the six sites investigated in this study.

# 1 Table appendix

**Table A.1** Sediment Mn extracted in each step of the sequential procedure. N.D.: not determined because of complete dissolution of the mineral in the preceding extraction step. The small amount of Mn standards used during the extraction (20 mg) led to high standard deviations.

<b>Standards</b>	<b>(1) Mn Asc. μmol g<sup>-1</sup></b>	<b>(2) Mn HCl μmol g<sup>-1</sup></b>	<b>(3) Mn Dith. μmol g<sup>-1</sup></b>	<b>(4) Mn Oxa. μmol g<sup>-1</sup></b>	<b>(5) Mn HNO<sub>3</sub> μmol g<sup>-1</sup></b>	<b>Total extracted Mn μmol g<sup>-1</sup></b>
Mn nodule	1967±238	271±88	5±1	3±1	0.1±0.2	2246
Pyrolusite	7319±427	581±102	476±362	23±13	0.3±0.1	8399
Birnessite	8511±1774	112±25	N.D.	N.D.	N.D.	N.D.
Manganite	1543±184	495±26	1010±86	123±36	2±0.0	3172
Bixbyite	6093±1235	1173±164	5556±771	N.D.	N.D.	12822
Hausmannite	4573±439	1286±22	4803±1074	805±366	0.6±0.0	11467
Rhodochrosite	52±7	8178±153	N.D.	N.D.	N.D.	8229
Alabanite	3336±643	7496±234	N.D.	N.D.	N.D.	10831
Hureaulite	4960±1810	175±118	N.D.	N.D.	N.D.	5134
Switserrite	6239±45	231±106	N.D.	N.D.	N.D.	6470
Mn/Fe (6)	4917±86	109±26	N.D.	N.D.	N.D.	5026
Mn/Fe (2)	3955±108	64±12	N.D.	N.D.	N.D.	4019
Mn/Fe (0.5)	2182±48	25±5	N.D.	N.D.	N.D.	2207
Mn/Fe (0.1)	625.8±16.8	6.9±1.6	N.D.	N.D.	N.D.	632.6
Smectite-1	0.5±0.1	1.9±0.4	0.6±0.0	1.2±0.8	0.1±0.0	4.3
Smectite-2	0.5±0.0	0.6±0.1	1.0±0.4	0.7±0.0	0.1±0.0	2.9





## Chapter 3

# Dissolved Mn(III) is a key redox intermediate in sediments of a seasonally euxinic coastal basin

---

R. Klomp<sup>1,2</sup>, O.M. Żygadłowska<sup>2</sup>, M.S.M. Jetten<sup>1</sup>, V.E. Oldham<sup>3</sup>, N.A.G.M. van Helmond<sup>1,2</sup>  
C.P. Slomp<sup>1</sup>, W.K. Lenstra<sup>1,2</sup>

<sup>1</sup>Department of Microbiology, Radboud Institute for Biological and Environmental Sciences, Radboud University, Heyendaalseweg 135, 6525 AJ Nijmegen, the Netherlands

<sup>2</sup>Department of Earth Sciences, Utrecht University, Princetonlaan 8a, 3584 CB Utrecht, the Netherlands

<sup>3</sup>Graduate School of Oceanography, Rhode Island University, 215 S Ferry Rd, Narragansett, RI 02882, USA

This chapter was published in *Biogeosciences*:

Klomp, R., Żygadłowska, O. M., Jetten, M. S. M., Oldham, V. E., Van Helmond, N. A. G. M., Slomp, C. P., & Lenstra, W. K. (2025). Dissolved Mn(III) is a key redox intermediate in sediments of a seasonally euxinic coastal basin. *Biogeosciences*, 22, 751–765. <https://doi.org/10.5194/egusphere-2024-1706>

## Abstract

Manganese (Mn) is an essential micronutrient and key redox intermediate in marine systems. The role of organically complexed dissolved Mn(III) (dMn(III)-L) as an electron acceptor and donor in marine environments is still incompletely understood. Here, we use geochemical depth profiles of solutes and solids for the sediment and overlying waters and a reactive transport model to reconstruct the seasonality in sedimentary dMn(III)-L dynamics and benthic Mn release in a eutrophic, seasonally euxinic coastal basin (Lake Grevelingen, the Netherlands). Our model results suggest that dMn(III)-L is a major component of the dissolved Mn pool throughout the year. According to the model, there are three major sources of pore water dMn(III)-L when oxygen (O<sub>2</sub>) is present in the bottom water, namely reduction of Mn oxides coupled to the oxidation of Fe(II), reduction of Mn oxides coupled to organic matter degradation and oxidation of Mn(II) with O<sub>2</sub>. Removal of pore water dMn(III)-L is inferred to primarily take place through reduction by dissolved Fe(II). When bottom waters are euxinic in summer, model-calculated rates of sedimentary Mn cycling decrease strongly, because of a lower supply of Mn oxides. The dMn(III)-L transformations in summer mostly involve reactions with Fe(II) and organic matter. Modelled benthic release of Mn mainly occurs as dMn(III)-L when bottom waters are oxic, as Mn(II) upon initial bottom water euxinia and as both Mn(II) and dMn(III)-L when the euxinia becomes persistent. Our model findings highlight strong interactions between the sedimentary Fe and Mn cycles. Dissolved Mn(III)-L is a relatively stable and mobile Mn species, when compared to Mn(II), and is therefore more easily transported laterally throughout the coastal zone and possibly also to open marine waters.

## Keywords

Manganese dynamics, benthic flux, reactive transport modelling, micronutrient

## Introduction

Manganese (Mn) is an essential micronutrient and is one of the most abundant transition metals in natural environments (Raven, 1990; Neretin et al., 2003). In marine systems, dissolved Mn is present as either Mn(II) or Mn(III) complexed to organic ligands (dMn(III)-L) (Burdige, 1993; Luther, 2010; Madison et al., 2013). Importantly, dMn(III)-L can act as either an electron acceptor or donor and can thereby play a key role as a redox intermediate in marine sediments (Kostka et al., 1995; Trouwborst et al., 2006; Madison et al., 2013). Sediments may act as a source of both dissolved Mn(II) and dMn(III)-L to overlying waters (Oldham et al., 2019). The redox state of the dissolved Mn will determine its reactivity and mobility and thus its ultimate fate in the water column (Oldham et al., 2017a; Lenstra et al., 2020).

Sedimentary Mn cycling is driven by interactions between Mn and other redox sensitive compounds (Burdige, 1993). For example, reductive dissolution of Mn oxides, which leads to mobilization of dissolved Mn, can be coupled to the oxidation of organic matter (OM), hydrogen sulfide (H<sub>2</sub>S), ferrous iron (Fe(II)) or methane (CH<sub>4</sub>) (Postma, 1985; Burdige, 1993; Aller, 1994; Beal et al., 2009). Interactions between Mn oxide and ammonium (NH<sub>4</sub><sup>+</sup>) have also been proposed (Hulth et al., 1999; Thamdrup and Dalsgaard, 2000). The occurrence of this process in marine environments is still debated, however. Dissolved Mn may be in the form of Mn(II) or dMn(III)-L (Madison et al., 2013; Luther et al., 2018). Dissolved Mn(II) can precipitate as Mn-carbonate when alkalinity is high (Calvert and Pedersen, 1996; Lepland and Stevens, 1998) and can adsorb onto Mn oxide minerals (van der Zee et al., 2001).

In the presence of oxygen (O<sub>2</sub>), for example in surface sediments in marine settings with oxygenated waters, dissolved Mn(II) and dMn(III)-L can be oxidized, forming Mn oxides. When there is little O<sub>2</sub> penetration into the sediment or when macrofauna are present, the dissolved Mn may escape to the overlying water (Slomp et al., 1997; McManus et al., 2012; Lenstra et al., 2020). In oxic waters, dissolved Mn may oxidize to Mn oxides and settle under gravitational forcing thereby enhancing the supply of Mn oxides to the sediment (Sulu-Gambari et al., 2017; Lenstra et al., 2021a). When bottom waters are anoxic, sediments will eventually become depleted of reactive Mn oxides and dissolved Mn can accumulate in the water column (Lenz et al., 2015; Dellwig et al., 2018).

Part of the Mn released from the sediment could consist of dMn(III)-L (Oldham et al., 2019). Dissolved Mn(III) is highly reactive, but the complexation with organic ligands can result in a meta-stable complex (Kostka et al., 1995). The strength of

the bond between Mn(III) and the ligand determines the reactivity of dMn(III)-L (Luther et al., 2015; Oldham et al., 2015, 2017b). The Mn(III)-L complex can be the dominant form of dissolved Mn in sediment pore water and in the water column (e.g. Trouwborst et al., 2006; Madison et al., 2013; Oldham et al., 2017b). Oxidation of Mn(II) and reduction of Mn(IV) are suggested to occur via one-electron step transitions with dMn(III)-L as an intermediate product (Luther, 2005). Formation of dMn(III)-L has been proposed to mainly take place via reduction of Mn oxides coupled to OM degradation or oxidation of Mn(II) by O<sub>2</sub> (Madison et al., 2013). Other pathways that produce dMn(III)-L include reduction of Mn oxides coupled to oxidation of Fe(II) and H<sub>2</sub>S (Madison et al., 2013). Removal of dMn(III)-L is suggested to mainly occur via oxidation by O<sub>2</sub> to Mn(IV) (Madison et al., 2013). Reduction of dMn(III)-L by oxidation of Fe(II), H<sub>2</sub>S, nitrite (NO<sub>2</sub><sup>-</sup>) and OM is also possible (Kostka et al., 1995; Oldham et al., 2015, 2019; Karolewski et al., 2021), but does not necessarily always occur (Oldham et al., 2015, 2019).

In recent years, the number of areas that experience eutrophication and deoxygenation has increased strongly (Diaz & Rosenberg, 2008; Breitburg et al., 2018). Anoxia initially stimulates benthic release of dissolved Mn, since the dissolved Mn will no longer be re-oxidized near the sediment-water interface (Pakhomova et al., 2007; Lenstra et al., 2021a). Furthermore, organic carbon (C<sub>org</sub>) oxidation rates and the benthic release of dissolved Mn can be positively correlated (Berelson et al., 2003; McManus et al., 2012). At present we do not know to what extent dMn(III)-L contributes to dissolved Mn released from the sediment and what processes control the redox state in which Mn leaves the sediment.

The aim of this study is to understand the effects of seasonal euxinia on dMn(III)-L dynamics. This is studied in sediments in a seasonally euxinic coastal basin (Lake Grevelingen, the Netherlands). We combine detailed sediment and pore water analyses with a reactive transport model that, for the first time, includes a detailed Mn(III) cycle, to investigate the main drivers of sedimentary Mn cycling and the benthic release of Mn. Our model results suggest that dMn(III)-L is released from the sediment both when bottom waters are oxic and euxinic. Furthermore, our results highlight the importance of dissolved Fe(II) for the mobilization of Mn and release of dissolved Mn from the sediment in seasonally euxinic basins.

## Methods

### Study area

Lake Grevelingen is a coastal marine system in the south-west of the Netherlands (Fig. 1). It is a former estuary that was closed by a dam on the landward side in 1964 and a dam on the seaward side in 1971, in response to major flooding in the area. A sluice on the seaward side enables sea water exchange with the North Sea. The lake has an average depth of 5.1 m but is intersected by former tidal channels with several deeper basins (Egger et al., 2016).

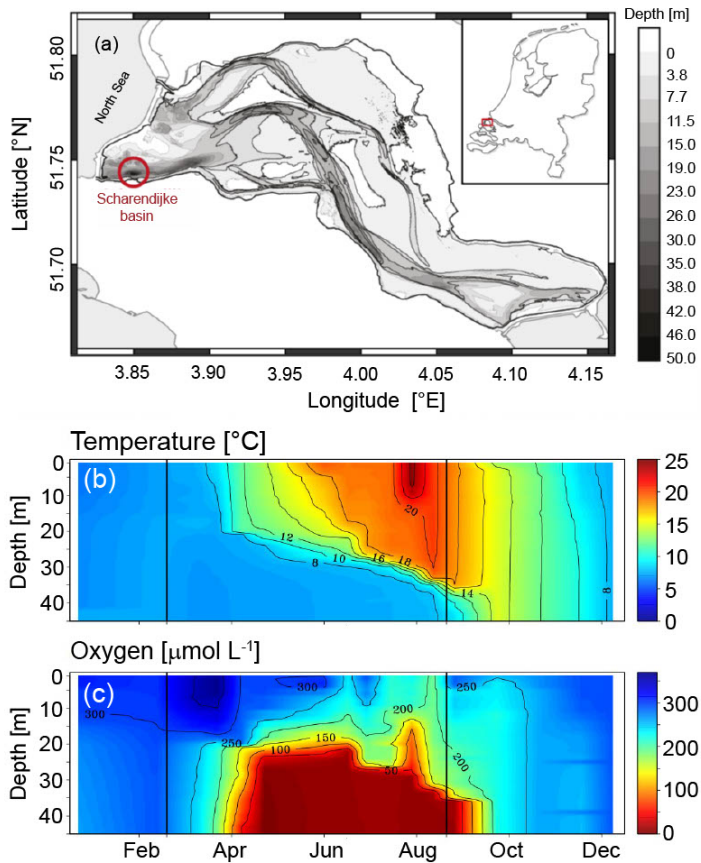


**Figure 1.** (a) Map of Lake Grevelingen indicating the location of the Scharendijke basin (adapted from Egger et al., 2016). (b) Temperature and (c)  $\text{O}_2$  concentrations as measured by Rijkswaterstaat (Directorate-General for Public Works and Water Management of the Netherlands). The observations by Rijkswaterstaat were carried out every two weeks to one month, giving a total of 19 time points in 2020 in the water column of the Scharendijke basin throughout 2020 (Adapted from Żygadłowska et al., 2023). The black vertical lines indicate the dates of sampling in March and September.

In this study, we focus on Scharendijke basin, located in the deepest part of the lake (Fig. 1; 51.742°N, 3.849°E; water depth of 45 m). During summer, temperature-driven stratification of the water column leads to the development of anoxic and sulfidic bottom waters, as recorded by the seasonal drawdown of molybdenum from the water column and its consequent sedimentary enrichment (Egger et al., 2016; Żygadłowska et al., 2023, 2024a). Water column euxinia was confirmed by direct measurements of H<sub>2</sub>S in 2021 (Żygadłowska et al., 2024a, b). Each year, the water column mixes again in autumn, resulting in bottom water reoxygenation. Scharendijke basin is a relatively narrow and deep basin in an overall shallow lake (Figure 1). As a consequence, vertical transport settling of suspended matter is expected to be supplemented by lateral transport of material from shallower areas near the sediment-water interface. The sediment at this site is characterized by a high sedimentation rate (~13 cm yr<sup>-1</sup>) and high rates of OM oxidation (~249 mmol C m<sup>-2</sup> d<sup>-1</sup>) which is also reflected in a shallow sulfate-methane transition zone at around 20 cm depth in the sediment (Egger et al., 2016). High sulfate reduction rates lead to significant build-up of H<sub>2</sub>S in the sediment in summer (Egger et al., 2016). Macrofauna are absent from the sediment in Scharendijke basin (based on visual observations of sediment sieved over 0.5 mm). In 2020, two field campaigns were carried out with RV *Navicula*, one when the water column was mixed and bottom waters were oxygenated (March) and one when the water column was stratified and bottom waters were euxinic (September). During these field campaigns, the water column and sediment was sampled as described in detail below. Additional sampling was carried out in eight field campaigns, one in each month from March to October 2021, as described in the supplement (Section 1).

### **Water column sampling**

Depth profiles of temperature and O<sub>2</sub> were obtained from the water column with a CTD (Seabird SBE 911 plus) equipped with an oxygen sensor (SBE43) during the cruise in September 2020. Most O<sub>2</sub> sensors, including the SBE43, measure a background signal when O<sub>2</sub> is absent. Winkler titrations cannot be used for calibration, because these also have artefacts when O<sub>2</sub> concentrations are low (Grégoire et al., 2021). Therefore we assume absence of O<sub>2</sub> when oxygen concentrations are low and concentrations do not change with increasing water depth (Żygadłowska et al., 2023). Water samples were collected with a 10 L Niskin bottle at discrete depths (1-5 m depth resolution) in September 2020. Samples were obtained for analysis of Mn(II) and dMn(III)-L and stored in a N<sub>2</sub> purged aluminum bag at -20°C until analysis.

### **Sediment and pore water collection**

During both sampling campaigns in 2020, four sediment cores were collected with a UWITEC gravity corer with transparent PVC core liners of 120 cm length with a 6 cm

inner diameter. During sampling, the surface sediment remained intact. The first core was sectioned for pore water and solid phase analyses at a depth resolution of 1 cm in a glove bag under a  $N_2$  atmosphere on board the ship. The sediment was placed in 50 ml centrifuge tubes and subsequently centrifuged at 4500 rpm for 20 minutes to separate the pore water from the solid phase. Pore water was collected for all samples in the upper 10 cm, for samples from every second cm between 10 and 50 cm and every fifth cm from 50 cm until the bottom of the core. The supernatant was filtered over 0.45  $\mu\text{m}$  pore size filters (i.e. capturing the aqueous and colloidal fractions; Raiswell and Canfield (2012) under a  $N_2$  atmosphere in a glove bag and subsequently sub-sampled for the analysis of  $NH_4^+$ , sulfate ( $SO_4^{2-}$ ), alkalinity,  $H_2S$ , total dissolved Fe and Mn and dissolved Mn(II) and dMn(III)-L. The samples for  $H_2S$  analysis were diluted five times in a 2% Zn-acetate solution in a glass vial and stored at 4°C. Samples for the analysis of  $NH_4^+$  and, in September, for the analysis of  $NO_2^-$  and nitrate ( $NO_3^-$ ) were stored at -20°C. The samples for  $SO_4^{2-}$  and alkalinity were stored at 4°C. Samples for total dissolved Fe and Mn (TD Fe and TD Mn) were acidified with 10  $\mu\text{L}$  35% suprapure HCl per ml of sample and stored at 4°C. Samples for the analysis of dissolved Mn(II) and dMn(III)-L and the sediment residues were stored in  $N_2$  purged aluminum bags at -20°C.

The second core, with pre-drilled holes at 2.5 cm intervals covered with tape prior to coring, was used directly after retrieval to collect samples for pore water  $CH_4$  concentrations. Plastic cut off syringes were used to transfer 10 ml of sediment directly into 65 ml glass bottles filled with saturated NaCl solution. The bottles were then stoppered, capped and stored upside down until analysis. Note that degassing of  $CH_4$  during the sampling may lead to an underestimation of the total  $CH_4$  concentrations, especially when  $CH_4$  concentrations are high (Egger et al., 2017; Jørgensen et al., 2019). The third core was sectioned at a resolution of 1 cm intervals to determine sediment porosity. The sediment was placed into pre-weighed 50 ml centrifuge tubes. The fourth core was used for high-resolution depth profiling of  $O_2$  with micro-electrodes as described in (Żygadłowska et al., 2023).

### Chemical analysis of pore water and water column samples

Pore water  $NH_4^+$  was analyzed spectrophotometrically with the indophenol blue method (Solórzano, 1968). Concentrations of  $NO_2^-$  and  $NO_3^-$  were measured with a Gallery™ Automated Chemistry Analyzer type 861 (Thermo Fisher Scientific; detection limit of 1  $\text{mmol L}^{-1}$ ). Concentrations of  $SO_4^{2-}$  were measured using ion chromatography (Metrohm 930 Compact IC Flex; detection limit for  $SO_4^{2-}$  of 50  $\mu\text{mol L}^{-1}$ ). Alkalinity was measured through titration with 0.01 M HCl, within 24 h of sampling. Samples for  $H_2S$  were determined spectrophotometrically, using an acidified solution of phenylenediamine and ferric chloride, where  $H_2S$  is the sum

of  $S^{2-}$ ,  $HS^-$  and  $H_2S$  (Cline, 1969). Total dissolved Fe and Mn were determined by Inductively Coupled Plasma Optical Emission Spectroscopy (ICP-OES, Perkin Elmer Avio; detection limit  $0.1 \mu\text{mol L}^{-1}$  and  $0.03 \mu\text{mol L}^{-1}$  for Fe and Mn respectively).

Dissolved Mn(II) and dMn(III)-L concentrations were determined simultaneously via a kinetic spectrophotometric method using porphyrin, cadmium chloride and an imidazole borate buffer as described previously (Madison et al. 2011; detection limit of  $1 \text{ mmol L}^{-1}$  for Mn). The kinetics of the Mn(II) – porphyrin reaction depends on environmental characteristics such as salinity (Thibault de Chanvalon and Luther, 2019) and should therefore be determined for each site separately. Here, the kinetic constant value for Mn(II) was determined in triplicate on an aliquot of sample in which the dissolved Mn was completely reduced by adding an excess of hydroxylamine (Oldham et al., 2015; for kinetic curves of the triplicate analysis see Fig. S1). All samples were analyzed in triplicate using a 1 cm pathlength quartz cuvette in a Shimadzu UV-1900i spectrophotometer (for examples of the kinetic curves, see Fig. S2). Our analyses were all carried out under normal atmospheric conditions. Strongly bound Mn(III)-ligand complexes cannot be measured via this method (Oldham et al., 2015; Kim et al., 2022). Therefore, the difference between the sum of measured Mn(II)/Mn(III)-L and the total dissolved Mn measured by ICP-OES can be interpreted as the amount of Mn(III)-L that is bound to strong ligands.

Prior to the analysis of  $CH_4$ , a 10 ml  $N_2$  headspace was injected in the bottle. After seven days, when equilibrium between the water and gas phase was established,  $CH_4$  was measured with a Thermo Finnigan Trace<sup>TM</sup> gas chromatograph (Flame Ionization Detector; limit of detection  $0.02 \mu\text{mol L}^{-1}$ ).

### **Solid phase analyses**

Porosity was determined based on the weight loss upon drying the samples in an oven at  $60^\circ\text{C}$ . Sediment residues for the anoxic analyses were freeze-dried and subsequently ground with an agate mortar and pestle under a  $N_2$  environment. For analysis of  $C_{\text{org}}$  content, aliquots of ca. 300 mg of the powdered sediment were decalcified with 1 M HCl (2-step wash; Van Santvoort et al., 2002), dried, weighed and powdered. The aliquot was analyzed with an elemental analyzer (Fisons Instruments model NA 1500 NCS) and the C content was corrected for the weight loss during decalcification. The accuracy and precision of the analyses was determined based on measurements of the internationally certified soil standard IVA2. The certified value for IVA2 is 0.732 wt.% C. The mean value that was obtained in this study for IVA2 ( $n=24$ ) was 0.722 wt.% C, with a standard deviation of 0.009 wt.% C. The analytical uncertainty based on duplicates ( $n=15$ ) was 0.11 wt.% C for organic C.

A second aliquot (50 – 100 mg) was analyzed via a sequential extraction procedure to determine the speciation of Fe following a combination of the methods from Poulton and Canfield (2005) and Claff et al. (2010) as described by Kraal et al. (2017) and Mn (Lenstra et al., 2021b). The extraction procedure consists of the following five steps: (1) a mixture of 0.057 M ascorbic acid, 0.17 M sodium citrate and 0.6 M sodium bicarbonate, pH of 7.5, to extract Fe oxides and easily reducible Mn, (2) 1 M HCl to extract reducible crystalline Fe oxides, Fe carbonate, FeS and Mn carbonate, (3) 0.35 M acetic acid, 0.2 M Na<sub>3</sub> citrate and 50 g L<sup>-1</sup> Na dithionite, pH 4.8, to extract crystalline Fe and Mn oxides, (4) 0.2 M ammonium oxalate and 0.17 M oxalic acid to extract recalcitrant Fe oxides and non-reactive Mn such as Mn associated with clay minerals, (5) 65% HNO<sub>3</sub> was used to extract pyrite and Mn associated with pyrite. Extracted Fe and Mn in step 1, 2 and 5 was measured with ICP-OES (ICP-OES, Perkin Elmer Avio; detection limit 0.1 μmol L<sup>-1</sup> and 0.03 μmol L<sup>-1</sup> for Fe and Mn respectively). The average recovery for Fe and Mn was 106% and 100%, respectively and the average analytical uncertainty based on duplicates (n=16) was 3.2% and 2.6%, respectively. Extracted Fe in steps 2, 3 and 4 was determined spectrophotometrically using the phenanthroline method (APHA, 2005). Average analytical uncertainty based on duplicates (n=16) was < 13.4% for all fractions of the three sequential extraction procedures. Mn extracted in step 3 and 4 is not measured, because this is mainly Mn associated with clays (Lenstra et al., 2021b), which is not relevant in this study. The concentration of Fe oxides is assumed to be the sum of the Fe extracted in steps 1, 3 and 4. The Fe extracted in step 2 is not taken into account for Fe oxides, because a separation of Fe(II) and Fe(III) on selected samples, to separate Fe oxides from Fe(II) containing minerals like FeS and Fe carbonate, indicated that nearly all Fe in this step was present as Fe(II). The concentration of Mn oxides is assumed to be the Mn extracted in step 1 (Anschutz et al., 2005; Lenstra et al., 2021b).

### Calculation of benthic diffusive fluxes

Diffusive fluxes of dissolved Mn across the sediment-water interface were calculated with Fick's law of diffusion, based on the gradient in total Mn concentration between the bottom water and the pore water in the upper cm of the sediment (at an average depth of 0.5 cm) by applying the formula:

$$J = -\varphi D_s \frac{dC}{dz} \quad (1)$$

where J is the diffusive flux in mmol m<sup>-2</sup> d<sup>-1</sup>,  $\varphi$  is the porosity of the sediment, D<sub>s</sub> is the diffusion coefficient for Mn in the sediment in m<sup>-2</sup> d<sup>-1</sup>, C is the concentration of Mn in mmol m<sup>-3</sup> and z is the sediment depth in m. In our calculations, we assumed

all Mn was present as Mn(II), The  $D_s$  for Mn(II) was corrected for temperature and salinity using the R package CRAN: *marelac* (Soetaert et al., 2010), taking into account the tortuosity of the sediment (Boudreau, 1996).

### Reactive transport model

A 1-dimensional reactive transport model, written in R (version 3.6.2) and modified from Egger et al. (2016) and Lenstra et al. (2018), was used to model the sedimentary Mn cycle, including the dynamics of both dissolved Mn(II) and dMn(III)-L. The model, a standard multicomponent reactive transport model, is based on the principles that are outlined in, for example, Van Cappellen and Wang (1996). The modelled components include 9 solids and 12 solutes (Table S1). Solids are transported by advection (burial), while solutes are transported both by advection and molecular diffusion. The model includes 36 reactions (Table S2, S3). The reaction parameters were obtained from the literature or constrained using the model (Table S3, S4). Chemical and physical constants were calculated using the *marelac* package (Soetaert et al., 2010) and transport coefficients were calculated using the *reactran* package (Soetaert and Meysman, 2012) and were, where relevant, adjusted for environmental characteristics at the study site (Table S5). The diffusion coefficient for dMn(III)-L was set to a lower value than that of Mn(II), because the diffusive behavior of metal-ligand complexes is typically controlled by the organic ligand (Furukawa and Takahashi, 2008; Table S6).

The model describes the upper 100 cm of the sediment column, which is divided into 1000 model layers of 1 mm. The boundary conditions are set at the top of the sediment and are defined as fixed concentrations for solutes and fluxes for solids (Table S7). The model was fit to the data set for 2020. In a spin up of the model, the boundary conditions were fixed until steady state was reached after 60 years, as in Egger et al. (2016). The model was then run for 20 years, in which the seasonal cycle of oxic – euxinic conditions was simulated by varying the bottom water  $O_2$  and  $H_2S$  concentration, the influx of Fe-oxides, Mn oxides and OM and the sedimentation rate (Fig. S3). The key purpose of the model application was to determine the seasonality in the production and removal pathways of dMn(III)-L in the sediment and estimate the rate of diffusive release of dMn(III)-L and Mn(II) to the overlying water. Here we specifically focus on the general trends in the key processes that regulate the seasonal dMn(III)-L dynamics in a eutrophic basin. As the model focusses on these general trends, the overall picture of Mn dynamics at this site will not change due to uncertainties related to, for example, the sample resolution in the top part of the sediment.

In the model, high rates of  $\text{CH}_4$  production lead to an overestimation of  $\text{CH}_4$  concentrations because  $\text{CH}_4$  bubble formation is not included. Adding bubble formation would not improve our main model results regarding  $\text{dMn(III)-L}$  dynamics, however, but would increase model uncertainty. We note that a perfect model fit of the data is not expected, due to the complexity of the system and the strong seasonal variations at our study site which also vary between years. This is especially true for the fit to the solid phase profiles since such variations in the reactivity and input flux of solid phases are not specifically included in the model (Table S4, S5). A detailed model description is provided in supplement section 2.

A sensitivity analysis was performed to investigate the response of the benthic release of  $\text{dMn(III)-L}$  and  $\text{Mn(II)}$  to variations in OM input. The input of OM was varied by a factor of 0.01 to 2, relative to the base line scenario, leading to average OM oxidation rates ranging from 0.6 to 143  $\text{mmol C m}^{-2} \text{d}^{-1}$  in the months when bottom waters were oxygenated and 0.9 to 219  $\text{mmol C m}^{-2} \text{d}^{-1}$  in months with euxinic conditions. To obtain insight in the processes controlling the transformation and benthic release of Mn, reaction rates were integrated over the upper 10 cm of the sediment.

A forward simulation of pore water and solid phase data collected during 8 sampling events, one in each month from March to October 2021, was performed to verify the model.

## Results

### Water column and pore water profiles

In March 2020, the water column of Scharendijke basin was fully oxygenated (Fig. 1). In September, in contrast,  $O_2$  depletion was observed below a water depth of 35 m (Fig. 2) and dissolved Mn, primarily present as dMn(III)-L, accumulated to concentrations of up to  $22 \text{ mmol L}^{-1}$  in the anoxic waters (Fig. 2). Small enrichments in Mn(II) and dMn(III)-L were observed above the redox cline at depths of 32 and 30 m, respectively.

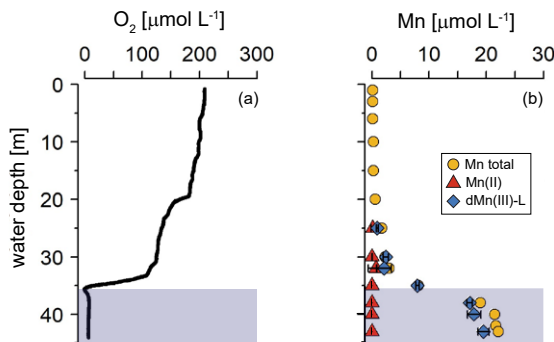


**Figure 2** (a) Water column  $O_2$  and (b) total dissolved Mn and dissolved Mn(II) and dMn(III)-L (error bars represent standard deviation;  $n=3$ ) in the Scharendijke basin as observed in September 2020. The shaded area indicates the anoxic part of the water column.

The seasonal contrast in bottom water oxygen was reflected in the  $O_2$  concentration in the sediment: while  $O_2$  was present in the upper 0.6 cm of the sediment in March 2020,  $O_2$  was absent in September 2020 (Fig. 3; for a zoom of the top 20 cm, see Fig. S6). In September,  $NO_2^-$  and  $NO_3^-$  did not exceed the detection limit of  $1 \mu\text{mol L}^{-1}$  and showed no trend with depth. Concentrations of  $NH_4^+$ , alkalinity and  $CH_4$  increased with sediment depth to maximum values of  $\sim 15$ , 80 and  $4 \text{ mmol L}^{-1}$ , respectively. In the surface sediment (upper 10 cm) the profiles of  $NH_4^+$  and alkalinity showed a distinct seasonality, however, with higher concentrations in September compared to March. Profiles of  $SO_4^{2-}$  and  $H_2S$  also varied between the two seasons seasonally with  $SO_4^{2-}$  being removed at a shallower depth in September than in March and the zone of high  $H_2S$  concentrations (i.e. 1.5 to  $5 \text{ mmol L}^{-1}$ ) shifting upwards by 10 cm. Dissolved Fe, in contrast, was abundantly present in the top 10 cm of the sediment in March, even reaching values of up to  $1.1 \text{ mmol L}^{-1}$ , but was nearly absent from the pore water in September. Similarly, concentrations of dissolved Mn reached a maximum of  $437 \text{ mmol L}^{-1}$  near the sediment-water

interface in March but were much lower in September. The peak in dissolved Mn in the upper 10 cm of the sediment in March was found to consist of two partially overlapping peaks, with that of dMn(III)-L (up to  $380 \text{ mmol L}^{-1}$ ) explaining the sharp rise in dissolved Mn in the top cm of the sediment, and a broad peak in dissolved Mn(II) (up to  $257 \text{ mmol L}^{-1}$ ) accounting for most (generally >75%; Fig. S4) of the remaining Mn in the top 10 cm. Between 10 and 30 cm, dissolved Mn was mainly present as dMn(III)-L (up to 100% of the total dMn pool) and below 30 cm dissolved Mn(II) and dMn(III)-L contributed equally, both varying between 25% and 75% of the total dMn pool. In September, dissolved Mn was mainly present in the form of dMn(III)-L, which almost always accounted for >50% of the total dMn pool (Fig. S5).

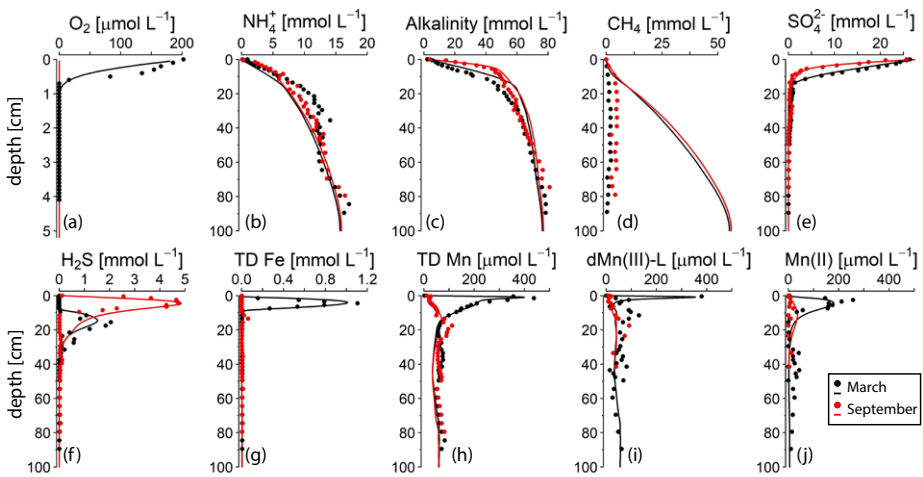


**Figure 3** Pore water profiles of key components in March (black) and September (red) 2020. The dots represent measured concentrations, the lines indicate the results of the reactive transport model. Note the different depth scale on the y-axis for  $\text{O}_2$ . TD Fe and TD Mn refer to total dissolved Fe and total dissolved Mn. Profiles of Mn(II) and dMn(III)-L with standard deviation error bars ( $n = 3$ ) and the contribution to TD Mn (in %) can be found in Fig. S4, S5. No  $\text{O}_2$  was detected in the sediment in September 2020. A zoom of the top 20 cm of the profiles is presented in Fig. S6.

The diffusive benthic Mn fluxes calculated with Fick's law of diffusion, based on the concentrations of the total dissolved Mn, were  $2.1 \text{ mmol m}^{-2} \text{ d}^{-1}$  in March and  $0.09 \text{ mmol m}^{-2} \text{ d}^{-1}$  in September.

### Solid phase profiles

The solid phase profiles of  $C_{\text{org}}$ , Fe- and Mn oxides and Mn carbonate reflect the strong seasonality of biogeochemical processes in the basin. The  $C_{\text{org}}$  content in the top 10 cm of the sediment was much lower in March 2020 ( $\sim 2.5 \text{ wt\%}$ ) compared to September 2020 ( $\sim 3.5 \text{ wt\%}$ ) (Fig. 4). In March, when  $\text{O}_2$  was present in the bottom water, the top part

of the sediment was enriched in Fe and Mn oxides and Mn carbonate. In September, when bottom waters were euxinic, surface enrichments in Fe and Mn oxides and Mn carbonate were absent (Fig. 4). The oscillations in the solid phase records are preserved upon burial of the sediment. For profiles of all the Fe and Mn fractions, we refer to the supplement (Fig. S7, S8). Porosity values vary between 0.98 and 0.88, with a general trend towards lower values deeper in the sediment (Fig. S7, S8).

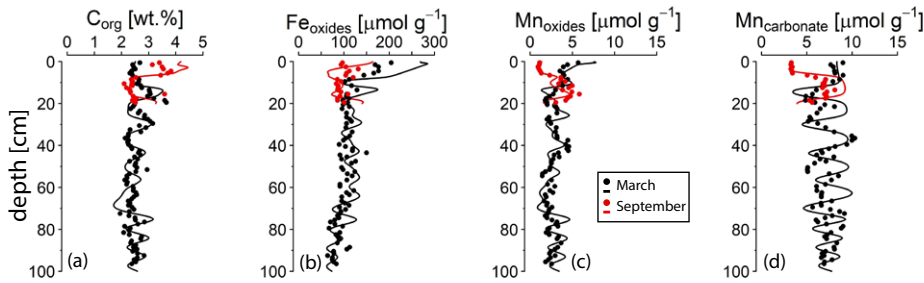


**Figure 4** Solid phase profiles of key components in March (black) and September (red) 2020. The dots represent measured values, the lines indicate the results of the reactive transport model. Fe oxides refer to the sum of the Fe extracted in the ascorbic acid, CDB and ammonium oxalate extraction steps. Mn oxides refer to the Mn that is extracted in the ascorbic acid step. The profiles for all extraction steps are shown in Fig. S7 and S8.

## Sedimentary reactive transport modelling

### Model fit

The reactive transport model generally describes the depth trends in the pore water and solid phase profiles for March and September 2020 quite well (Fig. 3, 4). For the pore water, the only exceptions are the modelled  $\text{CH}_4$  profile and the profile of  $\text{dMn(III)-L}$  between 10 and 20 cm. For the solid phase profiles, the amplitude of the change in  $C_{\text{org}}$ , Fe oxide and Mn carbonate content is not always fully captured. In the next sections, we will primarily focus on a description of the model results for 2020 that are relevant to  $\text{dMn(III)-L}$  dynamics.

### Dissolved Mn(III)-L dynamics in the sediment

Depth-integrated reaction rates show that, according to the model, the formation of  $\text{dMn(III)-L}$  in March 2020 is driven equally by reduction of Mn oxides coupled to OM degradation and Fe(II) oxidation and oxidation of dissolved Mn(II) by  $\text{O}_2$  (each  $\sim 0.3 \text{ mmol m}^{-2} \text{ d}^{-1}$ ; Fig. 5; for reaction rate profiles see Fig. S9) with a negligible role for reduction of Mn oxides by  $\text{H}_2\text{S}$ . Removal of  $\text{dMn(III)-L}$  in March occurs via reduction coupled to Fe(II) oxidation ( $0.55 \text{ mmol m}^{-2} \text{ d}^{-1}$ ), oxidation by  $\text{O}_2$

(0.1 mmol m<sup>-2</sup> d<sup>-1</sup>) and benthic release (0.21 mmol m<sup>-2</sup> d<sup>-1</sup>). Besides oxidation by O<sub>2</sub>, dissolved Mn(II) precipitates as Mn carbonate and is released to the water column. In September 2020, the input of Mn oxides is 9 times lower than in March, leading to much lower rates of Mn cycling. Formation of dMn(III)-L is still coupled to OM degradation (0.03 mmol m<sup>-2</sup> d<sup>-1</sup>) and oxidation of Fe(II) (0.01 mmol m<sup>-2</sup> d<sup>-1</sup>) but now oxidation of H<sub>2</sub>S also contributes (0.01 mmol m<sup>-2</sup> d<sup>-1</sup>). Removal of dMn(III)-L in September mainly takes place via benthic release (0.03 mmol m<sup>-2</sup> d<sup>-1</sup>) and reduction of dMn(III)-L coupled to oxidation of Fe(II) (0.02 mmol m<sup>-2</sup> d<sup>-1</sup>). Again, Mn(II) is removed as Mn carbonate and via benthic release.

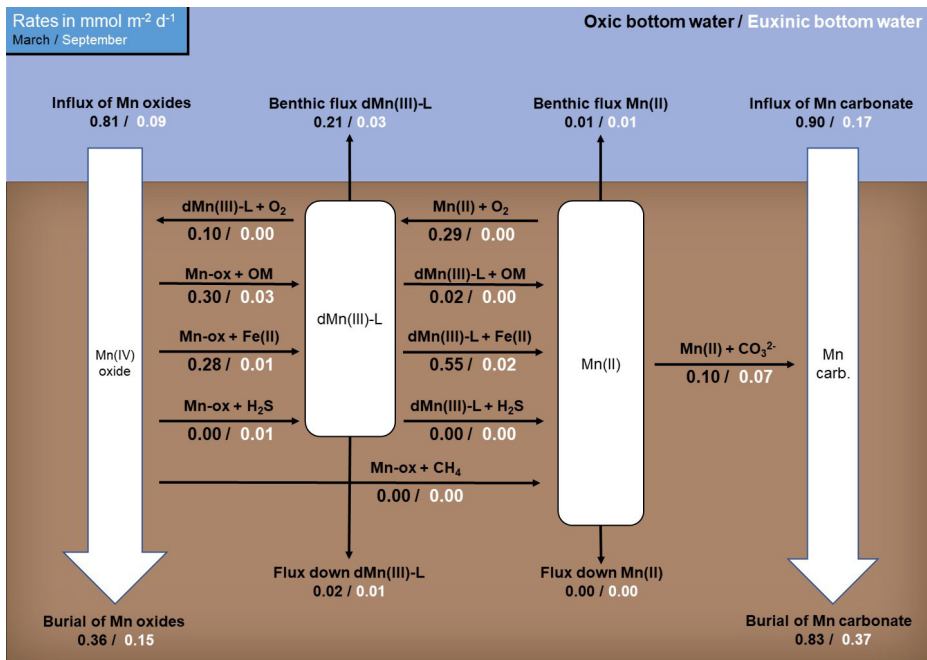


**Figure 5** Rates of Mn cycling in March (black) and September (white) 2020 as calculated with the reactive transport model. Numbers represent depth integrated reaction rates in mmol m<sup>-2</sup> d<sup>-1</sup>. Note that the rates are not balanced because the system is not at steady state. The depth profiles of the reaction rates can be found in Fig. S9.

Our model also allows us to assess trends in depth-integrated rates of dMn(III)-L production and removal in the sediment throughout the year (Fig. 6; see Fig. S10 for modelled pore water profiles in the months between March and September 2020). Taking October as the starting point of the oxic period that lasts until April, we see that production of dMn(III)-L via reduction of Mn oxides coupled to OM degradation initially dominates. Over time, reduction of Mn oxides coupled to Fe(II) oxidation and oxidation of dissolved Mn(II) by O<sub>2</sub> become increasingly important.

Following the onset of anoxia in May, reduction of Mn oxides by Fe(II) becomes the major source of dMn(III)-L. During the euxinic months, the role of reduction of Mn oxide by Fe(II) decreases and OM degradation becomes the major driver of Mn oxide reduction from August onwards, followed by H<sub>2</sub>S oxidation. Removal of dMn(III)-L from the sediment is dominated by reduction by dissolved Fe(II), especially during the oxic period, with additional loss through dMn(III)-L oxidation with O<sub>2</sub> (oxic period only) and benthic release.

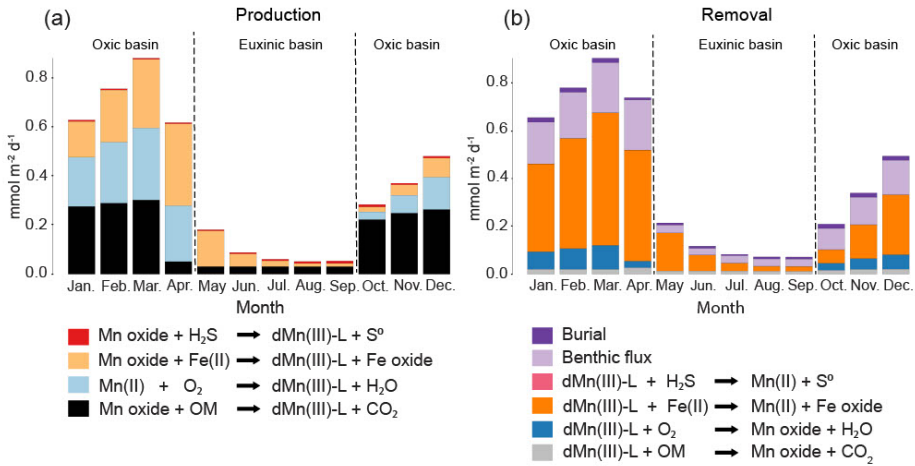


**Figure 6** Depth integrated reaction rates for the sediment processes that (a) produce dMn(III)-L and (b) that remove dMn(III)-L as calculated with the model. The rates are calculated for each month of one year (2020) and are given in mmol m<sup>-2</sup> d<sup>-1</sup>.

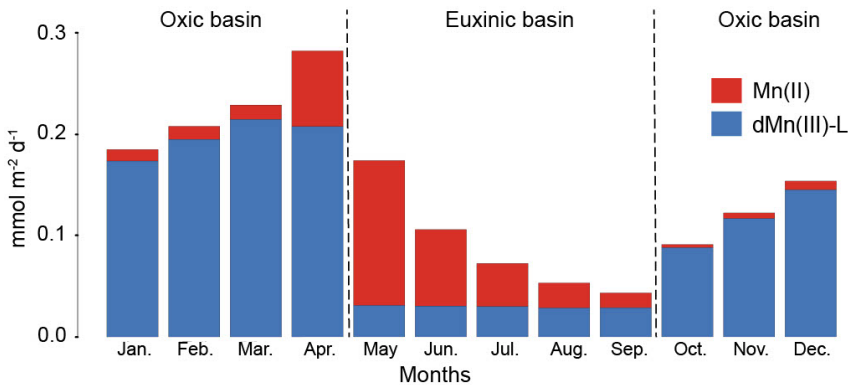


**Figure 7** Sediment-water exchange of dissolved Mn (mmol m<sup>-2</sup> d<sup>-1</sup>) calculated per month in 2020. The total dissolved Mn flux consists of dissolved Mn(II) and dMn(III)-L. Positive numbers indicate a flux from the sediment to the overlying water.

According to the model, the benthic release of dissolved Mn is highest in the period when the bottom waters are oxic (Fig. 7). During this time, the flux consists primarily of dMn(III)-L. Upon the onset of euxinia in May, the flux mainly consists of Mn(II). With time, the benthic flux of Mn(II) subsequently decreases allowing the relatively constant low flux of dMn(III)-L to gain relative importance.

### ***Sensitivity analysis***

To study the effect of variations in OM degradation rates on the benthic release of Mn, a model sensitivity analysis in which the input of OM was varied was performed. The sensitivity analysis revealed that, in the model, average rates of formation and removal of dMn(III)-L for the oxic and euxinic periods are highly dependent on OM oxidation rates (Fig. 8). Rates of all processes involving dMn(III)-L initially increase upon a rise in OM oxidation rates and then show a variable response, either decreasing (Fe(II), O<sub>2</sub>), remaining largely constant (OM) or increasing (H<sub>2</sub>S). Reactions involving dissolved Fe(II) generally dominate. The role of processes involving Fe(II) diminishes, however, during the euxinic months when rates of OM oxidation are above 150 mmol m<sup>-2</sup> d<sup>-1</sup>.

According to the model, the average benthic flux of Mn during the oxic period is highly sensitive to OM oxidation rates between 0 and 50 mmol m<sup>-2</sup> d<sup>-1</sup> and shows a strong increase before stabilizing (Fig. 8). Most of the Mn is released as dMn(III)-L. The pattern is different for the euxinic period: here, again an initial increase in the Mn flux is observed when OM oxidation rates vary between 0 and 10 mmol m<sup>-2</sup> d<sup>-1</sup>, but this is followed by a strong decrease. In this case, most of the Mn is released as Mn(II), except for the model runs with the highest OM oxidation rate: here dMn(III)-L gains importance.

### ***Forward simulation***

The forward simulation for 2021 using depth profiles of pore water NH<sub>4</sub><sup>+</sup>, alkalinity, SO<sub>4</sub><sup>2-</sup>, H<sub>2</sub>S, TD Fe, TD Mn and sediment Mn oxides and Mn carbonates obtained for 2021 shows that, without any additional fitting, our model is able to capture the major trends in the sedimentary Mn cycle and key pore water constituents over a spring-summer-fall cycle (Fig. S11).

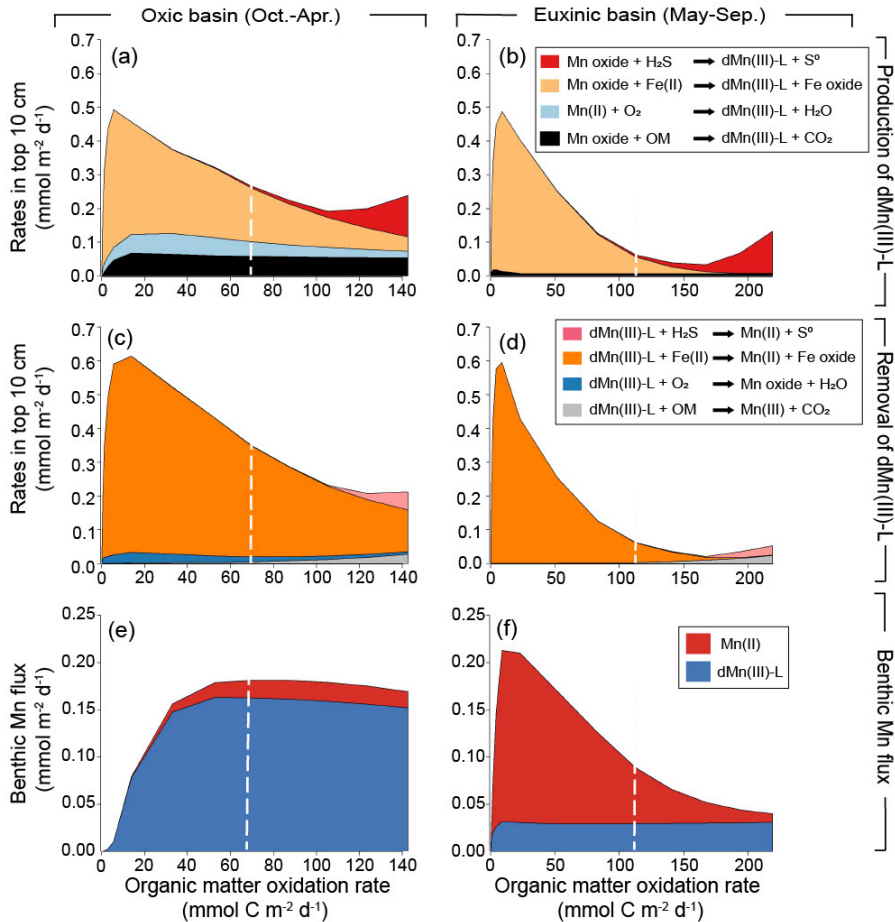


**Figure 8** Depth-integrated reaction rates (0 – 10 cm) of formation (a, b) and removal (c, d) of dMn(III)-L as a function of rates of organic matter oxidation in the sensitivity analysis. Note that the months when the basin is oxic (October – April; a, c) and euxinic (May – September; b, d) are separated. Average benthic flux of dissolved Mn(II) and dMn(III)-L as a function of the rate of organic matter oxidation in the months when the basin is oxic (e; October - April) and when the basin is euxinic (f; May - September). The vertical white dashed line represents the baseline run.

## Discussion

### **Mn(III) is a key pore water component in a eutrophic coastal system**

Dissolved Mn(III)-L is frequently observed in pore waters at sites where  $O_2$  is present in the surface sediment (Madison et al., 2011, 2013; Oldham et al., 2019). Here, we show that dMn(III)-L is also a key pore water component in a setting where  $O_2$  is absent and bottom waters are euxinic (Fig. 3). The results of our reactive transport model suggest that the pathways of production and removal of dMn(III)-L strongly depend on the pore water composition, with Fe(II) playing a critical role.

In March 2020, when bottom waters were oxic, a maximum in dMn(III)-L was observed in the top centimeter. This maximum is based on one individual data point, but we note that it is based on triplicate analyses (Fig. S4) and is in accordance with the peak in total dissolved Mn determined via an independent procedure (ICP-OES; Fig. S4). Additionally, such a sharp peak in dMn(III)-L at the oxic/anoxic interface is expected when  $O_2$  is involved in the production of dMn(III)-L (Madison et al., 2013). The model underestimates the dMn(III)-L concentrations between depths of 10 to 20 cm, which we attribute to an incomplete understanding of the processes that impact dMn(III)-L production and formation in sulfidic sediments. We note that the good fit of the model for most pore water and sediment components for 2020 and, as an outcome of the forward modelling, for 2021, gives confidence in the results.

According to the model, formation of dMn(III)-L in the pore water at our site in March is driven by - at equal rates - reduction of Mn oxides by OM and Fe(II) and oxidation of dissolved Mn(II) by  $O_2$  (Fig. 5). This contrasts with the production pathways of dMn(III)-L estimated from pore water profiles and solid phase data for different sites in the Saint Lawrence Estuary and Gulf, which pointed towards a dominant role for oxidation of Mn(II) by  $O_2$  (Madison et al., 2013). This difference is likely due to the exceptionally large input of OM and Fe oxides at our study site, with a modelled average input of  $\sim 240 \text{ mmol C m}^{-2} \text{ d}^{-1}$  and  $\sim 19 \text{ mmol reactive Fe m}^{-2} \text{ d}^{-1}$  throughout the year (Fig. S3; approximately half of the reactive Fe is accounted for by Fe extracted in ascorbic acid Fig. S7, S8), compared to maximally  $10 \text{ mmol C m}^{-2} \text{ d}^{-1}$  and  $0.6 \text{ mmol Fe m}^{-2} \text{ d}^{-1}$  (Fe extracted with ascorbic acid) in the St. Lawrence Estuary and Gulf (Oldham et al., 2019).

In September 2020, when  $O_2$  was absent from the pore water at our site, Mn oxide concentrations in the top layer of the sediment were low compared to March. This was likely the result of a lower input of Mn oxides when the bottom water was sulfidic, linked to quick reduction of Mn oxides in the water column. Under these

conditions, dMn(III)-L was mainly formed via reduction of Mn oxides by OM, with a smaller contribution of Mn oxide reduction by H<sub>2</sub>S and Fe(II) (Fig. 5). Strikingly, dMn(III)-L co-occurred with H<sub>2</sub>S in the pore water, despite H<sub>2</sub>S concentrations of several millimolar (Fig. 3). A co-occurrence of dMn(III)-L and H<sub>2</sub>S was observed previously in estuarine waters at H<sub>2</sub>S concentrations of several micromolar (Oldham et al., 2015). In this previous work, the co-occurrence was attributed to stabilization of dMn(III)-L by organic ligands that kinetically hindered Mn(III) reduction by H<sub>2</sub>S (Oldham et al., 2015). Our results suggest that stabilization of dMn(III)-L against reduction by H<sub>2</sub>S is even possible when H<sub>2</sub>S concentrations reach several millimolar.

According to our model, most dMn(III)-L at the study site is removed through reduction by Fe(II) (Fig. 5), explaining the strong counter gradients between dMn(III)-L and dissolved Fe in March (Fig. 3; Fig. S6). Apparently, the ligands that stabilize dissolved Mn(III) do not shield the Mn(III) against reduction by Fe(II). The larger role of Fe(II) as a reductant for dMn(III)-L then observed in the study by Madison et al. (2013) may be explained by the approximately 20 times higher Fe(II) concentrations at our site. Previous reactive transport modelling has highlighted the role of Fe(II) in the reduction of Mn oxides (Van Cappellen & Wang, 1996). What is novel here is that dissolved Fe(II) not only plays a key role in Mn oxide reduction and dMn(III)-L production but also in dMn(III)-L removal. We note that this role of Fe(II) in dMn(III)-L dynamics came to a halt in August and September when the Fe-oxides that accumulated in winter were completely reduced and dissolved Fe precipitated with H<sub>2</sub>S as FeS and FeS<sub>2</sub>. Taken together, this indicates that, in Fe rich coastal systems, sediment Fe dynamics can be an even more important driver of Mn cycling than previously considered (e.g. Madison et al., 2013). The results of the sensitivity analysis highlight that the role of Fe(II) in dMn(III)-L cycling holds over a wide range of OM oxidation rates (Fig. 8).

Due to its organic complexation the diffusion coefficient of dissolved Mn(III) is expected to be lower compared to that of dissolved Mn(II) (Kalinichev and Kirkpatrick, 2007; Furukawa and Takahashi, 2008). Additionally, due to heterogeneity within the ligands that can stabilize dissolved Mn(III) (Madison et al., 2013; Oldham et al., 2015, 2017b), the diffusion coefficient of the complex of dMn(III)-L can vary per location. We find that a difference in diffusion coefficient between dMn(III)-L and Mn(II) is essential to describe the sharp gradients in the dissolved Mn profiles in the model. Without a lower diffusion coefficient for dMn(III)-L it is not possible to form a sharp peak in dMn(III)-L near the sediment-water interface in our model (Fig. S12). Notably, all modelling studies of sedimentary Mn cycling to date focus only on dissolved Mn(II) excluding dMn(III)-L, which can explain why similar sharp

gradients in dissolved Mn near the sediment water interface have so far been difficult to capture (e.g. Slomp et al., 1997; Reed et al., 2011b). The adjusted diffusion coefficient for dMn(III)-L is  $16.6 \text{ cm}^2 \text{ yr}^{-1}$ , ca. 8 times lower than the diffusion coefficient for Mn(II) ( $132.6 \text{ cm}^2 \text{ yr}^{-1}$ ; Table S6). When we assume all dissolved Mn is present as Mn(II) the calculated diffusive flux of dissolved Mn would be ca. 10 and 3 times higher than when we consider both Mn(II) and dMn(III)-L in March and September, respectively. The lower diffusion coefficient of dMn(III)-L when compared to Mn(II) also implies that calculated diffusive fluxes across the sediment-water interface will be overestimated if all Mn is assumed to be present as Mn(II) (Fig. S13).

### Seasonality in benthic Mn fluxes

The model results imply that throughout the year, both dissolved Mn(II) and dMn(III)-L contribute to the release of Mn from the sediment to the overlying water (Fig. 7). The flux is highest and primarily consists of dMn(III)-L under oxic conditions in winter and spring, when the input of Mn oxides and recycling of Mn near the sediment-water interface is highest. The high contribution of dMn(III)-L to the benthic Mn flux in the oxygenated basin results from faster oxidation of Mn(II) with  $\text{O}_2$  compared to dMn(III)-L, which leads to a build-up of dMn(III)-L just below the sediment-water interface and subsequently a high benthic flux of dMn(III)-L.

When euxinic bottom-water conditions are established in summer, the modelled benthic flux primarily consists of Mn(II), because Mn(II) is no longer oxidized by  $\text{O}_2$  (Fig. 7). However, a fraction of the Mn released from the sediment remains dMn(III)-L, indicating that a part of the dMn(III)-L released is a product of Mn oxide reduction rather than Mn(II) oxidation. As sediments become depleted in Mn oxides, typically during persistent hypoxia or anoxia, the benthic flux of Mn is known to strongly decrease (Slomp et al., 1997; Lenstra et al., 2021a). We find that the benthic flux of Mn decreases substantially as soon as the basin becomes euxinic, which likely indicates that highly reactive Mn oxides are quickly removed from the sediment when the input of Mn oxides decreases as a result of the bottom water euxinia. This is supported by the pore water and sediment data for the fieldwork campaigns between March and October in 2021 (Supplements section 1; Fig. S11). The TD Mn in the pore water already decreases between March and April and remains low throughout the euxinic period that lasts from June to September (Żygadłowska et al., 2024a). We note that part of the dissolved Mn(II) in the pore water precipitates as Mn carbonate and hence is retained in the sediment. To visualize that both variations in Mn carbonate formation and input of Mn carbonate contribute to the seasonal variation in the sediment, a model run without Mn carbonate precipitation was performed (Fig. S14).

A new finding here is that, at the end of the anoxic period, the benthic Mn flux mainly consists of dMn(III)-L. The continuous release of dMn(III)-L from the sediment during the period of anoxia is reflected in the accumulation of dMn(III)-L in the anoxic part of the water column in September (Fig. 2). When bottom water O<sub>2</sub> re-establishes in October, the influx of Mn and Fe oxides, the rates of sedimentary Mn cycling and the benthic flux of Mn all increase. In subsequent months, the benthic flux of dMn(III)-L and the importance of Fe in Mn cycling continues to increase until just before the onset of a new euxinic period (Fig. 6, 7).

The sensitivity analysis reveals that the benthic fluxes of Mn(II) and dMn(III)-L are also dependent on the rate of OM oxidation in the sediment (Fig. 8). Nevertheless, the general patterns that emerged from the simulation for 2020, still hold: when bottom water O<sub>2</sub> is present, dMn(III)-L release from the sediment to the overlying water dominates over Mn(II) release. The reverse is found during the euxinic period when taken as a whole. Taken together, our results highlight that while Fe(II) dynamics play a critical role in dMn(III)-L production and removal in our Fe- and OM-rich coastal sediment, the presence of bottom water O<sub>2</sub> ultimately determines whether, on a yearly basis, Mn(II) or dMn(III)-L is the dominant form of Mn that escapes to the overlying water. Regardless of the bottom water redox conditions, the model always predicts some benthic release of dMn(III)-L.

## Implications

Our results imply that dMn(III)-L should be considered as a potential pore water constituent when studying sedimentary Mn cycling in OM- and Fe-rich coastal sediments. When dMn(III)-L is released into anoxic waters, it can act as an oxidant and reductant, with potential implications for various redox interactions, as previously shown for anoxic water columns (e.g. Trouwborst et al., 2006; Yakushev et al., 2007; Oldham et al., 2015). When, in contrast, O<sub>2</sub> is present in the bottom water, dissolved Mn(II) will be readily oxidized to dMn(III)-L when it is exposed to O<sub>2</sub> near the sediment-water interface. As a consequence, dMn(III)-L is the main form in which dissolved Mn may leave the sediment (Fig. 7). The ligand stabilizing dMn(III)-L may not only slow down diffusion but is also likely to slow down the formation of solid phase Mn oxides (Sander & Koschinsky, 2011; Oldham et al., 2021). Because Mn oxides are subject to gravitational settling (e.g. Sulu-Gambari et al., 2017; Hermans et al., 2021) and dMn(III)-L is not, the dMn(III)-L is expected to be transported further away from the sedimentary source (Lenstra et al., 2020). Additionally, trace metals such as cobalt, nickel and zinc, can adsorb to the negatively charged surface of Mn oxides (Koschinsky and Hein, 2003). When transport of Mn is in the form of dMn(III)-L instead of Mn oxides, these trace metals will no longer adsorb to the Mn

oxides and the transport of the trace metals will be decoupled from the transport of Mn (Oldham et al., 2021; Lenstra et al., 2022).

## Conclusions

Our combined seasonal field and modelling study reveals that dissolved Mn(III) (dMn(III)-L) is a key component of the Mn cycle in sediments of a seasonally euxinic coastal basin. Dissolved Mn(III)-L accounts for the majority of dissolved Mn in the pore water and coexists with high concentrations of H<sub>2</sub>S. Results of a multicomponent reactive transport model suggest that, at our study site, reduction of Mn oxides coupled to oxidation of Fe(II) and organic matter and oxidation of Mn(II) by O<sub>2</sub> are the primary sources of the dMn(III)-L when O<sub>2</sub> is present near the sediment water interface. However, when the bottom waters are euxinic, reactions with dissolved Fe(II) likely dominate both the production and removal of dMn(III)-L. Modelled benthic Mn fluxes suggest that while dMn(III)-L is released from the sediment throughout the year, there is a distinct seasonal contrast: in the model, release of dMn(III)-L dominates when bottom waters are oxic while a transition to euxinia leads to a temporary increased role for Mn(II). The benthic release of dMn(III)-L, both under oxic and euxinic bottom waters, in combination with a higher mobility of dMn(III)-L in the water column when compared to Mn(II), may contribute to lateral transport of Mn from coastal zones to open marine waters.

### Code and data availability

The data presented in this paper are available in the supplements. The data and model presented in the study are also deposited in the Zenodo repository, doi: 10.5281/zenodo.14509408.

### Conflict of interest

The authors declare that they have no conflict of interest.

### Acknowledgements

We thank the captain and crew of the R/V *Navicula*, A. Tramper and M. Hermans for their support during the sampling campaigns. We are also grateful to T. Claessen, C. Mulder, J. Visser and H. de Waard, for analytical assistance at Utrecht University. This research was financially supported by ERC Synergy grant MARIX (854088) and the Netherlands Earth System Science Center (NESSC 024002001). WKL acknowledges support from a NESSC Travel Grant and Veni grant VI.Veni.222.332.

**Author contributions**

RK, WL and CS designed the research and wrote the paper with comments provided by all authors. OZ, NvH, and WL performed the sampling. RK, OZ, NvH, and WL performed the geochemical analyses. VO instructed on the dissolved Mn(II)/Mn(III) method. RK and WL wrote the reactive transport model code and performed the model simulations. RK, OZ, NvH, WL, CS and MJ interpreted the data. All authors contributed to the article and approved the submitted version.

## Supplements

### Description of the fieldwork campaigns performed in 2021

Sampling of the sediment at Scharendijke basin was performed during 8 sampling campaigns with RV *Navicula* each month from March to October 2021, following the same methods used in the fieldwork campaigns in 2020 presented in this study. An additional sampling event in August / September 2021 is reported in Żygadłowska et al. (2024a, b). These results are not included here, because we focus on the monthly output of the reactive transport model. During each campaign, a sediment core was collected using a UWITEC corer with a transparent PVC core liner (120 cm length, 6 cm inner diameter) to collect samples for  $\text{NH}_4^+$ , alkalinity,  $\text{SO}_4^{2-}$ ,  $\text{H}_2\text{S}$ , TD Fe, TD Mn and during four campaigns, for the determination of Mn oxide and Mn carbonate. The core was sectioned at a 1 cm resolution under a  $\text{N}_2$  environment, the sections were subsequently centrifuged to separate the pore water from the solid phase. The supernatant was filtered over 0.45  $\mu\text{m}$  pore size filters. Samples for the analysis of  $\text{NH}_4^+$  were stored at  $-20^\circ\text{C}$  and later analyzed using the indophenol blue method (Solórzano, 1968). The samples for alkalinity and  $\text{SO}_4^{2-}$  were stored at  $4^\circ\text{C}$  until analysis. Alkalinity was measured through titration with 0.01 M HCl, within 24 h after sampling and  $\text{SO}_4^{2-}$  was measured using ion chromatography (Metrohm 930 Compact IC Flex; detection limit for  $\text{SO}_4^{2-}$  of 50  $\mu\text{mol L}^{-1}$ ). The samples for  $\text{H}_2\text{S}$  analysis were diluted five times in a 2% Zn-acetate solution in a glass vial and stored at  $4^\circ\text{C}$ . These samples were analyzed using the phenylenediamine and ferric chloride method (Cline, 1969). Samples for TD Fe and Mn were acidified with 10  $\mu\text{L}$  35% suprapure HCl per ml of sample and stored at  $4^\circ\text{C}$ . These samples were analyzed via ICP-OES (Perkin Elmer Avio; detection limit 0.1  $\mu\text{mol L}^{-1}$  and 0.03  $\mu\text{mol L}^{-1}$  for Fe and Mn respectively). Samples for the analysis of the sediment residues were stored in  $\text{N}_2$ -purged aluminum bags at  $-20^\circ\text{C}$ . Later, the samples were freeze-dried and ground with an agate mortar and pestle under a  $\text{N}_2$  environment. Solid phase speciation of Mn was then determined using a sequential extraction procedure as described in Lenstra et al. (2021b).

### Detailed model description

The reactions in the model describe organic matter (OM) degradation involving a range of electron acceptors combined with secondary reactions of the reaction products (Table S5). Degradation of OM is facilitated, in successive order, by reduction of  $\text{O}_2$ ,  $\text{NO}_3^-$ ,  $\text{MnO}_2$ ,  $\text{Fe}(\text{OH})_3$  and  $\text{SO}_4^{2-}$  and finally OM is degraded via methanogenesis (Table S2; Froelich et al., 1979; Reed et al., 2011a; Rooze et al., 2016). Monod kinetics are used to describe the sequence of electron acceptors in OM degradation (Boudreau, 1997). In Monod kinetics, the oxidant with the highest

metabolic free energy yield is used preferentially, until this species becomes limiting and the next oxidant in the sequence is used preferentially (Boudreau, 1996; Van Cappellen & Wang, 1996). The OM is assumed to include carbon (C), nitrogen (N) and phosphorus (P) in a ratio of C:N:P = 106:15.45:1 (based on Egger et al., 2016b). Hence, the rate of OM degradation in the sediment is directly linked to the  $\text{NH}_4^+$  profiles. In the model, reduction of  $\text{MnO}_2$  can be coupled to oxidation of OM, Fe(II),  $\text{H}_2\text{S}$  and  $\text{CH}_4$  (Table S2). Reduction of  $\text{MnO}_2$  by OM, Fe(II) and  $\text{H}_2\text{S}$  is modeled as one electron transfer steps with Mn(III) as the product (Madison et al., 2013). Reduction of  $\text{MnO}_2$  by  $\text{CH}_4$  is modeled as a two electron transfer with Mn(II) as a product, because, to our knowledge, the one electron transfer step that is theoretically possible has never been demonstrated. Reduction of  $\text{MnO}_2$  with  $\text{NH}_4^+$  as discussed by Hulth et al. (1999) and Thamdrup and Dalsgaard (2000) is not incorporated in the model, because the quantitative importance of this reaction is not well known. Reduction of dMn(III)-L is assumed to occur with Fe(II),  $\text{H}_2\text{S}$  and OM to form Mn(II), while oxidation of Mn(III) is assumed to occur with  $\text{O}_2$  to form  $\text{MnO}_2$ . Reduction of dMn(III)-L by  $\text{NO}_2^-$  as described by Karolewski et al. (2021) is not incorporated in the model. Production of  $\text{NO}_2^-$  in the anoxic sediment is unlikely and concentrations in September are below the detection limit. Oxidation of Mn(II) with  $\text{O}_2$  and precipitation as  $\text{MnCO}_3$  removes Mn(II). Dissolved inorganic carbon in the model is the sum of carbon in  $\text{HCO}_3^{2-}$  and  $\text{CO}_2$ , which are produced or consumed in reactions. The dominant effect of adsorption of dissolved Mn(II) to solid phase Mn is related to transport through bioturbation (Slomp et al., 1997). At sites with little or no bioturbation, as is the case here, the effect of Mn(II) adsorption on modeled pore water profiles will be limited.

Depending on whether a compound is a solid or solute, its generic mass conservation is described by Eq. S1 or Eq. S2, respectively.

$$(1 - \varphi) \frac{\partial C_s}{\partial t} = -(1 - \varphi)v \frac{\partial C_s}{\partial z} + \sum R_s \quad (\text{S1})$$

$$\varphi \frac{\partial C_{aq}}{\partial t} = \varphi D' \frac{\partial^2 C_{aq}}{\partial z^2} - \varphi u \frac{\partial C_{aq}}{\partial z} + \sum R_{aq} \quad (\text{S2})$$

In these equations,  $\varphi$  is the sediment porosity,  $t$  is time (yr),  $C_s$  and  $C_{aq}$  are the concentrations of the solid and dissolved species ( $\text{mol L}^{-1}$ ), respectively,  $D'$  is the diffusion coefficient of dissolved species in the porous medium ( $\text{cm}^2 \text{yr}^{-1}$ ),  $z$  is the distance from the Sediment-Water Interface (SWI; cm),  $v$  and  $u$  ( $\text{cm yr}^{-1}$ ) are advective velocities of solids and dissolved species, respectively and  $\sum R_s$  and  $\sum R_{aq}$  are net rates of chemical reactions of solid and dissolved species, respectively.

For porosity, a depth-dependent function is used to account for sediment compaction (Meysman et al., 2005; Reed 2011a; eq S3):

$$\varphi(z) = \varphi_{\infty} + (\varphi_0 - \varphi_{\infty})e^{-\frac{z}{\lambda}} \quad (S3)$$

In this equation,  $\varphi_0$  is the porosity at the SWI,  $\varphi_{\infty}$  is the porosity at depth and  $\lambda$  is the porosity attenuation factor/e-folding distance (Table S5).

In the last 20 years of the model run, the seasonal cycle of oxic – euxinic conditions was simulated by varying the bottom water  $O_2$  and  $H_2S$  concentration, the influx of Fe oxides, Mn oxides, Mn carbonates and OM and the sedimentation rate (Fig. S3). The boundary conditions for the bottom water concentration of  $O_2$  were based on monitoring by Rijkswaterstaat (Directorate-General for Public Works and Water Management of the Netherlands) as reported in Żygadłowska et al. (2023a). The bottom water  $H_2S$  was varied together with  $O_2$  and was either 0, or the concentration measured in the bottom water in September ( $111.8 \text{ mmol L}^{-1}$ ). Input of metal oxides was varied together with  $O_2$  and was fitted to the sediment profiles. The input of Mn carbonates was also varied to fit the sediment profiles, because authigenic Mn carbonate formation alone was insufficient to induce the observed oscillations. OM input was varied to fit the sediment profiles. The input of OM and the sedimentation rate in April differ from those in the other oxic months, because the effect of a spring bloom was simulated. Such variations in OM input are in line with variations in primary productivity and OM supply from the North Sea known for this system (Hagens et al., 2015). Sedimentation rates for the model run until 2016 (4 years before the end of the model run) were based on Egger et al. (2016;  $13.3 \text{ cm yr}^{-1}$ ). Between 60 – 80 cm depth, which is around where the shift in sedimentation rates is assumed, a shift in the oscillations is visible in for example the  $C_{\text{org}}$  and Mn oxides sediment profiles (Fig. 4). This shift is modeled by varying the input of these compounds through the seasons. For the last 4 years the sedimentation rate was set to  $20 \text{ cm yr}^{-1}$ , based on the onset of the shallowest peak in  $C_{\text{org}}$  at 20 cm depth (Fig. 4), which marks the  $C_{\text{org}}$  deposition of the previous year (i.e. spring 2019).

## Figures

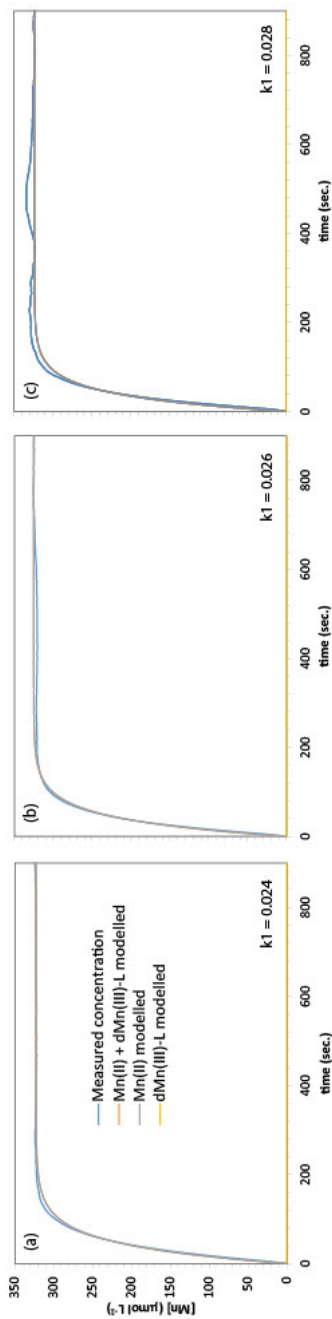


**Figure S1** Kinetic curves (triplicates) that were used to determine the  $k_1$  value for the kinetic reaction of Mn(II) at this site. In the lower right corner of the graph, the  $k_1$  values are indicated.

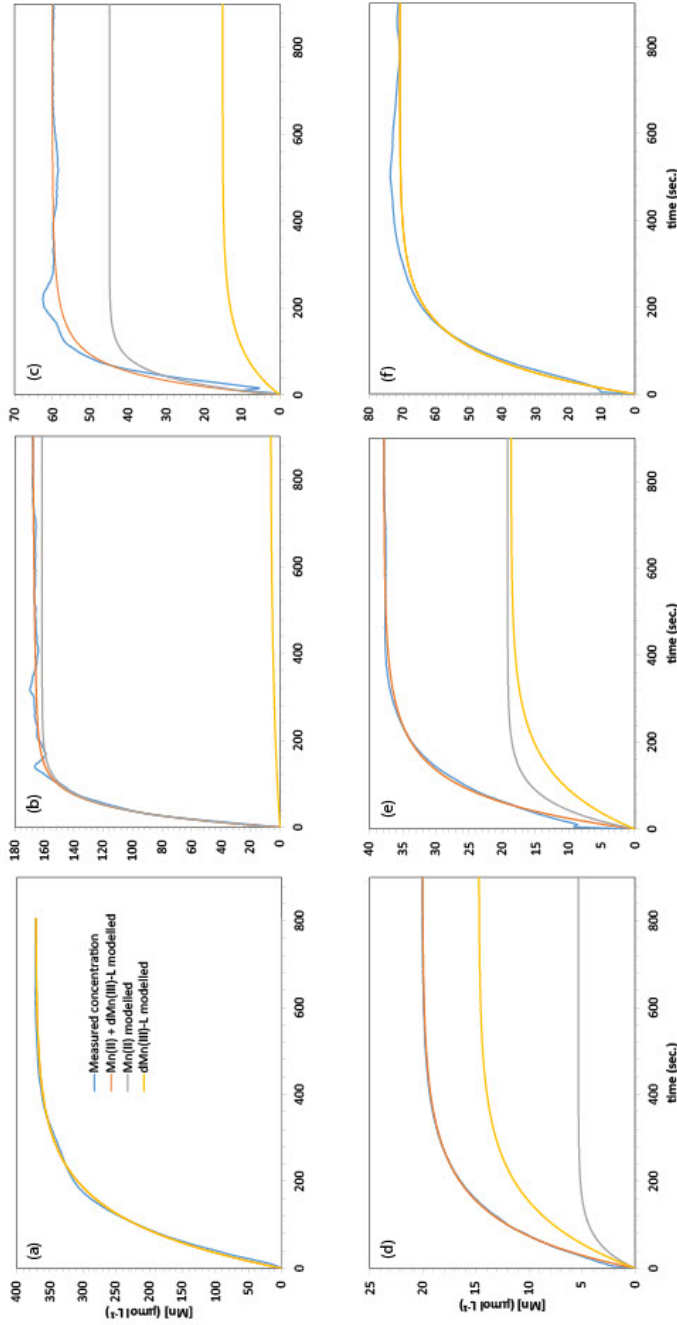


**Figure S2** Kinetic curves that were measured and modeled Mn(II) and dMn(III)-L concentrations used to determine the Mn(II) and dMn(III)-L content of the samples from (a) 0 – 1 cm; (b) 6 – 7 cm; (c) 43 – 44 cm in March 2020 and (d) 1 – 2 cm; (e) 7 – 8 cm; (f) 23 – 24 cm in September 2020.

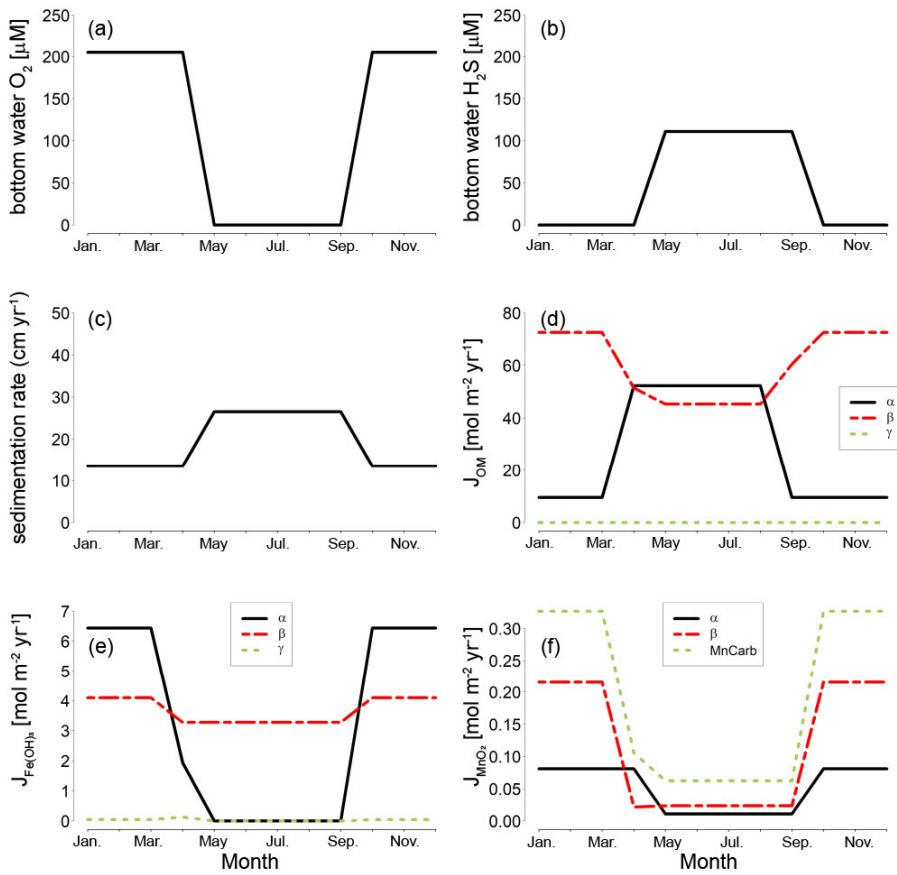


**Figure S3** Seasonal variation in bottom water  $O_2$  and  $H_2S$ , sedimentation rate, and in the flux of Fe oxides ( $J_{Fe(Ox)_2}$ ), flux of Mn oxides ( $J_{MnO_2}$ ) and flux of organic matter ( $J_{OM}$ ) at the sediment-water interface in the final year of the model simulations.

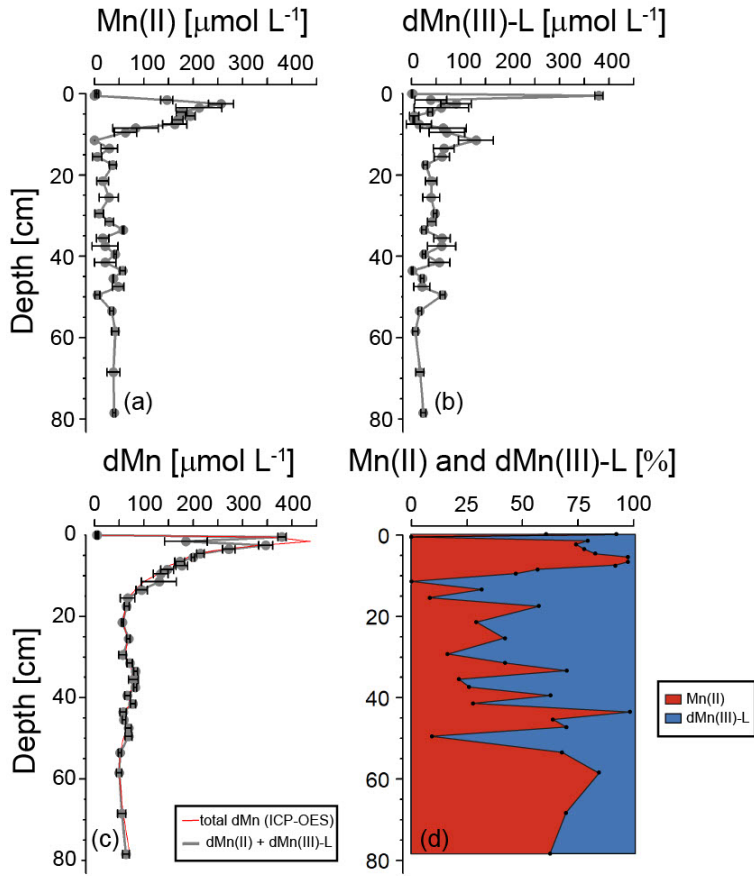


**Figure S4** (a), (b) Data collected through spectrophotometric analysis of Mn(II) and dMn(III)-L in March, including error bars showing standard deviation ( $n=3$ ). (c) The sum of Mn(II) and dMn(III)-L measured spectrophotometrically, including error bars showing standard deviation ( $n=3$ ), compared with the total dissolved Mn measured with ICP-OES. (d) The contribution of Mn(II) and dMn(III)-L to the total dissolved Mn pool (determined as the sum of Mn(II) and dMn(III)-L) as percentage.

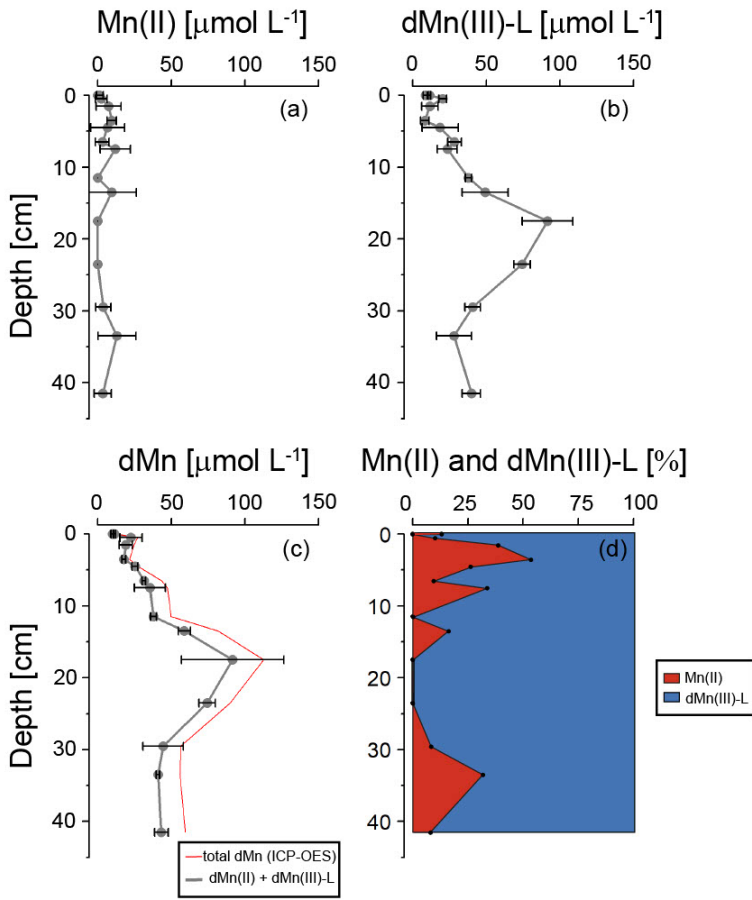


**Figure S5** (a), (b) Data collected during the spectrophotometric analysis of Mn(II) and dMn(III)-L in September, including error bars showing standard deviation ( $n = 3$ ). (c) The sum of Mn(II) and dMn(III)-L measured during the spectrophotometric method including error bars ( $n = 3$ ), compared with the total dissolved Mn measured with ICP-OES. (d) The contribution of Mn(II) and dMn(III)-L to the total dissolved Mn pool (determined as the sum of Mn(II) and dMn(III)-L) as a percentage.

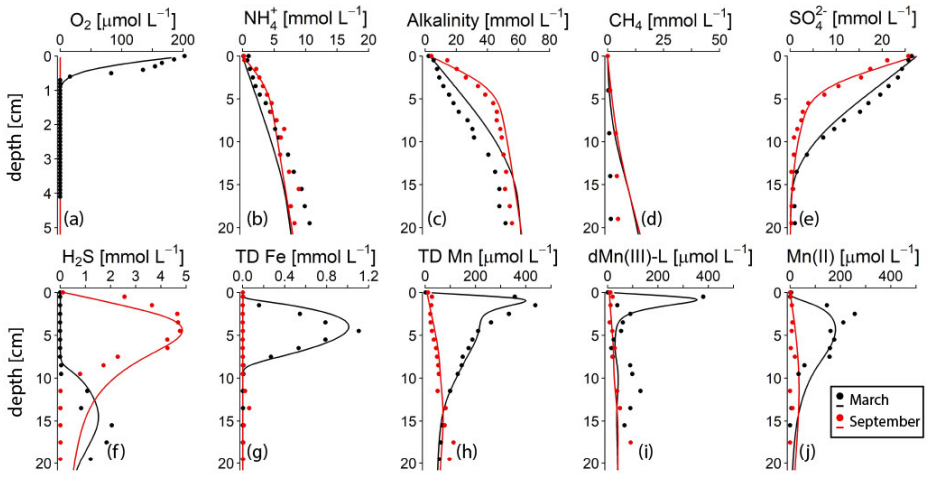


**Figure S6** Top 20 cm of the pore water profiles of key components in March (black) and September (red) 2020. The dots represent measured concentrations, the lines indicate the results of the reactive transport model. Note the different depth scale on the y-axis for  $O_2$ . TD Fe and TD Mn refer to total dissolved Fe and total dissolved Mn. Profiles of Mn(II) and dMn(III)-L with standard deviation error bars ( $n = 3$ ) and the contribution to TD Mn (in %) can be found in Fig. S2, S3. No  $O_2$  was detected in the sediment in September 2020 (Żygadłowska et al. 2023).

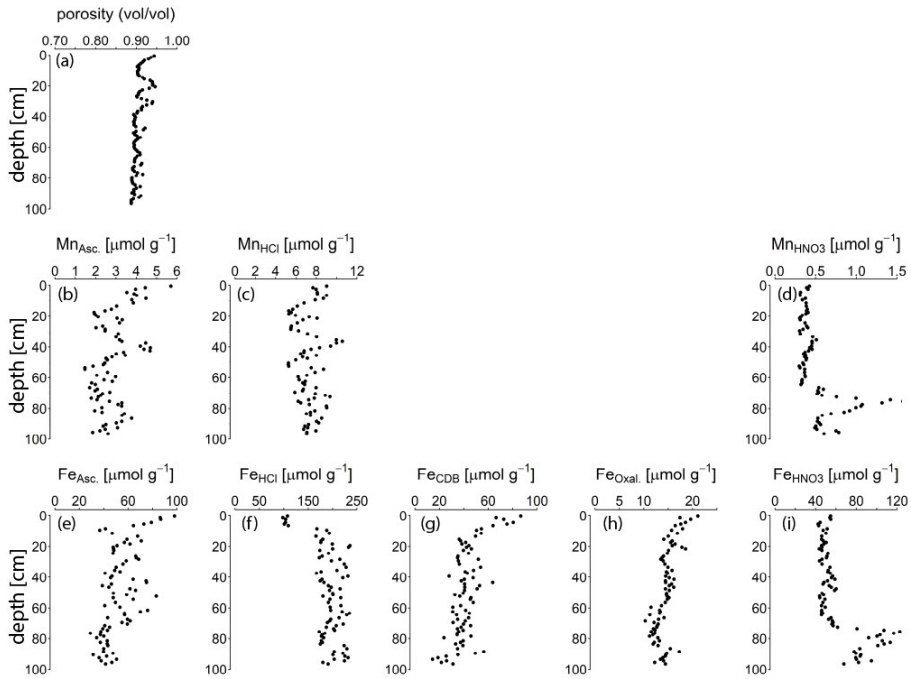


**Figure S7** Porosity and all Mn and Fe fractions as determined in the sequential extraction, for the sediment collected in March 2020.

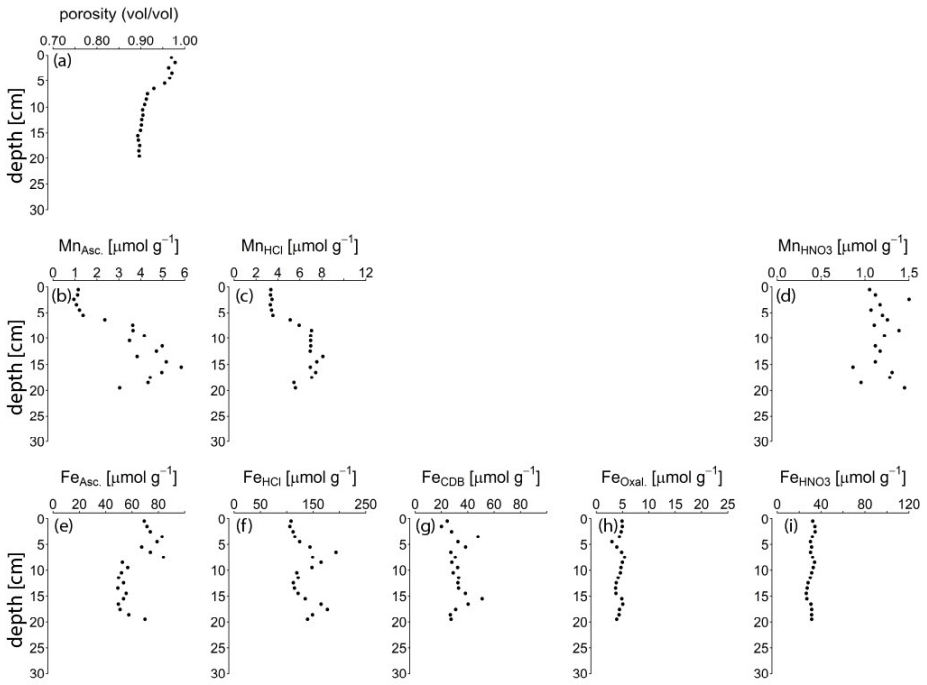


**Figure S8** Porosity and all fractions extracted for Mn and Fe in the sequential extraction, for the sediment collected in September 2020 (0-20 cm).

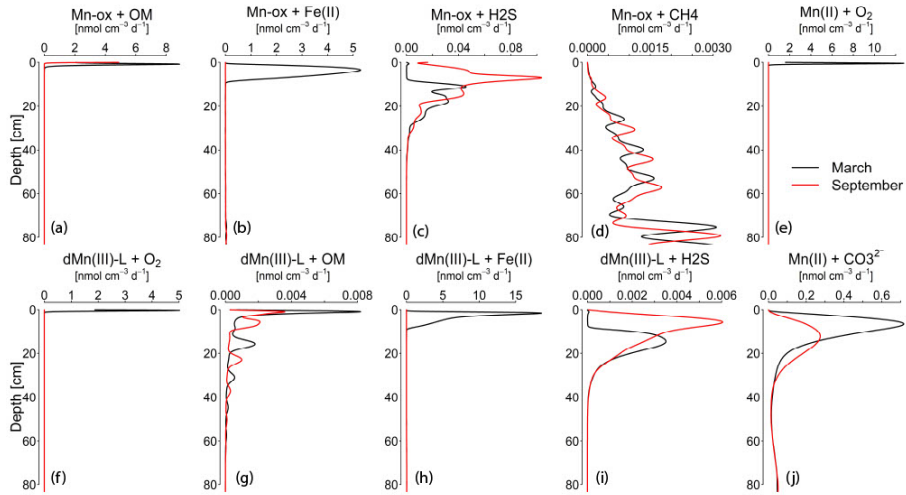


**Figure S9** Depth profiles of the reaction rates, which form the basis for the rate integrations shown in Fig. 4.

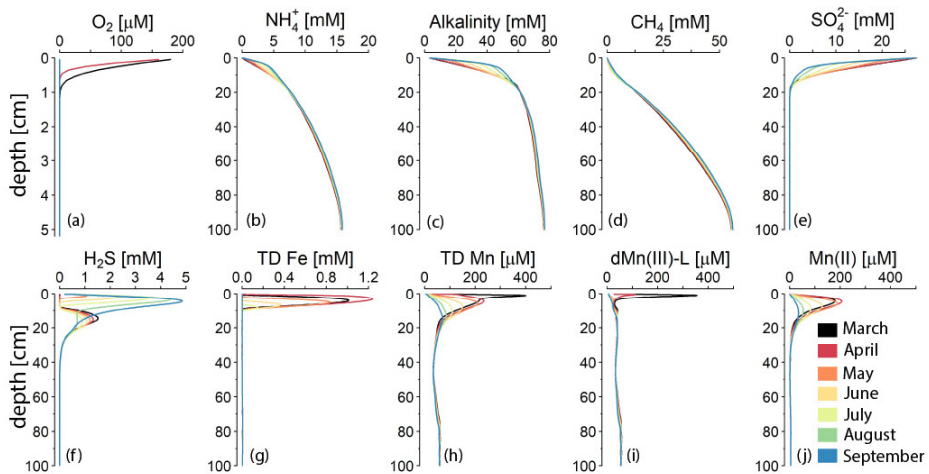


**Figure S10** The change in pore water profiles between March and September when anoxic conditions develop in the basin. With the reactive transport model, pore water profiles can be extrapolated to months where no fieldwork was done in 2020.

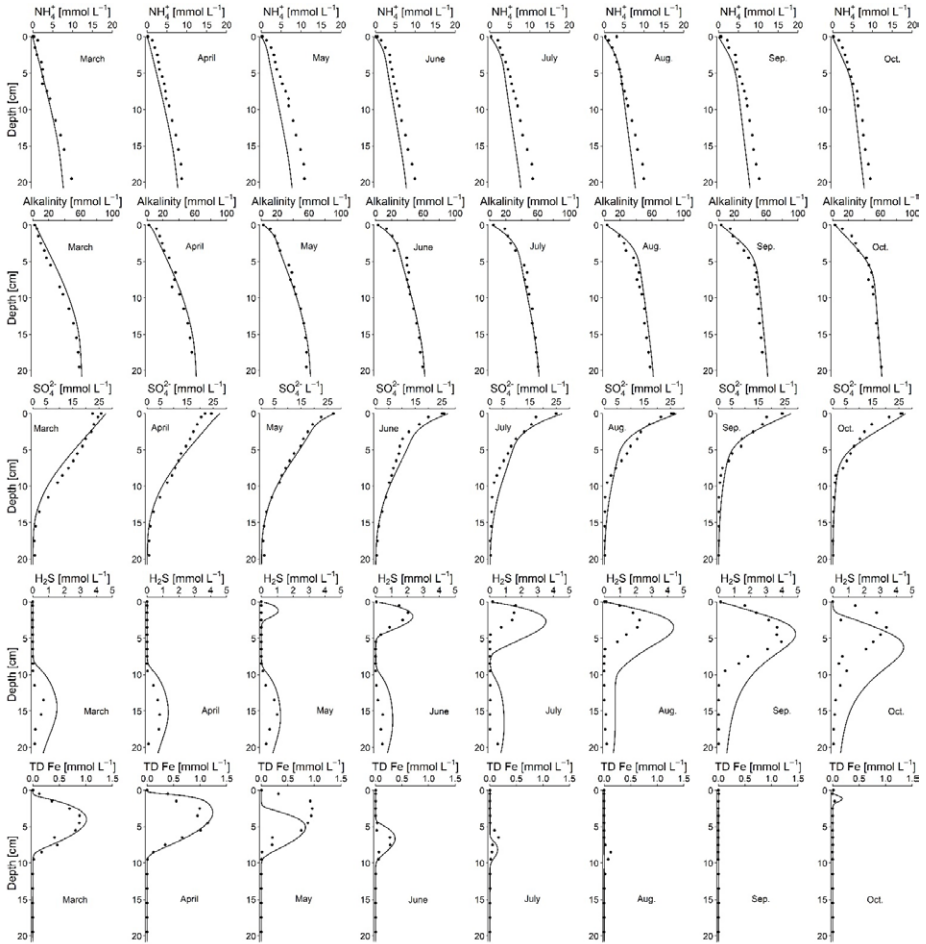


**Figure S11** Forward simulation of the reactive transport model to  $\text{NH}_4^+$ , alkalinity,  $\text{SO}_4^{2-}$ ,  $\text{H}_2\text{S}$ , TD Fe, TD Mn and, for 4 months, Mn oxides and Mn carbonates obtained during 8 sampling campaigns performed between March and October 2021. In 2021, Scharendijke experienced euxinia from June until September (Żygadowska et al., 2024a). Part of this dataset was previously published in Żygadowska et al. (2024a, b). The figure continues on the next page.

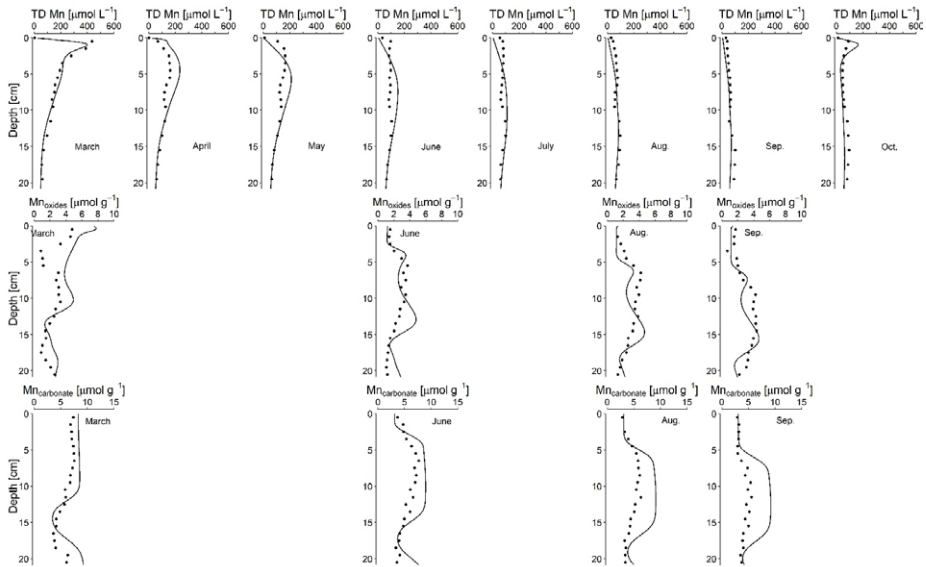
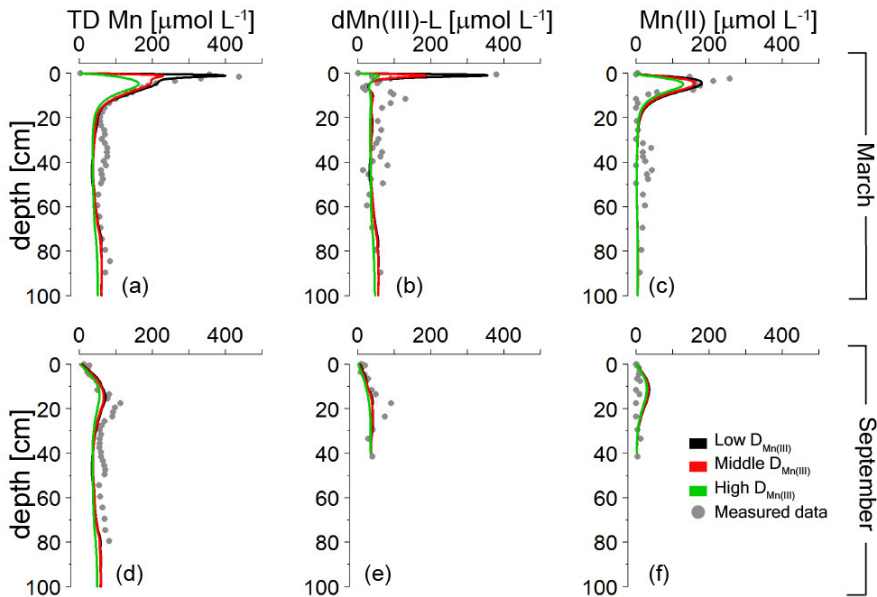
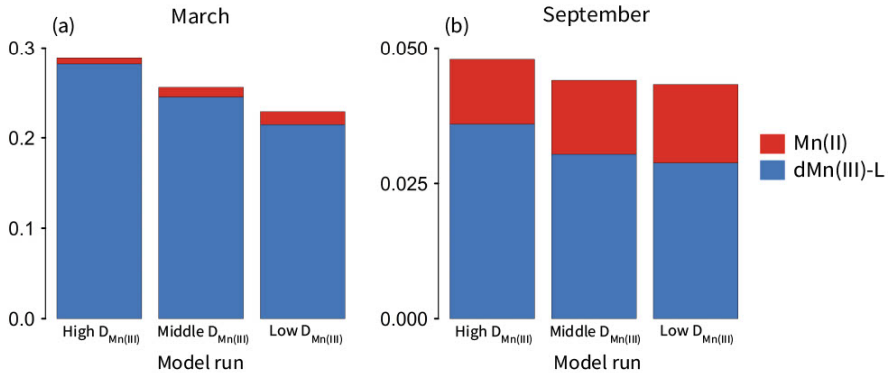


Figure S11 Continued



**Figure S12** Model runs with different diffusion coefficients for dissolved Mn(III). The diffusion coefficients used and the range of diffusion coefficients for dissolved organic matter given in literature can be found in Table S6. When the diffusion coefficient decreases, the peak of dissolved Mn(III)-L and total dissolved Mn near the sediment-water interface in March is no longer well described by the model. The diffusion coefficient does not have a large effect on the pore water profiles of Mn(II) and dMn(III)-L in September.



**Figure S13** Variation in the benthic flux of dissolved Mn over the model runs with changing diffusion coefficient for dMn(III)-L ( $D_{Mn(III)}$ ) in March (A) and September (B). Note the different y-axes for the different months. The figure shows that a lower diffusion coefficient for dMn(III)-L results in a lower benthic flux of total Mn and dMn(III)-L, but a slightly higher benthic flux of Mn(II). The values for the high, middle and low  $D_{Mn(III)}$  can be found in Table S6.

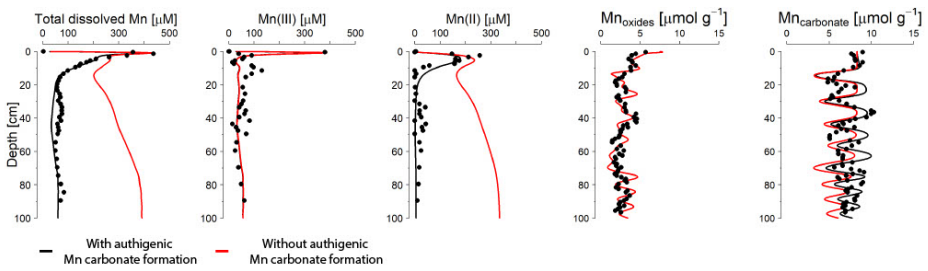


**Figure S14** Model output when authigenic Mn carbonate precipitation is turned off in red versus the model base run in black. The difference in Mn carbonate concentrations between the model without Mn carbonate precipitation and the base run indicate the amount of Mn carbonate that, according to the model, has formed within the sediment.

## Tables

**Table S1** Chemical species included in the model

Species	Notation
<b>Solids</b>	
Organic Matter <sup>a</sup>	OM <sup>α/β/γ</sup>
Iron oxides <sup>a</sup>	Fe(OH) <sub>3</sub> <sup>α/β/γ</sup>
Iron monosulfide	FeS
Pyrite	FeS <sub>2</sub>
Elemental Sulfur	S <sup>0</sup>
Siderite	FeCO <sub>3</sub>
Vivianite	Fe <sub>3</sub> (PO <sub>4</sub> ) <sub>2</sub>
Manganese oxide <sup>b</sup>	MnO <sub>2</sub> <sup>α/β</sup>
Manganese carbonate	MnCO <sub>3</sub>
<b>Solutes</b>	
Chloride	Cl <sup>-</sup>
Oxygen	O <sub>2</sub>
Nitrate	NO <sub>3</sub> <sup>-</sup>
Sulfate	SO <sub>4</sub> <sup>2-</sup>
Methane	CH <sub>4</sub>
Dissolved iron	Fe <sup>2+</sup>
Ammonium <sup>c</sup>	ΣNH <sub>4</sub> <sup>+</sup>
Hydrogen sulfide <sup>c</sup>	ΣH <sub>2</sub> S
Phosphate <sup>c</sup>	ΣH <sub>3</sub> PO <sub>4</sub>
Dissolved Inorganic Carbon	DIC
Dissolved manganese (II)	Mn <sup>2+</sup>
Dissolved manganese(III)-L	Mn <sup>3+-L</sup>

<sup>a</sup> Consists of three types of species: reactive (α), less reactive (β) and non-reactive (γ)

<sup>b</sup> Consists of two types of species: reactive (α) and less reactive (β)

<sup>c</sup> Σ denotes that all species of an acid are included.

**Table S2** Reaction pathways and stoichiometries implemented in the model

<b>Primary redox reactions</b>	
$OM^{\alpha,\beta} + a O_2 \rightarrow a CO_2 + b \Sigma NH_4^+ + c \Sigma H_3PO_4 + a H_2O$	R1
$OM^{\alpha,\beta} + 0.8 a NO_3 + 0.8 a H^+ \rightarrow a CO_2 + b \Sigma NH_4^+ + c \Sigma H_3PO_4 + 0.4 a N_2 + 1.4 a H_2O$	R2
$OM^{\alpha,\beta} + 4a MnO_2^a + 2 a H^+ \rightarrow 4a Mn^{3+} - L + a CO_2 + b \Sigma NH_4^+ + c \Sigma H_3PO_4 + 2 a H_2O$	R3
$OM^{\alpha,\beta} + 4a Fe(OH)_3^a + 4a \chi Fe_{ox}P + 12 a H^+ \rightarrow 4a Fe^{2+} + a CO_2 + b \Sigma NH_4^+ + (c + 4a \chi) \Sigma H_3PO_4 + 13a H_2O$	R4
$OM^{\alpha,\beta} + 0.5a SO_4^{2-} + a H^+ \rightarrow a CO_2 + b \Sigma NH_4^+ + c \Sigma H_3PO_4 + 0.5a \Sigma H_2S + a H_2O$	R5
$OM^{\alpha,\beta} \rightarrow 0.5a CO_2 + b \Sigma NH_4^+ + c \Sigma H_3PO_4 + 0.5a CH_4$	R6
<b>Secondary and other reactions</b>	
$O_2 + Fe^{2+} + 8 H_2O + 4 \chi \Sigma H_3PO_4 \rightarrow 4 Fe(OH)_3^a + 4 \chi Fe_{ox}P + 8 CO_2$	R7
$2 O_2 + FeS \rightarrow SO_4^{2-} + 2 Fe^{2+} + 4 H^+$	R8
$7 O_2 + 2 FeS_2 + 2 H_2O + 4 SO_4^{2-} \rightarrow 2 Fe^{2+} + 4 H^+$	R9
$2 O_2 + \Sigma H_2S + 2 HCO_3^- \rightarrow SO_4^{2-} + 2 CO_2 + 2 H_2O$	R10
$2 O_2 + CH_4 \rightarrow CO_2 + 2 H_2O$	R11
$2 Fe(OH)_3^a + 2 \chi Fe_{ox}P + H_2S + 4 CO_2 \rightarrow 2 Fe^{2+} + 2 \chi \Sigma H_3PO_4 + S^0 + 4 HCO_3^- + 2 H_2O$	R12
$Fe^{2+} + \Sigma H_2S \rightarrow FeS + 2 H^+$	R13
$FeS + \Sigma H_2S \rightarrow FeS_2 + H_2$	R14
$SO_4^{2-} + CH_4 + CO_2 \rightarrow 2 HCO_3^- + \Sigma H_2S$	R15
$CH_4 + 8 Fe(OH)_3^{a,\beta} + 8 \chi Fe_{ox}P + 15 H^+ \rightarrow HCO_3^- + 8 Fe^{2+} + 8 \chi \Sigma H_3PO_4 + 21 H_2O$	R16
$4 S^0 + 4 H_2O \rightarrow 3 \Sigma H_2S + SO_4^{2-} + 2 H^+$	R17
$FeS + S^0 \rightarrow FeS_2$	R18
$Fe(OH)_3^a + \chi Fe_{ox}P \rightarrow Fe(OH)_3^\beta + \chi \Sigma H_3PO_4$	R19
$2 Fe(OH)_3^\beta + 2 \chi Fe_{ox}P + \Sigma H_2S + 4 CO_2 \rightarrow 2 Fe^{2+} + 2 \chi \Sigma H_3PO_4 + S^0 + 4 HCO_3^- + 2 H_2O$	R20
$2 O_2 + \Sigma NH_4^+ + 2 HCO_3^- \rightarrow NO_3^- + 2 CO_2 + 3 H_2O$	R21
$3 Fe^{2+} + 2 \Sigma H_3PO_4 \rightarrow Fe_3(PO_4)_2 + 4 H^+$	R22
$Fe^{2+} + CO_3^{2-} \rightarrow FeCO_3$	R23
$FeCO_3 + \Sigma H_2S \rightarrow FeS + CO_2 + H_2O$	R24

**Table S2** Continued

Primary redox reactions	
$\text{Fe}_3(\text{PO}_4)_2 + 3 \Sigma \text{H}_2\text{S} \rightarrow 2 \text{FeS} + 2 \Sigma \text{H}_3\text{PO}_4 + 4 \text{H}^+$	R25
$\text{Mn}^{2+} + \text{HCO}_3^- + \text{OH}^- \rightarrow \text{MnCO}_3 + \text{H}_2\text{O}$	R26
$4 \text{Mn}^{2+} + \text{O}_2 + 4 \text{H}^+ + \text{L} \rightarrow 4 \text{Mn}^{3+} - \text{L} + 2 \text{H}_2\text{O}$	R27
$\text{MnO}_2^{a,\beta} + \text{Fe}^{2+} + \text{H}_2\text{O} + \text{H}^+ + \text{L} \rightarrow \text{Fe}(\text{OH})_3^a + \text{Mn}^{3+} - \text{L}$	R28
$\text{MnO}_2^a + \Sigma \text{H}_2\text{S} + 2 \text{H}^+ + \text{L} \rightarrow \text{S}^0 + \text{Mn}^{3+} - \text{L} + 2 \text{H}_2\text{O}$	R29
$\text{MnO}_2^a \rightarrow \text{MnO}_2^\beta$	R30
$\text{MnO}_2^\beta + \Sigma \text{H}_2\text{S} + 2 \text{H}^+ + \text{L} \rightarrow \text{S}^0 + \text{Mn}^{3+} - \text{L} + 2 \text{H}_2\text{O}$	R31
$4 \text{MnO}_2^{a,\beta} + \text{CH}_4 + 7 \text{H}^+ \rightarrow 4 \text{Mn}^{2+} + \text{HCO}_3^- + 5 \text{H}_2\text{O}$	R32
$4 \text{Mn}^{3+} - \text{L} + 2 \text{O}_2 + 4 \text{H}^+ \rightarrow 4 \text{MnO}_2^a + 2 \text{H}_2\text{O} + \text{L}$	R33
$\text{Mn}^{3+} - \text{L} + \Sigma \text{H}_2\text{S} \rightarrow \text{S}^0 + \text{Mn}^{2+} + \text{L}$	R34
$\text{Mn}^{3+} - \text{L} + \text{Fe}^{2+} + 3 \text{H}_2\text{O} \rightarrow \text{Mn}^{2+} + \text{Fe}(\text{OH})_3^a + 3 \text{H}^+ + \text{L}$	R35
$4 \text{Mn}^{3+} - \text{L} + \text{OM}^a + \text{H}_2\text{O} \rightarrow 4 \text{Mn}^{2+} + \text{CO}_2 + 3 \text{H}^+ + \text{L}$	R36

Organic matter is of the form  $((\text{CH}_2\text{O})_a (\text{NH}_4^+)_b (\text{H}_3\text{PO}_4)_c)$ , where  $a=1$ ,  $b=1/15.45$  and  $c=106/1$ .  $\alpha$ ,  $\beta$ , &  $\gamma$  describe different fractions (i.e. highly reactive, less reactive and refractory).  $\chi$  describes the P:Fe ratios of  $\text{Fe}(\text{OH})_3$  and has a value of 0.3 in the model.

**Table S3** Reaction equations implemented in the model

<b>Primary redox reaction equations</b>	
R1 = $k_{\alpha,\beta} \text{OM}^{\alpha,\beta} \left( \frac{[\text{O}_2]}{K_{m,\text{O}_2} + [\text{O}_2]} \right)$	E1
R2 = $k_{\alpha,\beta} \text{OM}^{\alpha,\beta} \left( \frac{[\text{NO}_3^-]}{K_{m,\text{NO}_3^-} + [\text{NO}_3^-]} \right) \left( \frac{K_{m,\text{O}_2}}{K_{m,\text{O}_2} + [\text{O}_2]} \right)$	E2
R3 = $k_{\alpha,\beta} \text{OM}^{\alpha,\beta} \left( \frac{[\text{MnO}_2]}{K_{m,\text{MnO}_2} + [\text{MnO}_2]} \right) \left( \frac{K_{m,\text{NO}_3^-}}{K_{m,\text{NO}_3^-} + [\text{NO}_3^-]} \right) \left( \frac{K_{m,\text{O}_2}}{K_{m,\text{O}_2} + [\text{O}_2]} \right)$	E3
R4 = $k_{\alpha,\beta} \text{OM}^{\alpha,\beta} \left( \frac{[\text{Fe}(\text{OH})_3]}{K_{m,\text{Fe}(\text{OH})_3} + [\text{Fe}(\text{OH})_3]} \right) \left( \frac{K_{m,\text{MnO}_2}}{K_{m,\text{MnO}_2} + [\text{MnO}_2]} \right) \left( \frac{K_{m,\text{NO}_3^-}}{K_{m,\text{NO}_3^-} + [\text{NO}_3^-]} \right) \left( \frac{K_{m,\text{O}_2}}{K_{m,\text{O}_2} + [\text{O}_2]} \right)$	E4
R5 = $k_{\alpha,\beta} \text{OM}^{\alpha,\beta} \left( \frac{[\text{SO}_4^{2-}]}{K_{m,\text{SO}_4^{2-}} + [\text{SO}_4^{2-}]} \right) \left( \frac{K_{m,\text{Fe}(\text{OH})_3}}{K_{m,\text{Fe}(\text{OH})_3} + [\text{Fe}(\text{OH})_3]} \right) \left( \frac{K_{m,\text{MnO}_2}}{K_{m,\text{MnO}_2} + [\text{MnO}_2]} \right) * \left( \frac{K_{m,\text{NO}_3^-}}{K_{m,\text{NO}_3^-} + [\text{NO}_3^-]} \right) \left( \frac{K_{m,\text{O}_2}}{K_{m,\text{O}_2} + [\text{O}_2]} \right)$	E5
R6 = $k_{\alpha,\beta} \text{OM}^{\alpha,\beta} \left( \frac{K_{m,\text{SO}_4^{2-}}}{K_{m,\text{SO}_4^{2-}} + [\text{SO}_4^{2-}]} \right) \left( \frac{K_{m,\text{Fe}(\text{OH})_3}}{K_{m,\text{Fe}(\text{OH})_3} + [\text{Fe}(\text{OH})_3]} \right) \left( \frac{K_{m,\text{MnO}_2}}{K_{m,\text{MnO}_2} + [\text{MnO}_2]} \right) * \left( \frac{K_{m,\text{NO}_3^-}}{K_{m,\text{NO}_3^-} + [\text{NO}_3^-]} \right) \left( \frac{K_{m,\text{O}_2}}{K_{m,\text{O}_2} + [\text{O}_2]} \right)$	E6
<b>Secondary redox and other reaction equations</b>	
R7 = $k_1 [\text{O}_2] [\text{Fe}^{2+}]$	E7
R8 = $k_2 [\text{O}_2] [\text{FeS}]$	E8
R9 = $k_3 [\text{O}_2] [\text{FeS}_2]$	E9
R10 = $k_4 [\text{O}_2] [\sum \text{H}_2\text{S}]$	E10
R11 = $k_5 [\text{O}_2] [\text{CH}_4]$	E11
R12 = $k_6 [\text{Fe}(\text{OH})_3^{\alpha}] [\sum \text{H}_2\text{S}]$	E12
R13 = $k_7 [\text{Fe}^{2+}] [\sum \text{H}_2\text{S}]$	E13
R14 = $k_8 [\text{FeS}] [\sum \text{H}_2\text{S}]$	E14
R15 = $k_9 [\text{SO}_4^{2-}] [\text{CH}_4]$	E15
R16 = $k_{10} [\text{Fe}(\text{OH})_3^{\alpha,\beta}] [\text{CH}_4]$	E16
R17 = $k_{11} [\text{S}^0]$	E17

**Table S3** Continued

<b>Secondary redox and other reaction equations</b>	
R18 = $k_{12} [\text{FeS}] [\text{S}^0]$	E18
R19 = $k_{13} [\text{Fe}(\text{OH})_3^\alpha]$	E19
R20 = $k_{14} [\text{Fe}(\text{OH})_3^\beta] [\Sigma \text{H}_2\text{S}]$	E20
R21 = $k_{15} [\text{O}_2] [\text{NH}_4^+]$	E21
R22 = $k_{16} [\text{Fe}^{2+}] [\text{HPO}_4^{2-}]$	E22
R23 = $k_{17} [\text{Fe}^{2+}] [\text{HCO}_3^-]$	E23
R24 = $k_{18} [\text{FeCO}_3] [\Sigma \text{H}_2\text{S}]$	E24
R25 = $k_{19} [\text{Fe}_3(\text{PO}_4)_2] [\Sigma \text{H}_2\text{S}]$	E25
R26 = $k_{20} [\text{Mn}^{2+}] [\text{HCO}_3^-]$	E26
R27 = $k_{21} [\text{Mn}^{2+}] [\text{O}_2]$	E27
R28 = $k_{22} [\text{MnO}_2^{\alpha,\beta}] [\text{Fe}^{2+}]$	E28
R29 = $k_{23} [\text{MnO}_2^\alpha] [\Sigma \text{H}_2\text{S}]$	E29
R30 = $k_{24} [\text{MnO}_2^\alpha]$	E30
R31 = $k_{25} [\text{MnO}_2^\beta] [\Sigma \text{H}_2\text{S}]$	E31
R32 = $k_{26} [\text{MnO}_2^{\alpha,\beta}] [\text{CH}_4]$	E32
R33 = $k_{27} [\text{Mn}^{3+} - \text{L}] [\text{O}_2]$	E33
R34 = $k_{28} [\text{Mn}^{3+} - \text{L}] [\Sigma \text{H}_2\text{S}]$	E34
R35 = $k_{29} [\text{Mn}^{3+} - \text{L}] [\text{Fe}^{2+}]$	E35
R36 = $k_{30} [\text{Mn}^{3+} - \text{L}] [\text{OM}^\alpha]$	E36
R37 = $k_{31} [\text{OM}^\alpha]$	E37
R38 = $k_{32} [\text{NO}_3^-] [\text{CH}_4]$	E38
R39 = $k_{33} [\text{CO}_2] [\text{H}_2] \left( \frac{K_{m,\text{SO}_4^{2-}}}{K_{m,\text{SO}_4^{2-}} + [\text{SO}_4^{2-}]} \right) \left( \frac{K_{m,\text{Fe}(\text{OH})_3}}{K_{m,\text{Fe}(\text{OH})_3} + [\text{Fe}(\text{OH})_3]} \right) \left( \frac{K_{m,\text{MnO}_2}}{K_{m,\text{MnO}_2} + [\text{MnO}_2]} \right) * \left( \frac{K_{m,\text{NO}_3^-}}{K_{m,\text{NO}_3^-} + [\text{NO}_3^-]} \right) \left( \frac{K_{m,\text{O}_2}}{K_{m,\text{O}_2} + [\text{O}_2]} \right)$	E39

**Table S4** Reaction parameters used in the model

Parameter	Value	Unit	Source	Values in literature
$k_a^*$	1.62	yr <sup>-1</sup>	a, b	0.05 – 1.62
$k_\beta^*$	0.0086	yr <sup>-1</sup>	b, d	0.0025 - 0.0086
$K_{O_2}$	20	μmol L <sup>-1</sup>	c	1 – 30
$K_{NO_3}$	20	μmol L <sup>-1</sup>	c	4 – 80
$K_{MnO_2}$	32	μmol L <sup>-1</sup>	c	4 – 32
$K_{Fe(OH)_3}$	65	μmol L <sup>-1</sup>	c	65 – 100
$K_{SO_4^{2-}}$	1.6	μmol L <sup>-1</sup>	c	1.6
$k_1$ (E7)	1.4*10 <sup>5</sup>	mmol yr <sup>-1</sup>	c	1.4*10 <sup>5</sup>
$k_2$ (E8)	300	mmol yr <sup>-1</sup>	c	300
$k_3$ (E9)	1	mmol yr <sup>-1</sup>	c	1
$k_4$ (E10)	160	mmol yr <sup>-1</sup>	c	160
$k_5$ (E11)	100	mmol yr <sup>-1</sup>	c	107
$k_6$ (E12)	80	mmol yr <sup>-1</sup>	c, g, i	8 - 100
$k_7$ (E13)	11840	mmol yr <sup>-1</sup>	b, d	100 - 14800
$k_8$ (E14)	0.0003	mmol yr <sup>-1</sup>	e, i	0.0003 – 0.0074
$k_9$ (E15)	1.344	mmol yr <sup>-1</sup>	c, g	10 (c) – 120 (g)
$k_{10}$ (E16)	3.04*10 <sup>-6</sup>	mmol yr <sup>-1</sup>	g, i	1.6*10 <sup>-7</sup> – 0.0074
$k_{11}$ (E17)	3	yr <sup>-1</sup>	f	3
$k_{12}$ (E18)	0.1	mmol yr <sup>-1</sup>	f, g	0.001 - 7
$k_{13}$ (E19)	0.1	yr <sup>-1</sup>		model constrained
$k_{14}$ (E20)	0.444	mmol yr <sup>-1</sup>	c, j	0.004 – 100
$k_{15}$ (E21)	19500	mmol yr <sup>-1</sup>	c, d	5000 – 39000
$k_{16}$ (E22)	0.052	mmol yr <sup>-1</sup>		model constrained
$k_{17}$ (E23)	0.000351	mmol yr <sup>-1</sup>	i	0.0027
$k_{18}$ (E24)	0.0008	mmol yr <sup>-1</sup>		model constrained
$k_{19}$ (E25)	8*10 <sup>-4</sup>	mmol yr <sup>-1</sup>	i	8*10 <sup>-4</sup>
$k_{20}$ (E26)	0.05565	mmol yr <sup>-1</sup>	k	0.265
$k_{21}$ (E27)	15000	mmol yr <sup>-1</sup>	c	800 - 20000
$k_{22}$ (E28)	2.652	mmol yr <sup>-1</sup>	f, k	0.002 - 2
$k_{23}$ (E29)	1	mmol yr <sup>-1</sup>	c	< 100000 (20)
$k_{24}$ (E30)	1.8	yr <sup>-1</sup>	f	1.8
$k_{25}$ (E31)	0.02	mmol yr <sup>-1</sup>	c	< 100000 (20)
$k_{26}$ (E32)	0.000019	mmol yr <sup>-1</sup>	k	0.0017
$k_{27}$ (E33)	144	mmol yr <sup>-1</sup>		model constrained
$k_{28}$ (E34)	64	mmol yr <sup>-1</sup>		model constrained
$k_{29}$ (E35)	0.025	mmol yr <sup>-1</sup>		model constrained

**Table S4** Continued

Parameter	Value	Unit	Source	Values in literature
$k_{30}$ (E36)	$2.5 \cdot 10^{-4}$	mmol yr <sup>-1</sup>		model constrained
$k_{31}$ (E37)	0.15	yr <sup>-1</sup>		model constrained
$k_{32}$ (E38)	0.5	mmol yr <sup>-1</sup>		model constrained
$k_{33}$ (E39)	0.03675	yr <sup>-1</sup>		model constrained

a) Moodley et al. (2005); b) Reed et al. (2011a) c) Van Cappellen & Wang (1996); d) Reed et al. (2016); e) Rickard (1997); f) Berg et al. (2003); g) Rooze et al. (2016); h) Egger et al. (2016a); i) Egger et al. (2016b); j) Lenstra et al. (2018)

\*Following the approach of Reed et al. (2011b), we have assumed different reactivities of the organic matter towards the electron acceptors. The following factors have been used for the a fraction: O<sub>2</sub> = 1, NO<sub>3</sub> = 3, MnO<sub>2</sub> = 2.8, Fe(OH)<sub>3</sub> = 0.3, SO<sub>4</sub><sup>2-</sup> = 1.7, methanogenesis = 0.5; for the b fraction the following factors have been used: O<sub>2</sub> = 1, NO<sub>3</sub><sup>-</sup> = 3, MnO<sub>2</sub> = 1, Fe(OH)<sub>3</sub> = 0.3, SO<sub>4</sub><sup>2-</sup> = 1, methanogenesis = 3.

**Table S5** Environmental parameters used in the model. Values of porosity, temperature, salinity and the sedimentation rate are based on data for the study site.

Parameter	Symbol	Value	Unit
Porosity at surface	$f_0$	0.944	vol/vol
Porosity at depth	$f_\infty$	0.888	vol/vol
Porosity e-folding distance	$g$	60	cm
Sediment density	$r$	2.65	$\text{g cm}^{-3}$
Temperature	$T$	8.4	$^{\circ}\text{C}$
Salinity	$S$	35	-
Pressure	$P$	5.5	bar
Tortuosity	$q^2$	$1 - 2\ln(f)$	-
Molecular diffusion coefficient corrected for tortuosity	$D'$	$D' =$	$\text{cm}^2 \text{yr}^{-1}$
Sediment accumulation rate**	$F_{\text{Sed}}$	**	$\text{g cm}^{-2} \text{yr}^{-1}$
Advective velocity at surface	$n_0$		$\text{cm yr}^{-1}$
Advective velocity at depth	$n_\infty$		$\text{cm yr}^{-1}$
** Sedimentation rate variations over the years			
Year	December – July	July - December	Unit
0 – 60	2.97	2.97	$\text{g cm}^{-2} \text{yr}^{-1}$
60 – 75	0.69	3.93	$\text{g cm}^{-2} \text{yr}^{-1}$
75 – 80	3.93	2.00	$\text{g cm}^{-2} \text{yr}^{-1}$

**Table S6** The various diffusion coefficients used for Mn(III) ( $D_{\text{Mn(III)}}$ ) to evaluate the effect of the choice of the diffusion coefficient for Mn(III) when it forms a complex with an organic ligand.

Name	Scenario	Value	Range in literature	Sources
High $D_{\text{Mn(III)}}$	DMn(III) = DMn(II) As calculated by reactran package	132.6 cm <sup>2</sup> yr <sup>-1</sup>	-	<i>a</i>
Middle $D_{\text{Mn(III)}}$	DMn(III) is within the range of diffusion coefficients for dissolved organic matter	33.1 cm <sup>2</sup> yr <sup>-1</sup>	22.7 – 81 cm <sup>2</sup> yr <sup>-1</sup>	<i>b, c</i>
Low $D_{\text{Mn(III)}}$	DMn(III) is constrained by the model, by fitting Mn(III) to the collected data. This is the DMn(III) that is used in the model throughout the paper.	16.6 cm <sup>2</sup> yr <sup>-1</sup>	-	

Sources: *a*) Soetaert & Meysman (2012); *b*) Burdige et al. (1999); *c*) Burdige et al. (2004)

**Table S7** Boundary conditions of solids and solutes at the sediment-water interface in the model. For the time-dependent fluxes of  $OM^{a,\beta,\gamma}$ ,  $Fe(OH)_3^{a,\beta,\gamma}$ ,  $MnO_2^{a,\beta}$  and  $MnCO_3$  and concentration of  $O_2$  the minimum and maximum fluxes and concentrations are given. For all chemical species, a zero-gradient boundary condition was specified at the bottom of the model domain.

Solids	Flux at sediment-water interface		Unit
	Min	Max	
FeS	0.4 * 10 <sup>-4</sup>		mol m <sup>-2</sup> yr <sup>-1</sup>
FeS <sub>2</sub>	0		mol m <sup>-2</sup> yr <sup>-1</sup>
S <sup>0</sup>	0		mol m <sup>-2</sup> yr <sup>-1</sup>
FeCO <sub>3</sub>	2		mol m <sup>-2</sup> yr <sup>-1</sup>
Fe <sub>3</sub> (PO <sub>4</sub> ) <sub>2</sub>	0		mol m <sup>-2</sup> yr <sup>-1</sup>
Solutes	Bottom water concentrations		Unit
	Min	Max	
OM <sup>a</sup>	9.51	52.31	mol m <sup>-2</sup> yr <sup>-1</sup>
OM <sup>b</sup>	45.36	72.58	mol m <sup>-2</sup> yr <sup>-1</sup>
OM <sup>g</sup>	0.001	0.001	mol m <sup>-2</sup> yr <sup>-1</sup>
Fe(OH) <sub>3</sub> <sup>a</sup>	0.0028	6.44	mol m <sup>-2</sup> yr <sup>-1</sup>
Fe(OH) <sub>3</sub> <sup>b</sup>	3.28	4.68	mol m <sup>-2</sup> yr <sup>-1</sup>
Fe(OH) <sub>3</sub> <sup>g</sup>	0	0	mol m <sup>-2</sup> yr <sup>-1</sup>
MnO <sub>2</sub> <sup>a</sup>	0.0108	0.081	mol m <sup>-2</sup> yr <sup>-1</sup>
MnO <sub>2</sub> <sup>b</sup>	0.0235	0.216	mol m <sup>-2</sup> yr <sup>-1</sup>
MnCO <sub>3</sub>	0.0624	0.163	mol m <sup>-2</sup> yr <sup>-1</sup>
O <sub>2</sub>	0	0.205	mmol L <sup>-1</sup>
ΣH <sub>2</sub> S	0	0.111	mmol L <sup>-1</sup>
Cl <sup>-</sup>	532		mmol L <sup>-1</sup>
NO <sub>3</sub> <sup>-</sup>	0		mmol L <sup>-1</sup>
SO <sub>4</sub> <sup>2-</sup>	27.49		mmol L <sup>-1</sup>
CH <sub>4</sub>	0		mmol L <sup>-1</sup>
Fe <sup>2+</sup>	0		mmol L <sup>-1</sup>
ΣNH <sub>4</sub> <sup>+</sup>	0		mmol L <sup>-1</sup>
ΣH <sub>3</sub> PO <sub>4</sub>	0		mmol L <sup>-1</sup>
DIC	3		mmol L <sup>-1</sup>
Mn <sup>2+</sup>	0		mmol L <sup>-1</sup>
Mn <sup>3+</sup>	0		mmol L <sup>-1</sup>



## Chapter 4

# Eutrophication threatens the ANME methane filter in coastal sediments by sulfide inhibition

---

A.J. Wallenius<sup>1\*</sup>, R.Klomp<sup>1,2\*</sup>, J. Venetz<sup>1</sup>, P. Dalcin Martins<sup>1,3</sup>, M. Sivan<sup>4</sup>, N. Dotsios<sup>1</sup>, M.A.H.J. van Kessel<sup>1</sup>, O.M. Żygadłowska<sup>1,2</sup>, N.A.G.M. van Helmond<sup>1,2</sup>, W.K. Lenstra<sup>1,2</sup>, C.P. Slomp<sup>1,2</sup>, M.S.M. Jetten<sup>1</sup>

\*These authors contributed equally to this work

<sup>1</sup>Department of Microbiology, Radboud Institute for Biological and Environmental Sciences, Radboud University, Heyendaalseweg 135, 6525AJ Nijmegen, the Netherlands

<sup>2</sup>Department of Earth Sciences, Utrecht University, Princetonlaan 8a, 3584 CB Utrecht, the Netherlands

<sup>3</sup>Institute for Biodiversity and Ecosystem Dynamics, University of Amsterdam, The Netherlands

<sup>4</sup>Institute for Marine and Atmospheric Research Utrecht, Utrecht University, Princetonplein 5, 3584CC Utrecht, the Netherlands

## Abstract

Coastal sediments are increasingly a source of the greenhouse gas methane as eutrophication and deoxygenation favour microbial methane production over removal. Reports from eutrophic coastal systems show that the sediment microbial methane filter by anaerobic methanotrophic (ANME) archaea is often shallower and a lot less efficient. Yet, the underlying cause for the weakening of this filter is not fully understood. Here, we investigated what causes the ANME filter to fail. We present biogeochemical and microbiological data from a seasonally anoxic coastal system, Marine Lake Grevelingen, that show that sulfide toxicity drives the collapse of the ANME-based methane filter. We find that high organic matter loading during summer stratification fuels intense sulfate reduction, depleting the sediment's iron oxide buffer allowing sulfide to accumulate to millimolar concentrations. This sulfide intrusion is toxic to the resident ANME-2ab and ANME-3 populations, which thrive only transiently in a narrow, low-sulfide niche, leading to a shutdown of methane oxidation. In contrast, a diverse methanogenic community flourishes under these conditions, resulting in a system that strongly favors net methane production. Our findings reveal that the expansion of coastal dead zones can severely weaken the sedimentary methane filter, creating a positive feedback on climate change.

## Keywords

microbial methane filter, eutrophication, sulfide, ANME

## Introduction

Methane is a key greenhouse gas, and the recent decade has seen a sharp rise in atmospheric concentrations, mostly as a result of increased release from natural sources (Michel et al., 2024). In marine sediments, most biological methane is produced through the breakdown of organic matter by methanogenic archaea (Reeburgh, 2007). The majority of this methane is oxidized by anaerobic methane-oxidizing (ANME) archaea acting in concert with sulfate-reducing bacteria (SRB). Together they form a microbial methane filter in the so-called sulfate-methane transition zone in the sediment (SMTZ) (Knittel and Boetius, 2009). Natural methane emissions are therefore the result of an interplay between counteracting processes in the microbial methane cycle; only when methanogenesis (production) exceeds anaerobic methane oxidation (AOM; removal) will methane be released into the overlying water column and, potentially, to the atmosphere.

Increased methane emissions have been reported from shallow coastal systems, which currently contribute already up to 75% of all marine methane emissions (Rosentreter et al., 2021). Coastal systems are hugely impacted by anthropogenic eutrophication due to high nutrient inputs from rivers and agricultural run-off, which leads to high rates of primary production. This, in turn, can lead to deoxygenation, which affects all marine life. Rising temperatures are also exacerbating eutrophication-driven deoxygenation (Breitburg et al., 2018). Increased temperatures promote water column stratification, leading to permanent or seasonal deoxygenation of bottom waters. The associated increase in anaerobic degradation of organic matter provides abundant substrates for methanogenesis. Over time, prolonged water column anoxia may lead to euxinia, where toxic hydrogen sulfide from the sediment accumulates in bottom waters. Euxinia is fatal for most higher life and results in so-called dead zones (Diaz and Rosenberg, 2008). In such settings, methane production by methanogenic archaea may be even more stimulated because of the input of readily available organic substrates (Reeburgh, 2007). Indeed, increased methane emissions due to methane production exceeding removal are reported for eutrophic systems (Żygadłowska et al., 2023, 2024b; Lapham et al., 2024; Wallenius et al., 2025), but the exact controls are not yet well understood.

Methane release from coastal sediments is highest at sites with a shallow SMTZ (Lapham et al., 2024; Żygadłowska et al., 2024b). Methanogenic archaea are often even found above the SMTZ (Deng et al., 2025; Wallenius et al., 2025). In contrast, methanotrophic ANME may be challenged by high rates of methane production and a narrow zone of methane removal, since ANME have notoriously slow growth rates and need time to build up sufficient biomass (Nauhaus et al., 2007; Lenstra et al.,

2023). This also implies that a high sedimentation rate is disadvantageous for ANME in establishing a stable zone for methane removal (Egger et al., 2016). Prolonged exposure to sulfide may inhibit the ANME methane filter in brackish coastal sediments (Dalcin Martins et al., 2024). However, the precise role of these mechanisms in controlling ANME biomass and the balance between methane production and removal remains unclear. With increasing warming, deoxygenation, and eutrophication of coastal areas, understanding the controls on the microbial methane filter in the SMTZ is crucial in view of projections of potential future methane emissions.

In this study, we investigated the seasonal methane dynamics in coastal sediments impacted by anthropogenic eutrophication. Our study site, Marine Lake Grevelingen (NL) is characterized by a high input of organic matter and seasonal stratification of the water column that results in bottom water euxinia (Żygadłowska et al., 2024b; Klomp et al., 2025). Due to an extremely high sedimentation rate of  $20 \text{ cm yr}^{-1}$ , we were able to monitor the effects of eutrophication-driven deoxygenation on the biogeochemical cycles in different sediment layers between seasons. We hypothesized that the eutrophication of this system favours methanogenic archaea while inhibiting the ANME methane filter. We followed the seasonal changes in redox conditions with a range of (geo)chemical analyses of sediments and porewater. We combined this with measurements of ex-situ rates of methane production and removal, and analysis of the microbial community involved in methane cycling. Our results show that sulfide inhibits the buildup of ANME biomass in these rapidly accumulating sediments, leading to high methane emissions, suggesting that the global expansion of marine dead zones could substantially weaken this natural methane sink and create a positive feedback on climate change.

## **Main text – Results and Discussion**

### **Oxygen depletion in the bottom waters drives anaerobic metabolism in the sediment**

Seasonal oxygen depletion in the bottom water of Marine Lake Grevelingen dramatically altered the sediment's biogeochemistry, fostering intense anaerobic metabolism fueled by a high influx of fresh organic matter. Following the onset of euxinia in June (Fig. S1), the organic carbon content in the surface sediment surged from a baseline in March of  $\sim 2\text{--}3 \text{ wt}\%$  to over  $4 \text{ wt}\%$ , a likely consequence of the settling of organic matter following algal blooms (Fig. 1a; Hagens et al., 2015). A similar high peak of  $4 \text{ wt}\%$  at a sediment depth of 18 cm (in March) can be traced back to the increased burial of organic carbon in the summer of the previous year, using molybdenum peaks as time

markers (Fig. S2). The fresh layer of organic matter was progressively buried, with the peak reaching a 5 cm depth by September (Fig. 1a). Sulfate penetrated to a depth of 18 cm in March but only to 8 cm by September due to an increase in sulfate reduction rates (SRR) in the surface sediment following the organic matter pulse in June (Fig. 1b-c). The SRR increased from 100–200  $\text{nmol cm}^{-3} \text{d}^{-1}$  in March (a typical range for similar coastal regions (Howarth and Jørgensen, 1984; Egger et al., 2016; Findlay et al., 2020)) to a peak of 1194  $\text{nmol cm}^{-3} \text{d}^{-1}$ , a 10-fold increase, rapidly shoaling the sulfate penetration zone. Moreover, Pearson analysis indicated a strong correlation between organic matter and sulfate from June onwards ( $r > 0.6$ ,  $p < 0.05$ ; Fig S3.).

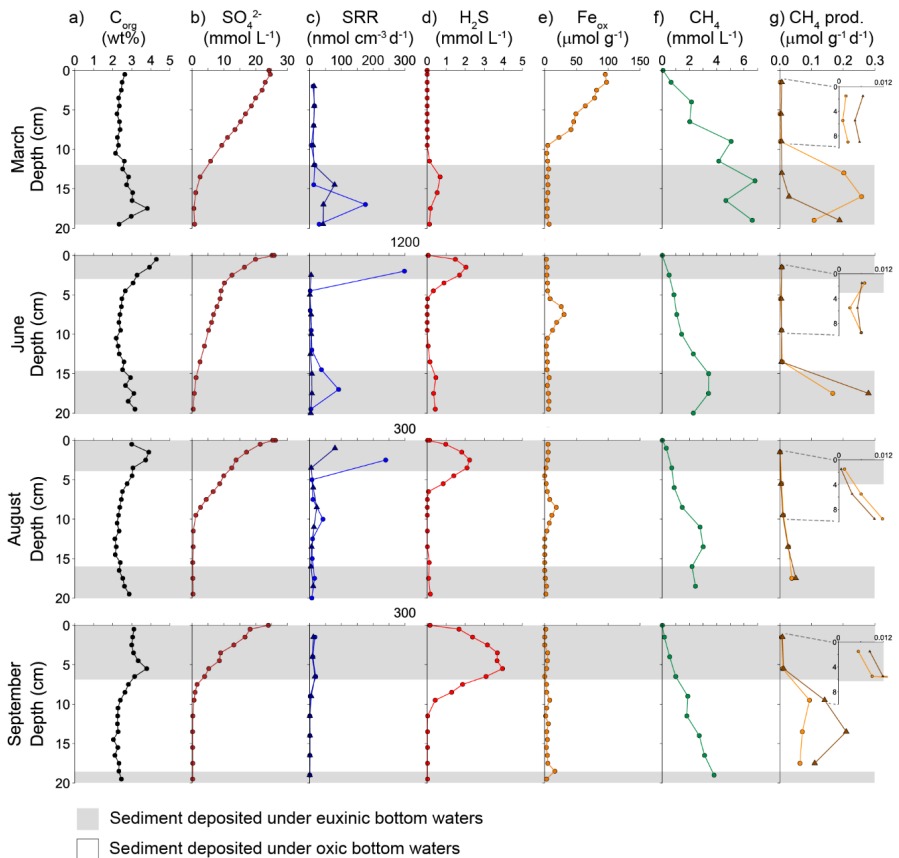


**Fig. 1** Geochemical profiles and rates of microbial processes across the top 20 cm of the sediment in March, June, August and September 2021 for a) total organic carbon; b) sulfate; c) sulfate reduction rate (SRR); d) sulfide; e) iron oxides; f) methane and g) methane production. For SRR and methane production two separate cores were used for the analysis. The grey shading indicates sediment deposited under euxinic bottom waters and no shading indicates sediment deposited under oxic bottom waters, as explained in Fig. S1.

The surge in sulfate reduction led to a rapid accumulation of sulfide, which had been absent in the surface sediment during oxic conditions (Fig. 1d), reflected in a strong positive correlation of sulfide and  $C_{org}$  from June onwards ( $r > 0.9$ ,  $p < 0.05$ ). The sediment's initial buffer of iron oxides that removes sulfide by abiotic reactions forming iron sulfide minerals (Rickard and Luther, 2007) was present at up to  $100 \mu\text{mol g}^{-1}$  in the top 10 cm in March. However, upon an increase in SRR it was rapidly consumed and completely depleted by September (Fig. 1e). Once this buffer was exhausted, free sulfide accumulated to high concentrations (4 mM) in the surface sediment, expanding the sulfidic zone to 12 cm depth. This amount of sulfide is high even for eutrophic coastal sediments (Thamdrup et al., 1994; Kamyshny et al., 2024). Taken together, the high organic matter input and summer stratification resulted in euxinia in the bottom waters, which, in turn, led to a shoaling of the redox zones in the sediment and accumulation of sulfide upon iron oxide depletion.

### **Methanogens favoured over methanotrophs**

Prolonged euxinia and high rates of deposition of organic matter are expected to provide conditions that are conducive for methanogenesis (Egger et al., 2016). Indeed, we observed high porewater methane throughout the seasons (up to  $6 \text{ mmol L}^{-1}$  in March), supported by active methanogenesis in the top 20 cm of sediment (Fig. 1f-g). In March, methanogenesis rates reached up to  $0.26 \mu\text{mol CH}_4 \text{ g dw}^{-1} \text{ d}^{-1}$  and notably overlapped with the zone of active sulfate reduction, suggesting the two processes co-occurred rather than competed for substrate, as suggested for other systems (Maltby et al., 2016; Sela-Adler et al., 2017). In September the methanogenic zone notably shifted upwards into the sediment deposited under oxic bottom waters, whereas previously the highest activity was seen in the sediment layers deposited during euxinia (Fig. 1g). Microbial community analysis confirmed the widespread activity of a highly diverse methanogenic community in the top 20 cm as taxa with all main methanogenic pathways, i.e. hydrogenotrophic, methylotrophic and acetoclastic were present (Fig. S4). The highest abundance of methanogenic archaea was observed in the most organic-rich layers (Fig. 1a, 2a), and especially methylotrophic methanogens were abundant in these layers, with a positive Spearman correlation throughout the year ( $r > 0.8$  except September  $> 0.6$ ; Fig. S3). Mixotrophic *Methanosarcina* reads overlapped most of the time with hydrogenotrophic taxa, suggesting that they favour hydrogenotrophic metabolism in these sediments and it is the main source of methane in Lake Grevelingen sediments (Wallenius et al., 2025, Sivan et al. 2025).

Whereas methanogenesis was highly active in the top 20 cm of the sediment in all seasons, AOM was limited and transient. No AOM was detected in March and, when it appeared in June and increased in August, the process was confined to a narrow

zone in the oxic deposition layers (8-11 cm) with a maximum rate of  $4.3 (\pm 1.1) \text{ nmol CH}_4 \text{ g dw}^{-1} \text{ d}^{-1}$ ; 50-fold lower than maximum methanogenesis rates (Fig. S5, Table S1). The clumped isotopic composition of methane (Young et al., 2017) measured in July showed distinct signals in the top 16 cm of the sediment compared to the lower depths (Fig. S6), further supporting the presence of active AOM in the SMTZ during summer, albeit at very low rates. However, the shift in the isotopic signal was less pronounced than typically expected for AOM (Adnew et al., 2025), which could be due to overlapping contributions from both methanogenesis and AOM. In September, AOM was undetectable again.

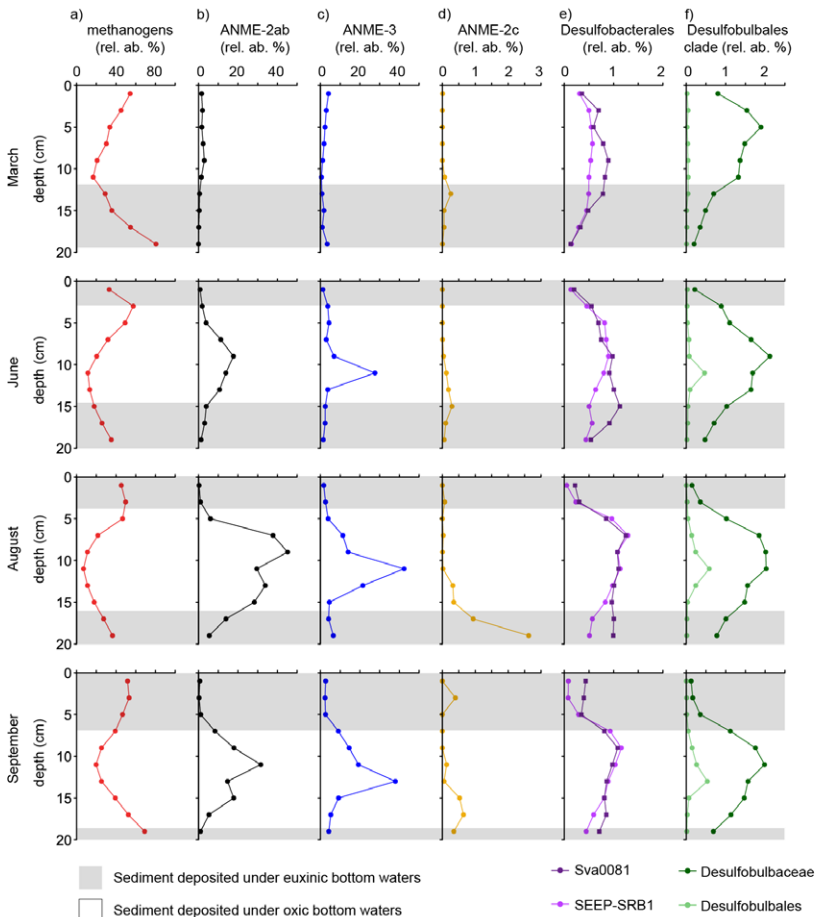


**Fig. 2** Relative abundance of methanogenic (a) and methanotrophic (b-d) archaea and potential syntrophic SRB for AOM (e-f) per depth in each season. Note the varying x axis for the different taxa. For a) all known methanogenic taxa were pooled, see Fig. S4 for relative abundances of individual taxa. The SRB shown were selected based on correlation analysis with ANME-2ab and ANME-3. The grey shading indicates sediment deposited under euxinic bottom waters and no shading indicates sediment deposited under oxic bottom waters.

Although reported for this site before (Egger et al., 2016; Żygadłowska et al., 2023), the limited role of AOM, which is most pronounced in March and September, is surprising. This transient activity directly coincided with the abundance of ANME archaea. ANME reads were negligible (< 4%) in March but increased to 45 % in June and by August the two clades detected, ANME-2ab and ANME-3, constituted > 80% of the archaeal reads within the AOM zone, before decreasing again in September (Fig. 2b-c). The ANME community showed clear niche partitioning. ANME-2ab occupied a broader zone (5-15 cm) and grew fastest at 9 cm depth

(Fig. 2b). Their abundance correlated with the increase of *Desulfobulbaceae* reads, as well as *Desulfosacrinaceae* groups SEEP-SRB1 and Sva0081 (Table S3.), all putative SRB partners in AOM (Fig. 2e-f; Lösekann et al., 2007; Schreiber et al., 2010; Metcalfe et al., 2021). ANME-3 were almost entirely restricted to 11 cm depth, where sulfate was nearly depleted and their abundance correlated almost perfectly with the DBB clade *Desulfobulbales* (Lösekann et al., 2007). We also recovered reads of ANME-2c in low abundance, primarily in the sulfate-depleted methanogenic zones, supporting earlier observations of their role as potential methanogens in hydrocarbon-rich sediments (Sarno et al., 2024).

Overall, our results show that eutrophication and seasonal bottom-water anoxia promote a robust and diverse methanogenic community, allowing the methane production zone to expand upwards. In contrast, although a methane filter constituted by ANME-2ab and ANME-3 and SRB started to establish in June, it could not keep up with methane production and ultimately collapsed in September, documented by the lack of AOM activity and decrease in ANME abundance.

### **Sulfide accumulation drives the collapse of the inefficient methane filter**

To understand what is inhibiting or restricting ANME in the sediment, we analysed and overlaid the monthly profiles of microbial relative abundance with selected geochemical and activity profiles, i.e. sulfide, SRR and organic carbon (Fig. 3). We found that in all seasons, ANME are restricted to a narrow zone in the sediment that was deposited in the winter months during oxic bottom water conditions and we found strong negative correlations between ANME archaea and  $C_{org}$  (Fig. 1,3, S3).

In these profiles, we also see a niche separation with ANME-2ab present in the entire oxic deposition zone, whereas ANME-3 only reaches above 10% relative abundance in a narrow 5 cm section. However, in contrast to relative archaeal abundance based on 16S rRNA gene amplicon analysis (Fig. 2), the copy numbers

based on qPCR of archaeal 16S rRNA gene copies in the same samples shows that both clades grow best in the middle of the oxic deposition zone (Fig. 3). Both clades rapidly increased in abundance from March to June, with doubling times in the oxic zone of  $\sim 1.5$ -4 weeks, which is very fast for ANME archaea *in-situ* or *in-vitro* (Table S2; Nauhaus et al., 2007; Orphan et al., 2009; Timmers et al., 2015; Ruff et al., 2019). In contrast to the trends in ANME abundance, SRRs are highest in the organic matter-rich zones deposited during bottom water euxinia and sulfide is present in the porewater in these zones (Fig 3). Once iron oxides were exhausted, sulfide was no longer buffered and could diffuse downward. We propose that this sulfide intrusion into the underlying, oxic deposition layers inhabited by ANME archaea was likely strongly contributing to the failure of the methane filter as ANME and sulfide concentrations  $> 1$  mM do not overlap (Fig. 3). This is supported by a significant negative correlation between sulfide levels and the abundance of ANME in June and August ( $r < -0.9$  for ANME-2ab;  $r < -0.7$  for ANME-3). In line with inhabiting a broader zone, ANME-2ab appear to tolerate higher sulfide concentrations ( $\sim 1$  mM; Fig S7), though its activity seems to occur only in the absence of sulfide. In contrast, ANME-3 exhibit a lower tolerance for sulfide ( $< 0.5$  mM), which might explain the restriction to a much narrower zone. While the sulfide-sensitive ANME filter becomes less active or collapses, the methanogenic archaea thrive in the sulfidic zones. This is supported by the high relative abundance (Fig 2.) and strong positive correlation of different methanogenic clades and sulfide ( $r < 0.8$ ; Fig. S3), further demonstrating how seasonal euxinia promotes net methane production in these sediments.

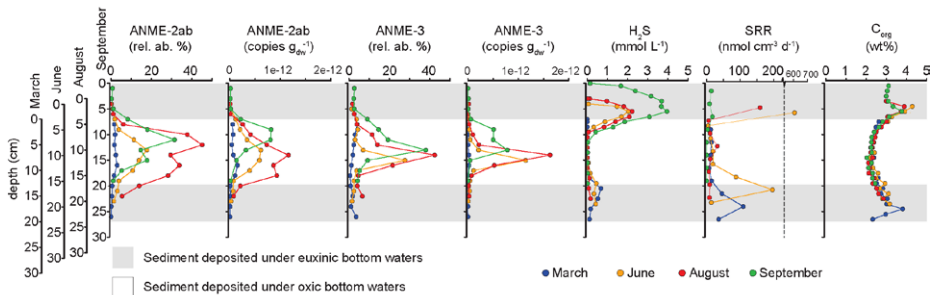


**Fig. 3** The relative abundance and copy numbers of ANME-2ab and ANME-3 and the concentrations of key sediment characteristics linked to organic matter degradation; sulfide ( $H_2S$ ), sulfate reduction rate (SRR) and Organic C from March to September, overlaid with shifted scale to reflect the new sediment input.

## Genomic insights into sulfide metabolism and toxicity in ANME

To elucidate the mechanism of sulfide inhibition in ANME, we analyzed the sulfur metabolism in the two ANME MAGs recovered from Lake Grevelingen sediments belonging to the two dominant clades; ANME-2a (family *Ca. Methanocomedenaceae*, genus *Kmv04*) and ANME-3 (*Ca. Methanovorans*). Both MAGs possess complete pathways for assimilatory sulfate reduction, but they differ in the key enzymes for sulfite reductase; the last step that produces sulfide from sulphite, a toxic intermediate (SFig. 8; Yu et al., 2018). The ANME-3 genome encodes a Group I F<sub>420</sub>-dependent sulfite reductase (*Fsr*), which is suggested to have a role in sulphite detoxification (Johnson and Mukhopadhyay, 2008). We hypothesize that in high-sulfide environments, this enzyme may suffer from product inhibition, leading to a toxic intracellular buildup of sulfite. However, Group I *Fsr* proteins are widespread in sulfide-tolerant methanogens, thus the functionality of this enzyme needs further study to understand why ANME-3 are so sensitive toward sulfide. The ANME-2a genome lacks a complete *Fsr* complex but instead contains an *aSir*/Group I *Dsr*-LP protein which has been found in all ANME clades (Yu et al., 2018). Additionally, the genome encodes Group III *Dsr*-LP, that was upregulated in *Ca. Methanoperedens* cells exposed to sulfide stress (Echeveste Medrano et al., 2025). Both proteins have the same function as sulfite reductase in the methanogen *M. maripaludis* (Day et al., 2024). We hypothesize, that, like Group I *Fsr* in ANME-3, Group III *Dsr*-LP might result in product inhibition in high-sulfide environments, leading to sulfite toxicity in the cell, but it maybe less susceptible than Group I *Fsr* in ANME-3. Furthermore, we surveyed the MAGs for multiheme cytochromes (MHC) as these are potential targets for sulfide inhibition by blocking extracellular electron transfer (Liu et al., 2012). Methanogens have generally relatively few or no large MHCs, but surprisingly ANME-3 genomes encode multiple, probably gained through horizontal gene transfer since their last methanogenic ancestor (Woods et al., 2024). Indeed, the ANME-2a genome contained nine MHCs while ANME-3 encoded seven. Thus, our analysis reveals multiple potential causes for sulfide toxicity in the different ANME clades, and the differences in their enzyme repertoire could further explain the niche separation of the clades.

Sulfide toxicity in ANME has been suggested before in eutrophic coastal sediments (Dalcin Martins et al., 2024). ANME also have been shown to negatively correlate with sulfide concentrations in hydrothermal vent sediments (Biddle et al., 2012). Additionally, ANME are absent from some methane-rich sediments that would otherwise be expected to host an active methane filter if not for high sulfide concentrations (Semler and Dekas, 2025), all observations that further strengthen our findings. Furthermore, clade-specific niche separation for ANME has been

reported before, with ANME-2ab usually preferring sulfate-rich sediments at the top of the SMTZ, where sulfide concentrations are low (Biddle et al., 2012; Chen et al., 2022). ANME-3 are less commonly found in seep habitats, and up to now there is no comprehensive view of their overall habitat, although some studies suggest they might be very susceptible to sulfide inhibition (Chen et al., 2022; Semler and Dekas, 2025). Thus, we suggest that the niche-separation of different ANME clades is partially driven by their differing susceptibility to porewater sulfide concentrations.

We conclude that eutrophication and deoxygenation shifts the balance of the methane cycle towards net production and increased methane emissions as 1) seasonal bottom water euxinia promotes anaerobic organic matter degradation leading to sulfide accumulation 2) once sulfide accumulates due to loss of iron oxide buffer it spreads into the methane oxidation zone, where 3) ANME archaea are inhibited by sulfide toxicity which collapses the methane filter, while 4) methanogenic archaea thrive in such sulfidic organic matter rich conditions and can expand their zone towards the sediment-water interface. While the specific cellular mechanisms of sulfide toxicity warrant further investigation, our results highlight the urgent need for actions to reduce nutrient input in coastal waters to prevent the expansion of these dead zones and limit further increases in methane emissions.

## Materials and Methods

### Sampling location and sample collection

Our study site is the deepest basin (Scharendijke basin; 45 m) of Marine Lake Grevelingen in the Netherlands, which has a salinity of 29-33. The marine lake suffers from eutrophication and temperature-driven water column stratification in the summer months, leading to deoxygenation and euxinia in the bottom waters from June to September (Żygadłowska et al., 2024b); Fig. S1). Previous studies have recorded high benthic fluxes of methane, part of which escapes to the atmosphere (Żygadłowska et al., 2024b; Venetz et al., 2024). The bottom water redox conditions can be tracked with sediment molybdenum (Mo) as a proxy for bottom water euxinia as shown in Żygadłowska et al. (2024a), allowing an accurate estimation of the sediment accumulation between seasons (Fig. S2). Water column, sediment and porewater depth profiles were determined during four sampling campaigns with R/V *Navicula* in March, June, August and September 2021. This allowed us to capture the transition from an oxic, well-mixed system to a stratified euxinic system (Fig S1). Dissolved oxygen and sulfide in the water column were measured as described previously (Żygadłowska et al., 2024a). During each sampling campaign, seven

sediment cores were collected using a UWITEC corer and PVC core liners (120 cm length, 6 cm inner diameter). Core 1 was sampled for methane porewater, cores 2 and 3 for sulfate reduction rates (SRR), core 4 for DNA and porosity, core 5 for anoxic porewater sampling and cores 6 and 7 for ex-situ rates of methane production and oxidation. In this study, we focus on the upper 20 cm of the sediment.

### **Sediment and porewater sampling**

Methane samples were collected immediately after core retrieval using a liner with two rows of holes drilled at 5 cm intervals on opposite sides of the liner, offset by 2.5 cm and covered with tape. From each hole, 10 mL of sediment was taken with a cut-off plastic syringe and transferred into a 65 mL glass bottle filled with saturated NaCl solution. The bottles were topped up with the saturated NaCl solution, closed with rubber stoppers and aluminium screw caps and stored upside down until analysis. We note that methane concentrations might be underestimated, due to possible degassing during sample collection (Egger et al., 2017; Jørgensen et al., 2019). To collect porewater and solid phase samples, one core was sliced in a glove bag under a nitrogen atmosphere at a depth resolution of 1 cm. Each slice was placed in a 50 mL centrifuge tube and centrifuged at 4000 rpm for 20 min. The supernatant from each tube was filtered through a 0.45 µm nylon syringe filter in a glove bag and subsampled under a nitrogen atmosphere for analysis of  $\text{SO}_4^{2-}$  and  $\text{H}_2\text{S}$ . The remaining sediments were stored anoxically at  $-20^\circ\text{C}$  to be processed later. All samples were stored at  $4^\circ\text{C}$ ; samples for  $\text{H}_2\text{S}$  analysis were stored in a glass vial with 2 % zinc acetate solution (2 mL), and samples for dissolved Mn and dissolved Fe were stored in polypropylene vials, acidified with 35 % suprapur HCl (10 µL of acid per 1 mL of sample).

For clumped isotope measurements, 7 x 1L bottles from the bottom water and 1L of sediment from 8 different depths were collected, closed with a leak-tight cap and treated with  $\text{HgCl}_2$  to stop any microbial activity.

### **Porewater analysis**

Porewater  $\text{CH}_4$  was analysed by first adding 10 mL of nitrogen to each bottle while allowing the same volume of liquid to escape, and after equilibration of the gas and water phase (7 days),  $\text{CH}_4$  concentrations were measured with a Thermo Finnigan Trace™ gas chromatograph equipped with an FID (limit of detection is  $0.02 \mu\text{mol L}^{-1}$ ). Concentrations of  $\text{H}_2\text{S}$  were measured using the phenylenediamine and ferric chloride method (Cline, 1969; detection limit of  $1 \mu\text{mol L}^{-1} \text{H}_2\text{S}$ ).  $\text{SO}_4^{2-}$  concentrations were determined with ion chromatography (Metrohm 930 Compact IC Flex; detection limit of  $50 \mu\text{mol L}^{-1}$  for  $\text{SO}_4^{2-}$ ).

### Sediment analysis

The solid sediment samples were freeze-dried and subsequently ground with an agate mortar and pestle, under an N<sub>2</sub> environment. The powdered sediment samples were used for analysis of organic carbon (C<sub>org</sub>) and Fe oxide. For organic C analysis, a subsample of 250 mg was treated with 1 M HCl to remove carbonates (Van Santvoort et al., 2002). The samples were oven-dried for three days at 60 °C, re-powdered and analyzed for their carbon content using a Fisons Instruments NA 1500 NCS analyzer. Organic carbon content was corrected for the weight loss upon decalcification and the salt content of the freeze-dried sediment. Accuracy and precision of the organic C analysis was determined by incorporation of an internationally certified soil standard (IVA2; 0.732 wt.% C). The mean value obtained in this study (n=15) was 0.739 +/- 0.005 wt.% C. Analytical uncertainty based on duplicates (n=8) was 0.05 wt.% C.

To determine the Fe oxide concentrations in the sediment, about 50 – 100 mg of a freeze-dried subsample was treated with 1 M HCl for 6 h at room temperature. The extracted Fe(III) concentration in the supernatant was measured colorimetrically immediately after the extraction using the phenanthroline method (APHA, 2005). The average analytical uncertainty of this method based on duplicates (n=7) was 14.3%. Porosity was determined based on the weight loss upon oven-drying at 60 °C.

### Sulfate reduction rates

Sediment samples were taken from two pre-drilled replicate cores (diameter 2 cm; 5 cm vertical resolution) which were taped prior to coring. From each hole, 5 mL of wet sediment was extracted immediately after core retrieval using cut-off syringes, which were sealed with parafilm and stored under nitrogen atmosphere in the dark at 4°C.

Within 24 hours after coring, a volume of 100 µl carrier-free <sup>35</sup>SO<sub>4</sub><sup>2-</sup> (100 kBq) was injected in the syringes and the resulting hole was sealed with parafilm. The sediment was incubated for 24 h in the dark at 4°C under an inert N<sub>2</sub> atmosphere before it was transferred to a 50 mL centrifuge tube containing 20 mL oxygen-free 20% Zn-acetate to precipitate dissolved sulfide and terminate microbial activity (Fossing and Jorgensen, 1989; Kallmeyer et al., 2004).. The samples were subsequently stored frozen (-20°C) under a N<sub>2</sub> atmosphere. Upon analysis, the thawed samples were centrifuged for 20 min at 4000 rpm, the supernatant was collected for a separate measurement and the sediments were washed twice with deoxygenated water (10 mL) and centrifuged to remove remaining porewater and unreacted <sup>35</sup>SO<sub>4</sub><sup>2-</sup>. The reduced S was extracted with an acidic chrome chloride solution for 48 h and captured in 20% Zn-acetate via the passive diffusion method

described before (Burton et al. 2008). The formed radioactive  $H_2S$  was determined by mixing the Zn-acetate solution 1:2 vol:vol with Ecoscint XR (NAT1396, Scientific Laboratory Supplies, UK), which was analysed on an automatic triple-to-double coincidenc ratio liquid scintillation counter (Hidex 600 SL, LabLogic Systems Limited, UK). The  $SO_4^{2-}$  reduction rates were then calculated using the activity (decays per minute) of the radiolabelled total reduced inorganic S ( $\alpha_{TRIS}$ ) with the total added  $SO_4^{2-}$  radiotracer ( $\alpha_{TOT}$ ) as described in Kallmeyer et al. (2004):

$$SRR = [SO_4^{2-}] * \phi * \frac{\alpha_{TRIS}}{\alpha_{TOT}} * \frac{1}{t} * 1.06 \quad (\text{eq. 1})$$

where  $\phi$  is the porosity,  $\alpha_{TRIS}$  is the radiolabeled total reduced inorganic sulfur,  $\alpha_{TOT}$  is the total added  $SO_4^{2-}$  radiotracer,  $t$  is the incubation time in days, 1.06 is the correction factor for the expected isotopic fractionation.

### Clumped isotope measurements

To extract methane for isotope measurements, the bottles with bottom water were shaken while the sediment bottles were allowed to settle horizontally. To extract dissolved methane, 100 mL of nitrogen gas was added to each bottle while allowing the same volume of water to escape into a syringe, where 10 mL headspace was added with nitrogen. After 2 h equilibration of the gas and water phase, the headspace in the syringe was collected for measurement. The 100 mL headspace was collected by returning the 100 mL of water into the sample while letting the headspace gas out into a new syringe. This was repeated five times per sample to get a high enough methane yield for measurements. The  $CH_4$  isotopes were measured as previously described in (Sivan et al., 2024).

### Methanogenesis and AOM rate measurements

To determine methanogenesis and AOM rates, 10 g of sediment from selected depths was weighed into a 60 ml serum bottle inside an anaerobic chamber, stoppered, capped and flushed with 100% Ar leaving 0.5 bar overpressure. Samples were prepared within 48 h of sampling in duplicate using two different cores. The methanogenesis bottles were stored in the dark at 4°C and shaken lightly and the amount of  $CH_4$  in the headspace was measured 1-2 times a day for one week by injecting 100  $\mu$ l of headspace gas into a HP5890 gas chromatograph (Agilent) equipped with a Porapak Q column and a thermal conductivity detector. The AOM bottles were amended with 20%  $^{13}C$ - $CH_4$  and 5%  $CO_2$  in the headspace and incubated in the dark at 4°C while gently shaking. We used the increase in the ratio of  $^{13}C/^{12}C$ - $CO_2$  as a proxy for methane oxidation which was monitored by measuring  $^{12}C$ - $CO_2$  and  $^{13}C$ - $CO_2$  in the headspace once a day for a period of one

week by injecting 50  $\mu\text{l}$  of headspace gas into a GC-MS (Gas chromatograph-mass spectrometer; Agilent tech 5975c inert MSD). The first measurement was performed 24 h after gas addition to equilibrate the headspace gas.

### DNA extraction and 16S rRNA amplicon sequencing

DNA was isolated from the original sediment with the DNeasy PowerSoil Pro DNA isolation kit (Qiagen, Venlo, Netherlands) according to the manufacturer's instructions, with two modifications: the sample was bead-beaten on a TissueLyser LT (Qiagen) for 10 min at 50Hz and the DNA was eluted into 50  $\mu\text{l}$  DPEC-treated water (Invitrogen, Carlsbad, United States). Archaeal 16S rRNA amplicon sequencing was performed on the Illumina MiSeq Next Generation Sequencing platform by Macrogen (Seoul, South Korea) using Herculanase II Fusion DNA Polymerase Nextera XT Index Kit V2, yielding 2x300bp paired end reads. Primers used were Arch349F (5'-GYGCASCAGKCGMGAAW-3') and Arch806R (5'-GGACTACVSGGGTATCTAAT-3'; Takai and Horikoshi, 2000). The primers used for bacterial 16S rRNA gene amplification were Bac341F (5'-CCTACGGGNGGCWGCAG-3'; (Herlemann et al., 2011) and Bac806R (5'-GGACTACHVGGGTWTCTAAT-3'; (Caporaso et al., 2012). The optimal trimming parameters were determined with Figaro (Weinstein et al., 2019), and trimming and further processing were done using the DADA2 pipeline (v1.8; Callahan et al., 2016) in Rstudio to cluster the reads into amplicon sequence variants (ASVs), chimera removal and taxonomic classification using SILVA 16S rRNA database (v138.1; Quast et al., 2013). Microbial community data analysis was performed with phyloseq (v1.36.0; McMurdie and Holmes, 2013), retaining only reads classified at phylum level, and visualised using the package ggplot2 (v3.3.5; Wickham, 2016). Raw reads are accessible on the National Center for Biotechnology Information (NCBI) website under the accession number PRJNA1257658.

### Statistical analysis

Spearman correlations between environmental parameters ( $\text{CH}_4$ ,  $\text{FeOx}$ ,  $\text{SO}_4^{2-}$ ,  $\text{H}_2\text{S}$ , and  $\text{C}_{\text{org}}$ ) and methane-cycling archaea counts were calculated using the `rcorr()` function from the `Hmisc` package (v5.2-3; <https://github.com/harrelfe/Hmisc>). To visualize these relationships, the `quickcor()` function from the `ggcor` package (v0.9.4.3) was used. This allowed for simultaneous visualization of Spearman correlations between microbial taxa and environmental variables, as well as Pearson correlations among the environmental variables themselves. Additionally, to identify putative SRB partners for ANME, Spearman rank correlations and corresponding p-values were calculated in R using the `cor.test()` function between the relative abundances of archaeal ANME genera and bacterial families across all samples.

## Metagenomic sequencing and analysis

We sequenced two depths, 9-11 cm and 15-17 cm, for further analysis of the SMTZ community. Short-read metagenomic sequencing was performed with a TruSeq DNA PCR-free library with an insert size of 550bp on NovaSeq6000 (Illumina) platform, producing  $2 \times 150$ bp paired-end reads (100 Gbp/sample). Raw read data is uploaded to NCBI short read sequence archive (SRA) under accession numbers SRR33663672 and SRR33663671. We used singleM (Woodcroft et al., 2024) to characterize the samples taxonomically and find any ANME reads in the samples. We used the output to filter the raw reads with khmer (Crusoe et al., 2015) to only retain reads with coverage between 20-50 to as the most abundant ANME taxa were in this fraction. The filtered reads were assembled and binned using the Aviry pipeline (v.0.11.0; Newell et al., 2024). The reads were trimmed with fastp (v0.24.0; Chen, 2023), assembled with metaSPAdes (v. 4.0.0; Nurk et al., 2017), mapped with CoverM (v0.7.0; Aroney et al., 2025) and binned with Vamb (v3.0.2; Nissen et al., 2021), MetaBAT and MetaBAT2 (v2.15; Kang et al., 2015, 2019), Semibin (Pan et al., 2022), Rosella (v0.5.5; <https://rhysnewell.github.io/rosella/>) and DASTool (v. 1.1.2; Sieber et al., 2018). The metagenomically assembled genomes (MAGs) were taxonomically classified with GTDB-Tk release 220 (v2.4.0; Chaumeil et al., 2020). MAG completeness and contamination was estimated with CheckM2 (v1.0.2; Aroney et al., 2025).

We recovered two ANME metagenome annotated genomes (MAGs) and analysed those further. Genomes were annotated with DRAM v1.0 (Shaffer et al., 2020) with default parameters except for the option `--min_contig_size 1000`. Novel or poorly annotated sulfur metabolism genes were investigated more in depth by blastp analyses using reference sequences from ANME and methanogens from a previous study (Yu et al., 2018). Sulfite reductases were identified via minimum bitscore of 180 and confirmed via phylogenetic analyses. For that, protein sequences were aligned with muscle v3.8.31 (Edgar, 2004), trimmed with trimAl v1.4.rev22 (Capella-Gutiérrez et al., 2009) using the option `-gappycout`, placed in a tree built with FastTree v 2.1.10 (Price et al., 2010), and visualized with iTol v7 (Letunic and Bork, 2021). Raw read data and ANME MAGs are accessible on the NCBI site under BioProject PRJNA1167897.

## Quantative Polymerase Chain Reaction (qPCR) for archaeal abundance

Archaeal 16S rRNA gene was quantified with pArch519F (CAG CMG CCG CGG TAA) and Arch806R primers. The reaction mix (20  $\mu$ l) consisted of 10  $\mu$ l PerfeCTa Quanta SYBR Green FastMix (Quanta Bio, USA), 1  $\mu$ mol (500 nM) of both the reverse

and forward primers, 3  $\mu$ l of template DNA and 5  $\mu$ l sterile ultrapure water. The following programme was used: initial denaturation (3 min at 95°C), denaturation (30 s at 95°C), annealing (30 s at 60°C), elongation (30 s at 72°C); after 40 cycles a melt curve from 54.5 to 95°C with increments of 0.5°C was measured to check for PCR specificity. Single-copy archaeal 16S rRNA gene carrying pGEM-T Easy vector plasmids (Promega, The Netherlands) were used for quantification calibration.

## Supplementary material

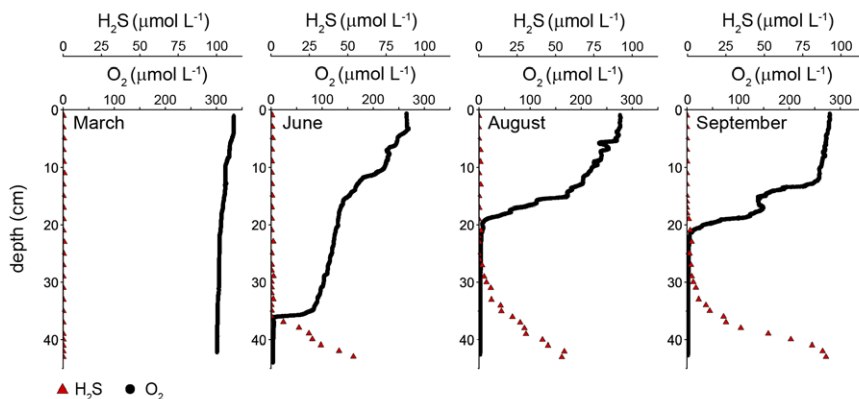


**Fig. S1** Sulfide and oxygen concentrations in the water column in March, June, August and September 2021. In March, the water column was fully oxygenated but by June water column stratification and deoxygenation had resulted in euxinic bottom waters.

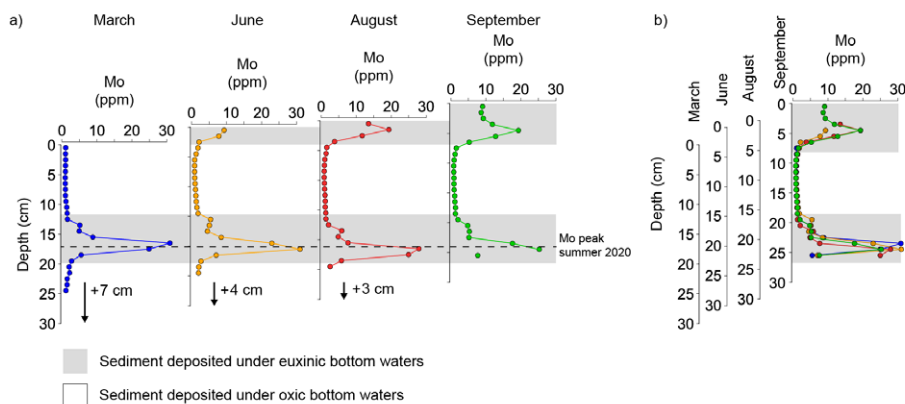


**Fig. S2** Scheme of sedimentation history at our study site. Sedimentary molybdenum enrichments are formed due to formation of thiomolybdates in the presence of free sulfide in the water column and around the sediment–water interface (Helz et al., 1996; Erickson and Helz, 2000; Zygadłowska et al., 2024a). Since the enrichment in Mo is assumed to behave conservatively, a change in depth of the Mo maximum formed during one period of euxinia can be used to determine the amount of sediment accumulated over time (Zygadłowska et al., 2024a). a) Sediment Mo profiles for March, June, August and September with the depth corrected so that the peak in Mo that formed in summer 2020 overlaps. The downward arrows in the plot represent the depth correction due to fresh sediment deposition. Grey shading indicates the sediment that was deposited under euxinic bottom waters and no shading indicates sediment that was deposited under oxic bottom waters. b) Sediment Mo profiles with depth correction of each month overlaid. Again, the grey shading indicates the sediment that was deposited under euxinic bottom waters and no shading indicates sediment that was deposited under oxic bottom waters. The same principle is applied to make figure 4.

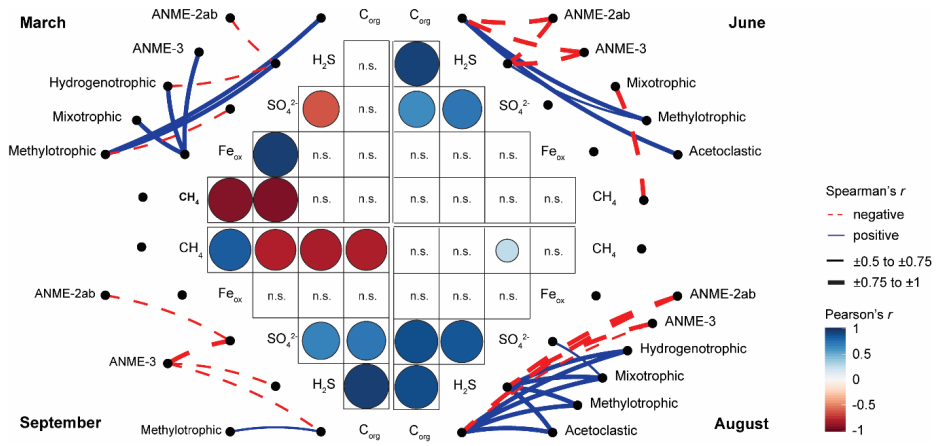


**Fig. S3** Correlations between methane cycling taxa and porewater chemistry in the Grevelingen Sediment throughout the year. Positive and negative Spearman's  $r$  between counts of methane cycling taxa and porewater chemistry ( $\text{CH}_4$ ,  $\text{Fe}_{\text{ox}}$ ,  $\text{SO}_4^{2-}$ ,  $\text{H}_2\text{S}$  and  $\text{C}_{\text{org}}$ ) are indicated by blue, solid and red, dashed lines respectively. Edge width indicates moderate  $\pm 0.5$  to  $\pm 0.75$ , or strong  $\pm 0.75$  to  $\pm 1$  spearman's  $r$ . Pearson correlations between porewater chemistry (Pearson  $r$ ) is illustrated as blue (positive) or red (negative) circles. Circle size indicated Pearson's  $r$ . Only correlations  $p < 0.05$  were used for this graph. Not significant correlations were either not illustrated or indicated by n.s. (=not significant).

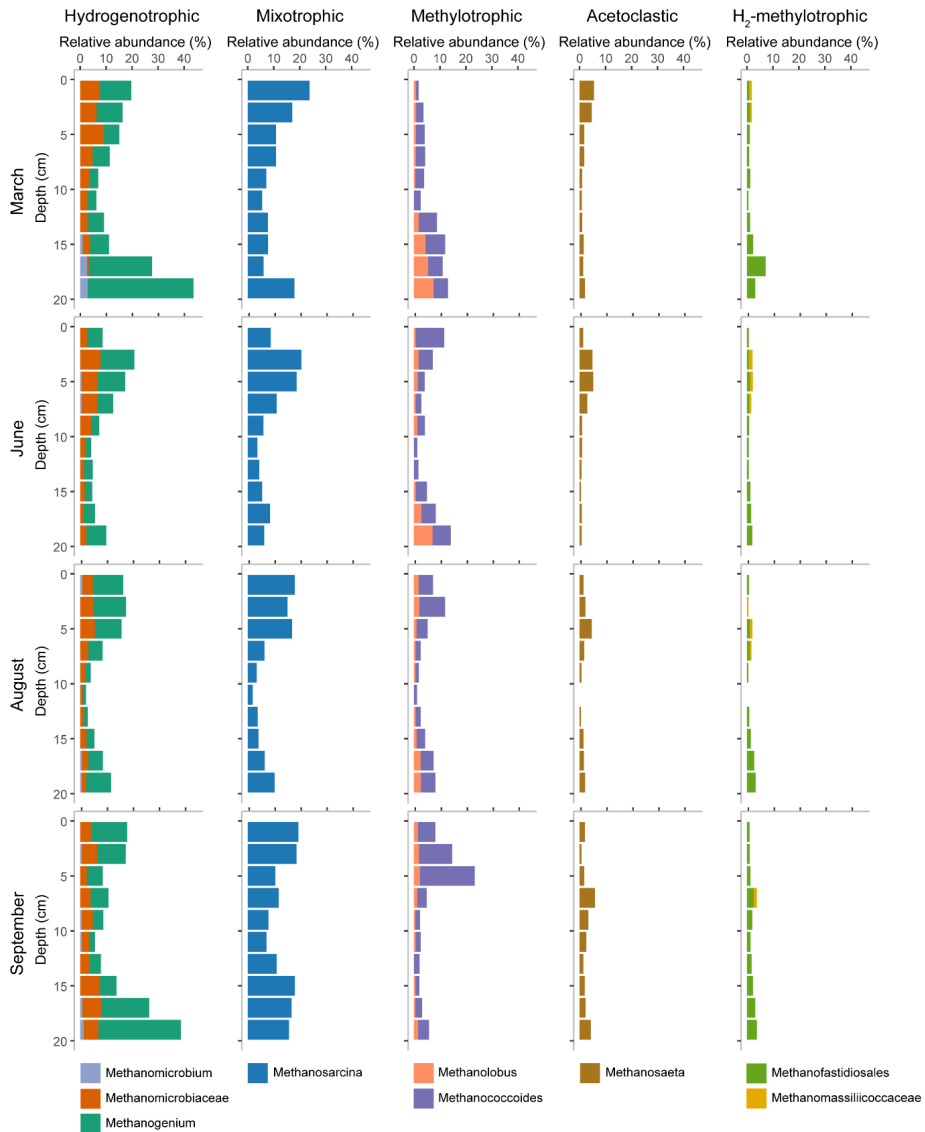


**Fig. S4** The distribution and diversity of methanogenic archaea and methanogenic pathways in the sediment for March, June, August and September 2021. The methanogenic taxa are grouped by their most likely metabolic pathway to produce methane in each month across the sediment profile. The taxa are classified to genus or highest identified level. Only taxa with >2% abundance in at least 2 samples are included.

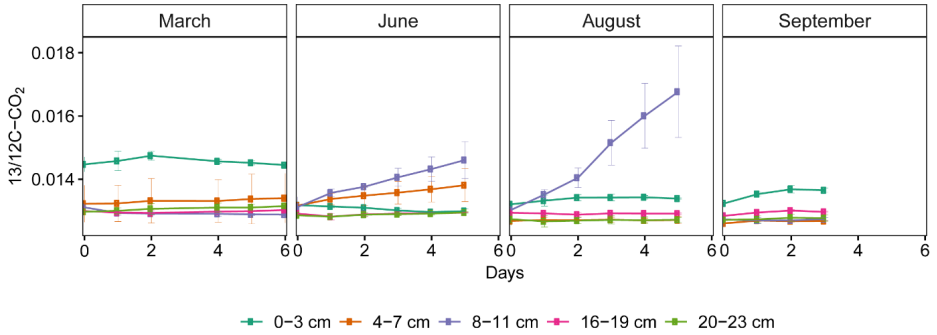


**Fig. S5** AOM activity in incubations of sediment from March, June, August and September 2021. AOM activity was measured by following the  $^{13}/^{12}\text{C}-\text{CO}_2$  ratio in the headspace gas after  $^{13}\text{CH}_4$  addition over a maximum of 6 days. Error bars represent variation in duplicate samples.

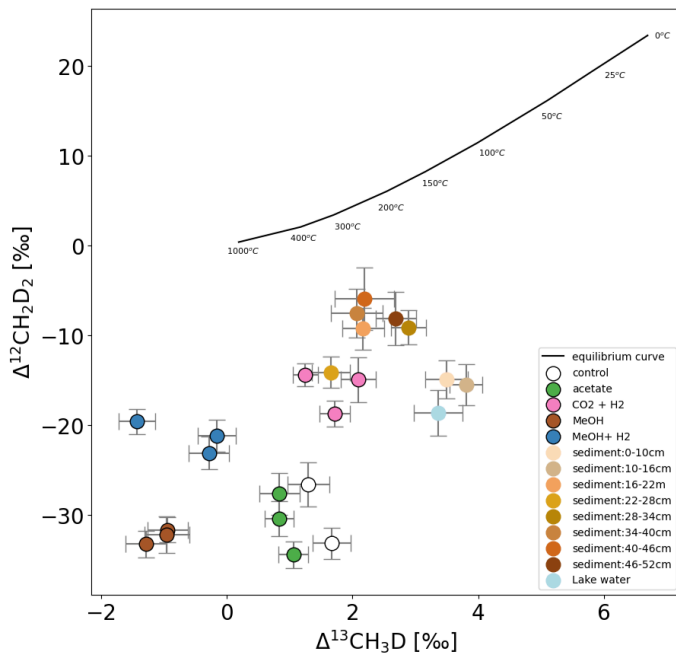


**Fig. S6** Clumped isotopes of  $\text{CH}_4$  from different sediment depths sampled in July and the bottom water sampled in June. As a reference, the clumped isotopic composition of methane from Sivan et al. 2025 (accepted) is used for pathway-specific methanogenesis signatures.

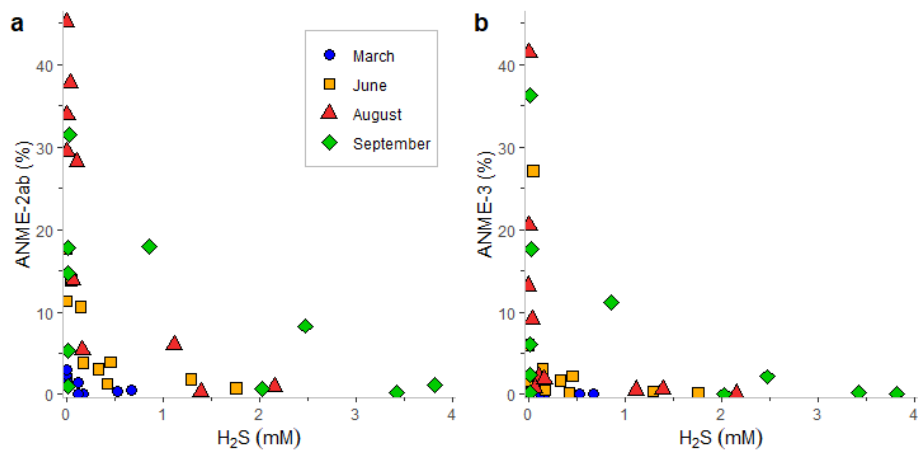


**Fig. S7** Sulfide ( $\text{H}_2\text{S}$ ) concentrations inversely correlate with ANME abundance. ANME-2ab (a) and ANME-3 (b) relative abundances plotted against sulfide concentration in each month.

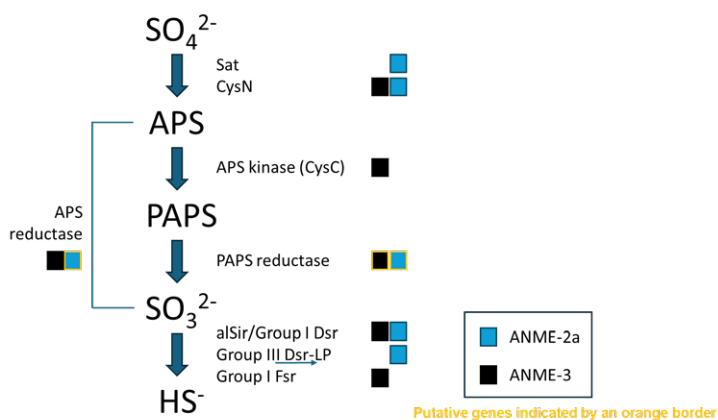


**Fig. S8** Sulfur metabolism potential in ANME-2a and ANME-3 MAGs from Lake Grevelingen sediments.

**Table S1** Methane oxidation rates in nmol  $\text{CH}_4$  per gram of dry sediment per day. Rates are based on duplicate measurements and standard deviation is indicated in brackets.

Depth	March	June	August	September
0-3cm	0	0	0.1	0
4-7cm	0	0	0.1	0
8-11cm	0	2.8	4.3	0
16-19cm	0	0	0.1	0
20-23cm	0	0	0.2	0

**Table S2** Calculated growth rate and doubling time in days and weeks for ANME-2ab and ANME-3 in the oxic sediment layers from March to June, June to August, March to August and August to September in 2021. Negative growth rate reflects lower cell numbers from one period to another and is marked as 'NA' for doubling time as growth is not happening.

Depth (cm)	Month	Interval (days)	ANME-2ab			ANME-3		
			Growth rate (1/day)	Doubling time (days)	Doubling time (weeks)	Growth rate (1/day)	Doubling time (days)	Doubling time (weeks)
3	March-June	0-80	0.008	91.9	13.1	0.014	48.3	6.9
5	March-June	0-80	0.021	33.0	4.7	-0.005	n.a	n.a
7	March-June	0-80	0.021	33.7	4.8	0.013	54.6	7.8
9	March-June	0-80	0.017	40.1	5.7	0.029	23.7	3.4
11	March-June	0-80	0.022	32.2	4.6	0.072	9.6	1.4
13	March-June	0-80	0.050	13.9	2.0	0.060	11.6	1.7
5	June-August	80-147	0.003	217.8	31.1	-0.002	n.a	n.a
7	June-August	80-147	0.003	248.1	35.4	0.011	63.2	9.0
9	June-August	80-147	0.003	266.3	38.0	0.000	1964.4	280.6
11	June-August	80-147	0.010	67.5	9.6	0.005	129.9	18.6
13	June-August	80-147	0.012	58.4	8.3	0.023	30.4	4.3
15	June-August	80-147	0.038	18.2	2.6	0.008	83.9	12.0
3	March-August	0-147	-0.011	n.a	n.a	-0.013	n.a	n.a
5	March-August	0-147	0.013	53.8	7.7	-0.004	n.a	n.a
7	March-August	0-147	0.012	55.6	7.9	0.012	58.2	8.3
9	March-August	0-147	0.011	65.4	9.3	0.016	43.2	6.2
11	March-August	0-147	0.016	42.2	6.0	0.042	16.6	2.4
13	March-August	0-147	0.032	21.4	3.1	0.043	16.2	2.3

Table S2 Continued

Depth (cm)	Month	Interval (days)	ANME-2ab			ANME-3		
			Growth rate (1/day)	Doubling time (days)	Doubling time (weeks)	Growth rate (1/day)	Doubling time (days)	Doubling time (weeks)
15	March-August	0-147	0.032	21.9	3.1	0.021	32.8	4.7
7	August-Sept	147-188	-0.015	n.a	n.a	-0.014	n.a	n.a
9	August-Sept	147-188	0.003	252.7	36.1	0.021	32.7	4.7
11	August-Sept	147-188	-0.009	n.a	n.a	-0.029	n.a	n.a
13	August-Sept	147-188	-0.024	n.a	n.a	0.010	71.2	10.2
15	August-Sept	147-188	-0.048	n.a	n.a	-0.012	n.a	n.a

Table S3 The Spearman correlation and significance (p-value) of ANME-2ab and ANME-3 with the known putative partner SRB. The values are calculated with all samples from the four seasons together.

Bacterial genus or highest classified taxa	ANME-2ab	p-value	ANME-3	p-value
SEEPSRB1	0.927017	0	0.727392	4.72E-07
Sva0081.sediment.group	0.856473	0	0.593058	7.63E-05
Desulfobulbaceae	0.840338	0	0.607129	4.71E-05
Desulfobulbales	0.795872	4.50E-08	0.583677	1.04E-04



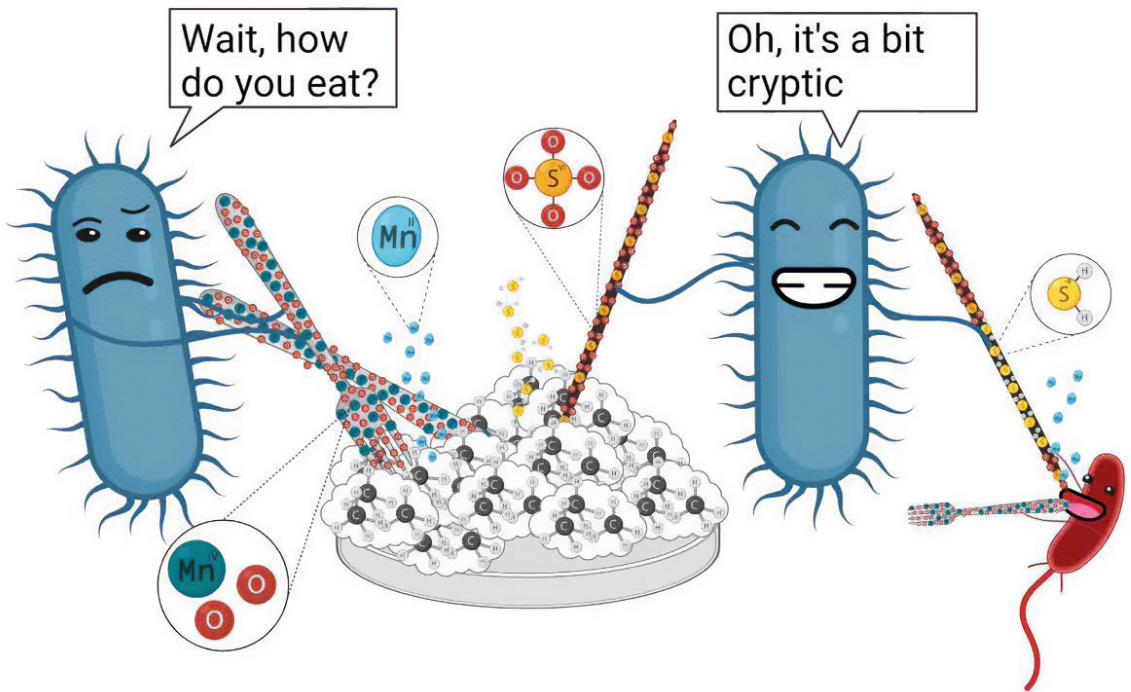


Illustration made by Merijn Schutgens

## Chapter 5

# Potential for manganese oxide driven anaerobic methane oxidation in sediments of a seasonally euxinic coastal basin

---

R. Klomp<sup>1,2\*</sup>, A.J. Wallenius<sup>1\*</sup>, N.A.G.M. van Helmond<sup>1,2</sup>, W.K. Lenstra<sup>1,2</sup>,  
O.M. Żygadłowska<sup>2</sup>, M.S.M. Jetten<sup>1</sup>, C.P. Slomp<sup>1,2</sup>

\*These authors contributed equally to this work

<sup>1</sup>Department of Microbiology, Radboud Institute for Biological and Environmental Sciences, Radboud University, Heyendaalseweg 135, 6525AJ Nijmegen, the Netherlands

<sup>2</sup>Department of Earth Sciences, Utrecht University, Princetonlaan 8a, 3584 CB Utrecht, the Netherlands

## Abstract

Methane (CH<sub>4</sub>) is a strong greenhouse gas that, in marine sediments, is produced via methanogenesis and removed via oxidation with electron acceptors such as oxygen, sulfate and metal oxides. In this study, we explore the potential for manganese driven anaerobic oxidation of methane (Mn-AOM) in rapidly accumulating sediments in a seasonally euxinic coastal marine basin (Scharendijke basin, Lake Grevelingen, the Netherlands). Using geochemical sediment and porewater profiles, we show that, at our study site, Mn oxides are buried in the methanic zone. Sediment incubations amended with <sup>13</sup>C-CH<sub>4</sub> and various Mn forms indicate that the Mn oxide minerals birnessite, pyrolusite and manganite can enhance CH<sub>4</sub> oxidation, whereas ligand bound dissolved Mn(III) does not. We attribute this to either direct Mn-AOM, where Mn oxides act as the electron acceptor, and/or indirect Mn-driven AOM via cryptic sulfur cycling. Results of 16S rRNA gene amplicon sequencing of the incubated sediment point towards a likely role for anaerobic methanotrophic archaea of the clades ANME-2ab and ANME-3 in direct and indirect Mn-driven AOM, respectively. An increase in relative abundance of the methanogen *Methanosarcina* in several of the incubations suggests that these versatile methanogens benefit from Mn oxide reduction. This study demonstrates potential for Mn-driven AOM in sediments from a eutrophic, seasonally euxinic coastal basin, and expands the range of electron acceptors involved in CH<sub>4</sub> removal in such systems.

## Keywords

Manganese oxide, Methane oxidation, ANME, *Methanosarcina*, seasonally euxinic basin

## Introduction

Methane (CH<sub>4</sub>) is a greenhouse gas with a concentration in the atmosphere that has more than doubled since the start of the Industrial Revolution (Saunio et al., 2020). In anoxic marine sediments, methanogens produce CH<sub>4</sub> via methanogenesis as the final step in organic matter degradation (Froelich et al., 1979). Although coastal regions only cover a small part of the marine environment, their CH<sub>4</sub> emissions may contribute up to 75% of the total marine CH<sub>4</sub> flux (Hamdan & Wickland, 2016). Typically, a major proportion of the produced CH<sub>4</sub> is removed in the sediment via anaerobic oxidation of CH<sub>4</sub> (AOM) coupled to SO<sub>4</sub><sup>2-</sup> reduction by a consortium of anaerobic methane-oxidizing archaea (ANME) and sulfate-reducing bacteria (SRB; Knittel & Boetius, 2009). Other electron acceptors, such as nitrate/nitrite (N-AOM; Raghoebarsing et al., 2006), iron (Fe) and manganese (Mn) oxides (Fe-AOM, Mn-AOM; Beal et al., 2009; Egger et al., 2015; Cai et al., 2018; Leu et al., 2020), have also been linked to AOM. Although Fe oxides are typically more abundant than Mn oxides in marine sediments, the Mn oxide birnessite is thermodynamically a more favorable electron acceptor for AOM, as shown with gene-based and bioenergetic modelling (Lenstra et al., 2023; Wallheimer et al. 2025).

Typically, Mn oxides are enriched in oxic surface sediments. Reductive dissolution upon burial generally leads to loss of the Mn oxides through biotic and abiotic processes, producing dissolved Mn (Burdige, 1993), either as dissolved Mn(II) (dMn(II)) or, when stabilized by organic ligands, dissolved Mn(III) bound to ligands (dMn(III)-L; Madison et al., 2011). Upward diffusion into oxygenated sediment layers can result in re-oxidation of the dissolved Mn and precipitation as Mn oxides (Adelson et al., 2001; Slomp et al., 2013). Burial of Mn oxide minerals into the methanic zone is promoted by non-steady state conditions such as variations in Mn oxide input, high sedimentation rates or bioturbation (März et al., 2008; Riedinger et al., 2014; Lenstra et al., 2023). Both dMn(II) and dMn(III)-L can be present in the methanic zone, as products of Mn oxide reduction, or via downward diffusion (Klomp et al., 2025). In the methanic zone, the dMn(III)-L could act as an electron acceptor for AOM.

In freshwater systems, Mn-AOM is commonly associated with *Candidatus Methanoperedens* (ANME-2d; Ettwig et al., 2016; Leu et al., 2020; Su et al., 2020). In a bioreactor inoculated with freshwater sediment and enriched in *Ca*. *Methanoperedens*, for example, CH<sub>4</sub> oxidation was directly coupled to Mn oxide reduction, presumably via extracellular electron transport involving multiheme *c*-type cytochromes (Leu et al., 2020). An indirect role for Mn in AOM was observed when Mn oxides chemically oxidized reduced sulfur (S) species, such as iron sulfide (FeS<sub>x</sub>) and organically bound S,

forming  $\text{SO}_4^{2-}$  in a cryptic S cycle that fueled AOM (Su et al., 2020). Besides solid phase Mn oxides, dMn(III)-L was also tested for AOM in freshwater sediments, however AOM was not detected (Szeinbaum et al., 2020). Mn-AOM has also been proposed to occur in marine sediments (Beal et al., 2009), but the main microbial players and pathways remain enigmatic (Wallenius et al., 2021; Xue et al., 2025). Fe-AOM in brackish and marine sediments has been linked to the ANME clades ANME-2ab (family *Methanocomedenaceae*), and potentially involves a bacterial metal-reducing partner (Aromokeye et al., 2020; Rasigraf et al., 2020). ANME-2ab are also hypothesized to be involved in Mn-AOM in marine sediments (Xu et al., 2021).

In the laboratory experiments to date assessing the use of solid phase Mn as an electron acceptor for AOM, only the Mn(IV) oxides birnessite ( $\text{MnO}_2 \cdot n \text{H}_2\text{O}$ ) and vernadite ( $\text{MnO}_2 \cdot n \text{H}_2\text{O}$ ) were tested (e.g. Beal et al., 2009; Ettwig et al., 2014; Su et al., 2020; Xu et al., 2021). In the natural environment, Mn oxides may also be present in more crystalline form, e.g. as manganite ( $\text{Mn(III)OOH}$ ) or pyrolusite ( $\text{Mn(IV)O}_2$ ); e.g. Burdige et al., 1992; Sulu-Gambari et al., 2016; Luo et al., 2018). Since the crystallinity and redox state of Mn oxide minerals will affect their reactivity and bioavailability (Burdige et al., 1992), variations in rates of  $\text{CH}_4$  oxidation by different Mn oxide minerals are expected.

In this study, we examine the role of different forms of Mn, namely the Mn oxides birnessite, pyrolusite, manganite and of dMn(III)-L in AOM. We focus on rapidly accumulated sediments in a seasonally euxinic marine coastal basin (Scharendijke basin, Lake Grevelingen, the Netherlands), where Mn oxides are buried in the methanic zone of the sediment and dMn(III)-L is present in the porewater (Żygadłowska et al., 2023; Klomp et al., 2025). We combine geochemical sediment and porewater profiles with results of sediment incubations using isotopically labelled  $\text{CH}_4$  and the various Mn oxides and dMn(III)-L. The microbial community in the incubations was analyzed using 16S rRNA gene amplicon sequencing. We find strong indications for AOM directly coupled to Mn reduction by ANME-2ab and for S-AOM by ANME-3 via a cryptic S cycle driven by bacterial Mn reduction.

## Materials and methods

### Study area

Lake Grevelingen is a coastal marine lake in the southwest of the Netherlands. The lake is a former estuary of the river Rhine that was dammed at the landward side in 1964 and at the seaward side in 1971. The lake has an average water depth of

around 5 m, but is intersected by former tidal channels with deep basins that can reach depths of up to 45 m (Hagens et al., 2015; Egger et al., 2016). Exchange with water from the North Sea is enabled by sluices in the dam at the seaward side, giving the lake a salinity of 29 – 33. The lake is highly eutrophic (Hagens et al., 2015).

This study focuses on sediments in the deepest part of the lake, the Scharendijke basin (51.742°N, 3.849°E). Here, temperature-driven stratification leads to seasonally euxinic conditions between May and September, recorded in the sediment by distinct enrichments of the redox-sensitive trace metal molybdenum (Mo; Egger et al., 2016; Żygadłowska et al., 2024a). The sedimentary Mo profiles can also be used to determine the rate of sediment accumulation, which is exceptionally high and varied between 13 - 20 cm yr<sup>-1</sup> over the last decade (Egger et al., 2016; van Helmond et al., 2025). The geometry of Scharendijke basin, i.e. relatively narrow and deep, leads to lateral transport of material from shallower areas of the lake, which supplements vertical settling of suspended matter, explaining the high sediment accumulation rates (Klomp et al., 2025). High input of organic matter leads to high rates of SO<sub>4</sub><sup>2-</sup> reduction. Furthermore, high rates of methanogenesis lead to strong benthic release of CH<sub>4</sub> via diffusion and ebullition (Żygadłowska et al., 2024b; Klomp et al., 2025). In winter, when the bottom water is oxygenated, the deposition of Fe and Mn oxides prevents the accumulation of sulfide (H<sub>2</sub>S) in the upper 10 cm of the sediment (Klomp et al., 2025). Through summer, due to the high sedimentation rates, the manganese oxides are buried into the methanic zone of the sediment. Besides solid phase Mn oxides, dMn(III)-L is also abundantly present in the methanic zone (Klomp et al., 2025).

### Sample collection

Sediment sampling in the Scharendijke basin was performed on board the RV *Navicula* in October 2021. Three sediment cores were collected using a UWITEC corer and PVC core liners (120 cm length, 6 cm inner diameter). One core was sectioned at a 1 cm resolution in a glove bag under a N<sub>2</sub> atmosphere. The sediment was transferred into 50 ml centrifuge tubes and centrifuged at 4500 rpm for 20 minutes to separate the porewater from the solid phase. The supernatant was filtered over 0.45 µm pore size filters under a N<sub>2</sub> atmosphere in a glove bag and subsampled for the analysis of SO<sub>4</sub><sup>2-</sup>, total dissolved Mn and Fe and H<sub>2</sub>S. The samples for SO<sub>4</sub><sup>2-</sup> were stored at 4°C. Samples for the analysis of total dissolved Mn and Fe were acidified with 10 µL 30% suprapur HCl per ml of sample and stored at 4°C whereas samples for H<sub>2</sub>S analysis were diluted five times in a 2% Zn-acetate solution in a glass vial and stored at 4°C. The residual sediment was stored in N<sub>2</sub> purged aluminum bags at -20°C until further processing for C<sub>org</sub>, total sulfur (S) and Mo, Mn and Fe oxides and FeS analysis.

A second core was used to sample for porewater  $\text{CH}_4$  determination. Through tape-covered pre-drilled holes at a 2.5 cm interval, 10 ml of sediment was transferred with plastic cutoff syringes into a 65 ml glass bottle filled with a saturated NaCl solution. The bottles were then stoppered, capped and stored upside down until analysis. Note that degassing of  $\text{CH}_4$  occurred during the sampling, which results in a strong underestimation of the  $\text{CH}_4$  concentrations (Egger et al., 2016; Jørgensen et al., 2019).

The third core was sectioned at a 5 cm resolution in a  $\text{N}_2$  filled glove bag to collect material for sediment incubations. The sediment was transferred into plastic bags and stored in  $\text{N}_2$  purged sealed aluminum bags at 4°C until the start of the experiments.

### Chemical analyses of sediment and porewater

Concentrations of  $\text{SO}_4^{2-}$  were determined via ion chromatography (Metrohm 930 Compact IC Flex; detection limit for  $\text{SO}_4^{2-}$  of 50  $\mu\text{mol L}^{-1}$ ). Total dissolved Mn and Fe were determined by Inductively Coupled Plasma Optical Emission Spectroscopy (ICP-OES, Perkin Elmer Avio; detection limit 0.1  $\mu\text{mol L}^{-1}$  and 0.03  $\mu\text{mol L}^{-1}$  for Fe and Mn, respectively). Concentrations of  $\text{H}_2\text{S}$  were measured spectrophotometrically using an acidified solution of phenylenediamine and ferric chloride, where  $\text{H}_2\text{S}$  is the sum of  $\text{S}^{2-}$ ,  $\text{HS}^-$  and  $\text{H}_2\text{S}$  (detection limit of 1  $\mu\text{mol L}^{-1}$ ; Cline, 1969).

The sediment was freeze-dried and ground with an agate mortar and pestle under a  $\text{N}_2$  atmosphere and subsequently split in oxic and anoxic aliquots for further analysis. The  $\text{C}_{\text{org}}$  content was determined on approximately 0.3 g of the oxic split that was decalcified with 1 M HCl (Van Santvoort et al., 2002), dried, weighed and powdered. Consecutively, the decalcified sample was analyzed on an elemental analyzer (Fisons Instruments model NA 1500 NCS) and the C content was corrected for the weight loss during decalcification. Accuracy and precision of this method was determined based on measurements of the internationally certified soil standard IVA2. The certified value for IVA2 is 0.732 wt.% C. The mean value that was obtained in this study for IVA2 ( $n=15$ ) was 0.739 wt.% C, with a standard deviation of 0.005 wt.% C. The analytical uncertainty based on duplicates ( $n=8$ ) for  $\text{C}_{\text{org}}$  was 0.05 wt.%. The total elemental composition of the sediment was determined after digestion of approximately 0.1 g of the oxic split in 2.5 ml mixed acid ( $\text{HNO}_3$ :  $\text{HClO}_4$ : 2:3) and 2.5 ml 40% HF at 90°C. After evaporation of the acid mixture, the residue was redissolved in 1 M  $\text{HNO}_3$  and the total elemental composition was determined via analysis on the ICP-OES for the total S content and via Inductively Coupled Plasma Mass Spectrometry (ICP-MS, Perkin Elmer NexION 2000) for the total Mo content of the sediment. The average analytical uncertainty based on duplicates ( $n = 8$ ) was 106 ppm for S and 114 ppb for Mo and the average recovery

rate was 103% for S and 97% for Mo. All elemental concentrations were corrected for the salt content of the freeze-dried sediment.

Two aliquots of the anoxic split (ca. 0.1 g) were subjected to a sequential extraction to determine the speciation of Mn and Fe. One of the aliquots was digested in a 1M HCl solution for 4 hours to extract easily reducible Fe(III) and Fe(II) minerals as described in Kraal et al. (2017). The concentrations of Fe(III) and Fe(II) were determined spectrophotometrically via the phenantroline method (APHA, 2005). The average analytical uncertainty based on duplicates (n = 5) was 0.14  $\mu\text{mol g}^{-1}$ . Speciation of Mn and further speciation of Fe was determined following the 5 step sequential extraction as described by Lenstra et al. (2021b). The steps were as follows: (1) 0.057 M ascorbic acid, 0.17 M sodium citrate and 0.6 M sodium bicarbonate (pH 7.5) which extracts poorly ordered Mn oxides and Mn associated with vivianite, (2) 1 M HCl which extracts Mn carbonates (3) 0.35 M acetic acid, 0.2 M Na citrate and 50 g L<sup>-1</sup> Na dithionite, pH 4.8, which extracts crystalline Fe and Mn oxides and Mn bound to clays (4) 0.2 M ammonium oxalate and 0.17 M oxalic acid which extracts recalcitrant Fe oxides, crystalline Mn oxides and Mn bound to clays (5) 65 % HNO<sub>3</sub> which extracts pyrite, including any associated Mn. The analytical uncertainty based on duplicates (n = 9) for all fractions was 5.69 and 0.25  $\mu\text{mol g}^{-1}$  for Fe and Mn, respectively.

Approximately 0.3 g of the anoxic splits was used to determine the FeS content, via the passive diffusion method as described by Burton et al. (2008). The FeS was extracted from the sediment via a 24h digestion in 6M HCl in a 50 ml polypropylene centrifuge tube. Released H<sub>2</sub>S was trapped in an alkaline zinc-acetate solution as zinc sulfide precipitates. Iodometric titration of the zinc-acetate solution was used to quantify the released sulfide (Burton et al., 2008). The analytical uncertainty based on duplicates (n = 4) was 2.56  $\mu\text{mol g}^{-1}$ .

### **Sediment incubations**

The potential for Mn-AOM was tested via incubations with sediment from the top layer of the sediment (0 - 5 cm) and from a sediment interval expected to contain Mn oxides below the SMTZ (15 - 20 cm; Klomp et al., 2025). Incubations were started within 3 months after sampling. The sediment was amended with various types of Mn oxides, namely birnessite, pyrolusite and manganite, and with dMn(III)-L, where the ligand was either strong or weak (Table 1). Furthermore, isotopically labelled <sup>13</sup>C-CH<sub>4</sub> was added to the incubations. Various chemical and microbial analysis described below were used to monitor CH<sub>4</sub> oxidation and key microbes in the incubations.

### **Preparation of the substrates**

Birnessite was synthesized by reducing  $\text{KMnO}_4$  with  $\text{C}_3\text{H}_5\text{NaO}_3$  at ambient temperature and pressure according to the protocol by Händel et al. (2013). Pyrolusite and manganite were obtained from the inhouse collection of Utrecht University; the original sources for pyrolusite and manganite were Alfa Aesar and Ward, respectively (Lenstra et al., 2021b). The mineralogy was verified using X-ray diffraction (Fig. S1). The crystallinity of Mn oxide minerals can affect their reactivity (Burdige et al., 1992). To compensate for the potential lower reactivity of crystalline pyrolusite and manganite compared to birnessite, higher concentrations of these minerals were added to the incubations (Table 1). Dissolved Mn(III)-L was prepared with a weak binding ligand, pyrophosphate, and a strong binding ligand, desferrioxamine B (DFOB), as described in Oldham et al. (2015). Isotopically labelled  $^{13}\text{C}$ - $\text{CH}_4$  was obtained from Cambridge Isotope Laboratories, Inc. (Andover, USA).

**Table 1** Overview of the different treatments performed in the incubation experiment.

<b>Treatment</b>	<b><math>^{13}\text{CH}_4</math> added</b>	<b>Amount of electron acceptor added</b>
Control, no substrate	-	-
$\text{CH}_4$ oxidation control	20% headspace	-
Birnessite; $\text{Mn(IV)O}_2 \cdot n \text{H}_2\text{O}$	20% headspace	10 $\text{mmol L}^{-1}$
Pyrolusite; $\text{Mn(IV)O}_2$	20% headspace	100 $\text{mmol L}^{-1}$
Manganite; $\text{Mn(III)OOH}$	20% headspace	100 $\text{mmol L}^{-1}$
dMn(III)-L strong ligand	20% headspace	1 $\text{mmol L}^{-1}$
dMn(III)-L weak ligand	20% headspace	1 $\text{mmol L}^{-1}$

### **Start of the incubations**

The bottles were pre-incubated for one week with the electron acceptor as indicated in Table 1, but without labelled  $\text{CH}_4$ , to remove as much FeS from the sediment as possible and prevent the formation of  $\text{SO}_4^{2-}$  via oxidation of FeS by Mn oxides in the subsequent incubations with labelled  $\text{CH}_4$ . The sediment was diluted in a 1:4 ratio with artificial HEPES buffered,  $\text{SO}_4^{2-}$ -free seawater (ASW; for composition, see Table S1) under a 98%  $\text{N}_2$  + 2%  $\text{H}_2$  atmosphere, and carefully homogenized. This mixture was equally distributed over sterile 120 ml serum bottles, so that each bottle contained 60 g of the mixture. The electron acceptors were added to the bottles (Table 1) and the bottles were stoppered and capped. The headspace was replaced with a 100%  $\text{N}_2$  environment and the bottles were placed on a shaking table (90 rpm) at room temperature for one week.

After the pre-incubation, the ASW was replaced with freshly prepared ASW and new electron acceptors were added to each bottle under a 98%  $\text{N}_2$  + 2%  $\text{H}_2$  atmosphere.

The headspace of the bottles was replaced with a headspace of 76% N<sub>2</sub>, 4% CO<sub>2</sub> and 20% <sup>13</sup>C-labelled CH<sub>4</sub> and the incubations were placed on a shaking table (90 rpm) at room temperature for 92 days.

### ***Sampling and analyses of the incubations***

From the start of the incubations, the ratio of <sup>13</sup>C-CO<sub>2</sub>/<sup>12</sup>C-CO<sub>2</sub> was determined weekly with a GC-MS (5975C inert MSD, Agilent, Santa Clara, CA, USA). When CO<sub>2</sub> concentrations are very low, the <sup>13</sup>C-CO<sub>2</sub>/<sup>12</sup>C-CO<sub>2</sub> ratio measured by the GC-MS decreases, because the <sup>13</sup>C-CO<sub>2</sub> reaches the detection limits faster than <sup>12</sup>C-CO<sub>2</sub> (Fig. S2). Upon the addition of Mn oxides, CO<sub>2</sub> was drawn from the headspace (Fig. S2), possibly linked to an increase in pH in the liquid due to high Mn oxide reduction rates (Silburn et al., 2017). The increase in pH upon Mn reduction is expected to be limited, however, due to the HEPES buffer in the medium. The drawdown of CO<sub>2</sub> from the headspace was highest in the incubations amended with pyrolusite and manganite, since extra Mn oxides were added to compensate for the expected lower reactivity of these minerals (Burdige et al., 1992). To compensate for the loss of CO<sub>2</sub> from the headspace, new CO<sub>2</sub> was injected into the headspace of all bottles amended with Mn oxide minerals after 52 days.

Every two weeks, the supernatant was sampled to analyze concentrations of SO<sub>4</sub><sup>2-</sup>, H<sub>2</sub>S and total dissolved Mn. Concentrations of SO<sub>4</sub><sup>2-</sup>, H<sub>2</sub>S and total dissolved Mn were analyzed as described above. During the setup of the pre-incubations and at the end of the incubations, sediment was sampled for DNA isolation. The samples for DNA isolation were stored frozen (-20°C) until analysis via 16S rRNA amplicon sequencing.

DNA was isolated from approximately 0.2 g of defrosted sediment with DNeasy PowerSoil DNA isolation kit (Qiagen, Venlo, Netherlands) after bead-beating for 10 minutes at 50 Hz on a TissueLyser LT (Qiagen, Venlo, Netherlands). DNA quantity and quality in the eluted sterile MilliQ were measured by NanoDrop 1000 (Thermo Fischer Scientific, Bremen, Germany) and by Qubit<sup>®</sup> 2.0 (Invitrogen, Waltham, MA, USA). The DNA was stored frozen at -20°C until further analysis.

Amplification of 16S rRNA genes was performed on samples from the incubations from the 15 – 20 cm depth, using primers Arch349F (5'-GYGCASCAGKCGMGAAW-3') and Arch806R (5'-GGACTACVSGGGTATCTAAT-3'; (Takai & Horikoshi, 2000) and Bac341F (5'CCTACGGNGGCWGCAG-3'; Herlemann et al., 2011) and Bac806R (5'GGACTACHVGGGTWTCTAAT-3'; Caporaso et al., 2012). The amplicon sequencing was performed on the Illumina MiSeq Next Generation Sequencing platform by

Macrogen (Seoul, South Korea) using Herculase II Fusion DNA Polymerase Nextera XT Index Kit V2, yielding 2x300bp paired-end reads. FastQC (v0.11.5; Andrews, 2010) was used to check the quality of the raw reads. Cutadapt (v1.158; Martin, 2011) was used to trim the paired-end reads to remove adapters. The DADA2 pipeline (v1.8; Callahan et al., 2016) was used in RStudio to cluster the reads into amplicon sequence variants (ASVs), remove chimera and determine the taxonomic classification using SILVA 16S rRNA database (v138.1; Quast et al., 2013). The package phyloseq (v1.36.0; McMurdie & Holmes, 2013) was used for microbial community data analysis. A differential analysis was performed with package DESeq2 (v.1.44.0; Love et al., 2014) to analyze the changes in microbial communities between the different incubations. The raw sequencing data can be accessed in the NCBI database under Bioproject number PRJNA1268434.

## Results

### Sediment and porewater chemistry

At the time of sampling in October 2021, two sediment intervals were enriched in Mo and  $C_{org}$ . These were the top 7 cm of the sediment and the layer between 19 and 25 cm depth, which was characterized by maximum Mo and  $C_{org}$  contents of 38 ppm and 3.4 wt%, respectively (Fig. 1a, b). Mn oxide contents varied between 1 and 5  $\mu\text{mol g}^{-1}$ , with a maximum content at 8 cm depth (Fig. 1c). Fe oxide content varied between 0 and 4  $\mu\text{mol g}^{-1}$ , with the highest content at 10 cm depth (Fig. 1d). Total S concentrations varied from 200 to 380  $\mu\text{mol g}^{-1}$ , with the lowest concentrations between 7 and 10 cm depth and the highest content near the sediment-water interface (Fig. 1e). FeS followed a similar trend with depth as total S and varied between 35 and 90  $\mu\text{mol g}^{-1}$ . Pyrite ( $\text{FeS}_2$ ) contents were below 4  $\mu\text{mol g}^{-1}$ . The sediment was depleted in  $\text{SO}_4^{2-}$  below 10 cm depth and  $\text{CH}_4$  was present throughout the sediment (Fig. 1f, g). Concentrations of dMn varied around 80  $\mu\text{mol L}^{-1}$ , with maxima near the sediment water interface and around 10 cm depth (Fig. 1h). Dissolved Fe was absent from the porewater and  $\text{H}_2\text{S}$  was present in the top 17 cm and reached a maximum concentration of 3.5  $\text{mmol L}^{-1}$  (Fig. 1i, j).

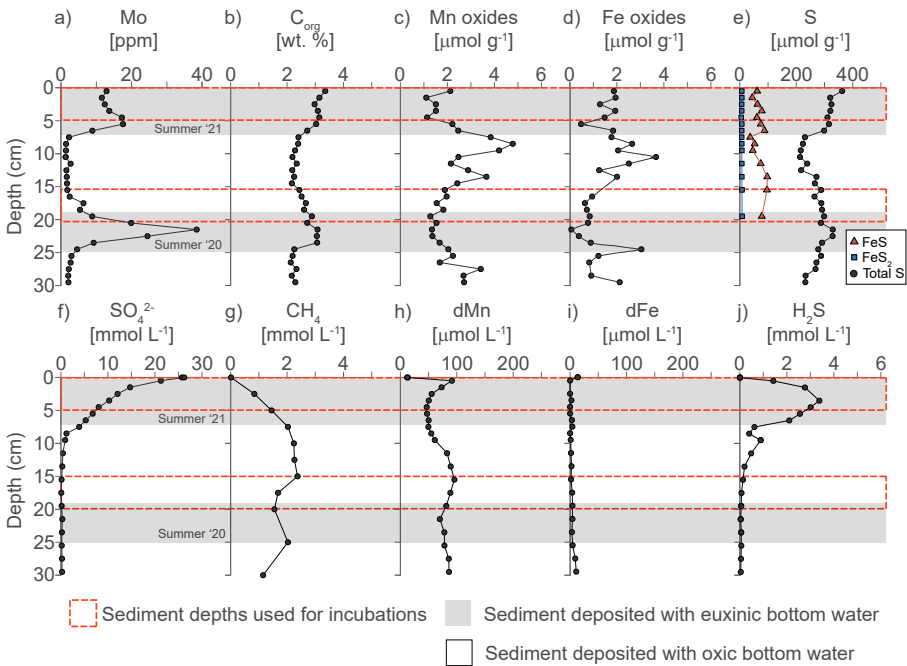


**Fig. 1** Sediment profiles of Mo,  $C_{org}$ , Mn oxides, Fe oxides, total S, FeS and FeS<sub>2</sub> and pore water profiles of  $\text{SO}_4^{2-}$ ,  $\text{CH}_4$ , dMn, dFe and  $\text{H}_2\text{S}$  in October 2021. The depth intervals surrounded by a red box indicate the depths that were used for the incubations. The gray shading represents the sediment that was deposited during bottom water euxinia and the white areas represent the sediment that was deposited during oxic bottom water conditions.

### Sediment Incubations

Based on sediment geochemistry, two sediment depths (i.e. 0 – 5 cm and 15 – 20 cm; Fig. 1) were chosen to study Mn-AOM. In the incubations with sediment from 0 – 5 cm depth, all bottles amended with Mn oxides showed a signal for  $\text{CH}_4$  oxidation (Fig. 2a-c), observed as an increase in the  $^{13}\text{C-CO}_2/^{12}\text{C-CO}_2$  ratio relative to the control after 22 - 29 days (with maximum values of 0.019, 0.028 and 0.027 for birnessite, pyrolusite and manganite, respectively, compared to 0.013 in the control). Soon after the increase, the  $\text{CO}_2$  isotope ratio decreased to the same values as the background ratio in all incubations. In the incubations with sediment from 15 – 20 cm depth, addition of birnessite led to an immediate increase in the ratio of  $^{13}\text{C-CO}_2/^{12}\text{C-CO}_2$ , reaching a value of 0.056, compared to 0.015 in the control, before leveling off after 36 days of incubation (Fig. 2d). The ratio increased again in this incubation only after the addition of both new Mn oxide and new  $\text{CO}_2$ . In the incubations where pyrolusite and manganite were added, the  $^{13}\text{C-CO}_2/^{12}\text{C-CO}_2$  ratio also increased compared to the control (Fig. 2e, f). However, the increase was much

smaller compared to the increase with birnessite (0.019 and 0.018 for pyrolusite and manganite, respectively, relative to 0.015 in the control incubation) and ratios decreased to below that in the control after a few weeks.

Concentrations of dMn increased to 3 – 4 mmol L<sup>-1</sup> in all bottles where Mn oxides were added (Fig. 2a-f). In the incubations with sediment from 0 – 5 cm, dMn increased after 22 – 29 days. In the incubations with sediment from 15 – 20 cm depth, dMn increased from the start of the experiment. Accumulation of SO<sub>4</sub><sup>2-</sup> occurred in the incubations with sediment from 0 – 5 cm depth where birnessite and pyrolusite were added, reaching concentrations around 1 and 4 mmol L<sup>-1</sup> with birnessite and pyrolusite, respectively (Fig. 3a-c). In the incubation with manganite, a SO<sub>4</sub><sup>2-</sup> concentration of only 0.2 mmol L<sup>-1</sup> was observed. In the incubations with sediment from 15 – 20 cm depth, the SO<sub>4</sub><sup>2-</sup> concentration reached 2 mmol L<sup>-1</sup> and 6 mmol L<sup>-1</sup> in the incubations with birnessite and pyrolusite, respectively, but no SO<sub>4</sub><sup>2-</sup> was detected in the incubation with manganite (Fig. 2d-f). The only incubation where H<sub>2</sub>S accumulated (up to 500 μmol L<sup>-1</sup>) was the incubation with birnessite for sediments from the 0 – 5 cm depth layer, (Fig. 3a).

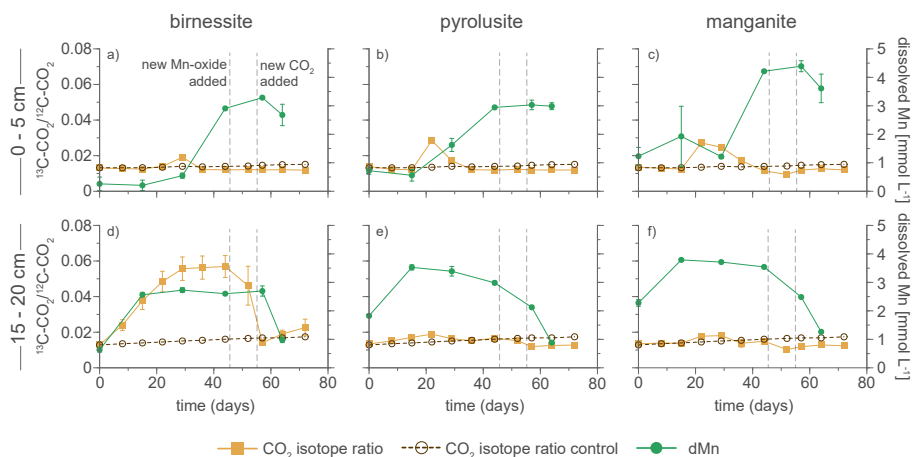


**Fig. 2** Headspace <sup>13</sup>CO<sub>2</sub>/<sup>12</sup>CO<sub>2</sub> ratios and dissolved Mn concentrations for the incubations with sediment from (a - c) 0 – 5 cm depth and (d - f) 15 – 20 cm depth amended with birnessite (a, d) pyrolusite (b, e) and manganite (c, f). The dashed lines indicate timepoints when new Mn oxides and new CO<sub>2</sub> were added to the incubations.

Addition of dMn(III)-L did not lead to an increase in the <sup>13</sup>C-CO<sub>2</sub>/<sup>12</sup>C-CO<sub>2</sub> ratio relative to the <sup>13</sup>C-CO<sub>2</sub>/<sup>12</sup>C-CO<sub>2</sub> ratio in the background control (Fig. 4). Concentrations of dMn in the experiment with sediment from 0 – 5 cm depth first increased and then decreased during the experiment, to a minimum of 0.1 mmol L<sup>-1</sup> (Fig. 4a, b). In the

incubations with sediment from 15 – 20 cm depth, dMn concentrations were stable, around 0.6 mmol L<sup>-1</sup> in the incubation with strong ligands (around 1.8 mmol L<sup>-1</sup> after the addition of new dMn(III)-L solution) and around 0.1 mmol L<sup>-1</sup> in the incubation with weak ligands (Fig. 4c, d). No SO<sub>4</sub><sup>2-</sup> accumulated in the bottles and the concentration of H<sub>2</sub>S was around 500 μmol L<sup>-1</sup> in the incubations with sediment from 0 – 5 cm depth and generally < 50 μmol L<sup>-1</sup> in the bottles with sediment from 15 – 20 cm (Fig. S3).

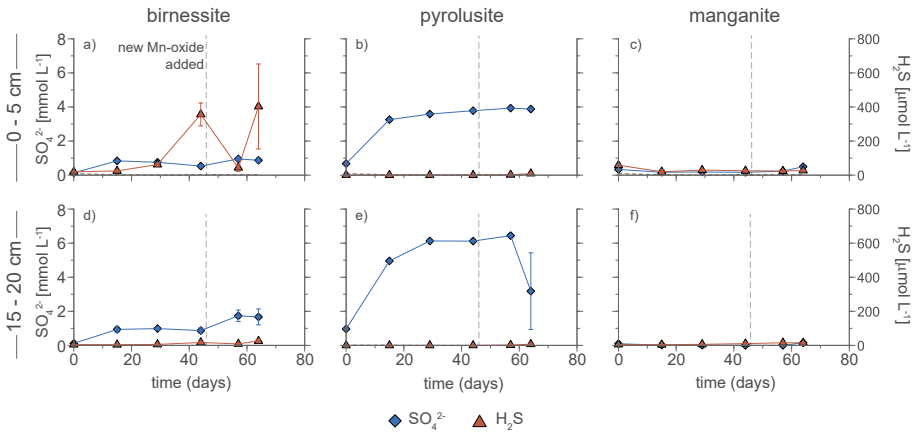


**Fig. 3** SO<sub>4</sub><sup>2-</sup> and H<sub>2</sub>S concentrations for the incubations with sediment from (a - c) 0 – 5 cm depth and (d - f) 15 – 20 cm depth spiked with (a, d) birnessite, (b, e) pyrolusite and (c, f) manganite over time. The dashed line represents the time point when new Mn oxide minerals were added to all incubation bottles.

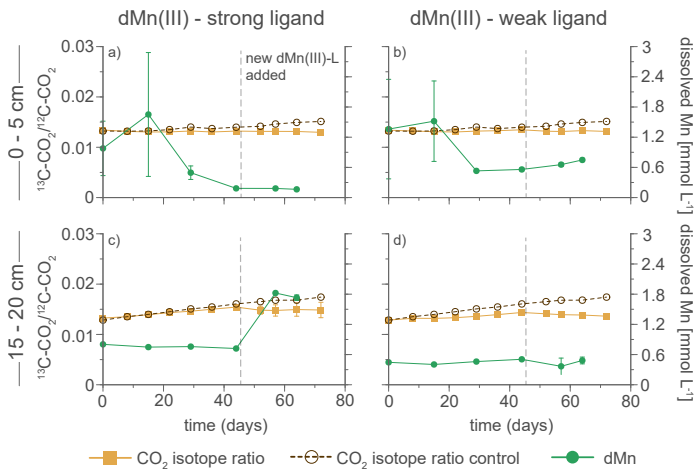


**Fig. 4** Headspace <sup>13</sup>C<sub>2</sub>/<sup>12</sup>C<sub>2</sub> ratios and dissolved Mn concentrations for the incubations with sediment from (a, b) 0 – 5 cm depth and (c, d) 15 – 20 cm depth spiked with (a, c) dMn(III)-L bound to a strong ligand and (b, d) dMn(III)-L bound to a weak ligand over time. The dashed lines indicate timepoints when new dMn(III)-L was added to the incubations.

## Diversity of ANME and SRB in the incubations

To determine which microorganisms were involved in Mn-AOM, the samples from incubations with sediment from 15-20 cm depth were analyzed with 16S rRNA gene amplicon sequencing (Fig. 5; Fig. S4) as this depth showed the most pronounced signal of CH<sub>4</sub> oxidation in the <sup>13</sup>C-CO<sub>2</sub>/<sup>12</sup>C-CO<sub>2</sub> ratio in the incubations with birnessite (Fig. 2d). At the start of the incubations, ANME-2ab reads covered only 0.2 % of the total archaeal reads, but their reads increased in all incubations. The largest increase in ANME-2ab reads was observed in the incubations with manganite (8.6 % ± 2.4) and pyrolusite (9.0 % ± 1.9). The relative abundance of ANME-3 was also low in the beginning (0.8 %), but ANME-3 were most enriched in the incubations with birnessite (13.6 % ± 0.2%) and pyrolusite (13.2 % ± 1.2%). The relative abundance of methanogenic *Methanosarcina* increased from 4 % at the start to 14 % in the control and pyrolusite-amended incubations and comprised 21.6 % of the total archaeal reads in the incubations with manganite (Fig. 5a). For the bacterial community, the changes were more substrate specific. Below, we discuss the changes of the most important bacterial families, which we selected based on differential abundances (Fig. S5, S6). The relative abundance of potential metal-reducing bacterial families, *Desulfobulbaceae*, Sva 1033 and *Geopsychrobacteraceae* increased relative to the start and control in all incubations where Mn oxides were added, especially with pyrolusite and manganite (Fig. 5b; Fig S4). *Desulfosarcinaceae*, a potential partner for ANME in SRB, increased in abundance in the incubations amended with birnessite and pyrolusite, but decreased in the presence of manganite. Members of S-oxidizing *Sulfurimonadaceae* increased from 3 % to 6 % in the control incubations, but decreased in all incubations where Mn oxides were added (Fig. 5b).

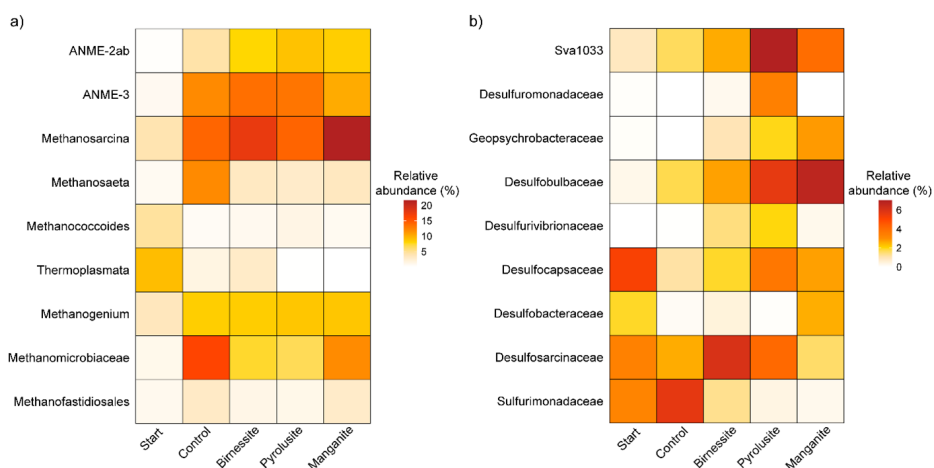


**Fig. 5** Relative abundance of (a) selected archaea and (b) bacteria based on 16S rRNA gene amplicon sequencing. The entire archaeal and bacterial communities can be found in supplementary figure S5.

## Discussion

### Burial of Mn oxides creates potential for Mn-AOM

Burial of Mn oxides below the SMTZ at the study site is the result of the seasonal variation in bottom water redox conditions in combination with very high rates of sedimentation ( $20 \text{ cm yr}^{-1}$ ) and organic matter input ( $\sim 86 \text{ mol m}^{-2} \text{ yr}^{-1}$ ; Klomp et al., 2025). When bottom waters are oxic in winter and spring, the surface sediment is enriched in Mn and Fe oxides and devoid of  $\text{H}_2\text{S}$  (Klomp et al., 2025; Żygadłowska et al., 2024a; van Helmond et al., 2025). When the bottom waters become euxinic, the supply of metal oxides from the water column decreases strongly, and the ongoing production of  $\text{H}_2\text{S}$  in the sediment leads to a removal of around 95% of the easily reducible Fe oxides from the upper part of the sediment via the precipitation of  $\text{FeS}_x$  (Fig. 1; van Helmond et al., 2025). Due to the high sedimentation rates and efficient  $\text{H}_2\text{S}$  removal by Fe oxides, a part of the Mn oxides deposited in winter ends up buried below the SMTZ in the absence of  $\text{H}_2\text{S}$  in October (Fig. 1). This sediment layer (15 – 20 cm) is also part of the zone where substantial numbers of ANME have been observed (Wallenius et al., 2025), enabling the potential for Mn-AOM.

Potential for Mn-AOM was detected in both studied sediment intervals (0 – 5 cm and 15 – 20 cm) and with several different Mn oxide minerals. Differences in AOM potential occurred between the two depths and between the different Mn oxide minerals (Fig. 3). The strongest signal for  $\text{CH}_4$  oxidation was observed with birnessite as an electron acceptor in the sediment depth interval of 15 – 20 cm. We also have indications that pyrolusite and manganite can be used for AOM, although in these incubations the signal for methane oxidation in the  $^{13}\text{C}\text{-CO}_2/^{12}\text{C}\text{-CO}_2$  ratio was masked by the drawdown of  $\text{CO}_2$  from the headspace (see methods). In both cases, the drawdown was higher in the incubations with pyrolusite and manganite, due to the higher concentrations of Mn supplied. In the incubation with the top 5 cm of the sediment, dissolved Mn formed after a lag phase and simultaneously with the onset of the  $\text{CH}_4$  oxidation signal, which subsequently faded away (Fig. 2). Importantly,  $\text{CH}_4$  oxidation was enhanced by all of the supplied Mn oxide minerals.

A cryptic S-cycle as a driver of  $\text{CH}_4$  oxidation (Holmkvist et al., 2011; Su et al., 2020) likely occurred in the incubations where birnessite and pyrolusite were added, since  $\text{SO}_4^{2-}$  accumulated (Fig. 3). A possible source for this  $\text{SO}_4^{2-}$  is the oxidation of FeS present in the sediment by the added Mn oxides (Fig 2; Luo et al., 2018). Another source for the  $\text{SO}_4^{2-}$  could be the release of S from the degradation of organic matter and consecutive oxidation of this S to  $\text{SO}_4^{2-}$  when Mn oxides are added to the sediment (Canfield et al., 2005). The presence of  $\text{SO}_4^{2-}$  even after a pre-incubation

with Mn oxides shows the importance of measuring  $\text{SO}_4^{2-}$  and  $\text{H}_2\text{S}$  when incubating marine sediment with alternative electron acceptors. Accumulation of  $\text{SO}_4^{2-}$  did not occur when manganite was added as an electron acceptor, which confirms the observations of Aller & Rude (1987) that, in marine sediments, Mn(III) minerals are less efficient in oxidizing reduced S species than Mn(IV) minerals. In laboratory experiments, manganite was also less efficient than birnessite in oxidizing FeS, likely because the former mineral solely consists of Mn(III) (Luo et al., 2018). The contribution of Mn(III) minerals to AOM is therefore expected to be through direct Mn-AOM, as a cryptic sulfur cycle is likely not possible due to the lower efficiency of Mn(III) in oxidizing reduced S species.

Incubations that were amended with dMn(III)-L did not show enhanced  $\text{CH}_4$  oxidation, which is in accordance with previous findings regarding dMn(III)-L and  $\text{CH}_4$  oxidation in a freshwater environment (Szeinbaum et al., 2020). During the incubations, concentrations of dMn were a factor 1.7 to 10 lower than the  $1 \text{ mmol L}^{-1}$  added to the bottles (Fig. 4). However, dMn was still present at concentrations comparable to porewater dMn(III)-L (Klomp et al., 2025). Metal-ligand complexes can vary over time, due to, for example, ligand exchange (Luther et al., 2015). Such exchange could contribute to degradation of Mn(III)-L complexes and/or Mn precipitation over time.  $\text{H}_2\text{S}$  was observed in all incubations amended with dMn(III)-L (Fig. S3) and has been shown to inhibit AOM (Dalcin Martins et al., 2024). However, in the depth interval from 15 – 20 cm  $\text{H}_2\text{S}$  concentrations were only  $50 \mu\text{mol L}^{-1}$ , and thus were unlikely to have been high enough for full inhibition of AOM (Dalcin Martins et al., 2024). We speculate that the lack of enhanced AOM could also result from shielding of the Mn(III) from the methanotrophic archaea by the organic ligand surrounding it, making the Mn(III) less available for the microbes. Furthermore, using dissolved Mn as an electron acceptor might require a different metabolic pathway than the extracellular electron transfer proposed for metal oxide reduction coupled to AOM in freshwater sediments (Leu et al., 2020). In summary, our results show evidence for a coupling of Mn oxide reduction and  $\text{CH}_4$  oxidation, which may be either direct or indirect (i.e. coupled to the sulfur cycle). We did not observe enhanced AOM with dissolved Mn(III)-L, however.

A  $\text{CH}_4$  oxidation signal was observed in the controls, indicating that some residual electron acceptors were still present at the start of the incubations (Fig. 2). No  $\text{SO}_4^{2-}$  was detected in the control incubations (Fig. 1, 2). Any  $\text{NO}_x$  will likely also have been completely removed by the time the incubations started (Rigutto et al., 2025). Hence, it is possible that Mn or Fe oxides drive the AOM in the control incubations. An increase in dMn or dFe in the control incubations, which would provide a strong

indication for active metal oxide reduction, was not observed, however. As an alternative, organic compounds such as humic acids in the sediment could act as an electron acceptor for AOM (Valenzuela et al., 2019, 2022; Pelsma et al., 2023).

### Microbial players in Mn driven AOM

Based on 16S rRNA genes recovered from the incubations from 15-20 cm depth after 92 days, we show that two methanotrophic archaea enriched in the incubations. These were ANME-2ab and ANME-3, with ANME-3 being present in a higher abundance than ANME-2ab (Fig. 5). The higher increase in relative abundance of ANME-2ab in the incubations where Mn oxide minerals were added compared to the control incubations indicates that these ANMEs may benefit from the addition of Mn oxides (Fig. 5). ANME-2ab have previously been linked to other electron acceptors than  $\text{SO}_4^{2-}$ , such as organic compounds and Fe oxides (Tu et al., 2017; Aromokeye et al., 2020; Pelsma et al., 2023). It is proposed that their large multi-heme cytochromes facilitate extracellular electron transfer, potentially allowing the ANME to directly reduce metal oxides (McGlynn et al., 2015; Scheller et al., 2016; Chadwick et al., 2022). ANME-2ab may also use a bacterial partner to couple  $\text{CH}_4$  oxidation to the reduction of metal oxides (Slobodkin et al., 2023). The main bacterial species that increased when Mn oxides were added, in parallel to the increase in ANME-2ab, were *Desulfobulbaceae*, Sva 1033 and *Geopsychrobacteraceae* (Fig. 4). *Desulfobulbaceae* are known bacterial partners for ANME (Lösekann et al., 2007; Green-Saxena et al., 2014) and some members have the potential to reduce metal oxides (Lovley et al., 1993; Müller et al., 2020). It is therefore possible that *Desulfobulbaceae* and ANME-2ab form a consortium in which  $\text{CH}_4$  oxidation by ANME-2ab is coupled to Mn oxide reduction by *Desulfobulbaceae*.

The relative abundance of ANME-3 also increased when compared to the start of the incubations. Although the overall increase of ANME-3 was higher compared to that of ANME-2ab, the increase of ANME-3 in Mn oxide amended incubations relative to the control samples was not as pronounced (Fig. 5). In the incubation where manganite was added, the increase in relative abundance of ANME-3 was even smaller than in the control incubations. The highest ANME-3 relative abundances were observed in the incubations where  $\text{SO}_4^{2-}$  was present, especially the incubations where birnessite and pyrolusite were added (Figs. 3, 4). This suggests that ANME-3 perform S-AOM that is fueled by Mn oxides via a cryptic S cycle, rather than directly coupled to Mn oxide reduction. ANME-3 can be independent from SRBs or in a consortium with members of the *Desulfobulbaceae* and *Desulfosarcinaceae* families (Lösekann et al., 2007). In our incubations, both *Desulfosarcinaceae* and *Desulfovibrionaceae* families show a similar pattern in

relative abundance as ANME-3, indicating that these could be potential bacterial partners for ANME-3 in S-AOM.

The relative abundance of *Methanosarcina* increased in the incubations where birnessite and manganite were added compared to the start and control (Fig. 5). A positive effect of Mn oxide on the relative abundance of *Methanosarcina* has been observed before, during anaerobic digestion (Chen et al., 2023; Tian et al., 2017). *Methanosarcina* is a metabolically versatile methanogen that can produce CH<sub>4</sub> from various organic compounds, but has also been shown to use extracellular electron transfer to obtain electrons to perform methanogenesis in syntrophy with a bacterial partner (Huang et al., 2021; Rotaru et al., 2014) and may also reduce Fe oxides (Ferry, 2020; Yang & Lu, 2022). Another possibility is that the addition of Mn oxides enhanced organic matter degradation, releasing substrates on which *Methanosarcina* could grow. Our results indicate that, in marine sediments, *Methanosarcina* may benefit from the presence of Mn oxides, regardless of the redox state, i.e. with both Mn(III) and Mn(IV) oxides.

### **The contribution of Mn-AOM to CH<sub>4</sub> removal**

Our experiments highlight the potential for Mn-AOM, either via direct coupling of CH<sub>4</sub> oxidation to Mn reduction, or via the production of SO<sub>4</sub><sup>2-</sup> when Mn oxides oxidized reduced S species in the sediment. If sufficient Mn oxides are present, Mn-AOM could contribute a few percent to total CH<sub>4</sub> oxidation in coastal sediments (Lenstra et al., 2023; Xiao et al., 2023). Generally, Mn oxide input into sediments is highest in coastal regions, especially near river mouths, as a result of the continental origin of the Mn oxides (Lenstra et al., 2022). Since these are also areas where methanogenesis rates are highest, Mn-AOM is likely especially important in these river-dominated coastal regions. High input of Mn oxides can also occur in coastal basins where the basin geometry contributes to focusing of sediment (Lenz et al., 2015; Dijkstra et al., 2016). Recycling of Mn, i.e. repeated oxidation and reduction of Mn at redox interfaces in the water column or sediment, contribute to retention of Mn in marine systems (Adelson et al., 2001; Sulu-Gambari et al., 2017). This implies that Mn can be oxidized and reduced many times before the Mn is either transported away in the water column or buried in the sediment as Mn carbonate (Sulu-Gambari et al., 2017; Lenstra et al., 2021a). Eutrophic systems where Mn recycling is strong and CH<sub>4</sub> is present close to the sediment-water interface, have a particularly high potential for interactions between CH<sub>4</sub> and Mn oxides.

Burial of Mn oxides into the methanic zone is promoted by non-steady state events like sedimentation pulses in large river delta systems (Kasten et al., 1998) or

extensive reworking of the sediment, for example, during mass movements along continental margins (Riedinger et al., 2014). Another mechanism that can result in the burial of Mn oxides below the sulfate-methane transition zone is a rapid shoaling of the  $\text{SO}_4^{2-}$  penetration depth due to changes in sedimentation rate or organic matter input, as suggested in the Bothnian Sea (Slomp et al., 2013; Lenstra et al., 2023). Notably, ANME-2ab make up for a significant part of the archaeal community in Bothnian Sea sediments (Rasigraf et al., 2020). Our work shows that, in marine systems where Mn oxides are buried in the methanogenic zone, ANME-2ab and/or ANME-3 could be involved in AOM coupled to reduction of Mn oxides.

## Conclusions

We studied the interactions between Mn oxides and  $\text{CH}_4$  in coastal marine sediments of a seasonally euxinic basin. We combined geochemical sediment and porewater profiles with results of batch incubations using various forms of oxidized Mn, namely birnessite ( $\text{Mn(IV)O}_2 \cdot n \text{H}_2\text{O}$ ), pyrolusite ( $\text{Mn(IV)O}_2$ ), manganite ( $\text{Mn(III)OOH}$ ) and dissolved Mn(III) bound to organic ligands. Our field data show burial of Mn oxides below the sulfate-methane transition zone, resulting from seasonal variation in bottom water redox conditions combined with a high sedimentation rate. Birnessite stimulated anaerobic oxidation of  $\text{CH}_4$  in sediment incubations. Pyrolusite and manganite appeared to do the same, while dissolved Mn(III) bound to organic ligands did not affect  $\text{CH}_4$  oxidation. In the incubations where birnessite and pyrolusite were added,  $\text{SO}_4^{2-}$  formed, likely via the oxidation of FeS in the sediment. This  $\text{SO}_4^{2-}$  could have driven the  $\text{CH}_4$  oxidation via a cryptic sulfur cycle. When manganite was added, no  $\text{SO}_4^{2-}$  formed, hence  $\text{CH}_4$  oxidation did not occur via a cryptic sulfur cycle. Methanotrophs of the ANME-2ab clades increased in relative abundance in all incubations where Mn oxide minerals were added compared to the control incubation, indicating that these organisms are likely involved in Mn driven methane oxidation. In the incubations where  $\text{SO}_4^{2-}$  formed upon addition of Mn oxides, ANME-3 increased in relative abundance, which suggests that these methanotrophs perform S-AOM and benefit from a cryptic sulfur cycle driven by Mn oxides. Furthermore, enrichment of the methanogen *Methanosarcina* in incubations where Mn oxides were added showed that these methanogens benefit from the presence of Mn oxides. Our results highlight the versatility of methanotrophs and show a potential role for Mn oxides in  $\text{CH}_4$  cycling in sediments of a seasonally euxinic basin.

### **Data availability**

The raw sequencing data of the 16S rRNA gene amplicon sequencing can be accessed in the NCBI database under Bioproject number PRJNA1268434. The data presented in this paper are deposited in the Zenodo database at <https://doi.org/10.5281/zenodo.16909310>.

### **Statements and Declarations**

The authors have no competing interests to declare that are relevant to the content of this article.

### **Acknowledgements**

We thank the captain and crew of the R/V *Navicula* and all MARIX participants for their support during the sampling campaign. We are also grateful to the team working at the GeoLab facilities of Utrecht University for analytical assistance.

### **Author contribution**

**Robin Klomp:** Writing – original draft, Writing – review & editing, Visualization, Methodology, Investigation, Formal analysis, Data curation. **Anna J. Wallenius:** Writing – review & editing, Visualization, Methodology, Investigation, Formal analysis, Data curation. **Niels A.G.M van Helmond:** Writing – review & editing, Methodology, Investigation, Data curation. **Wytze K. Lenstra:** Writing – review & editing, Methodology, Investigation, Data curation. **Olga M. Żygadłowska:** Writing – review & editing, Methodology, Investigation, Data curation. **Mike S.M. Jetten:** Writing – review & editing, Supervision, Project administration, Investigation, Funding acquisition, Data curation, Conceptualization. **Caroline P. Slomp:** Writing – review & editing, Writing – original draft, Supervision, Project administration, Methodology, Investigation, Funding acquisition, Formal analysis, Data curation, Conceptualization.

### **Funding**

This research was financially supported by European Research Council Synergy grant MARIX (854088) and H2020 Marie Skłodowska-Curie COFUND program (847504). This work was carried out under the program of the Netherlands Earth System Science Center (NESSC 024002001) and SIAM (024002002), financially supported by the Ministry of Education, Culture and Science (OCW). WKL acknowledges funding by the Dutch Research Council (NWO VI.Veni.222.332).

## Supplementary Material

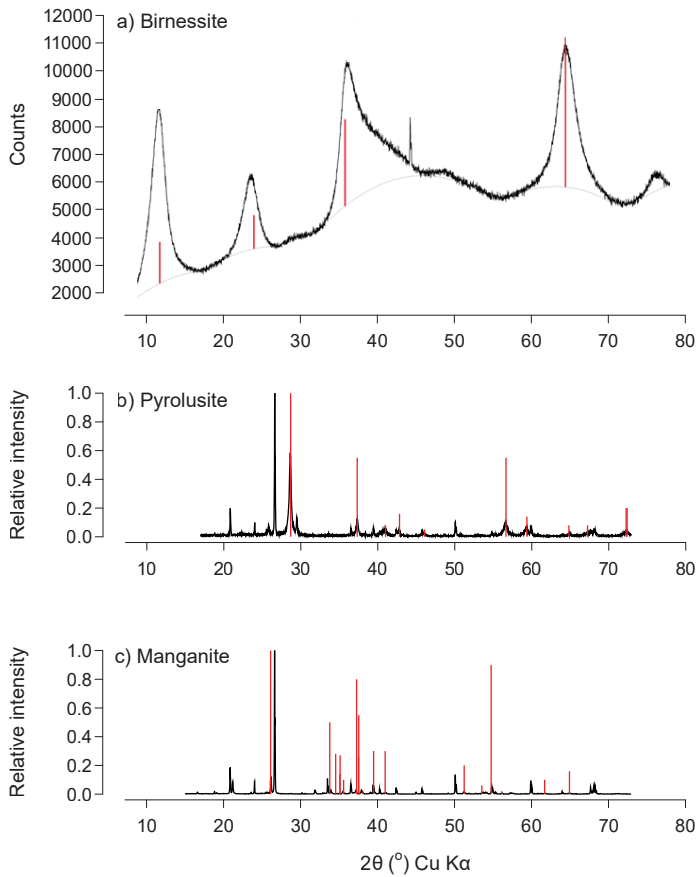


**Fig. S1** X-ray diffraction spectra for the Mn oxide minerals used in the incubation experiments, i.e. for (a) birnessite, (b) pyrolusite, (c) manganite. The black lines represent the results for the mineral samples; the red bars represent theoretical peaks for each mineral in the spectrum. The spectra for pyrolusite and manganite were obtained from Lenstra et al. (2021b).

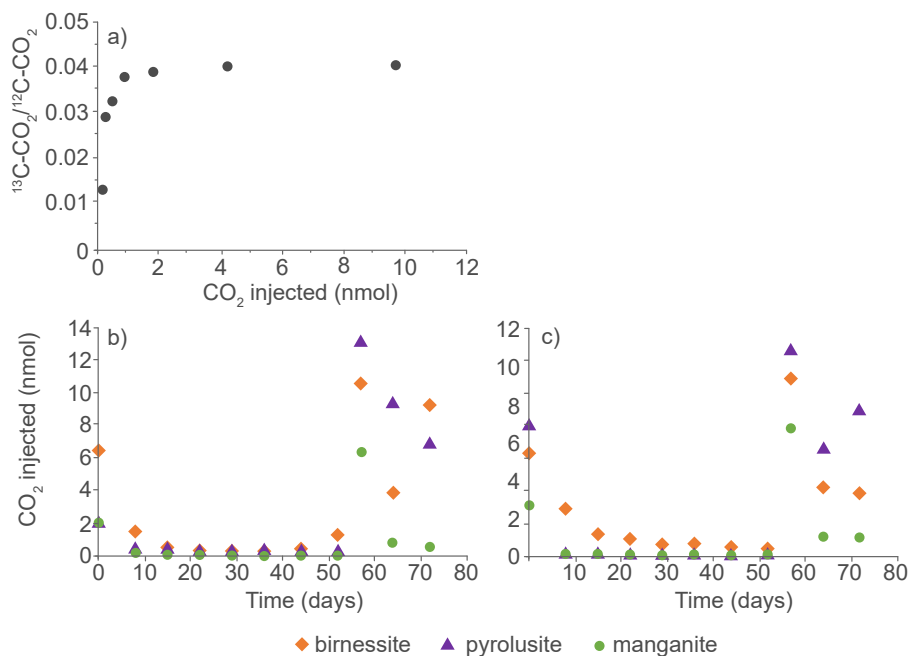


**Fig. S2** a)  $^{13}\text{C-CO}_2/^{12}\text{C-CO}_2$  ratio over a range of injected amounts of  $\text{CO}_2$  from a single sample. These results illustrate that the  $\text{CO}_2$  isotope ratio decreases when the injected  $\text{CO}_2$  is  $< 1$  nmol because of a lower detection limit for  $^{13}\text{C-CO}_2$  when compared to  $^{12}\text{C-CO}_2$ . b) the amount of  $\text{CO}_2$  injected in the GC-MS for the incubations where Mn oxides were added to the incubation with sediment from 0 – 5 cm. c) amount of  $\text{CO}_2$  injected in the GC-MS for the incubations amended with Mn oxides from 15 – 20 cm depth. These results show that the amount of  $\text{CO}_2$  injected in the incubations with Mn oxides was too low for an accurate analysis of the  $^{13}\text{C-CO}_2/^{12}\text{C-CO}_2$  ratio. Furthermore, the results show that incubations with birnessite generally contained more  $\text{CO}_2$  than incubations with pyrolusite and manganite.

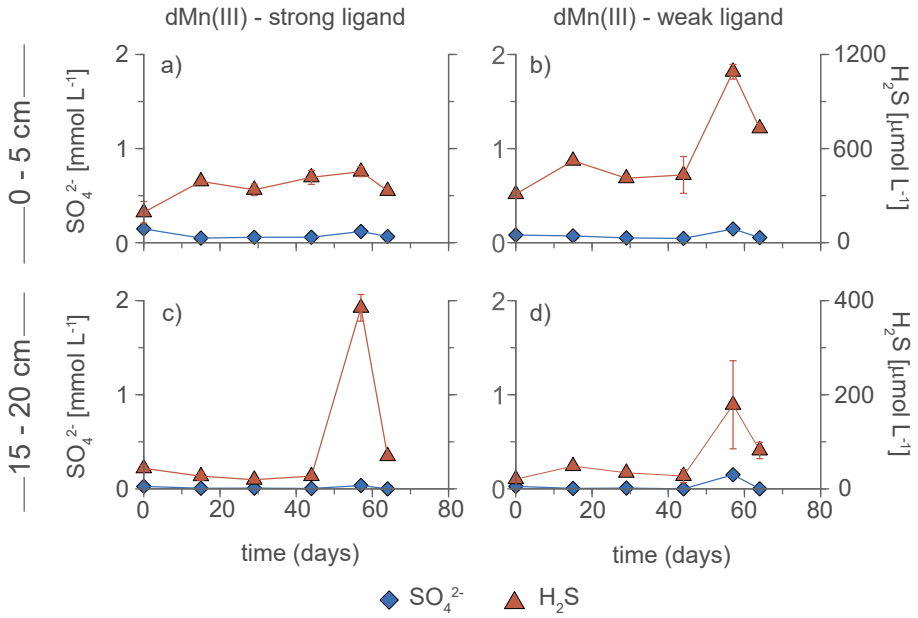


**Fig. S3** Concentrations of  $\text{SO}_4^{2-}$  and  $\text{H}_2\text{S}$  in the incubations of sediment from (a, b) 0 - 5 cm and (c, d) 15 - 20 cm depth amended with dissolved Mn(III).

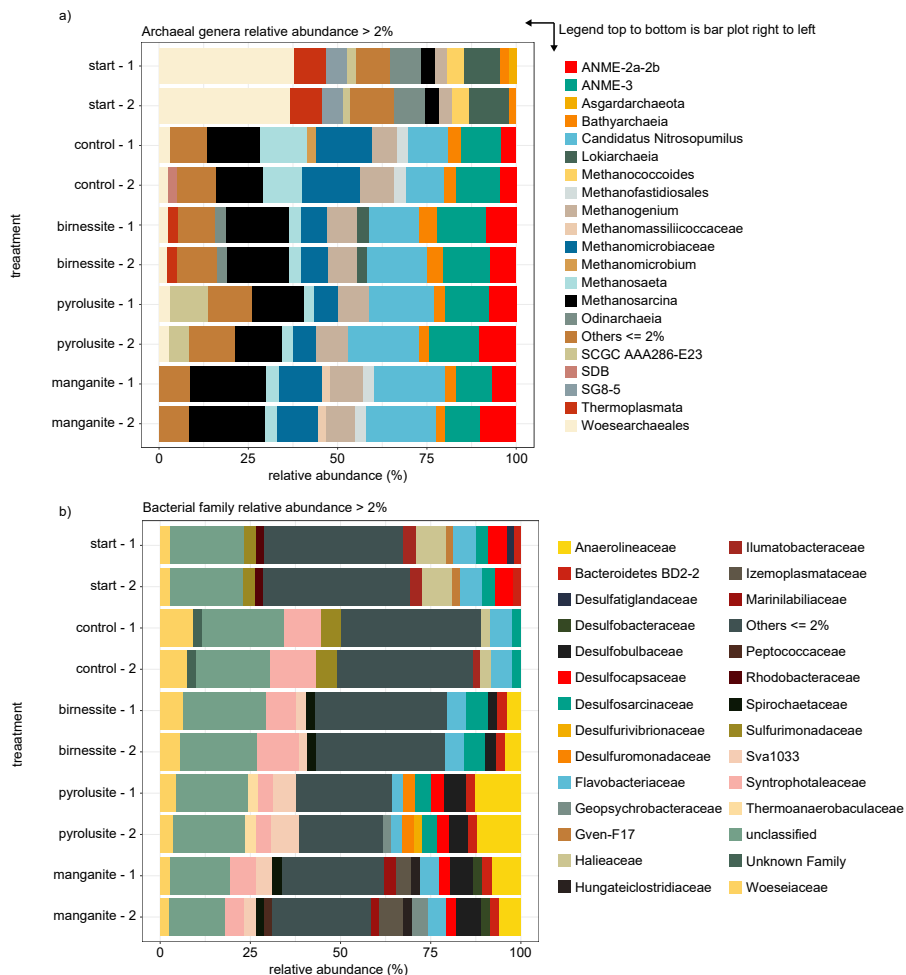


**Fig. S4** Relative abundance of the (a) archaeal genera and (b) bacterial families based on 16S rRNA amplicon sequencing of the sediment from 15 - 20 cm depth at the start of the incubation and at the end for the control and the incubations amended with Mn oxides (birnessite, pyrolusite and manganite). For each treatment, duplicate bottles were analyzed separately and results for each bottle are shown in the plot. Two samples were taken from the start material.

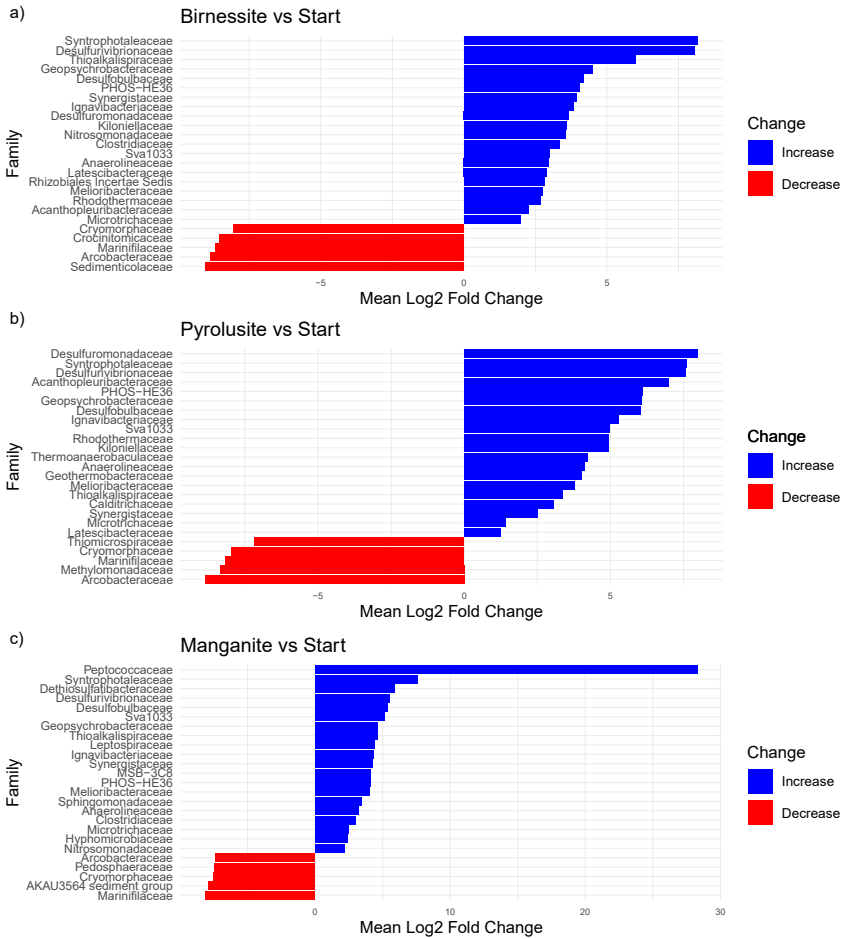


**Fig. S5** Change in the microbial community between the start and end point of the incubations with Mn oxides (a) birnessite, (b) pyrolusite, (c) manganite, based on differential abundance analysis. The blue bars represent an increase in relative abundance of an organism, compared to the start, while the red bars indicate a decrease.

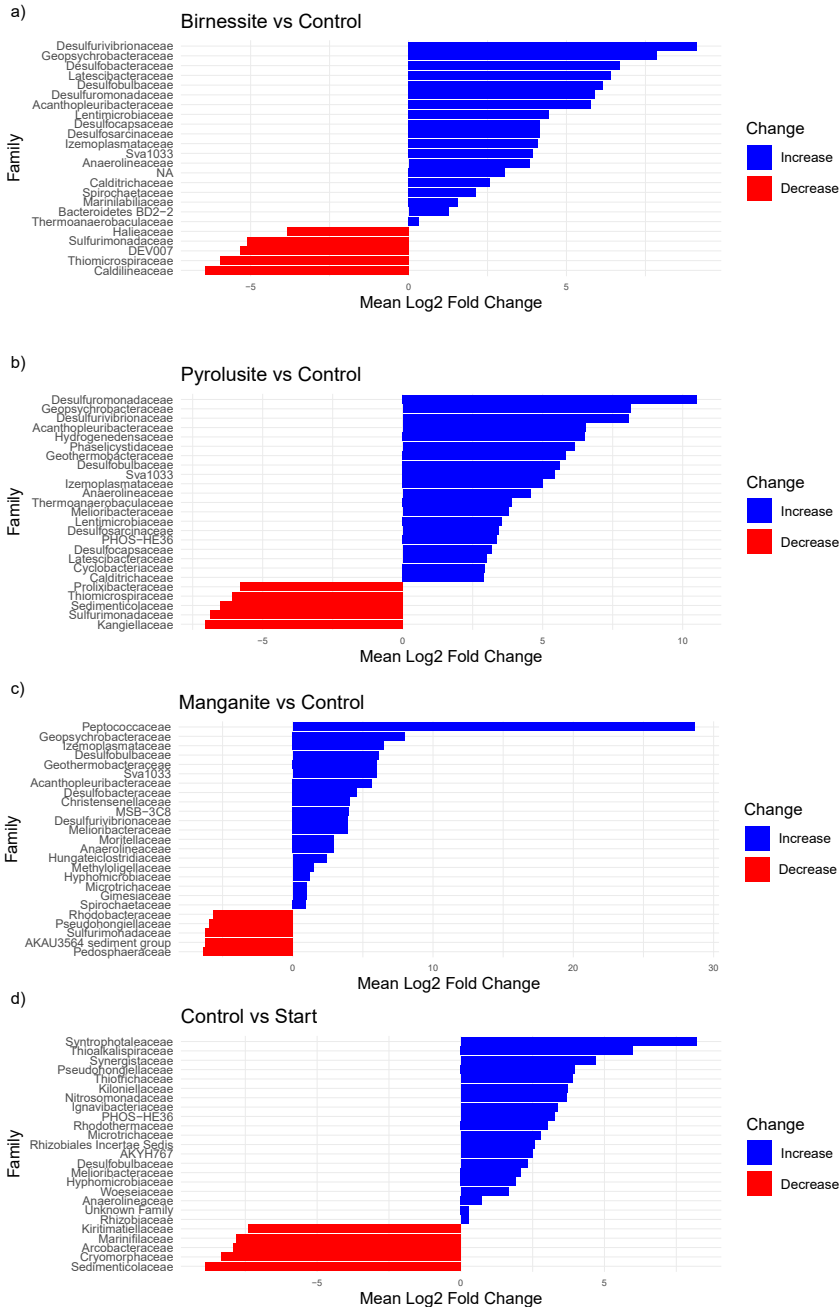


**Fig. S6** Change in the microbial community between the control incubation and end points of the incubations amended with Mn oxides (a) birnessite, (b) pyrolusite, (c) manganite, and (d) between the control and the starting material based on differential abundance analysis. The blue bars represent an increase in relative abundance of an organism compared to the control or start, while the red bars indicate an increase.

## Supplementary table

**Table S1** Composition of artificial HEPES buffered,  $\text{SO}_4^{2-}$  free seawater

<b>Chemical</b>	<b>Concentration</b>
<b>NaCl</b>	26 g L <sup>-1</sup>
MgCl <sub>2</sub> · 6H <sub>2</sub> O	5.0 g L <sup>-1</sup>
CaCl <sub>2</sub> · 2H <sub>2</sub> O	1.4 g L <sup>-1</sup>
KCl	0.5 g L <sup>-1</sup>
HEPES	20 mmol L <sup>-1</sup>



## Chapter 6

# ANME-2ab drive methane oxidation in brackish coastal sediments via multiple pathways

---

R. Klomp<sup>1,2\*</sup>, A.J. Wallenius<sup>1\*</sup>, M.A.W. Schutgens<sup>1</sup>, T. van Alen<sup>1</sup>, T. Röckmann<sup>3</sup>,  
M.S.M. Jetten<sup>1</sup>, C.P. Slomp<sup>1</sup>

\*These authors contributed equally to this work

<sup>1</sup>Department of Microbiology, Radboud Institute for Biological and Environmental Sciences,  
Radboud University, Heyendaalseweg 135, 6525AJ Nijmegen, the Netherlands

<sup>2</sup>Department of Earth Sciences, Utrecht University, Princetonlaan 8a, 3584 CB Utrecht,  
the Netherlands

<sup>3</sup>Institute for Marine and Atmospheric Research Utrecht, Utrecht University, Princetonplein 5,  
3584CC Utrecht, the Netherlands

## Abstract

Methane is a powerful greenhouse gas. Typically, a large fraction of the methane formed in coastal sediments is removed via anaerobic methane oxidation (AOM). Here, we demonstrate the potential for a range of AOM pathways in brackish coastal sediments by ANME-2ab archaea. At our study site, geochemical profiles indicate that AOM is primarily restricted to a shallow, metal-oxide-rich sulfate-methane transition zone (SMTZ). ANME-2ab were the sole methanotrophs detected, and metatranscriptomics showed the highest expression levels of the ANME-2ab genes in the SMTZ. AOM activity was observed in sediment incubations with various electron acceptors, including sulfate, metal oxides, and the organic matter analogue graphene oxide. Highest potential rates were observed in sediments from below the SMTZ, pointing towards fast stimulation of the deeper methanotrophic community when alleviating the electron acceptor limitation. The variety of AOM pathways and persistence of methanotrophs below the SMTZ likely contribute to the resilience of the microbial methane filter in brackish coastal sediments.

## Teaser

A resilient methane filter: active methanotrophy in and below the sulfate-methane-transition-zone in coastal sediments

## Introduction

Methane is a key greenhouse gas that in marine sediments is mainly produced by methanogenic archaea (Reeburgh, 2007). In most continental margin sediments, the methane is efficiently removed through anaerobic and aerobic oxidation (Knittel & Boetius, 2009). In coastal sediments, however, some of the methane may escape oxidation, especially when the zone of methanogenesis approaches the sediment-water interface (Lapham et al., 2024; Żygadłowska et al., 2024b). As a consequence, coastal regions may contribute up to 75% of total marine methane emissions, even though these systems account for only a small part of the oceanic surface area (Hamdan & Wickland, 2016). This makes it crucial to understand the microbial pathways contributing to methane removal in coastal sediments.

Coastal sediments typically receive high inputs of organic matter, which induce sharp redox gradients near the sediment-water interface (Burdige, 2007). Besides oxygen, which generally penetrates down to depths of only a few millimeters, other electron acceptors used to degrade organic matter are, in order of decreasing energy yield, nitrate/nitrite, manganese (Mn) oxide, iron (Fe) oxide and sulfate ( $\text{SO}_4^{2-}$ ; Froelich et al., 1979). When these electron acceptors are depleted, fermentation and methanogenesis are the remaining pathways (Canfield & Thamdrup, 2009). Most of the methane is thought to be removed through anaerobic oxidation of methane (AOM) with sulfate as the electron acceptor (S-AOM) in the so-called sulfate-methane transition zone (SMTZ) (Boetius et al., 2000; Orphan et al., 2002; Reeburgh, 2007).

In environments subject to non-steady state deposition, methane may also come into contact with metal oxides, creating an opportunity for a coupling between manganese and iron oxide reduction and AOM (Mn- and Fe-AOM, respectively; Wallenius et al., 2021 and references therein). The first evidence for potential Mn- and Fe-AOM was obtained from incubations of marine methane-seep sediments using  $^{13}\text{C}$ -labelled methane (Beal et al., 2009). Follow-up experimental and modeling studies confirmed a potential role for Mn- and/or Fe-AOM in brackish and marine sediments (Segarra et al., 2013; Riedinger et al., 2014; Egger et al., 2015; Aromokeye et al., 2020; Lenstra et al., 2023). Brackish sediments where an increased input of organic matter has led to an upward shift of the SMTZ are particularly conducive to Mn- and Fe-AOM, because of the presence of metal oxides in a zone with high methane concentrations (Egger et al., 2015; Rooze et al., 2016; Lenstra et al., 2023). Besides direct coupling of metal oxide reduction to AOM in such settings, metal oxides may also drive S-AOM via the production of  $\text{SO}_4^{2-}$  in a cryptic sulfur

cycle (Holmkvist et al., 2011; Norði et al., 2013; Su et al., 2020). Since there is no conclusive geochemical signature for Mn-AOM, Fe-AOM or cryptic sulfur cycling, the need to identify the microorganisms involved is important.

Typically, S-AOM is performed by a consortium of anaerobic methanotrophic archaea (ANME) and sulfate-reducing bacteria (SRB) (Boetius et al., 2000; Orphan et al., 2002). The clade Ca. Methanoperedenaceae (also known as ANME-2d) has been linked to Mn- and Fe-AOM reduction in freshwater sediments (Ettwig et al., 2016; Cai et al., 2018; Leu et al., 2020). In brackish and marine sediments, ANME-2d is typically only present at very low abundances and thus is unlikely to contribute to Mn- and Fe-AOM (Aromokeye et al., 2020; Rasigraf et al., 2020; Wallenius et al., 2021, 2025). Other subclades of ANME-2 may be involved instead, such as ANME-2ab, now classified as Ca. Methanocomedenaceae (Chadwick et al., 2022). ANME-2a was, for example, proposed to be linked to Fe-AOM based on sediment incubations for a marine site in the North Sea (Aromokeye et al., 2020). Similar depth trends in ANME-2a and total iron contents (Rasigraf et al., 2020) for sediments from the brackish Bothnian Sea for which Fe-AOM activity was reported earlier (Egger et al., 2015), also point to a potential role for ANME-2a in Fe-AOM. Finally, AOM may also be coupled to redox-active humic substances in natural organic matter (NOM-AOM) (Scheller et al., 2016; Valenzuela et al., 2017; Zhao et al., 2024). While in freshwater sediments, ANME-2d can be involved in NOM-AOM (Bai et al., 2019), various other ANME clades have been inferred to carry out the process in brackish and marine environments, including ANME-1b (anoxic marine water; van Grinsven et al., 2020), ANME-2a and 2c (marine methane seep; Scheller et al., 2016) and ANME-2ab (brackish canal sediment; Pelsma et al., 2023).

In this study, we examine the potential and in-situ relevance of various AOM pathways and the microbes involved in methane- and metal oxide-rich sediments from a brackish coastal sea (Bothnian Sea). We focus on sediments from within and below the SMTZ and assess the following electron acceptors in AOM: sulfate, Mn and Fe oxides and natural organic matter. A complementary set of methods was used, including geochemical profiling of sediment and pore water, 16S rRNA gene amplicon sequencing, metagenomics, metatranscriptomics, and sediment incubations using  $^{13}\text{C}$ -labelled methane. We find evidence for a range of AOM pathways, performed by ANME2-ab, with the highest in-situ activity in the SMTZ but the greatest potential activity deeper in the sediment, indicative of a resilient and easily reinvigorated methanotrophic community.

## Materials and methods

### Study site

The Bothnian Sea is a brackish oligotrophic coastal basin in the northern part of the Baltic Sea. Rivers are the main source of organic matter in the region. Inputs of this terrestrial organic matter vary greatly between years, linked to variations in rainfall and river discharge, and appear to be increasing, linked to climate change (Algesten et al., 2006; Lenstra et al., 2018). Land uplift in the Bothnian Sea region contributes to the transport of this material from shallow areas to the deeper basins (Leivuori & Niemistö, 1995). The input of marine organic matter has also gained importance over the past decades as a result of anthropogenic eutrophication (Kuliński et al., 2022). The increase in deposition of both terrestrial and marine organic matter is thought to be responsible for the observed shallowing of the SMTZ at many locations in the Bothnian Sea (Slomp et al., 2013; Egger et al., 2015; Rooze et al., 2016). Bothnian Sea sediments are metal oxide-rich, with frequent burial of metal oxides into and below the SMTZ (Slomp et al., 2013; Egger et al., 2015; Lenstra et al., 2018).

The sampling location, US2 (62°50.99' N; 18°53.53' E; Fig. S1), has a permanently oxygenated water column, a sediment accumulation rate of 1.6 cm yr<sup>-1</sup> and is characterized by a high input of metal oxides and a shallow SMTZ (Slomp et al., 2013). Macrofaunal activity, mainly by burrowing crustaceans and polychaetes, affects the sediment via bioturbation and bioirrigation (Josefson et al., 2012).

### Sediment and pore water collection

In May 2022, six sediment cores were collected on board Research Vessel KBV 181, using a Gemini corer system with transparent core liners of 8 cm inner diameter: one core for porewater and solid phase analysis, one for methane, one for sulfate reduction rates, one for porosity and DNA/RNA samples and two to collect material for incubation experiments.

For pore water and solid phase analysis, two bottom water samples were taken. The core was sectioned under a N<sub>2</sub> atmosphere in a glove bag at a 1 cm depth resolution until 10 cm depth and a 2 cm depth resolution below 10 cm depth. The sediment was transferred into 50 mL centrifuge tubes and centrifuged at 4500 rpm for 20 minutes to separate the sediment from the pore water. The sediment was stored in N<sub>2</sub> purged aluminum bags at -20°C until further processing for solid phase analysis. The supernatant was filtered (0.45 µm) in a N<sub>2</sub> filled glove bag and subsampled for analysis of alkalinity, SO<sub>4</sub><sup>2-</sup>, ammonium (NH<sub>4</sub><sup>+</sup>), dissolved Mn, Fe, phosphorus (P), sulfide (H<sub>2</sub>S) and dissolved inorganic carbon (DIC), including the DIC

C-isotopic signature. Aliquots for alkalinity and  $\text{SO}_4^{2-}$  were stored in polyethylene vials at 4°C until analysis. Samples for  $\text{NH}_4^+$  analysis were stored at -20°C. Samples for total dissolved Mn, Fe and P were acidified with 10  $\mu\text{L}$  30% suprapur HCl per milliliter of sample and stored at 4°C. Samples for  $\text{H}_2\text{S}$  analysis were diluted 5 times in 2% Zn acetate in a glass vial and stored at 4°C. Samples for DIC and DIC C-isotopic signal were stored in airtight glass vials without headspace and with 10  $\mu\text{L}$   $\text{HgCl}_2$  per 2 ml sample at 4°C.

Samples for the determination of  $\text{CH}_4$ , including C- and D-isotopes, and sulfate reduction rates were taken directly upon recovery from a core liner with pre-drilled holes at a 2.5 cm depth resolution covered with tape prior to coring. For  $\text{CH}_4$ , 10 ml of sediment was transferred directly into a 65 ml glass bottle filled with a saturated NaCl solution using pre-cut plastic syringes. Bottles were immediately stoppered, capped and stored upside down until analysis. For sulfate reduction rates, 5 ml of sediment was sampled using pre-cut syringes, which were sealed off with parafilm and stored in a  $\text{N}_2$  flushed aluminum bag at 4°C.

For porosity and DNA/RNA sample collection, a core was sectioned under atmospheric conditions in sections of 1 cm in the top 10 cm of the core and in sections of 2 cm below 10 cm. Part of the sediment was placed in pre-weighed centrifuge tubes and stored at 4°C until porosity analysis. Another part was conveyed to autoclaved Eppendorf tubes, frozen with liquid  $\text{N}_2$  and stored at -20°C for DNA and RNA analyses.

The remaining cores were stored at 4°C and sectioned within two weeks after retrieval under an  $\text{N}_2$  atmosphere at a 4 cm resolution. The sediment was placed in plastic bags and stored in  $\text{N}_2$  flushed aluminum bags at 4°C until use in sediment incubations.

### **Chemical analysis of solid phase**

Sample residues for the solid phase analysis were freeze-dried and ground with an agate mortar and pestle, all under a  $\text{N}_2$  atmosphere. Aliquots of the sediment (~300 mg) were used to determine  $\text{C}_{\text{org}}$  contents. The sediment was decalcified with 1 M HCl (via a two-step wash; Van Santvoort et al., 2002), dried, weighed and powdered in an agate mortar and pestle. The powdered sediment was analyzed using an elemental analyzer (Fison Instruments model NA 1500 NCS). The C content was corrected for weight loss during decalcification and an internationally certified soil standard IVA2 was used to determine the accuracy and precision of the analysis. The certified C content in IVA2 is 0.732 wt%, the measured mean value for C in IVA2 ( $n = 7$ ) was 0.716 wt% with a standard deviation of 0.004 wt%.

Another aliquot (~50 – 100 mg) was used to determine the mineral phases of Mn and Fe via a sequential extraction. For Mn, we used the extraction scheme of Lenstra et al. (2021b), for Fe, the procedure described by Kraal et al. (2017). Details are provided in supplemental Table S1 and S2. In the first step of the Fe extraction (1 M HCl), Fe(II) and Fe(III) were measured separately via the spectrophotometric method using 1-10 phenantroline (APHA, 2005), to distinguish Fe-oxides from reduced Fe minerals such as FeS and Fe carbonate. In the other steps, extracted Mn and Fe was measured via inductively coupled plasma – optical emission spectroscopy (ICP-OES; PerkinElmer Avio; detection limit  $0.1 \mu\text{mol L}^{-1}$  for Fe and  $0.02 \mu\text{mol L}^{-1}$  for Mn). The standard deviation over all extraction steps based on duplicates ( $n = 3$ ) was 2.5% for Fe and 2.4% for Mn.

Iron sulfide (FeS) concentrations were determined via the passive diffusion method as described by (Burton et al., 2008) on sediment aliquots of ~300 mg. The standard deviation based on duplicates ( $n = 3$ ) was 5.0%.

Total sediment Mn, Fe, P and S was determined via a sediment digestion of ~100 mg of sediment in 2.5 ml mixed acid ( $\text{HNO}_3$ ;  $\text{HClO}_4$ ; 2:3) and 2.5 ml 40% HF at  $90^\circ\text{C}$ . After evaporation of the acid mixture, the residue was redissolved in 1 M  $\text{HNO}_3$ . The solution was analyzed using ICP-OES with the following recoveries: 106% for Mn, 107% for Fe, 104% for P and 101% for S. The standard deviation ( $n=2$ ) was 1% for Mn, 1.1% for Fe, 1.1% for P and 2.1% for S. Porosity was determined based on the weight loss of the sample after drying in an oven at  $60^\circ\text{C}$ .

### Chemical analysis of pore water

Porewater Fe, Mn and P were measured via ICP-OES (PerkinElmer Avio; detection limit  $0.1 \mu\text{mol L}^{-1}$  for Fe,  $0.02 \mu\text{mol L}^{-1}$  for Mn,  $3.1 \mu\text{mol L}^{-1}$  for P). A 10 mL  $\text{N}_2$  headspace was injected into the  $\text{CH}_4$  bottles and after an equilibration time of 7 days, the headspace was analyzed on a Thermo Finnigan Trace™ gas chromatograph (flame ionization detector; limit of detection  $0.02 \mu\text{mol L}^{-1}$ ). The isotopic composition of  $\text{CH}_4$  ( $\delta^{13}\text{C}-\text{CH}_4$  and  $\delta\text{D}-\text{CH}_4$ ) was analyzed by Continuous Flow Isotope Ratio Mass Spectrometry (CF-IRMS) as described in Brass & Röckmann (2010) and Sapart et al. (2011). Porewater  $\text{SO}_4^{2-}$  was determined via ion chromatography (Metrohm 930 Compact IC Flex; detection limit of  $10 \mu\text{mol L}^{-1}$ ). Porewater  $\text{H}_2\text{S}$  was measured spectrophotometrically using the phenylendiamine and ferric chloride method (Cline, 1969; detection limit of  $1 \mu\text{mol L}^{-1}$ ). Alkalinity was measured within 24 h after sample collection through titration with 0.01 M HCl. Porewater DIC including its isotopic composition was determined after acidification of the sample with 85%  $\text{H}_3\text{PO}_4$  in an argon purged exetainer and measurement of the headspace on a

GasBench – Isotope Ratio Mass Spectrometer (GasBench II Delta V Advantage IRMA, Thermo Scientific). Concentrations of  $\text{NH}_4^+$  were determined via the indophenol blue spectrophotometric method (Solórzano, 1968).

### **Determination of $\text{SO}_4^{2-}$ reduction rates**

To determine  $\text{SO}_4^{2-}$  reduction rates, the samples were injected with 100 kBq  $^{35}\text{S}\text{-SO}_4^{2-}$  six days after core retrieval, sealed again and incubated for 24 h in  $\text{N}_2$ -purged aluminum bags at 4°C. The sediment was then transferred into a 50 mL centrifuge tube containing 20 mL oxygen-free 20% zinc-acetate to precipitate any sulfide formed and terminate microbial activity (Fossing & Jørgensen, 1989; Kallmeyer et al., 2004). The samples were stored at -20°C in aluminum  $\text{N}_2$  purged bags. Upon analysis, the samples were washed twice with oxygen-free bottom water and centrifuged to remove pore water and unreacted  $^{35}\text{S}\text{-SO}_4^{2-}$  (Egger et al., 2016). The reduced S was then extracted with an acidic chrome chloride solution for 48 h (Kallmeyer et al., 2004) and captured in 20% zinc acetate via the passive diffusion method as described in Burton et al. (2008). The formed radioactive sulfide was determined by mixing the 20% zinc-acetate 1:2 vol:vol with Ecoscint XR (NAT1396, Scientific Laboratory Supplies, UK) and analysis on an automatic triple-to-double coincidence ratio (TDCR) liquid scintillation counter (Hidex 600 SL, LabLogic Systems Limited, UK). Sulfate reduction rates were quantified by comparing the activity (decays per minute) of the radiolabeled total reduced inorganic sulfur ( $\alpha_{\text{TRIS}}$ ) to the total  $\text{SO}_4^{2-}$  radiotracer ( $\alpha_{\text{TOT}}$ ) as described in Kallmeyer et al. (2004):

Where  $\rho$  is the measured porosity,  $t$  is the incubation time in days and 1.06 is the correction factor for the expected isotopic fractionation (Jørgensen & Fenchel, 1974; Kallmeyer et al., 2004).

### **DNA extraction and 16S rRNA amplicon sequencing and analysis**

DNA was isolated with the DNeasy PowerSoil Pro DNA isolation kit (Qiagen, Venlo, Netherlands) according to the manufacturer's instructions after bead-beating the samples on a TissueLyser LT (Qiagen) for 10 min at 50Hz. Samples from the incubations were pre-incubated at 65°C for 10 min in the kit's C1 solution before bead-beating to increase archaeal DNA yields. 16S rRNA gene amplicon sequencing was performed on the Illumina MiSeq Next Generation Sequencing platform by Macrogen (Seoul, South Korea) using Herculase II Fusion DNA Polymerase Nextera XT Index Kit V2, yielding 2x300bp paired end reads. Archaeal primers used were Arch349F (5'-GYGCASCAGKCGMGAAW-3') and Arch806R (5'-GGACTACVSGGGTATCTAAT-3'; Takai & Horikoshi, 2000) and for bacteria Bac341F (5'-CCTACGGGNGGCWGCAG-3'; Herlemann et al., 2011) and Bac806R

(5'-GGACTACHVGGGTWTCTAAT-3'; Caporaso et al., 2012). The optimal trimming parameters were determined with Figaro (Weinstein et al., 2019), and trimming and further processing were done using the DADA2 pipeline (v1.8; Callahan et al., 2016) in Rstudio (v4.1.1; R Core Team, 2019) as explained previously (Wallenius et al., 2025). Raw reads are accessible on the National Center for Biotechnology Information (NCBI) website under the accession number PRJNA1306556.

### Metagenomic sequencing and analysis

The DNA from sediment depths of 16-20 cm and 28-32 cm was used for short-read metagenomic sequencing using a TruSeq DNA PCR-free library with an insert size of 550bp on NovaSeq6000 (Illumina) platform, producing 2 × 150bp paired-end reads (100 Gbp/sample). For long read sequencing with Nanopore, library preparation was done starting with 150 to 400 ng of DNA. The quality of the DNA was checked by agarose gel electrophoresis. The DNA Library construction was performed using the Native Barcoding Kit 24 V14 (SQK-NBD114-24), according to the manufacturer's protocol (Oxford Nanopore Technologies, Oxford, UK). The library was loaded on a Flow Cell (R10.4.1) and sequenced using the MinION Mk1C device (Oxford Nanopore Technologies, Oxford, UK), according to the manufacturer's instructions. Quality of the sequence reads was analyzed using fastqc (Andrews, 2010). We used singleM (Woodcroft et al., 2024) to characterize the samples taxonomically. The quality control, trimming, assembly and binning was done using the Aviary pipeline (v.0.11.0; Newell et al., 2025). The reads were trimmed with fastp (v0.24.0; Chen et al., 2018), assembled with metaSPAdes (v.4.0.0; Nurk et al., 2017), mapped with CoverM (v0.7.0; Aroney et al., 2025), and binned with MetaBAT and MetaBAT2 (v2.15; Kang et al., 2015, 2019), Semibin (Pan et al., 2022), Rosella (v0.5.5; <https://rhynewell.github.io/rosella/>) and DASTool (v.1.1.2.; Sieber et al., 2018). The metagenomically assembled genomes (MAGs) were taxonomically classified with GTDB-Tk release 220 (v2.4.0; Chaumeil et al., 2022) and the MAG completeness and contamination was estimated with CheckM2 (v1.0.2; Aroney et al., 2025). We also used differential coverage binning (Albertsen et al., 2013) as described previously (Wallenius et al. 2025, in prep) to recover one ANME MAG. Genomes were annotated with DRAM v1.0 (Shaffer et al., 2020) and metascan (Cremers et al., 2022). Genes involved in metal reduction were retrieved with FeGenie (Garber et al., 2020). Proteins were identified with prodigal (v2.6.3; Hyatt et al., 2010) and used to search for proteins with heme-binding motifs (>3).

### Metatranscriptomics

RNA was extracted from freeze-dried sediment from depths of 16-20 cm and 28-32 cm with the RNeasy PowerSoil Total RNA Kit (Qiagen, Hilden, Germany) with the following modifications to increase the RNA yield: the input amount was

increased to ~0.5 g sediment, in step 2 we added an extra 0.5 ml DEPC-treated water (Invitrogen, Carlsbad, United States) to increase the volume of the aquatic phase; in step 3 we added 4 ml of phenol/chloroform/isoamyl alcohol to counter-act for the increased humic acids; in step 9, one ml DEPC H<sub>2</sub>O was added before incubating 30 min at -20°C, and the final extraction was done with 25 ul SR7 volume to increase the RNA concentration. DNA contamination was removed with Invitrogen DNA removal kit (Fischer Scientific, USA). The quality of the RNA was checked using the 2100 Bioanalyzer instrument (Agilent technologies, USA) and the Agilent RNA 6000 Nano Kit according to the manufacturer's instructions. Metatranscriptomic sequencing was performed using a TruSeq stranded with NEB rRNA depletion kit (bacteria) (Illumina, USA) on a NovaSeqX (Illumina) platform, generating 150-bp paired-end reads with ~15 Gb throughput/sample. For both depths three biological replicates per depth from different extractions were sequenced. Raw sequences were quality trimmed and rRNA contaminant-filtered, mapped against the DRAM-generated scaffolds, and transcripts per million (TPM) values were generated using transcriptm v0.5 (<https://github.com/sternp/transcriptm>). Relative abundance was calculated using CoverM v0.6.1. Further analysis, including data visualization was done in RStudio v4.4.0. Map reads corresponding to coding DNA sequences (CDS) were converted into transcripts per million and pooled per genome to compare the relative abundance of MAGs expressed per sample.

### Incubation experiment

The AOM potential of various electron acceptors, namely O<sub>2</sub>, SO<sub>4</sub><sup>2-</sup>, Mn oxide, Fe oxide and graphene oxide, as an analogue for humic acid, was tested via batch incubations using sediment from within the SMTZ (16 - 20 cm) and below the SMTZ (28 - 32 cm). For both intervals, CH<sub>4</sub> and metal oxides overlapped in-situ. The incubations were started within six months of sediment collection.

The sediment was diluted in a 1:4 ratio with HEPES buffered artificial SO<sub>4</sub><sup>2-</sup>-free seawater (ASW; for composition see table S3) under an anoxic atmosphere. The sediment slurry was distributed over sterile 120 mL serum bottles, to a final amount of 60 g slurry per bottle. In the incubations with sulfate, 10 mmol L<sup>-1</sup> of Na<sub>2</sub>SO<sub>4</sub> solution was added. Manganese was added in the form of birnessite (7.5 mmol L<sup>-1</sup>; MnO<sub>2</sub>·nH<sub>2</sub>O) synthesized according to the protocol by Händel et al. (2013) and iron was added in the form of ferrihydrite (7.5 mmol L<sup>-1</sup>; FeO(OH)) synthesized as described in Raven et al. (1998). Both metal oxides were analyzed via X-ray diffraction to characterize the minerals (Fig. S2). Graphene oxide (C<sub>x</sub>H<sub>y</sub>O<sub>2</sub>) was added in a concentration of 200 mg L<sup>-1</sup>, after diluting graphene oxide paste (Merck KGaA, Darmstadt, Germany) in demineralized water and deoxygenating the solution. The bottles were closed with

capped rubber stoppers and, in the incubation with O<sub>2</sub>, air was injected to achieve 4% O<sub>2</sub> in the headspace. The sediment was first pre-incubated for one week, shaking at 90 rpm at room temperature with 100% N<sub>2</sub> headspace, to oxidize sediment FeS and minimize the release of SO<sub>4</sub><sup>2-</sup> in a cryptic sulfur cycle in the real incubations. After one week, the ASW was replaced by freshly prepared ASW under an anoxic atmosphere and new electron acceptors were added to each bottle, in the same concentrations as in the pre-incubations. The headspace was replaced by a headspace of 76% N<sub>2</sub>, 4% CO<sub>2</sub> and 20% <sup>13</sup>C-labelled CH<sub>4</sub> (Cambridge Isotope Laboratories, Inc., Andover, USA). The headspace in the O<sub>2</sub>-MO incubation was amended with 50% air, 4% CO<sub>2</sub> and 20% <sup>13</sup>C-CH<sub>4</sub>. The bottles were then placed at room temperature shaking at 90 rpm for 94 days. In the O<sub>2</sub>-MO incubation, new O<sub>2</sub> was added in the form of pure O<sub>2</sub> gas to a concentration of 4% of the headspace after 28 and 49 days. In the NOM-AOM incubations with sediment from below the SMTZ, new substrate was added to a concentration of 200 mg L<sup>-1</sup> after 56 days, when the activity stagnated likely due to substrate depletion.

The headspace was measured weekly for <sup>12</sup>C-CO<sub>2</sub> and <sup>13</sup>C-CO<sub>2</sub> concentrations on a gas-chromatograph coupled to a mass spectrometer (GC-MS; Agilent 5975C inert MSD, detection limit for accurate CO<sub>2</sub> isotope concentrations is 40 nmol CO<sub>2</sub>) to monitor <sup>13</sup>C-CH<sub>4</sub> oxidation. Upon addition of Mn oxides, the headspace concentration of CO<sub>2</sub> decreased, possibly because CO<sub>2</sub> was drawn into the dissolved phase upon an increase in the pH during Mn oxide reduction (Silburn et al., 2017). To prevent CO<sub>2</sub> concentrations below the detection limit, new CO<sub>2</sub> (4% of the headspace) was added to the Mn-AOM incubation with sediment from below the SMTZ after 49 days.

Every other week, a sample was taken from the medium with a N<sub>2</sub> purged syringe and needle through the stopper, which was used for the analysis of dissolved Mn and Fe (via ICP-OES, iCAP 6300 with detection limits of 0.02 and 0.18 μmol L<sup>-1</sup> for Mn and Fe, respectively), SO<sub>4</sub><sup>2-</sup> (via IC), H<sub>2</sub>S and dissolved Mn(II) and dissolved Mn(III) (spectrophotometrically, as described in Madison et al. (2011); Oldham et al. (2015)). Every four weeks, a sample was taken to determine dissolved CO<sub>2</sub>, including the CO<sub>2</sub> isotopes. A liquid sample of 0.5 ml was injected in an argon flushed 3 ml exetainer containing 1 ml 85% phosphoric acid and the headspace of the exetainer was injected into the GC-MS.

Samples for 16S rRNA amplicon sequencing were obtained at the start of the pre-incubations and from each bottle separately at the end of the incubation experiment of sediment from below the SMTZ (28 - 32 cm). These samples were processed as described in section 2.6.

## Results

### Methane oxidation in a shallow SMTZ

A distinct SMTZ was identified between 12 and 22 cm depth in the sediment at our study site (US2), characterized by strong counter gradients of sulfate and methane in the porewater (Fig. 1). A small fraction of the methane passed onwards to the zone above the SMTZ. Methane isotopic values of  $\delta^{13}\text{C}$  and  $\delta\text{D}$  were stable below the SMTZ, at values around  $-79\text{‰}$  and  $-265\text{‰}$ , respectively, and increased in the SMTZ to values of  $-61\text{‰}$  and  $-93\text{‰}$  (Fig. 1), respectively, indicating methane oxidation. Above the SMTZ, methane isotopic values were stable, apart from the uppermost 2 cm where both values increased.

Sulfate reduction rates were highest just above the SMTZ at a depth of 9 cm, reaching values of up to  $352 \text{ nmol cm}^{-3} \text{ d}^{-1}$  (Fig. 1). A second maximum in sulfate reduction rates was observed at the bottom of the SMTZ at a depth of 22 cm, reaching values of up to  $157 \text{ nmol cm}^{-3} \text{ d}^{-1}$ . Free sulfide was always below the detection limit in the porewater. Below the SMTZ, solid phase total S reached a maximum concentration of  $342 \text{ } \mu\text{mol g}^{-1}$  at 27 cm depth. A substantial part of the peak in total S, up to  $155 \text{ } \mu\text{mol g}^{-1}$ , consisted of FeS (Fig. 1).

Surface sediments were enriched in Mn and Fe oxides, reaching concentrations of up to  $106$  and  $379 \text{ } \mu\text{mol g}^{-1}$ , respectively (Fig. 1). At the upper boundary of the SMTZ, a peak in Mn oxides was present, which may partly consist of Mn phosphates dissolved in the same extraction step as the Mn oxides (Fig. S3 and table S1). Within the SMTZ, Mn oxide contents decreased to around  $20 \text{ } \mu\text{mol g}^{-1}$  and Fe oxide contents decreased from  $46 \text{ } \mu\text{mol g}^{-1}$  to  $0 \text{ } \mu\text{mol g}^{-1}$ . Mn oxides remained around  $20 \text{ } \mu\text{mol g}^{-1}$  but Fe oxides emerged again below 29 cm depth, reaching concentrations of up to  $29 \text{ } \mu\text{mol g}^{-1}$ . Dissolved Mn and Fe increased rapidly in the upper few cm of the sediment to around  $400$  and  $200 \text{ } \mu\text{mol L}^{-1}$ , respectively, and subsequently decreased, but at different depths (Fig. 1). Deeper in the sediment the concentrations of both Mn and Fe increased again, with dissolved Mn and Fe reaching maxima of  $566 \text{ } \mu\text{mol L}^{-1}$  and  $670 \text{ } \mu\text{mol L}^{-1}$ , respectively.

The  $\text{C}_{\text{org}}$  content was  $\sim 2.5 \text{ wt\%}$  in the top 20 cm of the sediment and decreased to around  $2 \text{ wt\%}$  below a depth of 20 cm (Fig. 1). Concentrations of  $\text{NH}_4^+$ , DIC and alkalinity increased strongly in the top 20 cm of the sediment, indicating the highest rates of organic matter degradation in this zone (Fig. 1). Below 20 cm,  $\text{NH}_4^+$  continued to increase with depth, whereas DIC and alkalinity concentrations stabilized around  $12$  and  $13 \text{ mmol L}^{-1}$ , respectively. Values of  $\delta^{13}\text{C}$  of DIC were

close to  $-5.5$  ‰ near the sediment water interface and decreased to a minimum of  $-15.4$  ‰ within the SMTZ (Fig. 1). Below the SMTZ, the  $\delta^{13}\text{C}$  of DIC increased to  $0.7$  ‰. Porosity decreased from 0.95 at the sediment surface to  $\sim 0.90$  at 5 cm depth and remained near this value at greater depth (Fig. S3).

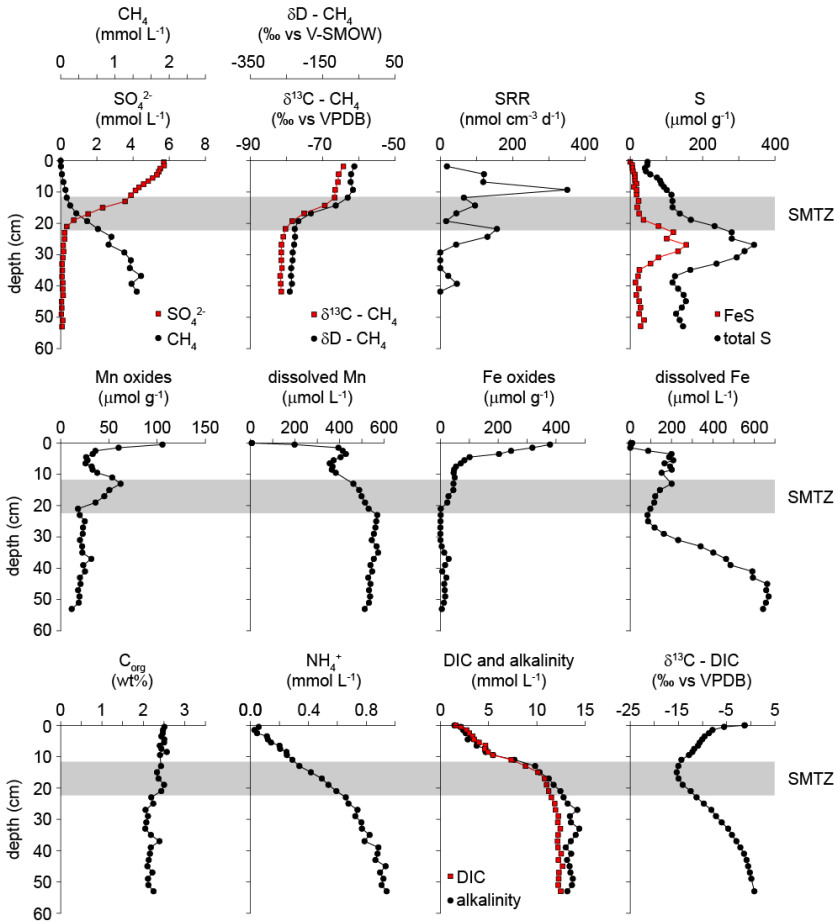


**Fig. 1** Pore water and sediment depth profiles and sulfate reduction rates for our study site US2. The zone indicated with gray shading indicates the SMTZ. The step used to determine Mn oxides may include Mn phosphates. Additional sediment Mn and Fe forms are shown in supplemental Fig. S4.

## Diversity of the microbial community

The 16S rRNA gene amplicon sequences revealed distinct communities of both archaea and bacteria, which in some cases were related to the boundaries of the SMTZ (Fig. 1 and 2). Ammonia-oxidizing archaea, unclassified *Nitrosopumilaceae* and '*Candidatus Nitrosopumilus*', covered  $> 65\%$  of all archaeal reads in the top 12 cm.

In the SMTZ (12 to 22 cm), ANME-2ab was the only methanotroph detected at a maximum abundance of 31%. Surprisingly, ANME-2ab even accounted for up to 61% of all archaeal reads in the interval from 24-34 cm below the SMTZ. We detected four abundant ANME-2ab ASVs with slightly different niches, with ASV\_1 dominating down to a depth of 34 cm, whereas the other ASVs were either more variable or restricted to the sediments below the SMTZ (Fig. S5). Below 28 cm, methanogenic genera *Methanosarcina*, *Methanoregula* and *Methanosaeta* together with Bathyarchaeia, appeared and became abundant from a depth of 34 cm onwards, indicating active methane production.

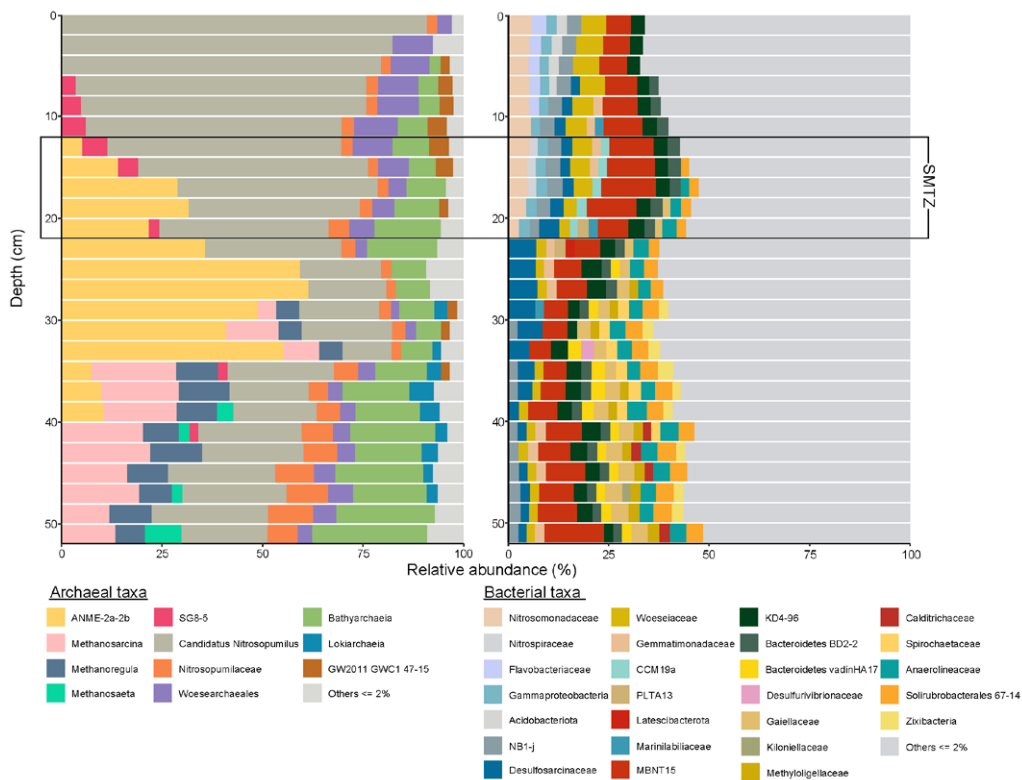


**Fig. 2** 16S rRNA gene amplicon sequencing relative abundances of archaeal DNA (left) and bacterial DNA (right). All taxa with < 2% abundance are grouped in 'Others'.

The bacterial community was highly diverse, with over 50% of taxa having a relative abundance of less than 2%. Despite this diversity, there was a clear difference in the most abundant taxa with sediment depth. Above and in the SMTZ (0 to 22 cm), *Nitrosomonadaceae*, *Nitrospiraceae*, *Flavobacteriaceae*, *Woeseiaceae*, unclassified Gammaproteobacteria, and the unclassified phylum NB1-j made up about 25%

of all bacterial reads. Between 18 and 34 cm depth, the SRB *Desulfosarcinaceae* was the most abundant bacterial group after the MBNT15 phylum, reaching up to 7% in relative abundance. Below 32 cm, bacterial diversity increased, with *Anaerolineaceae* and *Solirubrobacterales* being the most abundant taxa.

### Metabolic potential for sulfur, C1 and metal cycling

We sequenced the metagenomes from two depths, 16-20 cm (SMTZ) and 28-32cm (below the SMTZ), and in total 479 medium-quality (>50% completeness, <10% contamination) MAGs were obtained. These MAGs covered 38% (SMTZ) and 34 % (below the SMTZ) of the total metagenomic reads, thus a significant part of the community was not assembled and thus not analyzed. Based on the mapping of metagenomic reads (Fig. 3), the MAG with the highest relative abundance at both depths was *Defferimicrobium* (MAG US2\_17), which accounted for 4.4% of reads in the SMTZ and 2.0% below the SMTZ. As seen from the 16S rRNA gene amplicon profile of the sediment, the most abundant taxa differed significantly between the two depths. In the SMTZ, *Deferrimicrobiaceae* (US2\_15), Burkholderiales (US2\_35), Solirubrobacterales and Gammaprotebacteria (US2\_34) were the only bins with >1 % abundance. The sediment below the SMTZ was more diverse and only *Defferimicrobium* and Solirubrobacterales reached >1 % abundance. Curiously, MAGs representing likely SRBs (phylum Desulfobacterota) were higher in abundance below than in the SMTZ (Fig. 3). We recovered one ANME-2ab MAG (f\_\_Methanocomedenaceae; US2\_17) that, in line with 16S rRNA amplicon reads, was more abundant below the SMTZ (0.8%) when compared to the SMTZ (0.2%).

We screened the MAGs with > 0.2 % abundance at either depth for marker genes in S-cycling, C<sub>1</sub>-cycling and potential for extracellular electron transport (EET) or metal reduction/oxidation (Fig. 3). S-cycling potential was widespread across the MAGs, with dissimilatory sulfate reduction genes *dsrA* and/or *aprA* found in multiple MAGs that were more abundant below the SMTZ, such as the two Desulfobacterales MAGs. However, the sulfur-oxidizing Sulfomarinibacterales MAG (US2\_11) also encoded these genes and was more abundant in the SMTZ. In contrast, the sulfide:quinone oxidoreductase *sqr* was found in MAGs that were more abundant in the SMTZ and potentially used for sulfide detoxification. C<sub>1</sub>- cycle genes were scarce, indicating that the sediments harbor mainly heterotrophic clades. Only two MAGs with the marker gene for (reverse) methanogenesis, *mcrA*, were present; ANME-2ab (Methanocomedenaceae) and methanogenic *Methanoregula* (US2-13). Putative genes involved in EET and metal reduction/oxidation were found in multiple MAGs, which were often more abundant in the SMTZ (Fig. 3). Woeseiaceae MAG (US2\_43) encoded multiple cytochrome c or membrane proteins involved in electron

transfer across the membranes, i.e. RnfC from a complex that translocates proteins across the membrane and MtrA, MtrB and MtrC from the decaheme-cytochrome *c* that transfers electrons to the outer membrane. OmcS, OmcF and OmcZ, outer membrane cytochromes linked to metal reduction via EET, were present in a few genomes such as Desulfobacterota MAGs. Desulfobacterales\_UBA11574 that encoded OmcS, and the most abundant Deferrirombium that encoded OmcF. The ANME-2ab genome also showed potential for EET and metal reduction as RnfC and OmcZ homologue were detected in their genome.

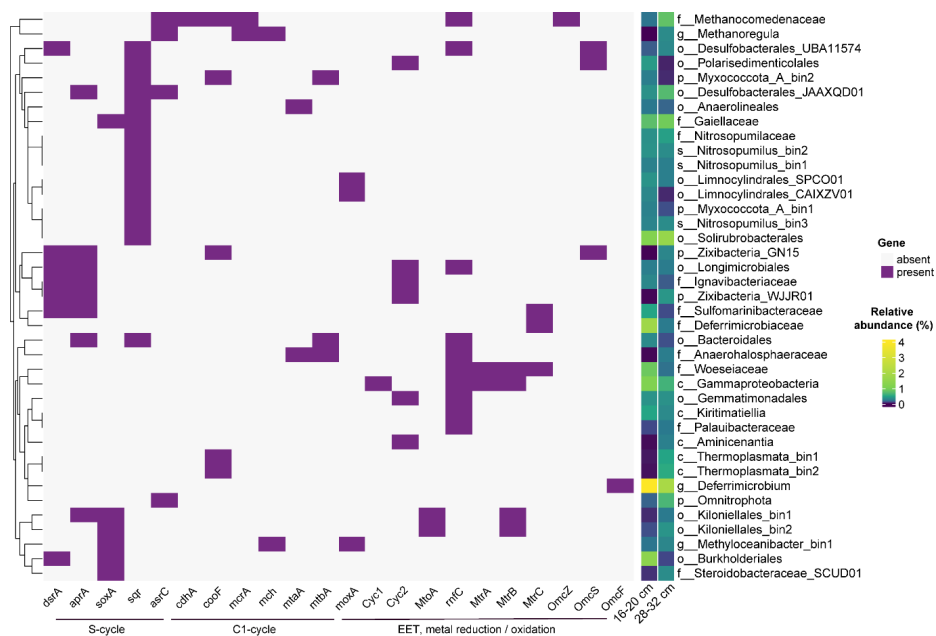


**Fig. 3** The metabolic potential of the most abundant MAGs (> 0.2% abundance at one depth) based on S-cycling genes (*dsrA*, *aprA*, *soxA*, *sqr*, *asrC*), C1-cycling (*cdhA*, *cooF*, *mcrA*, *mch*, *mtaA*, *mtbA*, *moxA*) and genes involved in metal reduction/oxidation or EET (*cyc1*, *cyc2*, *mtoA*, *mtrA*, *mtrC*, *omcZ*, *omcS*, *omcF*). The MAGs are named based on the lowest taxonomic rank with a classified name. The relative abundance of each MAG at the two depths is indicated in the two columns before the genome name.

### Metatranscriptomic analysis shows active ANME-2ab in the SMTZ

To identify the metabolically active members of the community that contribute to biogeochemical cycling, metatranscriptomes were sequenced from three replicates for each of the two depths. The analysis of mapped coding DNA sequence (CDS) reads revealed that the most active taxa were notably different from the most abundant taxa identified in the metagenomic DNA data (Fig. 3 and 4) as has been observed in other studies (e.g. Zhang et al., 2020). The proportion of unmapped reads was even

greater in the metatranscriptomic dataset than in the metagenomic dataset, as ~71 – 75 % of all transcripts did not map to the medium-quality MAGs analyzed. In the SMTZ, the most transcripts mapped to Aminicenantia\_bin2 (MAG US2\_47), which covered 12-22% of all CDS reads, and Xanthomonadales\_bin3 (US2\_56) with 7-8% relative abundance. Three putative SRBs, Desulfobacterales\_JAFDCJ01 (US2\_46), Desulfobacterales\_UBA11574 (US2\_27) and Desulfurivibrionaceae (US2\_55) covered ~6 % of the reads in the SMTZ, although they were either not in the top taxa at all or more abundant below the SMTZ in the metagenomic reads (Fig. S6). The Methanocomedenaceae (ANME-2ab) MAG had higher expression levels in the SMTZ than below the SMTZ with > 6 % and < 1% relative abundance, respectively.

The active community below the SMTZ differed greatly from that in the SMTZ (Fig. 4). In general, archaeal MAGs were much more abundant in the deeper layer, such as Bathyarchaeia and Thermoplasmata bins. However, almost a third of the transcripts (~20%) were covered by two Zixibacteria MAGs which were barely present in the SMTZ (0.001-0.2%).

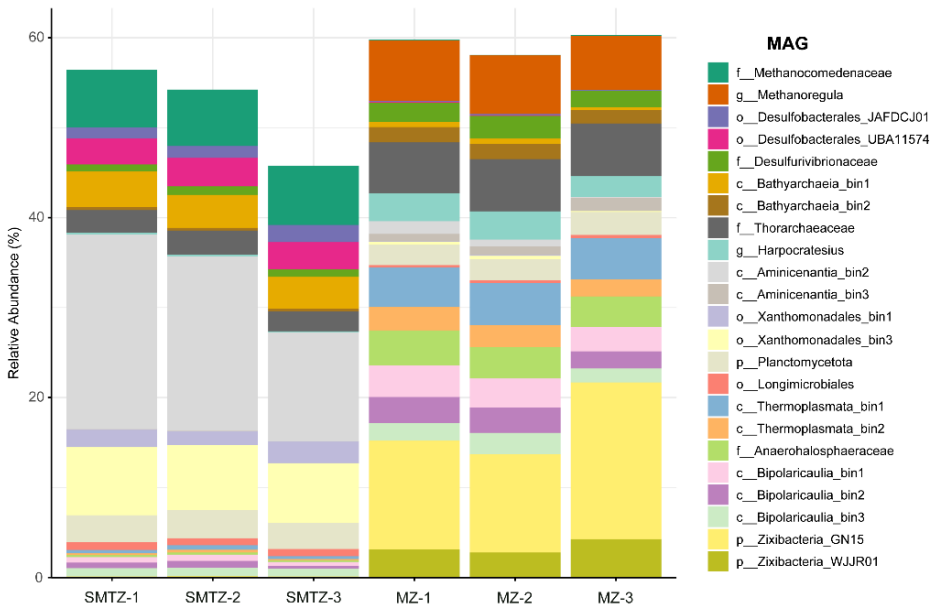


**Fig. 4** The relative abundance of expressed coding DNA sequence (CDS) reads of top MAGs at both depths (SMTZ: 16-20 cm; below the SMTZ in methanogenesis zone (MZ): 28-32 cm). Three replicates from each depth were sequenced for total RNA. The relative abundance here represents the percentage of total counts of coding genes per MAG detected in the transcriptome of each depth.

### Increased methane oxidation upon addition of electron acceptors

The potential of methane oxidation coupled to oxygen, sulfate, Mn and Fe oxide and graphene oxide, as an analogue for natural organic matter, was tested in sediment both from within the SMTZ (16 - 20 cm) and below the SMTZ (28 - 32 cm; Fig. 5). All incubations supplied with extra electron acceptor showed an increase in  $^{13}\text{C-CO}_2/^{12}\text{C-CO}_2$  ratio relative to the control where no electron acceptor was added, indicating active methane oxidation. Generally, the signal for methane oxidation was largest in the sediment from below the SMTZ (Fig. 5 and fig S8). Oxygen was the most effective electron acceptor added, inducing a methane oxidation rate of around  $216 \mu\text{mol cm}^{-3} \text{yr}^{-1}$  at both depths (Fig. 5 and fig S4). After oxygen, the highest methane oxidation rates were obtained with sulfate as electron acceptor with  $28.6 \pm 0.4$  and  $8.0 \pm 0.8 \mu\text{mol cm}^{-3} \text{yr}^{-1}$  for within and below the SMTZ, respectively. The methane oxidation rates in the Mn-, Fe- and NOM-AOM incubations were within a similar range, varying from 1.2 to  $3.3 \mu\text{mol cm}^{-3} \text{yr}^{-1}$  for sediments in the SMTZ and from 9.4 to  $15.5 \mu\text{mol cm}^{-3} \text{yr}^{-1}$  for those below the SMTZ.

Accumulation of  $\text{SO}_4^{2-}$  occurred in the  $\text{O}_2$ -MO (max.  $2.7 \text{ mmol L}^{-1}$  within the SMTZ and  $1.1 \text{ mmol L}^{-1}$  below the SMTZ), Mn-AOM (max.  $1 \text{ mmol L}^{-1}$  within the SMTZ and  $0.3 \text{ mmol L}^{-1}$  below the SMTZ) and NOM-AOM (max.  $0.3 \text{ mmol L}^{-1}$  within the SMTZ and  $0.5 \text{ mmol L}^{-1}$  below the SMTZ) incubations (Fig. S9). In the controls and Fe-AOM incubations, no  $\text{SO}_4^{2-}$  accumulated. Accumulation of  $\text{H}_2\text{S}$  was only observed in the S-AOM incubation from below the SMTZ (Fig. S9).

In the incubations where Mn oxide was added, dissolved Mn concentrations increased up to around  $2 \text{ mmol L}^{-1}$  within the first 30 days and subsequently stabilized for sediment from both depths (Fig. S9). Determination of the redox state of the dissolved Mn in incubations where Mn oxides were added showed that the accumulated dissolved Mn was almost exclusively Mn(II), indicating that reduction of Mn(IV) to Mn(II) occurs in one step and likely does not form dissolved Mn(III) as a reactive intermediate (Fig. S9). In the incubations with  $\text{O}_2$  as electron acceptor, accumulation of dissolved Mn up to a concentration of  $0.8 \text{ mmol L}^{-1}$  was also observed (Fig. S9). The other incubations had relatively stable dissolved Mn concentrations varying between  $0.2$  and  $0.4 \text{ mmol L}^{-1}$ .

In the incubations with Fe oxides, dissolved Fe increased from  $0.5$  to  $0.9 \text{ mmol L}^{-1}$  in the SMTZ and from  $0.2$  to  $0.5 \text{ mmol L}^{-1}$  in the incubation with sediment from below the SMTZ (Fig. S9). When  $\text{O}_2$  was added as an electron acceptor, dissolved Fe accumulated to values of up to  $1.1 \text{ mmol L}^{-1}$  and  $0.6 \text{ mmol L}^{-1}$  in the incubations with sediment from within and below the SMTZ, respectively. In the other incubations, dissolved

Fe was relatively stable or absent, apart from the incubations with graphene oxide, where the dissolved Fe concentrations fluctuated around  $0.2 \text{ mmol L}^{-1}$ .

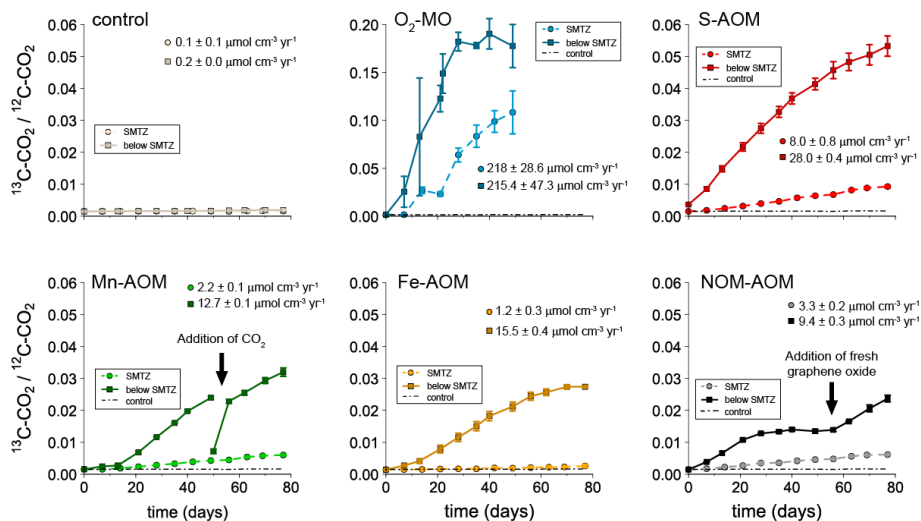


**Fig. 5**  $^{13}\text{C-CO}_2 / ^{12}\text{C-CO}_2$  ratios in the headspace of the incubation experiments for sediment from within the SMTZ (16–20 cm; circles) and from below the SMTZ (28–32 cm; squares). The  $\text{CH}_4$  oxidation rates are based on the increase in  $^{45}\text{C-CO}_2$  in the headspace and liquid of the incubations (Fig. S8). Note the different y-axis at the plot showing the  $\text{O}_2$ -MO incubations.

## ANME archaea drive methane oxidation in the AOM incubations

ANME-2ab was the most abundant archaeal taxa in the incubations with the deeper sediment layer, covering  $\sim 55\%$  of the total archaeal reads (Fig. S10). In the anoxic incubations, ANME reads increased significantly in the electron acceptor amended samples, but not in the control samples, underlining their role in AOM (Fig. 6a). Upon addition of Mn and Fe oxides, ANME-2ab increased by more than 20%, accounting for up to 75% of the relative archaeal abundance. *Methanosarcina* was the second most abundant archaea in all samples and increased the most in the control and graphene oxide treatments (3-fold and 2-fold, respectively).

The 16S rRNA gene amplicon analysis revealed distinct differences between the microbial community of incubations with oxygen versus other electron acceptors (Fig. 6). With oxygen, the largest changes in the bacterial community were seen in *Methylomonas* and *Methylotenera* which increased in relative abundance by 5–10%, indicating that dormant buried cells were activated upon oxygen amendment (Fig. 6b). In addition, potential sulfur oxidizing taxa *Sulfurimonas*, *Sulfurovum* and *Magnetovibrio* increased in these samples. Interestingly, the changes in the bacterial

community composition were highly substrate-dependent, although *Syntrophotalea* reads, of phylum Desulfobacterota, increased in all samples from <0.01% by 7-18%, the biggest increase was observed in the Fe-AOM and NOM-AOM treatments (Fig. 6b and Fig. S11). Also, other Desulfobacterota taxa increased, with *Trichloromonas* and *MSBL7* increasing in all but the control samples, whereas changes in other genera were more substrate-specific. Curiously, *SEEP-SRB1*, a putative SRB partner for ANME, increased only with sulfate, whereas other putative AOM syntrophs, uncharacterized Desulfobulbales, increased in Mn-AOM and Fe-AOM samples. The changes in heterotrophic bacteria involved in organic matter breakdown via fermentation, such as *Bacteroidetes*, were also substrate-specific (Fig. 6b).

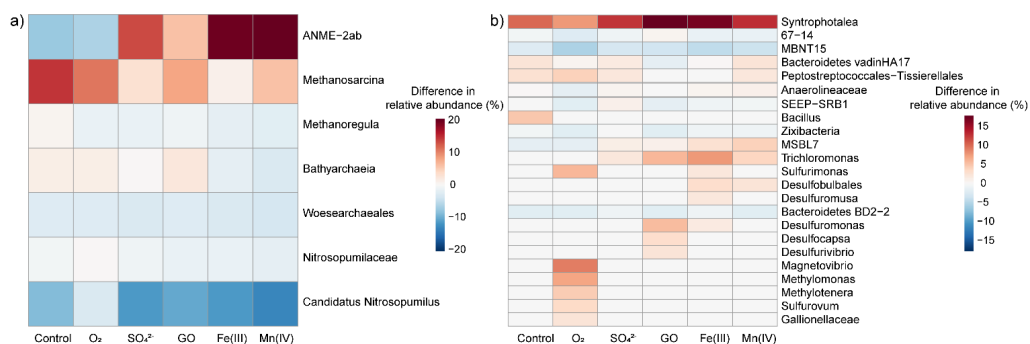


**Fig. 6** Changes in the relative abundance of microbial taxa in the sediment from below the SMTZ (28-32 cm) after the incubation with different electron acceptors compared to that at the start for (a) archaea and (b) bacteria.

## Discussion

### Two Distinct Zones of AOM

Our integrated analysis of sediments from the Bothnian Sea site reveals two vertically distinct zones of anaerobic oxidation of methane (AOM) which are both characterized by the presence of a metabolically versatile community of ANME-2ab archaea but differ in their porewater and sediment chemistry. The first is the canonical sulfate-methane transition zone (SMTZ), where AOM is primarily coupled to sulfate reduction. Here, multiple indicators point towards AOM *in-situ*. The second is a deeper, previously unrecognized zone below the SMTZ, where ANME-2ab persist and have the potential to couple AOM to a wide range of electron acceptors, although their *in-situ* activity appears to be limited. This finding is supported by a combination of geochemical profiling, DNA and RNA sequencing, and sediment incubation experiments, as discussed in detail below.

Active AOM in the SMTZ, which is located between depths of 12 and 22 cm (Fig. 1), is evident from the strong isotopic enrichment of  $^{13}\text{C}$  and D in the residual methane and depletion of  $^{13}\text{C}$  in DIC (Whiticar, 1999). This is corroborated by a peak in sulfate reduction and change in the gradient in porewater sulfate at the lower boundary of this zone, which is a typical feature in sediments where S-AOM occurs (Iversen & Jorgensen, 1985). Molecular analysis confirms these observations, with a high relative abundance of ANME-2ab archaea (a maximum of 31% of archaeal sequences) co-occurring with putative partner sulfate-reducing bacteria from the *Desulfosarcinaceae* family (Schreiber et al., 2010; Murali et al., 2023; Fig. 2). Furthermore, metatranscriptomic data reveal that the ANME-2ab gene transcripts are highly expressed within the SMTZ, accounting for over 6% of mapped transcripts. Besides sulfate, the SMTZ at our site also contains Mn and Fe oxides and abundant organic matter (Fig. 1), which may all act as potential electron acceptors in AOM (Fig. 5). The addition of sulfate, manganese oxides, iron oxides, and graphene oxide to sediment incubations all stimulated AOM at rates comparable to previous incubation studies with sulfate (range of 2 - 52  $\mu\text{mol CH}_4 \text{ cm}^{-3} \text{ sed yr}^{-1}$ ; Beal et al., 2009; Segarra et al., 2013; Aromokeye et al., 2020), Fe oxides (range of 0.035 - 6  $\mu\text{mol CH}_4 \text{ cm}^{-3} \text{ sed yr}^{-1}$ ; Beal et al., 2009; Segarra et al., 2013; Egger et al., 2015; Aromokeye et al., 2020; Xu et al., 2021) and Mn oxides (range of 0.20 - 14  $\mu\text{mol CH}_4 \text{ cm}^{-3} \text{ sed yr}^{-1}$ ; Beal et al., 2009; Segarra et al., 2013; Xu et al., 2021). However, the accumulation of sulfate in the incubations amended with Mn and graphene oxide makes it difficult to distinguish direct metal-AOM from AOM coupled to a cryptic sulfur cycle in these treatments (e.g. Holmkvist et al., 2011; Su et al., 2020). Taken together, these results provide strong indications that ANME-2ab are the primary microorganisms actively mediating AOM in the SMTZ, with S-AOM as the dominant pathway.

More surprisingly, we identified a second, deeper zone of potential AOM below the SMTZ. Here, the relative abundance of ANME-2ab is even higher, peaking at 61% of the archaeal community between 24 and 34 cm. This zone is depleted in sulfate but contains solid phase Mn and, in a few depth intervals, iron oxides that have been buried below the current SMTZ. The methane isotope profile does not show a clear signal for oxidation in this deeper layer (Fig. 1), but an AOM signal could be masked by concurrent methanogenesis (Seifert et al., 2006), which, based on the relative abundance of methanogens, starts below a depth of 28 cm (Fig. 2).

Direct observations for the metabolic potential of this deeper community are derived from our sediment incubation experiments. The addition of sulfate, Mn oxides, Fe oxides and graphene oxides all stimulated AOM, with consistently higher rates compared to the sediment within the SMTZ (Fig. 5), possibly linked

to a higher initial ANME biomass (Fig. 2 and Fig. S6). In every anaerobic incubation for the sediment interval from 28-32 cm, the relative abundance of ANME-2ab increased significantly, particularly in the presence of metal oxides, where they finally constituted up to 75% of the archaeal community (Fig. 6). The sediment incubations indicate that the ANME-2ab are capable of oxidizing methane using sulfate and the alternative electron acceptors tested, although again a cryptic sulfur cycle cannot always be excluded. Notably, the lack of sulfate accumulation in the iron-amended incubations points towards a direct coupling between AOM and iron reduction. Direct metal-AOM by ANME-2ab is supported by our genomic data, which show that the ANME-2ab MAG recovered from this site encodes a homologue for OmcZ (Fig. 3), a multiheme cytochrome known to be involved in extracellular electron transfer to metals in bacteria (Gu et al., 2023), although its function in ANME is not confirmed. Notably, the ANME-2ab in this deeper community were detectable through metatranscriptomics (Fig. S7), although their activity was lower compared to the community within the SMTZ. This strongly suggests that this deep ANME-2ab population is not dormant.

### **Environmental relevance**

The existence of a deep, active ANME-2ab community may be explained by the recent environmental history of the site. Geochemical evidence suggests that the lower boundary of the SMTZ has become shallower over the past decades. This is based on a previously observed depth of approximately 28 cm for the lower boundary of the SMTZ at this site (Slomp et al., 2013) and on the mismatch between the current position of the SMTZ and the FeS and total S peak in the sediment (Fig. 1). In a setting where H<sub>2</sub>S is largely restricted to the SMTZ or, as is the case here, is absent from the porewater, such solid phase sulfur peaks are expected within the SMTZ and not below (Riedinger et al., 2014; Egger et al., 2015). The upward shift of the SMTZ at our study site has left a large population of ANME-2ab stranded in a now sulfate-depleted environment. Our data suggest that this community has remained active using one or more solid phase electron acceptors, possibly partly through a cryptic sulfur cycle, thereby establishing a second, deeper microbial filter for methane. Such a low rate of AOM fueled by other electron acceptors than sulfate could also explain the presence of ANME-2ab below the SMTZ at sites where upward shifts in SMTZ depth have not occurred recently (Aromokeye et al., 2020; Deng et al., 2020; Dalcin Martins et al., 2024). In conclusion, a deep microbial methane filter, driven by ANME-2ab below the SMTZ, could be a general feature in many coastal sediments.

Our findings have significant implications for our understanding of coastal methane cycling. Eutrophication is expected to continue to increase globally (Breitburg et

al., 2018). Variations in river runoff due to climate change may lead to a fluctuating supply of organic matter and metal oxides to coastal systems, especially at high latitudes (Canuel et al., 2012; Lenstra et al., 2018). Combined, this may lead to a large variability in the depth of the SMTZ and the availability of metal oxides, and potentially, humic substances, to methanotrophs. The versatility of ANME-2ab in using these electron acceptors is expected to contribute to a more resilient methane filter in coastal brackish sediments in two ways. First, a substantial amount of methane could be removed by ANME below the SMTZ via AOM pathways other than S-AOM, given the relatively large overlap of methane with electron acceptors like Fe and Mn oxides at many coastal locations (Egger et al., 2015; Aromokeye et al., 2020; Lenstra et al., 2023; Xiao et al., 2023). Second, a downward shift of the SMTZ, as predicted by reactive transport models upon a decrease in organic matter supply (Rooze et al., 2016), could directly enable S-AOM by the ANME-2ab community deeper in the sediment. Methanotrophic archaea have notoriously low growth rates and S-AOM is thus often limited by ANME biomass (Dale et al., 2006; Lenstra et al., 2023). Hence, a rapid start of S-AOM by ANME-2ab upon a downward shift of the SMTZ, could increase the efficiency of the methane filter.

The persistence and versatility of the ANME-2ab community in using a range of electron acceptors in AOM should be incorporated in computer models designed to predict methane dynamics in coastal sediments (Lenstra et al., 2023; Wallheimer et al., 2025). Future research should also focus on quantifying the *in-situ* rates of Mn-, Fe- and NOM-driven AOM in brackish coastal sediments and in determining the global distribution of such AOM systems to refine estimates and models of the marine methane budget in a changing world (Wallenius et al., 2021; Saunois et al., 2025).

### Data availability

The dataset for this study is available through Zenodo at <https://doi.org/10.5281/zenodo.16920164>. Sequencing data is available at the National Center for Biotechnology Information (NCBI) website under the accession number PRJNA1306556.

### Acknowledgements

We thank the captain and crew, Anna Palmbo Bergman and Nina Dagberg for assistance during sampling aboard the KBV 181. We thank Anita van Leeuwen, Arnold van Dijk, Carina van Veen, Coen Mulder, John Visser, Sebastian Krosse and Thom Claessen for analytical assistance in the lab. This research was funded by ERC Synergy grant MARIX 854088 and NESSC NWO-OCW 024002001.

## Supplement

### Supplementary figures

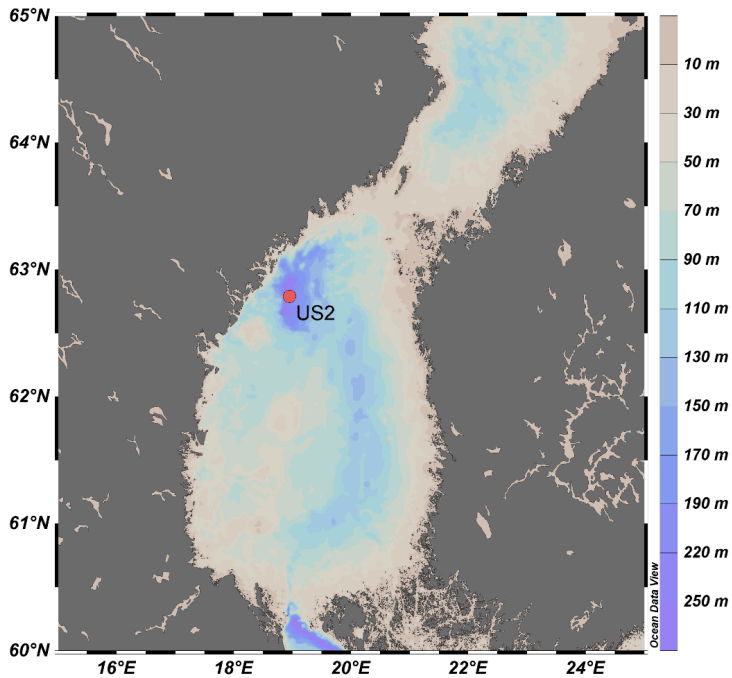


**Fig. S1** Map of the Bothnian Sea, including the location of site US2. Figure obtained with Ocean Data View (Schlitzer, 2023).

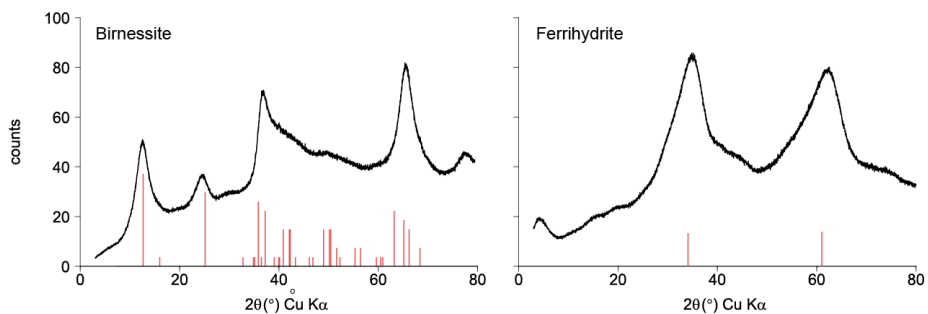


**Fig. S2** X-ray diffraction spectra of birnessite and ferrihydrite. The red bars indicate the theoretical positions of the  $2\theta$  peaks for birnessite (Lenstra et al., 2021b) and ferrihydrite (Das et al., 2011).

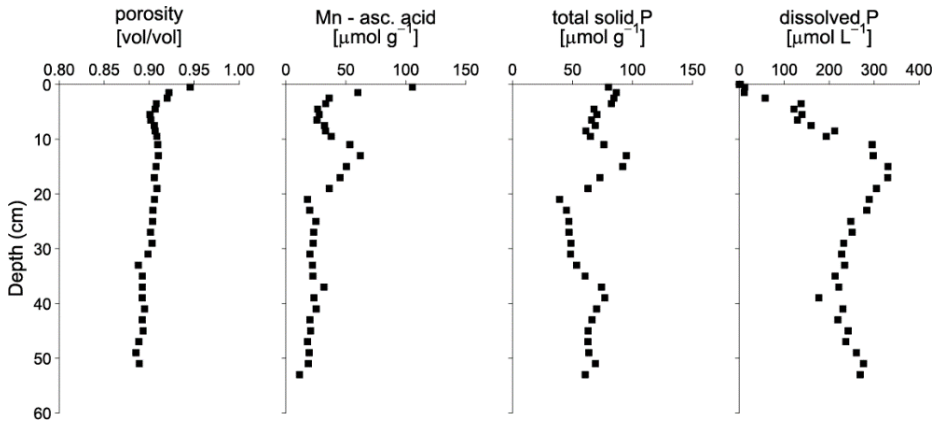


**Fig. S3** Sediment profiles of porosity, Mn extracted in ascorbic acid, total solid P and dissolved P. The maximum in Mn extracted in ascorbic acid between depths of 10 and 20 cm corresponds to a maximum in total solid P, which suggests that the peak represents a Mn phosphate phase. This zone also corresponds with the maximum dissolved P concentrations in the pore water.

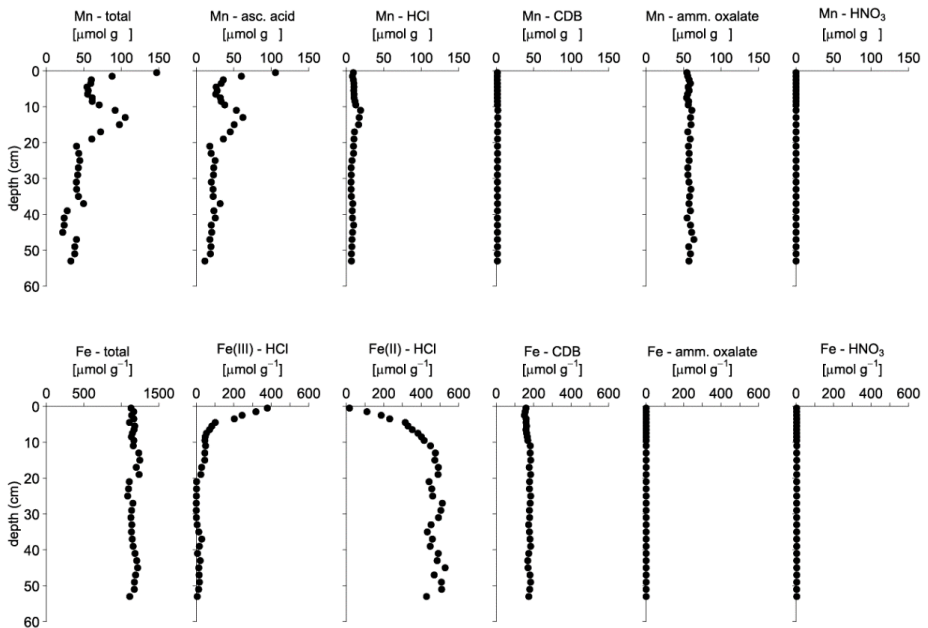


**Fig. S4** Sediment profiles of total Mn and Fe and from all steps in the sequential extractions. Ascorbic acid (asc. acid) extracts poorly ordered Mn oxides, HCl extracts Mn carbonates and easily reducible Fe(III) and Fe(II) minerals, sodium dithionite (CDB) extracts crystalline Fe and Mn oxides and Mn bound to clays, ammonium oxalate (amm. oxalate) extracts recalcitrant Fe oxides, crystalline Mn oxides and Mn bound to clays and HNO<sub>3</sub> extracts pyrite, including any associated Mn. Note the different range for the x-axis of Fe total.

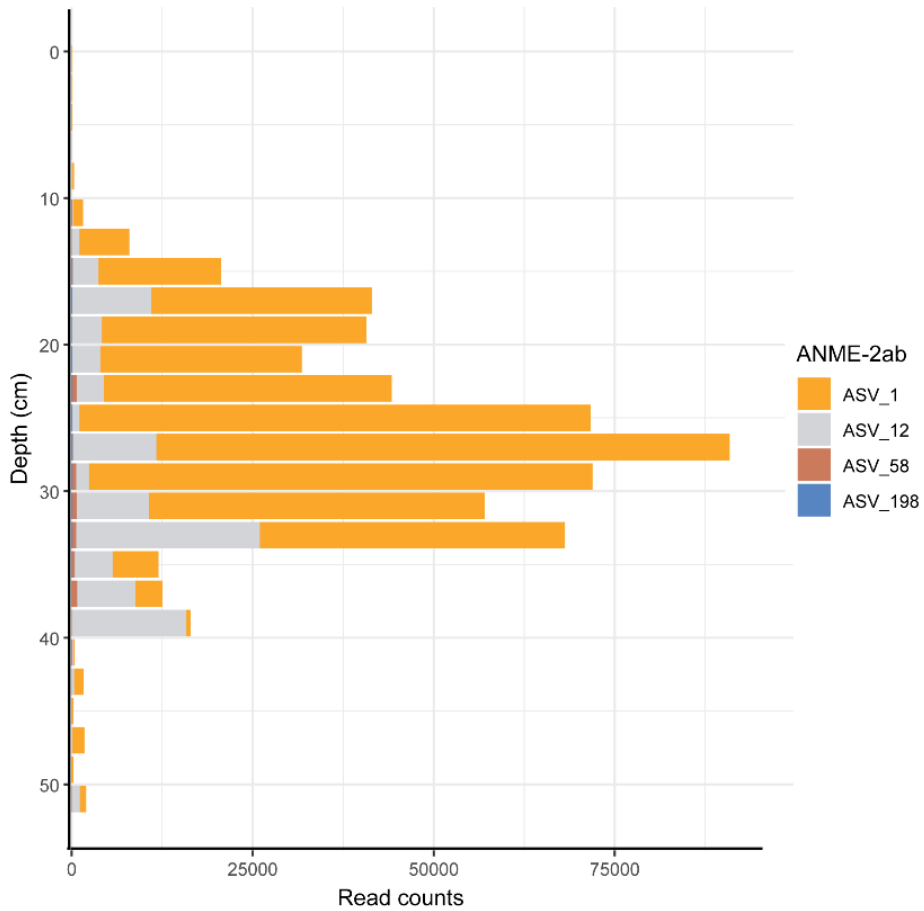


**Fig. S5** The total read counts of different ASVs assigned taxonomically to ANME-2ab across the sediment depths.

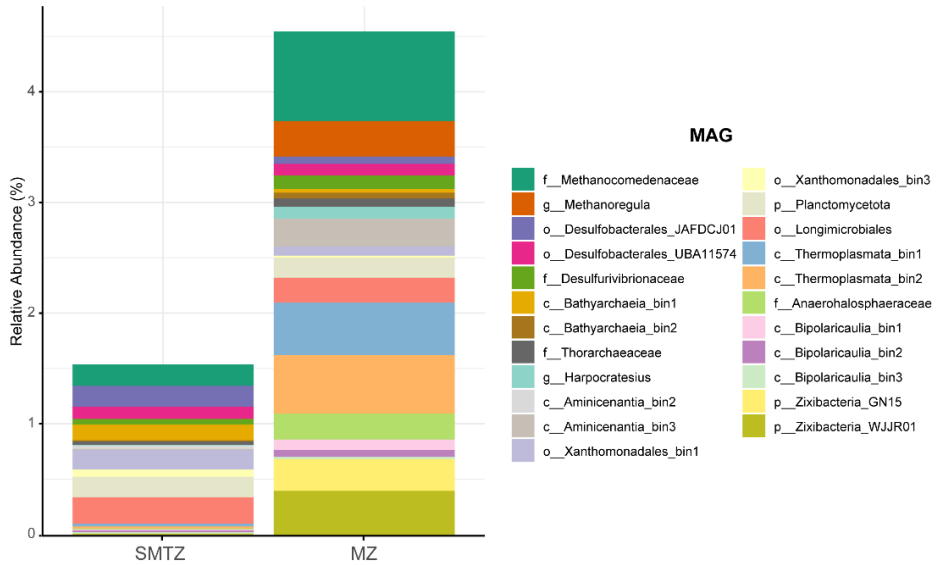


**Fig. S6** The MAGs with the highest coverage in metatranscriptome data (Fig. 4) in the SMTZ and below the SMTZ in the methanogenic zone (MZ), portrayed as relative abundance of reads mapped to the metagenome of each depth.

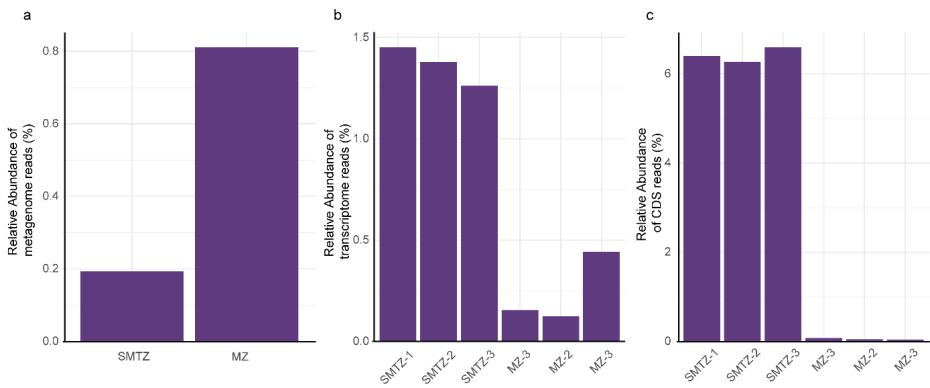


**Fig. S7** The abundance of ANME-2a MAG when mapped to a) the whole metagenome, b) the whole transcriptome; and c) the relative abundance of ANME-2a MAG CDS reads from all CDS reads mapped to analyzed MAGs in both the SMTZ and below the SMTZ in the methanogenic zone (MZ), portrayed as relative abundance of reads mapped to the metagenome of each depth.

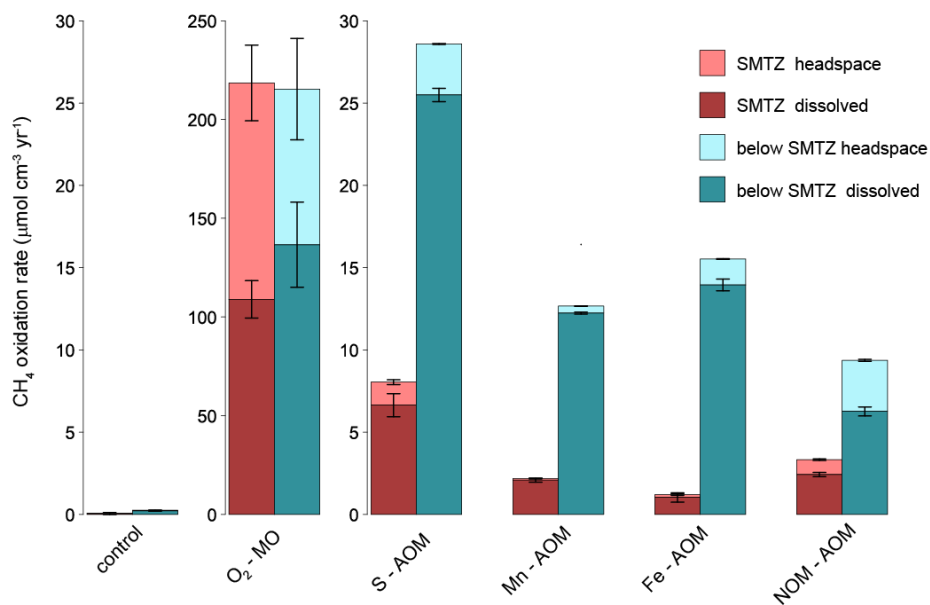


**Fig. S8** Maximum CH<sub>4</sub> oxidation rates in the different incubation experiments of sediment from within and below the SMTZ, calculated based on the increase in <sup>13</sup>C-CO<sub>2</sub> and <sup>12</sup>C-CO<sub>2</sub> in the headspace (lighter color) and the dissolved phase (darker color).



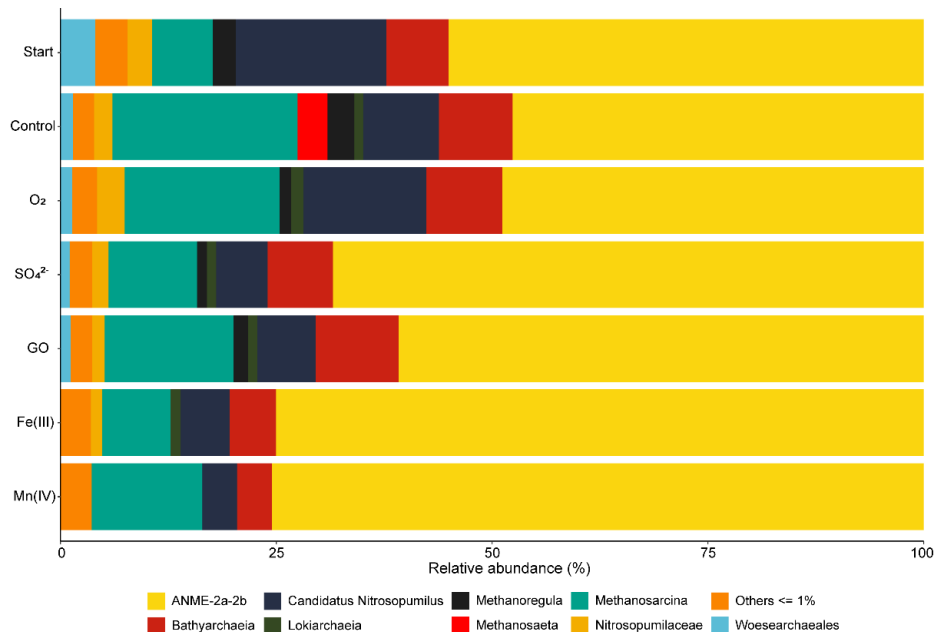


**Fig. S10** The relative abundance of archaeal taxa with >1% abundance in all AOM incubations and in the sediment at the start.

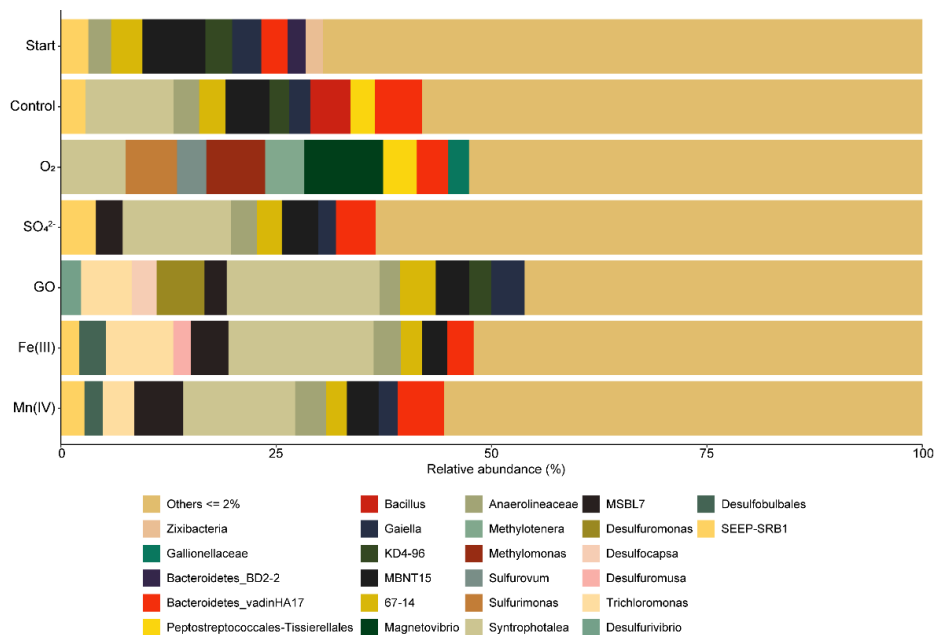


**Fig. S11** The relative abundance of bacterial taxa with >1% abundance in all AOM incubations and in the sediment at the start.

## Supplementary tables

**Table S1** Scheme for the sediment Mn extraction (Lenstra et al., 2021b)

Step	Extraction solution	Time of extraction (h)	Mineral phase targeted
1	0.17 M sodium citrate, 0.6 M sodium bicarbonate and 0.057 M ascorbic acid (pH 7.5)	24	Mn oxide and Mn phosphates
2	1 M HCl	4	Mn carbonate and Mn sulfides
3	50 g L <sup>-1</sup> sodium dithionite solution buffered with 0.35 M acetic acid/ 0.2 M sodium citrate to pH 4.8	4	Non-reactive Mn bound to clays
4	0.2 M ammonium oxalate / 0.17 M oxalic acid (pH 3.2)	6	Non-reactive Mn bound to clays
5	65% HNO <sub>3</sub>	2	Mn bound to and incorporated in pyrite

**Table S2** Scheme for the sediment Fe extraction (Kraal et al. (2017)

Step	Extraction solution	Time of extraction (h)	Mineral phase targeted
1	1 M HCl	4	Poorly ordered or pH-sensitive Fe(III) and Fe(II) minerals (e.g. ferrihydrite, siderite or Fe monosulfide)
2	50 g L <sup>-1</sup> sodium dithionite solution buffered with 0.35 M acetic acid/ 0.2 M sodium citrate to pH 4.8	4	Crystalline Fe oxides (goethite, hematite)
3	0.2 M ammonium oxalate / 0.17 M oxalic acid (pH 3.2)	6	Recalcitrant Fe oxides (magnetite)
4	65% HNO <sub>3</sub>	2	Pyrite

**Table S3** Composition of the artificial sulfate-free seawater (pH 7.5)

Compound	Concentration
NaCl	5.2 g L <sup>-1</sup>
MgCl <sub>2</sub> * 6 H <sub>2</sub> O	1 g L <sup>-1</sup>
CaCl <sub>2</sub> * 2 H <sub>2</sub> O	0.28 g L <sup>-1</sup>
KCl	0.1 g L <sup>-1</sup>
HEPES	20 mmol L <sup>-1</sup>



## Chapter 7

# Anaerobic oxidation of methane coupled to manganese oxide reduction by ANME-2ab in brackish coastal sediments

---

R. Klomp<sup>1</sup>, T.J. van Asselt<sup>2</sup>, E. Baas<sup>1</sup>, T. Behrends<sup>2</sup>, T. Berben<sup>1</sup>, R.A. Egas<sup>1</sup>, M.R. van Erk<sup>1,2</sup>, N.A.G.M. van Helmond<sup>1,2</sup>, P.A.G. ter Horst<sup>1</sup>, I.M.L. Rigutto<sup>1</sup>, T. Röckmann<sup>3</sup>, A.J. Wallenius<sup>1</sup>, O.M. Żygadłowska<sup>1,2</sup>, W.K. Lenstra<sup>1</sup>, M.S.M. Jetten<sup>1</sup>, C.P. Slomp<sup>1,2</sup>

<sup>1</sup>Department of Microbiology, Radboud Institute for Biological and Environmental Sciences, Radboud University, Heyendaalseweg 135, 6525AJ Nijmegen, the Netherlands

<sup>2</sup>Department of Earth Sciences, Utrecht University, Princetonlaan 8a, 3584 CB Utrecht, the Netherlands

<sup>3</sup>Institute for Marine and Atmospheric Research Utrecht, Utrecht University, Princetonplein 5, 3584CC Utrecht, the Netherlands

## Abstract

Methane (CH<sub>4</sub>) is a powerful greenhouse gas, and its emission from coastal systems is critically dependent on the balance between methanogenesis and CH<sub>4</sub> removal. Anaerobic oxidation of CH<sub>4</sub> (AOM) coupled to sulfate reduction is a key pathway, but the role of alternative electron acceptors, such as manganese (Mn) oxides, and the underlying microbial physiology remain elusive. Here, we examine the potential for Mn-driven AOM (Mn-AOM) in brackish coastal sediments at two sites in the Bothnian Sea. The overlapping presence of CH<sub>4</sub>, Mn oxides, dissolved Mn, and anaerobic methane-oxidizing archaea (ANME) of the clade ANME-2ab in sediment zones at the two sites points towards the potential for Mn-AOM. Laboratory incubations of sediment from these zones using <sup>13</sup>C-labelled CH<sub>4</sub> revealed stimulation of AOM upon addition of the Mn oxides, birnessite and pyrolusite, at one of the two sites. X-ray absorption spectroscopy of the sediment confirmed reductive dissolution of the added Mn oxides during the incubations. A role for cryptic sulfur cycling could be excluded since the addition of molybdate, an inhibitor for sulfate reduction, did not affect the Mn-AOM activity. In all incubations where AOM was stimulated by Mn oxides, members of ANME-2ab were the only methanotrophs and increased in relative abundance compared to the start and control. Metagenomic analysis revealed that the ANME-2ab genome encoded for all genes involved in the reverse methanogenesis pathway, and eleven multi-heme *c*-type cytochromes (MHCs), which can mediate extracellular electron transfer. Several MHCs of the ANME-2ab were similar to MHCs of freshwater metal-reducing ANME-2d, suggesting similar mechanisms for metal-driven AOM across ANME clades. These findings demonstrate that ANME-2ab can very likely couple Mn oxide reduction to CH<sub>4</sub> oxidation in brackish coastal sediments, highlighting that this process needs to be considered when studying CH<sub>4</sub> dynamics in coastal systems.

## Keywords

Anaerobic oxidation of methane, manganese oxides, coastal sediment, ANME

## Introduction

Methane (CH<sub>4</sub>) is a major greenhouse gas. In marine sediments, most CH<sub>4</sub> is produced by methanogenic archaea via methanogenesis (Reeburgh, 2007). Although typically a large fraction of the CH<sub>4</sub> is consumed through anaerobic and aerobic oxidation (Knittel & Boetius, 2009), part of the CH<sub>4</sub> may be released from the sediment, especially in coastal zones where the methanogenic zone is located close to the sediment-water interface (Hamdan & Wickland, 2016; Lapham et al., 2024; Żygadłowska et al., 2024). In coastal sediments, anaerobic oxidation of CH<sub>4</sub> (AOM) is the major sink for CH<sub>4</sub> (Wallenius et al., 2021), typically with sulfate (SO<sub>4</sub><sup>2-</sup>) as the main electron acceptor (Knittel & Boetius, 2009). However, metal oxides such as manganese (Mn) and iron (Fe) oxides can also act as an electron acceptor in AOM (Beal et al., 2009; Egger et al., 2015; Cai et al., 2018; Leu et al., 2020), and may account for an appreciable fraction of sedimentary CH<sub>4</sub> oxidation (Lenstra et al., 2023; Xiao et al., 2023). While in most aquatic sediments Fe oxides are more abundant than Mn oxides, bioenergetic modelling suggests that Mn oxides are thermodynamically more favorable as an electron acceptor in AOM (Wallheimer et al., 2025).

Manganese oxides are typically enriched in surface sediments and are generally removed via reductive dissolution upon burial into underlying anoxic sediments (Burdige, 1993). The dissolved Mn that forms can diffuse upwards into the oxic surface sediments and re-oxidize with oxygen, forming Mn oxides again (Slomp et al., 1997). Repeated Mn reduction and oxidation (“recycling”) at redox interfaces in sediments promotes the coupling of the Mn cycle to that of other elements such as sulfur and carbon (Burdige, 1993). Under non-steady state conditions, Mn oxides may be buried in anoxic, methanic sediments (Kasten et al., 1998; März et al., 2008; Riedinger et al., 2014; Lenstra et al., 2023). The concomitant presence of Mn oxides, CH<sub>4</sub> and elevated dissolved Mn in such settings has been interpreted to indicate Mn-AOM (Soyol-Erdene & Huh, 2013; Riedinger et al., 2014). However, there is, at present, no direct evidence for in-situ Mn-AOM in brackish coastal sediments.

Most studies of Mn-AOM have focused on freshwater systems. In such settings, Mn-AOM is commonly associated with members of the anaerobic methane-oxidizing archaea ANME-2d (family *Methanoperedenaceae*; Ettwig et al., 2016; Leu et al., 2020; Su et al., 2020). Using a bioreactor inoculated with freshwater sediment, it was shown that *Candidatus Methanoperedens manganicus* and *Ca. M. manganireducens* can directly couple reduction of Mn oxides to CH<sub>4</sub> oxidation, likely via extracellular electron transport using multiheme *c*-type cytochromes (MHCs; Leu et al., 2020). Manganese oxides can also stimulate oxidation of CH<sub>4</sub> by *Ca. Methanoperedens*

via cryptic sulfur cycling, in which  $\text{SO}_4^{2-}$  is produced upon oxidation of reduced sulfur compounds by Mn oxides (Su et al., 2020; Echeveste Medrano et al., 2025). Mn-AOM has also been suggested to occur in marine sediments (Beal et al., 2009), with ANME of the clade ANME-2ab (family *Methanocomedenacea*; Chadwick et al., 2022) proposed to be involved (Xu et al., 2021). Nonetheless, the identity and physiology of microorganisms contributing to Mn-AOM remain largely unresolved (Wallenius et al., 2021; Xue et al., 2025).

In this study, we assess the potential for Mn-AOM - including the microbial players involved - in metal- and  $\text{CH}_4$ -rich brackish coastal sediments characterized by non-steady state conditions. We focus on two sites in the Bothnian Sea (US5B, F26), combining sediment and porewater profiles from multi- and gravity cores. We use, amongst others,  $\text{CH}_4$  isotopic signatures to assess the zone where AOM likely occurs, X-ray absorption spectroscopy and sequential extractions to determine the sediment Mn speciation and 16S rRNA analyses to assess the composition of the microbial community. The microbial potential for Mn-AOM was determined via sediment incubations, using  $^{13}\text{C}$ -labelled  $\text{CH}_4$  and the addition of the Mn oxides birnessite and pyrolusite. Metagenome analyses were applied to identify the key microbial players in Mn-AOM in the incubations and to identify the genes that could be involved in the process. Our results show that ANME-2ab likely directly couple Mn reduction to  $\text{CH}_4$  oxidation, potentially through extracellular electron transfer (EET) and may contribute to AOM in brackish coastal sediments.

## Materials and Methods

### Site description

The two study sites, US5B (62°35'10.3" N 19°58'7.7" E; 232 m water depth; Fig. S1) and F26 (61°59'2.0" N 20°3'49.3" E; 150 m water depth; Fig. S1) are located in the Bothnian Sea, a brackish oligotrophic sea in the northern part of the Baltic Sea. Sediments rich in Mn oxides are widespread in the region (Slomp et al., 2013) with frequent burial and reduction of Mn oxides below the sulfate-methane transition zone (SMTZ). This unusual redox zonation has been ascribed to a shoaling of the SMTZ due to enhanced eutrophication and increased rates of sediment accumulation (e.g. Slomp et al., 2013; Egger et al., 2016; Lenstra et al., 2018). At site US5B, Fe-AOM has been demonstrated, which was linked to ANME-2ab (Egger et al., 2015; Rasigraf et al., 2020).

The Bothnian Sea formed at the end of the last glacial period as a freshwater lake (Jilbert et al., 2015). Sea level rise after the last ice age resulted in a permanent

connection with the North Sea and the establishment of brackish/marine conditions between 8000 and 7000 years ago (Andrén et al., 2011). This transition from freshwater to brackish conditions is characterized by a sedimentary enrichment in organic C and Mn carbonate (Jilbert et al., 2015; Häusler et al., 2017). At present, bottom waters are brackish and permanently oxygenated (Polyakov et al., 2022). Anthropogenic activities have led to an increase in nutrient input to the Bothnian Sea, and associated eutrophication of the basin over the past decades (Kuliński et al., 2022).

The histories of sediment accumulation rate at sites US5B and F26 differ considerably. The transition from freshwater to brackish/marine conditions, which is visible as a distinct change in the sediment lithology in Bothnian Sea sediments (Virtasalo et al., 2016), is situated at a depth of 3 m at US5B and at a depth of 5 m at F26 (Baas et al., *subm.*). This indicates that the average rate of sediment accumulation over the past ~7500 years at site US5B was lower than at site F26. Anthropogenic pollution of lead (Pb) in the Baltic Sea was at a maximum in the 1970s and can be traced back in the sediment record (Zillén et al., 2012). This indicates that the upper ~100 cm of the sediment at US5B and the upper ~20 cm at F26 were deposited in the last 50 years (Baas et al., *subm.*). These estimates lie within the range of recent sediment accumulation rates for these sites based on  $^{137}\text{Cs}$  dating (Mattila et al., 2006; Slomp et al., 2013).

### **Sediment and porewater collection**

In July 2023, sediment cores were collected on board the RV *Pelagia* using a multicorer (Oktopus GmbH, Germany) with 10 cm diameter transparent core liners to sample the upper 50 cm of the sediment and a gravity coring device to retrieve cores with a maximum length of 6 m. Upon core recovery, the gravity core was cut vertically into 100 cm sections and capped.

The sediment from a multicore and the 100 cm sections of the gravity core were directly sampled after core retrieval for porewater  $\text{CH}_4$  concentrations using core liners with pre-drilled holes with a 2.5 and 10 cm spacing, respectively, that were taped prior to coring. Samples of 10 mL were taken with cutoff syringes from each hole and immediately transferred to a 65 mL glass bottle filled with saturated salt solution. The bottles were stoppered, capped, and stored upside down until analysis. Note that degassing of  $\text{CH}_4$  may occur during sampling, which can lead to an underestimation of the total  $\text{CH}_4$  concentrations in the porewater, especially with high  $\text{CH}_4$  concentrations (Egger et al., 2017; Jørgensen et al., 2019).

Another multicore and the 100 cm sections of the gravity core were sampled for chemical analysis of the bottom water, porewater and solid phase. A detailed

description of the sampling procedure is provided in the supplementary materials Section 1. Porewater was collected via centrifugation and subsampled for the analysis of sulfide ( $\text{H}_2\text{S}$ ), dissolved inorganic carbon (DIC), ammonium ( $\text{NH}_4^+$ ),  $\text{SO}_4^{2-}$  and dissolved Mn. For  $\text{H}_2\text{S}$ , samples were pipetted into polypropylene vials and diluted 4 times with a degassed solution of 8 mL 1 mmol  $\text{L}^{-1}$  NaOH. Samples for DIC were diluted 9.8 times in a degassed solution of 7.5 g NaCl/L in polypropylene vials. For the analysis of  $\text{NH}_4^+$ , samples were stored in polyethylene vials at 4°C. Samples for  $\text{SO}_4^{2-}$  analysis were stored in polypropylene vials at 4°C. The samples for dissolved Mn were stored at 4°C in a polypropylene centrifuge tube, after acidification with 10  $\mu\text{L}$  suprapur HCl (30%) per mL of sample. Samples for  $\text{H}_2\text{S}$ , DIC and  $\text{NH}_4^+$  were analyzed on board within 24 hours after sample collection. The sediment residues were stored frozen at -20°C in  $\text{N}_2$  purged aluminum bags until further processing for the analysis of organic carbon ( $\text{C}_{\text{org}}$ ), total S and Mn mineral speciation.

A multicore was sectioned for DNA isolation under ambient atmospheric conditions at a sampling resolution of 2 cm (0 – 4 cm depth) and 4 cm (remainder of the core). The sediment was transferred into 50 mL centrifuge tubes, snap frozen with liquid  $\text{N}_2$  and stored at -80°C until further processing.

Sediment for DNA isolation and for incubation material was collected from the gravity core after the 100 cm sections of the core were split open into two equal parts. For each core section, sediment slices capturing a depth interval of 3 cm were collected at a 20 cm resolution. For DNA analysis, the sediment was transferred into 50 mL centrifuge tubes, snap frozen with liquid  $\text{N}_2$  and stored at -80°C until further processing. The incubation material was transferred into plastic bags that were immediately flushed with  $\text{N}_2$ , placed in  $\text{N}_2$ -purged aluminum bags and stored at 4°C.

### **Porewater analysis**

Concentrations of  $\text{H}_2\text{S}$ , DIC and  $\text{NH}_4^+$  were measured using two continuous gas-segmented flow QuAAtro Auto-Analysers (SEAL Analytical) using a LED as light source. The  $\text{H}_2\text{S}$  content was determined using para-aminodimethylaniline and ferric chloride (Grasshof and Chan 1969; limit of detection of 0.04  $\mu\text{mol L}^{-1}$ ), DIC was measured using the inversive chemistry spectrophotometer method (Stoll et al. 2001; limit of detection of 5.4  $\mu\text{mol L}^{-1}$ ) and  $\text{NH}_4^+$  was analyzed using phenol and sodium hypochlorite (Helder and De Vries 1979; limit of detection of 0.1  $\mu\text{mol L}^{-1}$ ). Porewater  $\text{SO}_4^{2-}$  was analyzed using ion chromatography (IC; Methrom 930 Compact IC Flex; detection limit for  $\text{SO}_4^{2-} < 0.01 \text{ mmol L}^{-1}$ ). Dissolved Mn was analyzed via Inductively Coupled Plasma-Optical Emission Spectroscopy (ICP-OES; iCAP 6300 with detection limits for Mn of 0.02  $\mu\text{mol L}^{-1}$ ).

Before the CH<sub>4</sub> analysis, 10 mL of N<sub>2</sub> headspace was injected into each bottle. After an equilibration phase of 7 days, CH<sub>4</sub> in the headspace was measured on a Thermo Finnigan Trace™ gas chromatograph (flame ionization detector; limit of detection for CH<sub>4</sub> of 0.02 mmol L<sup>-1</sup>). The isotopic composition of CH<sub>4</sub>, i.e. δ<sup>13</sup>C and δD, was analyzed by Continuous Flow- Isotope Ratio Mass Spectrometry (CF-IRMS; Brass & Röckmann, 2010; Sapart et al., 2011).

### Solid phase analysis

The sediment samples were freeze-dried and ground with an agate mortar and piston under a N<sub>2</sub> atmosphere and used for the analysis of sediment C<sub>org</sub>, total S and Mn, FeS and the Mn mineral speciation. For the analysis of C<sub>org</sub>, an aliquot of around 300 mg was decalcified using 1 M HCl (two step wash; Van Santvoort et al., 2002), dried, weighed and powdered. The decalcified aliquot was analyzed using an elemental analyzer (Elementar, Vario Micro Cube) after which C<sub>org</sub> was determined following correction for the weight loss during decalcification (analytical uncertainty based on duplicates, n = 12, was not larger than 0.037 wt.%). Total S and Mn were analyzed as described in (Baas et al., *subm.*). The average analytical uncertainty for S and Mn based on duplicates (n = 37) was always <16.5 % and <10 %, respectively. Aliquots of approximately 300 mg were used to determine the FeS content of the sediment, using the passive diffusion method described by Burton et al. (2008). The analytical uncertainty for FeS based on duplicates (n = 3) was < 14 %.

A sediment aliquot of ca. 100 mg was used to determine the solid phase Mn speciation using a 5-step sequential extraction (Lenstra et al. 2021b). In the first step, Mn oxides and Mn phosphates are extracted in an ascorbic acid solution. The second step extracts Mn carbonates and Mn sulfides in 1 M HCl. In the third and fourth step, crystalline Mn oxides and Mn associated with clay minerals are extracted in a sodium dithionite and an ammonium oxalate solution, respectively. The fifth step extracts Mn incorporated in pyrite minerals in 65 % HNO<sub>3</sub>. The average analytical uncertainty for the sequential extractions based on duplicates (n = 13) was < 13.2 % for all fractions.

### Incubation experiment

The potential for Mn-AOM was tested using incubations with sediment from zones of the gravity cores where Mn oxides, CH<sub>4</sub> and dissolved Mn were present (Fig. 1, 3). For US5B, sediment from the depth intervals 75.75 – 78.75 cm and 95.75 – 98.75 cm was combined. For F26, we combined sediments from the depth intervals 345 – 348 cm and 365 – 368 cm. Incubations were started in duplicate within 4 months

after collection of the sediment with a pre-incubation of one week where the electron acceptors,  $\text{SO}_4^{2-}$  or Mn oxide (birnessite or pyrolusite; Table 1), were added to the sediment to remove as much FeS from the sediment as possible, preventing a cryptic sulfur cycle in the subsequent incubations where AOM was tested. After the pre-incubations, the sediment was amended with  $^{13}\text{C-CH}_4$  and fresh electron acceptor. Molybdate ( $\text{MoO}_4^{2-}$ ) was added to a selection of the incubations with birnessite, to inhibit  $\text{SO}_4^{2-}$  reduction and suppress a cryptic sulfur cycle (Stoeva & Coates, 2019). Besides incubations with  $^{13}\text{C}$ -labelled  $\text{CH}_4$ , sediment was also incubated with  $^{13}\text{C}$ -labelled acetate and birnessite, to monitor heterotrophic Mn oxide reduction. See Table 1 for all treatments. A detailed explanation on substrate preparation and the start of the incubations can be found in the supplementary materials Section 2.

**Table 1** Substrate additions in the incubation experiment.

Name	Added e <sup>-</sup> donor	Added e <sup>-</sup> acceptor	Concentration e <sup>-</sup> acceptor*
no substrate control	-	-	-
$\text{CH}_4$ control	$^{13}\text{C-CH}_4$	-	-
$\text{CH}_4$ control + molybdate**	$^{13}\text{C-CH}_4$	-	-
Sulfate	$^{13}\text{C-CH}_4$	$\text{SO}_4^{2-}$	10 or 20 mmol L <sup>-1</sup>
Sulfate + molybdate**	$^{13}\text{C-CH}_4$	$\text{SO}_4^{2-}$	10 mmol L <sup>-1</sup>
Birnessite	$^{13}\text{C-CH}_4$	Birnessite	7.5 mmol L <sup>-1</sup>
Birnessite + molybdate***	$^{13}\text{C-CH}_4$	Birnessite	7.5 mmol L <sup>-1</sup>
Pyrolusite	$^{13}\text{C-CH}_4$	Pyrolusite	7.5 mmol L <sup>-1</sup>
Acetate**	$^{13}\text{C-acetate}$	Birnessite	7.5 mmol L <sup>-1</sup>

\*Note that in the pre-incubations, Mn oxides were added in a concentration of 4 mmol L<sup>-1</sup> in all relevant treatments. \*\*In the  $\text{CH}_4$  control and sulfate incubations, molybdate was added to one of the duplicates after 100 days of incubation \*\*\*In the incubations with birnessite, molybdate (10 mM) and labelled acetate (2.5 mM) were added after the pre-incubations.

The headspace concentrations of  $^{13}\text{C-CO}_2$  and  $^{12}\text{C-CO}_2$  were determined weekly on a gas chromatograph coupled to a mass spectrometer (GC-MS; Agilent 5975C inert MSD). Every other week, the supernatant was sampled through the stopper using a syringe with a sterile needle, for the analysis of dissolved Mn,  $\text{SO}_4^{2-}$  and  $\text{H}_2\text{S}$ . The samples for  $\text{SO}_4^{2-}$  and dissolved Mn were stored and analyzed as described above. Samples for  $\text{H}_2\text{S}$  were diluted five times in a 2 % Zn-acetate solution in a glass vial and stored at 4°C until spectrophotometric analysis using an acidified solution of phenylenediamine and ferric chloride, where  $\text{H}_2\text{S}$  is the sum of  $\text{S}^{2-}$ ,  $\text{HS}^-$  and  $\text{H}_2\text{S}$  (detection limit of 1  $\mu\text{mol L}^{-1}$ ; Cline, 1969). The sediment was sampled for DNA isolation prior to the pre-incubations and at the end of the incubations. The samples for DNA isolation were stored frozen (-20°C).

When Mn oxides were added, the concentrations of CO<sub>2</sub> in the headspace decreased, possibly linked to precipitation of Mn carbonate when dissolved Mn and alkalinity are high (Lenz et al., 2015), or to CO<sub>2</sub> drawdown into the liquid phase upon an increase in pH when Mn oxide reduction occurs (Silburn et al., 2017). When CO<sub>2</sub> concentrations became too low, the GC-MS was no longer able to measure the <sup>13</sup>C-CO<sub>2</sub> signal accurately and the <sup>13</sup>C-CO<sub>2</sub> / <sup>12</sup>C-CO<sub>2</sub> ratio decreases (Klomp et al., in prep.). To prevent a change in the CO<sub>2</sub> ratio due to low CO<sub>2</sub> concentrations, new CO<sub>2</sub> was added to the incubations where Mn oxides were added after 48 days at US5B and after 28 days at F26. This led to a reset of the <sup>13</sup>C-CO<sub>2</sub> / <sup>12</sup>C-CO<sub>2</sub> ratio. The decrease in CO<sub>2</sub> concentration in the headspace made it impossible to calculate reaction rates from the changes in <sup>13</sup>C-CO<sub>2</sub>.

To validate the effect of molybdate on SO<sub>4</sub><sup>2-</sup>-AOM and to obtain insight into the drivers of background CH<sub>4</sub> oxidation, 10 mmol L<sup>-1</sup> molybdate was added to one of the incubations with sediment from US5B amended with SO<sub>4</sub><sup>2-</sup> and to one of the CH<sub>4</sub> control incubations after 100 days of incubation (Table 1).

### **X-ray absorption spectroscopy**

To determine the Mn mineralogy, fluorescence X-ray absorption spectroscopy was performed on a selection of sediment samples in May 2025 on the Mn K-edge energy range (6500 – 6900 eV) at beamline BM23 at the European Synchrotron Radiation Facility (ESRF) in Grenoble, France (Mathon et al., 2015). For the sediment cores, a sample of the surface sediment, the incubated depth and, for US5B, the sediment just above the freshwater -brackish/marine transition was analyzed. For the incubations, samples from the start and end of the incubations of US5B sediment amended with <sup>13</sup>C-CH<sub>4</sub> and Mn oxides were analyzed. X-ray spectra for the analysis of the X-ray absorption near edge structures (XANES) were normalized and extracted using the ATHENA software package (v0.8.056; Ravel & Newville, 2005). The ATHENA software package was also used to perform linear combination fitting to identify and quantify the mineral phases of Mn, taking into account that phases present at low concentrations in the sediment may not always be detectable. Details on the procedure can be found in supplements section 3.

### **Microbial analysis**

The sediment collected for DNA analysis, both from the sediment profiles and incubations, was defrosted and homogenized. Approximately 0.2 g of sediment was transferred into a PowerBead tube from the DNeasy PowerSoil DNA isolation kit (Qiagen, Venlo, Netherlands). After the addition of lysis buffer, and to the samples from the sediment core additionally 100 µL DEPC water, the samples were

incubated at 65°C for 10 minutes. Subsequently, the samples were bead-beaten for 10 minutes at 50 s<sup>-1</sup> with a TissueLyser LT (Qiagen). DNA isolation was done according to the manufacturer's instructions. The quantity of DNA in the eluted sterile demineralized water was assessed by Qubit® 2.0 (Invitrogen, Waltham, Ma, USA). The isolated DNA was incubated at 65°C to de-activate DNase and stored frozen at -20°C until further analysis. The amount of sediment used and DNA extracted in the samples from the incubations is given in supplementary Table S2. For the sediment core, this information can be found in Fig. 1.

The DNA samples from the incubations with sediment from US5B amended with <sup>13</sup>C-CH<sub>4</sub> were sent for 16S rRNA gene amplification to analyze changes in the microbial community over time in the incubations. The 16S rRNA gene amplification and downward processing of the data was performed as described in Wallenius et al. (2025). A detailed description of the software and parameters used can be found in supplementary materials Section 4.

Shotgun metagenomic sequencing (TruSeq PCR-Free (550 bp insert), NovaseqX platform, MacroGen, Amsterdam, The Netherlands) was carried out on a selection of the samples from the sediment core and a selection of samples from the incubations, *i.e.*, the start sample and the end points for the incubations with sulfate, birnessite and birnessite with molybdate. The samples from the sediment core were analyzed for microbial relative abundance, using SingleM (Woodcroft et al., 2025) and normalized with 'SingleM summarise' to observe the relative abundance of ANME-2ab (*Methanocomedenacea* family). The samples from the sediment incubation were assembled and binned according to an adapted version of a previously published in-house bioinformatics pipeline (In 't Zandt et al., 2019). A detailed description of the bioinformatics pipeline, the software and parameters used can be found in supplementary materials Section 4. The samples from the incubations were analyzed using Metascan (v1.2-beta, --nokegg; Cremers et al., 2022) to observe changes in the *mcr* gene abundance, indicative for the potential of both anaerobic methanotrophy and methanogenesis (Evans et al., 2019), and using FeGenie (Garber et al., 2020) to analyze variations in metal reduction genes between the different incubation bottles and the starting material.

## Results

### Sediment and porewater profiles

The sediment at both sites was relatively rich in  $C_{org}$ , with a background of 2-3 wt% for the brackish sediments (Fig. 1). At site US5B, the freshwater sediments were lean in organic carbon and an enrichment in  $C_{org}$  was observed directly above the freshwater – brackish/marine transition at ca. 300 cm depth. At US5B, a strong enrichment in total S of almost 300  $\mu\text{mol g}^{-1}$  was observed above the freshwater – brackish/marine transition, followed by a second enrichment in the upper 50 cm of the sediment, which partly consisted of FeS. At F26, total S mostly varied around 100  $\mu\text{mol g}^{-1}$  except for the upper 50 cm of the sediment where contents ranged up to ca. 50  $\mu\text{mol g}^{-1}$ . At this site, FeS was present at a relatively constant background content of around 25  $\mu\text{mol g}^{-1}$  below a depth of 50 cm.

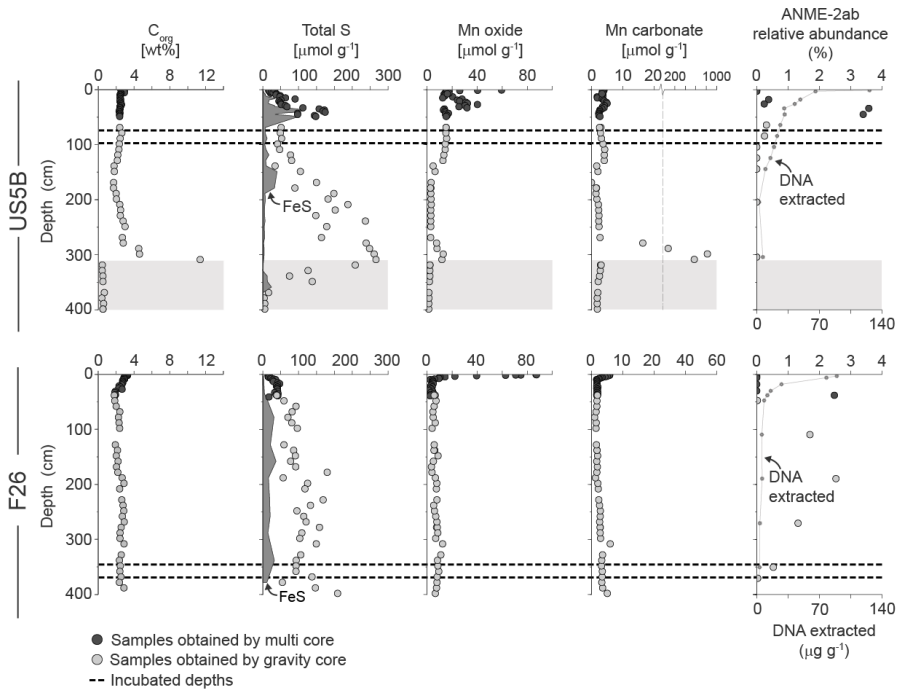


**Fig. 1** Sediment profiles of  $C_{org}$ , total S, Mn oxide and Mn carbonate, amount of DNA extracted and relative abundance of ANME-2ab in the total microbial community for sites US5B and F26 in July 2023. The horizontal dashed lines indicate the sediment depths used for incubations. Note the change in the x-axis for Mn carbonate at US5B. The profiles of all sediment Mn forms are shown in supplementary Fig. S3. The shading in the panel for US5B represents the freshwater sediments.

The surface sediment was enriched in Mn oxides at both sites, but Mn oxides also persisted at depth (Fig. 1). For example, sediment Mn oxide contents of ca.  $15 \mu\text{mol g}^{-1}$  were observed in the upper 150 cm of the sediment at site US5B and of up to  $10 \mu\text{mol g}^{-1}$  around 350 cm depth at site F26. The sediment of US5B was enriched in Mn carbonate directly above the freshwater – brackish/marine transition, reaching a maximum content of  $820 \mu\text{mol g}^{-1}$ . At this site, Mn carbonate contents were also elevated in the upper 150 cm of the sediment. At F26, only the surface sediment and the sediment below a depth of 200 cm contained appreciable Mn carbonates. The other Mn phases showed little change with depth, with the exception of the sediments deposited directly after the freshwater – brackish/marine transition at US5B; in these sediments Mn enrichments were observed in the extraction steps targeting crystalline Mn oxides, Mn oxides bound to clays and Mn associated with pyrite (Fig. S3).

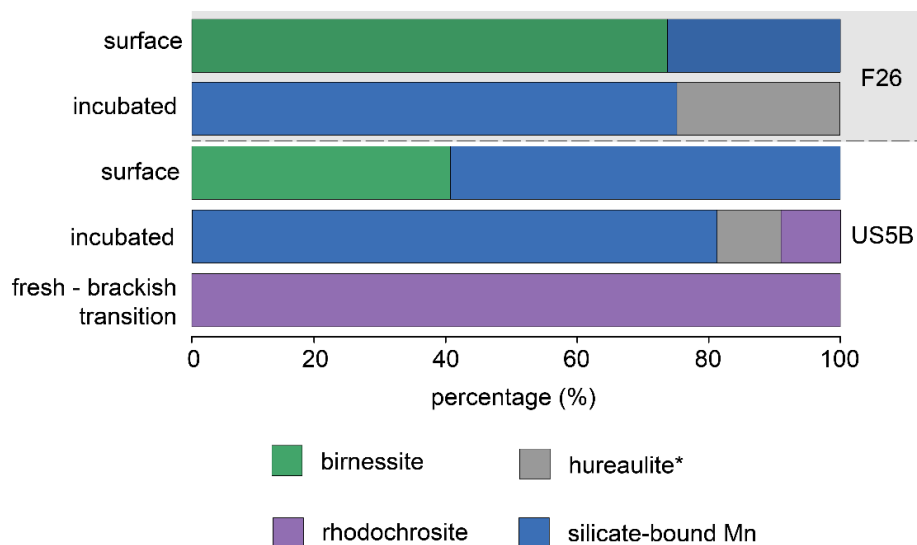


**Fig. 2** Results of linear combination fitting based on the XANES spectra (for spectra, see Fig. S4) from the surface sediment and the incubated sediment at US5B (0.75 cm and 78.75 cm depth, respectively) and F26 (0.75 cm and 358 cm depth, respectively). For US5B, also sediment from the freshwater – brackish/marine transition (298.75 cm depth) was analyzed. The outcome includes birnessite, rhodochrosite ( $\text{MnCO}_3$ ), hureaulite\* ( $\text{Mn}_3(\text{PO}_3\text{OH})_2(\text{PO}_4)_2 \cdot 4\text{H}_2\text{O}$ ), and silicate-bound Mn. The latter represents the contribution of a spectrum in the LCF collected from a sample with the lowest Mn contents (GC215; F26, 568 cm). \*Hureaulite represents a fraction of Mn(II) that is difficult to distinguish based on XANES spectra and likely represents adsorbed Mn(II) or Mn(II) precipitates other than  $\text{MnCO}_3$ .

Linear combination fitting based on the X-ray absorption spectra of selected depths indicated that birnessite was present in the surface sediment of both US5B and F26 and accounted for around 40 % and 73 % of the Mn mineral fraction, respectively

(Fig. 2). Deeper in the sediment, only Mn(II) phases were detected at both sites in addition to a signal of background Mn. Just above the fresh- to brackish water transition, Mn was only present as rhodochrosite.

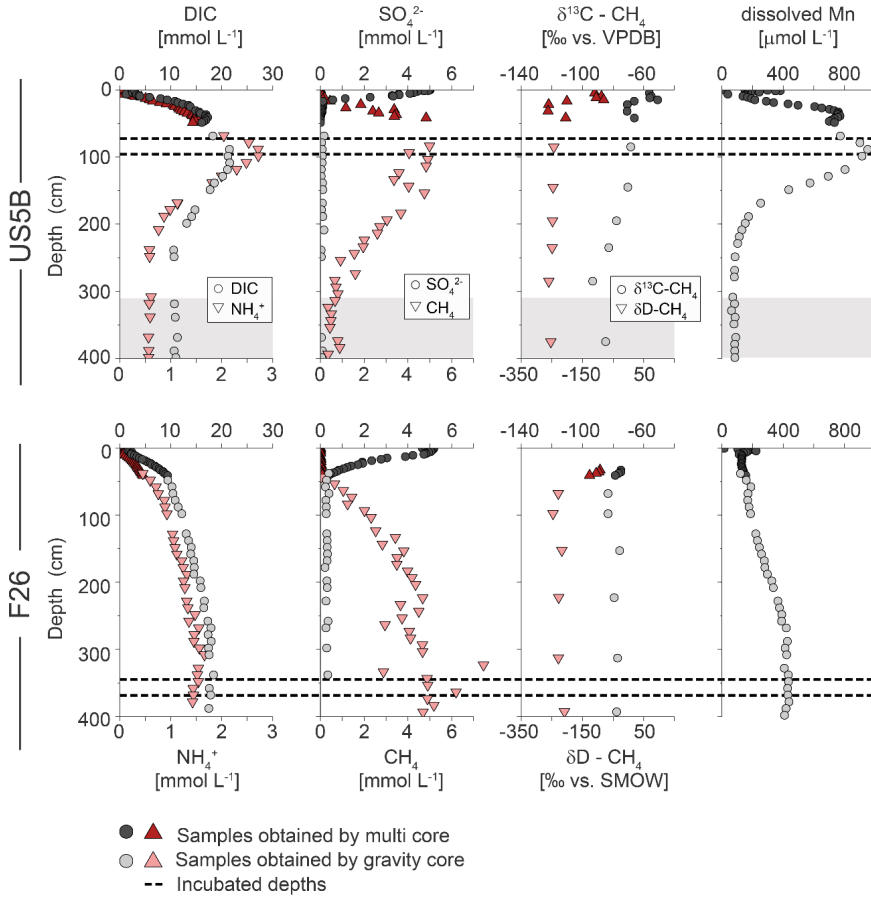


**Fig. 3** Porewater profiles of DIC,  $\text{NH}_4^+$ ,  $\text{SO}_4^{2-}$ ,  $\text{CH}_4$ ,  $\delta^{13}\text{C}-\text{CH}_4$ ,  $\delta\text{D}-\text{CH}_4$  and dissolved Mn for sites US5B and F26 in July 2023. The horizontal dashed lines indicate the depths used for incubations. The shading in the panel for US5B indicates the freshwater sediments.

In general, higher amounts of DNA were extracted at US5B when compared to F26 (Fig. 1). At both sites, the amount of extracted DNA decreased with depth in the sediment. ANME-2ab were the main methanotrophs detected in the sediment. At US5B, ANME-2ab were only detected between depths of 18 and 84 cm, with the highest relative abundance of around 3.5 % of the whole microbial community between depths of 34 and 45 cm (Fig. 1). At F26, ANME-2ab were present below 38 cm with the highest relative abundance at 38 cm and 189.5 cm depth (2.5 %).

Importantly, twice as much DNA was extracted at 38 cm depth when compared to 189.5 cm depth, hence the microbial biomass at 189.5 cm is expected to be lower. ANME-1 was detected only at site F26, at a depth of 370 cm, with a relative abundance of 0.07%.

Porewater concentrations of DIC and  $\text{NH}_4^+$  increased with depth at both sites, followed by a decrease below a depth of ca. 100 cm at site US5B and a levelling off of the increase at site F26 (Fig. 3). Porewater  $\text{SO}_4^{2-}$  was completely removed within the first 15 cm of the sediment at US5B and within the first 40 cm at site F26 (Fig. 3). Below the maximum depth of  $\text{SO}_4^{2-}$  penetration,  $\text{CH}_4$  was present, reaching concentrations of up to 5 - 6  $\text{mmol L}^{-1}$ . At site US5B,  $\text{CH}_4$  concentrations decreased again below a depth of 150 cm and reached a concentration of around 0.5  $\text{mmol L}^{-1}$  at 300 cm depth. Below 50 cm depth,  $\delta^{13}\text{C-CH}_4$  and  $\delta\text{D-CH}_4$  values showed little change with depth at both sites and were mostly around -80 ‰ and -240 ‰, respectively (Fig. 3). At US5B, values of  $\delta^{13}\text{C-CH}_4$  and  $\delta\text{D-CH}_4$  were at a minimum just below the maximum depth of  $\text{SO}_4^{2-}$  penetration. At depths where  $\text{CH}_4$  and  $\text{SO}_4^{2-}$  co-occurred,  $\delta^{13}\text{C-CH}_4$  and  $\delta\text{D-CH}_4$  increased towards the sediment surface, reaching maximum values of -50.9 ‰ and -80.8 ‰ at site US5B and values of -74.9 ‰ and -92.7 ‰ at site F26, respectively. No  $\text{H}_2\text{S}$  was detected in the porewater at either of the sites. Dissolved Mn concentrations were elevated near the sediment-water interface at both sites. At site US5B, the porewater was also enriched in dissolved Mn between depths of 15 and 200 cm, with a maximum concentration of ~950  $\mu\text{mol L}^{-1}$  at 89 cm depth. At F26, in contrast, dissolved Mn concentrations increased gradually with depth and reached a maximum of around 430  $\mu\text{mol L}^{-1}$  at and below 350 cm depth.

## Incubation experiment

### Chemical analyses

The ratio of  $^{13}\text{C-CO}_2/^{12}\text{C-CO}_2$  increased in all incubations of sediment from site US5B to which  $^{13}\text{C-CH}_4$  was added, indicating AOM. No change in the ratio with time was observed in any of the incubations from site F26 (Fig. 4). Hence, in the following, we focus on the results for US5B. In the methane control incubations, the  $^{13}\text{C-CO}_2/^{12}\text{C-CO}_2$  ratio increased from 0.014 to 0.020 during the experiment, indicating background  $\text{CH}_4$  oxidation without additional electron acceptors. The highest signal for AOM was observed when  $\text{SO}_4^{2-}$  was added as electron acceptor. Here, the  $^{13}\text{C-CO}_2/^{12}\text{C-CO}_2$  ratio reached a value of 0.042. In the incubations where Mn oxides were added,  $^{13}\text{C-CO}_2/^{12}\text{C-CO}_2$  increased faster compared to the methane control incubation. The  $^{13}\text{C-CO}_2/^{12}\text{C-CO}_2$  ratio in the incubations where birnessite was added, also together with molybdate, still increased at the end of the experiment, eventually

exceeding the ratio in the CH<sub>4</sub> control, whereas in the incubations amended with pyrolusite the CO<sub>2</sub> isotope ratio ceased to increase after 114 days.

Addition of molybdate to the SO<sub>4</sub><sup>2-</sup>-amended bottles after 100 days of incubation halted the increase in <sup>13</sup>C-CO<sub>2</sub>/<sup>12</sup>C-CO<sub>2</sub> immediately (Fig. 4). Upon addition of molybdate to the CH<sub>4</sub> control incubation, the CO<sub>2</sub> isotope ratio continued to increase for 42 days and then decreased (Fig. S5). After 114 days, molybdate was still present in all Mo-amended incubations (Table S3).

In all incubations where Mn oxides were added, dissolved Mn increased from the start of the incubations to concentrations of 1.5 to 2 mmol L<sup>-1</sup> and subsequently slightly decreased throughout the rest of the experiment (Fig. S6). In the incubations for site US5B with birnessite where no molybdate was added, SO<sub>4</sub><sup>2-</sup> accumulated to ca. 1.5 mmol L<sup>-1</sup> (Fig. S7). This did not occur in any other incubation. Concentrations of H<sub>2</sub>S were around the detection limit in all incubations (Fig. S7). In the incubations for site F26, SO<sub>4</sub><sup>2-</sup> accumulated in the incubations with birnessite and pyrolusite, reaching concentrations of around 2 and 1 mmol L<sup>-1</sup>, respectively (Fig. S8). Accumulation of H<sub>2</sub>S only occurred in the incubations amended with SO<sub>4</sub><sup>2-</sup>, but H<sub>2</sub>S concentrations never exceeded 100 μmol L<sup>-1</sup> (Fig. S8).

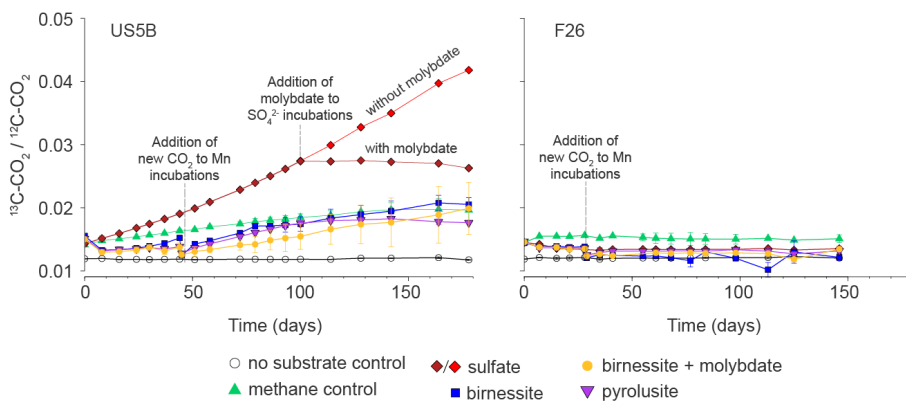


**Fig. 4** Headspace <sup>13</sup>C-CO<sub>2</sub>/<sup>12</sup>C-CO<sub>2</sub> ratios in the sediment incubations with <sup>13</sup>C-labelled CH<sub>4</sub> for site US5B and F26. Error bars show the standard deviation for duplicate incubations.

In the incubations amended with <sup>13</sup>C-labelled acetate, the <sup>13</sup>C-CO<sub>2</sub>/<sup>12</sup>C-CO<sub>2</sub> ratio strongly increased both for site US5B and site F26 within a few days, indicating rapid Mn oxide reduction. The ratio stabilized within two weeks at values of ~0.2 and ~0.3, respectively (Fig. 5). Dissolved Mn increased to around 3 mmol L<sup>-1</sup> and 2 mmol L<sup>-1</sup> in the incubations for sites US5B and F26, respectively.

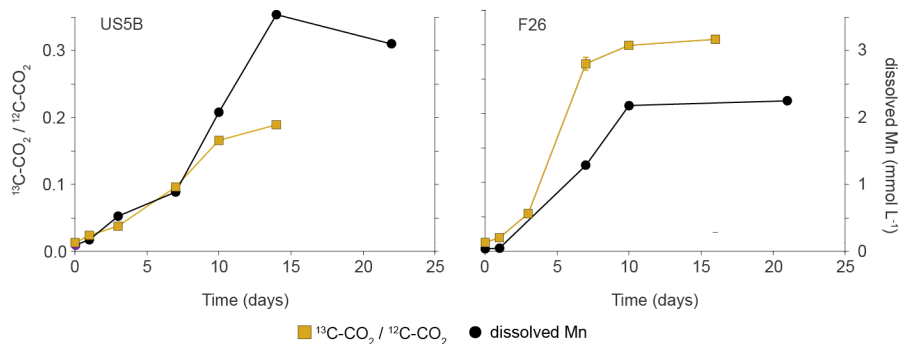


**Fig. 5** Headspace  $^{13}\text{C-CO}_2 / ^{12}\text{C-CO}_2$  ratios and dissolved Mn concentrations in the incubations with  $^{13}\text{C}$ -labelled acetate for site US5B and F26 over time. Error bars show the standard deviation for duplicate incubations.

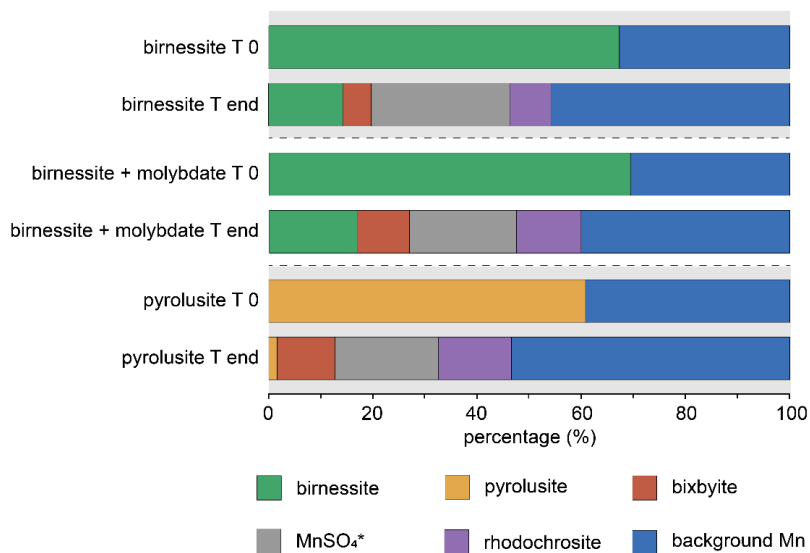


**Fig. 6** Results of linear combination fitting based on the XANES spectra (for spectra, see Fig. S4) of the start and end point of the incubations amended with birnessite, birnessite + molybdate and pyrolusite, for site US5B. The best reproductions were obtained when including spectra of birnessite, pyrolusite, bixbyite ( $\text{Mn}_2\text{O}_3$ ),  $\text{MnSO}_4^*$ , rhodochrosite ( $\text{MnCO}_3$ ) and background Mn in the fitting. \* $\text{MnSO}_4$  likely represents adsorbed Mn(II).

Linear combination fitting of the XANES spectra from sediment of the start and end of the incubations from site US5B amended with  $^{13}\text{C-CH}_4$  and the Mn(IV) oxide minerals birnessite and pyrolusite showed that these Mn oxides accounted for 60 to 70 % of the total Mn mineral phase at the start of the experiment (Fig. 6). At the end of the experiment, both incubations to which birnessite was added still

contained a substantial contribution of birnessite of around 15 % of the total Mn mineral phase. Pyrolusite, on the other hand, only made up for a negligible fraction of 2 % of the total Mn mineral phase at the end of the incubations. The XANES spectra of the sediment at the end of the incubations could be reproduced in the linear combination fitting including reference spectra of rhodochrosite ( $\text{MnCO}_3$ ), bixbyite ( $\text{Mn}_2\text{O}_3$ ) and  $\text{MnSO}_4$ . The latter Mn form likely represents the signal of adsorbed Mn(II).

### Microbial analyses

Samples from the incubations for site US5B amended with  $^{13}\text{C}\text{-CH}_4$  were analyzed using 16S rRNA gene amplicon sequencing to identify the micro-organisms involved in the observed  $\text{CH}_4$  oxidation. At the start of the incubations, ANME-2ab covered 11.1 % of the total archaeal reads (Fig. 7). The relative abundance of ANME-2ab did not change over the experiment in the no substrate control ( $10.8 \pm 0.6$ ) and decreased somewhat in the methane control (9.0 %) and when sulfate was added (9.9 %). When Mn oxides were added, the archaeal relative abundance of ANME-2ab increased. The highest increase was observed with the addition of birnessite + molybdate (to  $19.2\% \pm 1.1$ ), followed by pyrolusite (to  $15.9\% \pm 1.8$ ) and birnessite (to  $12.3\% \pm 0.8$ ).

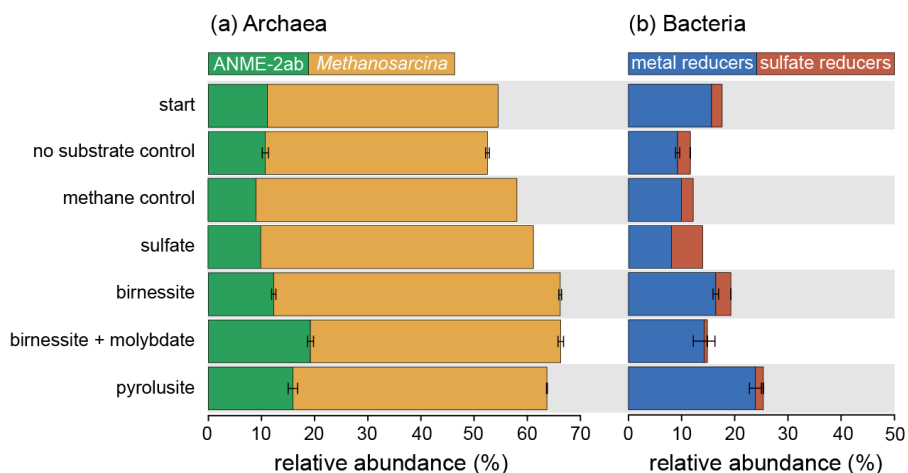


**Fig. 7** Relative abundances of key microbial groups based on 16S rRNA gene amplicon sequencing of the sediments of the incubations; (a) archaea and (b) bacteria. The relative abundance of sulfate reducers is the sum of the abundance of Desulfocapsaceae and Desulfosarcinaceae. The relative abundance of metal reducers is the sum of Geothermobacteraceae, Sva1033, Desulfuromonadaceae, Geobacteraceae, Geopsychrobacteraceae and Shewanellaceae. The error bars represent standard deviation between the duplicate incubations. No error bars are given for the methane control and sulfate, because molybdate was added to one of the duplicates during the experiment and only the incubation without molybdate is reported here. For the complete overview of all micro-organisms, see supplementary Fig. S9.

*Methanosarcina* was the most abundant methanogen and showed the largest increase in relative abundance for incubations with Mn oxides (Fig. 7; Fig. S9). The largest increase was observed in incubations with birnessite, where the relative abundance reached  $53.9\% \pm 0.5\%$ , compared to  $43.4\%$  in the start material.

Relative to the start of the incubations ( $15.6\%$ ), the contribution of bacterial metal reducers decreased in the control ( $9.3\% \pm 0.8\%$ ) and  $\text{SO}_4^{2-}$  ( $8.1\%$ ) incubations and remained similar when birnessite ( $16.4\% \pm 1.0\%$ ) and birnessite + molybdate were added ( $14.2\% \pm 4.1\%$ ; Fig. 7). In the incubation with pyrolusite ( $23.9\% \pm 2.3\%$ ), the relative abundance of metal reducers increased over the duration of the experiment.

The relative abundance of sulfate reducers increased most in the incubations with  $\text{SO}_4^{2-}$  ( $7.1\%$ ) and only slightly in those with birnessite ( $2.8\% \pm 0.0\%$ ), compared to the start material ( $2\%$ ; Fig. 7).

From the incubation with sediment from site US5B, a selection of samples was used for metagenomic analyses, namely samples from the start material and end material of one of the duplicates of the incubation bottles amended with  $\text{SO}_4^{2-}$ , birnessite and birnessite + molybdate. Compared to the start, the reads per million (RPM) of *mcrABG* genes, which are involved in  $\text{CH}_4$  oxidation, increased in all incubations, with the increase being largest in the incubation with birnessite + molybdate (Fig. S10). For the genes involved in metal cycling, the highest increase in RPM was observed in *dmkB* in the incubation with sulfate and birnessite, respectively (Fig. S10). Other genes that showed substantial increases were *eetB* and *fmnA* in the incubations where birnessite and birnessite + molybdate were added. The *ndh2* gene decreased in RPM in the incubations with sulfate and birnessite.

In total, eleven high-quality metagenome assembled genomes (MAGs) were obtained after assembly and binning of the metagenomic data (Completeness  $> 85\%$ ; Contamination  $< 5\%$ ; Strain heterogeneity  $< 10\%$ ; Table S4). Only one high-quality MAG could be assigned to ANME-2ab with the closest hit being f\_Methanocomedenaceae; g\_Kmv04 (89.5% complete, 1.31% contaminated and 0% strain heterogeneity) and was obtained from the end-point of the bottle where birnessite + molybdate were added as electron acceptor. The ANME-2ab MAG contained the full 'reverse methanogenesis' pathway and eleven MHC proteins (protein with  $\geq 3$  heme groups). The MHC proteins showed a marked variation in amino acid identity relative to each other (Fig. S11). Combined these MHCs could form a putative EET pathway, starting from the electron transport chain in the

membrane, through the S-layer to Mn-oxides. Two MHCs contain S-layer binding domains and are potentially involved in shuttling electrons through the S-layer. This could be in conjunction with the four MHCs that contain signal peptide, indicating a role in EET outside of the cell either from or to the S-layer MHCs (for details see supplements Table S6). When comparing the protein sequences that contain MHCs with MHC-containing proteins encoded in MAGs of *Ca. M. ferrireducens* (Cai et al., 2018), *Ca. M. manganireducens* and *Ca. M. manganicus* (Leu et al., 2020), six of the proteins have a strong similarity, four proteins have a moderate similarity and one protein is likely not significantly similar with the proteins reported in literature (See supplements section 2 and Table S6 for the details). Furthermore, the genome contained *fmnB* and *dmkB*, which are involved in bacterial EET (Light et al., 2018; Table S5). The role of *fmnB* and *dmkB* in archaea is unknown but potentially could play role in this ANME.

## Discussion

### CH<sub>4</sub> production in the brackish sediment

Elevated C<sub>org</sub> concentrations in sediments from the brackish phase at both US5B and F26 reflect the enhanced organic matter deposition in the Bothnian Sea after the transition from fresh to brackish water (Fig. 1; Jilbert et al., 2015; Häusler et al., 2017; Dijkstra et al., 2018c). The high porewater concentrations of NH<sub>4</sub><sup>+</sup> and DIC indicate high rates of organic matter degradation, with trends with depth that reflect a different history of the rate of input and degradation of organic matter between the sites (Fig. 3). On time scales of thousands of years, sediment accumulation and organic matter deposition rates were, on average, lower at US5B compared to F26. However, over the past century this has reversed (Mattila et al., 2006; Slomp et al., 2013; Baas et al., subm.). As a result, NH<sub>4</sub><sup>+</sup>, CH<sub>4</sub> and DIC concentrations reach a maximum in the upper 150 cm of the sediment at site US5B, whereas the concentrations of these compounds gradually increase with sediment depth at site F26 (Fig. 3). At site US5B, the maximum NH<sub>4</sub><sup>+</sup> and DIC concentrations are approximately twice those at site F26, which confirms the acceleration of rates of organic matter input and degradation at US5B.

Differences in CH<sub>4</sub> isotope signatures could reflect the contrast in sediment accumulation at both sites (Fig. S12; Whiticar, 1999). The isotopic signatures of the CH<sub>4</sub> at US5B reflects a mixture of acetate fermentation and carbonate reduction, whereas the signature of F26 reflects carbonate reduction as the dominant pathway (Fig. S12). Generally, methyl type fermentation is dominant in freshwater

systems while carbonate reduction is more important in marine systems (Whiticar, 1999). At US5B, most of the  $\text{CH}_4$  was formed over the past century, following the rapid increase in sedimentation rates and organic matter input (Slomp et al., 2013; Baas et al., *subm.*). At F26, in contrast, the  $\text{CH}_4$  formed over thousands of years. During the Holocene, a gradual freshening took place in the Bothnian Sea (Baas et al., *subm.*). This freshening could explain the shift from carbonate reduction as the main pathway of methanogenesis in the 'old'  $\text{CH}_4$  of F26 to a relatively higher contribution of methyl type fermentation in the 'younger'  $\text{CH}_4$  at US5B. Furthermore, the increase in eutrophication over recent decades (Kuliński et al., 2022) led to higher organic carbon burial and thus an increase in relative contribution of methyl type fermentation to methanogenesis.

### **$\text{CH}_4$ removal pathways**

A clear sulfate-methane transition zone (SMTZ) is visible at both sites (Fig. 3). Both  $\delta^{13}\text{C}\text{-CH}_4$  and  $\delta\text{D}\text{-CH}_4$  shift to higher values in the SMTZ, indicating  $\text{CH}_4$  oxidation (Whiticar, 1999; Fig. 3, S12). This is also the zone where most ANME-2ab are present (Fig. 1). It is therefore likely that, at both sites, the majority of the in-situ  $\text{CH}_4$  oxidation is performed by ANME-2ab, mainly coupled to  $\text{SO}_4^{2-}$  reduction. Relatively constant values of  $\delta^{13}\text{C}\text{-CH}_4$  and  $\delta\text{D}\text{-CH}_4$  below the SMTZ suggest that most of the  $\text{CH}_4$  oxidation takes place within the SMTZ (Fig. 3). However, the isotopic signature of methanogenesis can mask the signal of methanotrophy, especially in sediments where methanogenesis is high (Seifert et al., 2006; Egger et al., 2017). The occurrence of AOM below the SMTZ can therefore not be excluded based on the  $\text{CH}_4$  isotopic signature. The AOM activity in the  $\text{CH}_4$  control incubation at US5B indicates that AOM can occur without additional electron acceptors below the SMTZ at this site (Fig. S5). Continuation of this activity after the addition of molybdate showed that the AOM in the  $\text{CH}_4$  control incubation was independent of  $\text{SO}_4^{2-}$  (Fig. S5). It is thus likely that AOM coupled to other electron acceptors such as Fe and Mn oxides occurs below the SMTZ at site US5B (Fig. 1, 2), as has been shown previously for Fe oxides (Egger et al., 2015).

Burial of Mn oxides into the methanic part of the sediment typically indicates non-steady state conditions and high sedimentation rates (Kasten et al., 1998; März et al., 2008; Riedinger et al., 2014; Klomp et al., 2025). In the Bothnian Sea, burial of Mn oxides is further promoted by low  $\text{H}_2\text{S}$  concentrations in the porewater, because the majority of the  $\text{H}_2\text{S}$  that forms during  $\text{SO}_4^{2-}$  reduction is captured in authigenic Fe-sulfides (Slomp et al., 2013; Egger et al., 2015). At the depths where the sequential extractions suggest the presence of Mn oxides deeper in the sediment, increased dissolved Mn concentrations indicate that reduction of Mn oxides is or has been

actively taking place (Fig. 1, 3). Possible drivers for the reduction of Mn oxides are either organic matter degradation or  $\text{CH}_4$  oxidation (Soyol-Erdene & Huh, 2013; Riedinger et al., 2014).

### Potential for Mn-AOM

The incubations with sediment from US5B showed that the microbial community around 80 - 100 cm depth is capable of performing AOM with  $\text{SO}_4^{2-}$ , birnessite and pyrolusite (Fig. 4). The presence of molybdate, an inhibitor of  $\text{SO}_4^{2-}$  reduction (Wilson & Bandurski, 1958), does not affect the AOM signal in incubations with birnessite (Fig. 4). This indicates that reduction of birnessite can directly drive AOM in these coastal sediments, independent of a cryptic sulfur cycle.

Mineral crystallinity can affect the bioavailability of Mn oxides (Burdige et al., 1992). So far, all studies of Mn-AOM used either birnessite or vernadite, which are both amorphous Mn(IV) oxides (e.g. Beal et al., 2009; Ettwig et al., 2016; Su et al., 2020). Besides birnessite, we therefore tested the more crystalline Mn(IV) oxide pyrolusite for Mn-AOM potential. We found that mineral crystallinity does not strongly affect the bioavailability of Mn oxide for AOM in our incubations. When pyrolusite was added, the AOM signal halted after 114 days, likely due to the complete consumption of pyrolusite in the incubation bottles (Figs 4, S4, 6). A higher relative abundance of metal reducing bacteria and therefore higher rates of metal reduction in the incubation with pyrolusite compared to the incubations with birnessite can explain this difference (Fig. 7, Table S2). Structurally higher dissolved Mn concentrations in the incubations with pyrolusite also indicate more Mn reduction (Fig. S6). This strongly indicates that the sediment was depleted of pyrolusite after 114 days, when the AOM signal stopped. Combined with the absence of  $\text{SO}_4^{2-}$  and  $\text{H}_2\text{S}$  from the incubations with pyrolusite (Fig. S7), this shows that pyrolusite reduction is directly coupled to  $\text{CH}_4$  oxidation, without  $\text{SO}_4^{2-}$  as an intermediate.

Incubations with sediment of around 350 - 370 cm depth from F26 did not show an AOM signal after 146 days, despite immediate microbial activity in the incubations where birnessite and acetate were added (Fig. 5) and clear evidence of an active sulfur cycle (Fig. S8). We can, however, not exclude that AOM in F26 required more time to become detectable. The lack of an AOM signal is remarkable, since methanotrophs ANME-2ab were present in-situ at 350 cm depth (Fig. 1). However, the microbial biomass as judged from the total extracted DNA was  $\sim 7$  fold lower at the incubated depth of F26 compared to that of US5B (Fig. 1). It is therefore possible that the methanotrophic community in the sediment interval incubated at F26 was too small to show detectable AOM activity.

The relative abundance of ANME-2ab in archaeal 16S rRNA reads and their relevant genes in methanotrophy (*mcrABG*) increased in the incubations that showed AOM activity and were supplied with Mn oxides (Fig. 7, S10). Although ANME-2ab have previously been associated with Fe-AOM in brackish and marine sediments (Aromokeye et al., 2020; Rasigraf et al., 2020), they have also been hypothesized to play a role in Mn-AOM in marine sediments in other studies (Xu et al., 2021). Surprisingly, when only birnessite was added, the relative abundance of ANME-2ab did not increase as much as in the other incubations (Fig. 7). Meanwhile, the relative abundance of *Methanosarcina*, a methanogen suspected to be capable of metal reduction (Ferry, 2020; Yang & Lu, 2022), increased most in the incubations with birnessite. An absolute increase of *Methanosarcina* would suppress the relative abundance of ANME-2ab. We speculate that this suppression of ANME-2ab solely took place when only birnessite was added and not with the other incubations with Mn oxides, because addition of molybdate inhibited the interaction of *Methanosarcina* with birnessite and because the crystallinity of pyrolusite affects its availability for reduction by *Methanosarcina*.

Based on the increased presence of ANME-2ab in the incubations with sediment from US5B, we were able to obtain an 89.5 % complete metagenome assembled genome (MAG) (Table S4). The genome of the ANME-2ab MAG encoded for all genes necessary for CH<sub>4</sub> oxidation and several MHCs with a substantial variation in amino acid identity (Fig. S11; Table S5, S6), which have been postulated to participate in EET (Cai et al., 2018; Leu et al., 2020; Zhang et al., 2023; Ouboter et al., 2024). The ANME-2ab MAG encodes two MHC proteins containing S-layer binding domain(s) (Table S6). Both are located next to another MHC protein, potentially working in conjunction and resemble parts of large MHC proteins that are postulated to be involved in EET by *Ca. M. ferrireducens* and *Ca. M. manganireducens* (Cai et al., 2018; Leu et al., 2020). Together with the similarity of encoded MHCs to putative EET-related proteins from the metal-reducing ANME-2d it suggests that ANME-2ab can reduce metals via EET through MHCs. Our findings suggest that ANME-2ab are responsible for the coupling of Mn oxide reduction to oxidation of CH<sub>4</sub> in these brackish coastal sediments.

### Impact of Mn-AOM

Manganese driven AOM can account for a few percent of AOM in metal rich sediments (Lenstra et al., 2023; Xiao et al., 2023). We show that, when Mn oxides are buried into the methanic zone, ANME-2ab can likely couple the reduction of these Mn oxides directly to the oxidation of CH<sub>4</sub>. The occurrence of ANME-2ab ranges from continental margins to shallow-water permeable sediments and from brackish coastal basins to deep-sea cold CH<sub>4</sub> seeps (e.g. Cambon-Bonavita et al., 2009; Mason

et al., 2015; Ruff et al., 2016; Li et al., 2020; Rasigraf et al., 2020). In marine surface sediments, Mn oxides are ubiquitous (Post, 1999), but the input of Mn oxides is especially high in coastal regions, close to river mouths, due to the mainly terrestrial origin of Mn oxides (Lenstra et al., 2022). Coastal regions are also key sites for CH<sub>4</sub> emissions, because the SMTZ is relatively shallow due to high SO<sub>4</sub><sup>2-</sup> reduction rates driven by high rates of organic matter degradation (Żygadłowska et al., 2024b). As a result, Mn-AOM is expected to be most important in coastal sediments (Lenstra et al., 2023), with our work highlighting potential direct coupling of Mn reduction to CH<sub>4</sub> oxidation by ANME-2ab.

## Conclusions

In this study, we investigated sediments in which Mn oxides were found in the methanic zone in the presence of ANME-2ab. Sediment incubations where isotopically labelled methane (<sup>13</sup>C-CH<sub>4</sub>) and the Mn oxides birnessite and pyrolusite were added showed that CH<sub>4</sub> oxidation could directly be coupled to reduction of both Mn oxides, i.e. without a role for cryptic sulfur cycling. We show that this process is likely performed by ANME-2ab. Metagenome shotgun sequencing provided a metagenome assembled genome of ANME-2ab from the incubation with birnessite where SO<sub>4</sub><sup>2-</sup> reduction was inhibited by molybdate. This MAG contained all genes involved in the 'reverse methanogenesis' pathway and two genes used by bacteria to perform extracellular electron transfer (EET; *fmnB* and *dmkB*). The genome encoded for eleven multiheme c-type cytochromes, which show similarity with multiheme c-type cytochromes of freshwater ANME, potentially forming an EET pathway. This suggests that ANME-2ab can perform metal reduction via EET. We show that Mn-AOM is possible in brackish coastal sediments and is likely performed by ANME-2ab. Therefore, Mn-AOM should be considered when studying CH<sub>4</sub> dynamics in Mn oxide-rich coastal sediments.

### Data availability

All data presented in this paper is deposited on Zenodo and available at 10.5281/zenodo.17174800. The raw sequencing data can be accessed in the European Nucleotide Archive under the accession number PRJNA1314788.

### Declaration of competing interest

The authors declare that they have no known competing financial interests or personal relationships that could have appeared to influence the work reported in this paper.

## **Acknowledgements**

We thank the captain and crew of RV Pelagia, Emilia Heiskanen, Lina Piso, Nicky Dotsios, and Rahat Riaz for their support during the sampling campaigns. We are also thankful to Sebastian Krosse, Paul van der Ven, Anita van Leeuwen, Carina van Veen and Angelika Rosa for analytical assistance. This research was financially supported by European Research Council Synergy grant MARIX (854088). This work was carried out under the program of the Netherlands Earth System Science Center (NESSC 024002001) and SIAM (024002002), financially supported by the Ministry of Education, Culture and Science (OCW). WKL and RE acknowledge funding by the Dutch Research Council (NWO VI.Veni.222.332 and VI.Vidi.223.012, respectively).

## Appendix A. Supplementary material

The supplementary material contains a more detailed description of the sampling procedure (Section 1), incubation setup (Section 2), X-ray absorption spectroscopy (Section 3) and microbial analyses (Section 4). The figures in the supplementary material include a map of the sampling location (Fig. S1), the XRD spectra of the minerals used in the incubation (Fig. S2), the results of all Mn extraction steps for sediments from both locations (site US5B and F26; Fig. S3), the Mn-XANES spectra of the X-ray absorption spectroscopy (Fig. S4), a zoom of the  $^{13}\text{C-CO}_2/^{12}\text{C-CO}_2$  ratio of the  $\text{CH}_4$  in control incubations and the incubations amended with pyrolusite (Fig. S5), concentrations of dissolved Mn (Fig. S6),  $\text{SO}_4^{2-}$  and  $\text{H}_2\text{S}$  (Fig. S7, S8) in the incubations, all 16S rRNA amplicon sequencing data from the incubations (Fig. S9), the change of genes involved in methane oxidation and metal reduction in the incubations with sulfate, birnessite and birnessite + molybdate analyzed via shotgun metagenome analysis (Fig. S10), the amino acid identity of the MHCs from the ANME-2ab MAG (Fig. S11) and the  $\text{CH}_4$  isotope diagram for the  $\text{CH}_4$  isotopes in the porewaters of both locations (Fig. S12). The tables in the supplementary material show the composition of the medium used in the incubations (Table S1), the amount of DNA extracted in the samples from the incubations (Table S2), the amount of molybdenum measured in the incubations where it was added after 114 days of incubation (Table S3), an overview of the high quality MAGs obtained from the incubations (Table S4), the genes present in the high quality ANME-2ab MAG (Table S5) and a comparison of the protein sequences of the MHCs from the ANME-2ab MAG with MHCs of other ANME that likely perform EET (Table S6).

## **Supplement to “Anaerobic Oxidation of Methane Coupled to Manganese Oxide Reduction by ANME-2ab in Brackish Coastal Sediments”**

### **Supplement Section 1. Sampling procedures for the multi- and gravity core**

One of the multicores was used to collect sediment, bottom water and porewater immediately after retrieval. Bottom water samples were obtained from the overlying water with a syringe that was equipped with a three-way valve. The core was sectioned at a resolution of 0.5 cm (0 to 2 cm), 1 cm (2 to 10 cm) and 2 cm (20 to 50 cm) under a  $N_2$  atmosphere at 4°C. The sediment was centrifuged at 4000 rpm in a 50 ml centrifuge tube for 20 minutes to separate the porewater from the sediment. The supernatant was filtered over 0.45  $\mu\text{m}$  filters, under a  $N_2$  atmosphere, and subsampled for the analysis of sulfide ( $H_2S$ ), dissolved inorganic carbon (DIC), ammonium ( $NH_4^+$ ), sulfate ( $SO_4^{2-}$ ), and dissolved manganese (Mn).

The gravity core liners were pre-drilled at a 10 cm resolution with 2 cm diameter holes, which were taped prior to employment of the corer. After core recovery, the core liner was cut vertically into 100 cm sections, which were capped. The sections were sampled through the drilled holes as soon as possible using 20 ml cutoff syringe, for the analysis of solid phase samples and the solutes  $H_2S$ , DIC,  $NH_4^+$ ,  $SO_4^{2-}$  and dissolved Mn. The syringes for sediment and porewater collection were immediately sealed with parafilm and an elastic band and transported into a  $N_2$  filled glovebag at 4°C. Here, the sediment was extruded into a 50 mL centrifuge tube. The centrifuge tubes were centrifuged at 4000 rpm for 20 minutes and the extracted porewater was subsampled as described above for the multicores. Again, the sediment was stored frozen at -20°C in  $N_2$  purged aluminum bags until further processing.

## Supplement Section 2. Incubation setup

### Substrate preparation

Birnessite was synthesized via the reduction of  $\text{KMnO}_4$  with  $\text{C}_3\text{H}_5\text{NO}_3$  at ambient temperature and pressure (Händel et al., 2013). Pyrolusite was obtained from the inhouse collection of Utrecht University (Alfa Aesar; Lenstra et al., 2021b). The identity of both minerals was verified via X-ray diffraction (Fig. S2). Sulfate and molybdate stocks were prepared as 1 M  $\text{NaSO}_4^{2-}$  and 1 M  $\text{Na}_2\text{MoO}_4$  solutions in sterile demineralized water in stoppered serum bottles and consecutively made anoxic. Isotopically labelled  $^{13}\text{C}$ -acetate was obtained from Sigma Aldrich (Sodium acetate  $^{13}\text{C}$ -2), and used to make a 0.1 M stock solution in demineralized water in stoppered serum bottles and consecutively made anoxic.

### Start of the incubations

All incubations were started with a pre-incubation, where the electron acceptors for each treatment were added to the sediment to remove reduced sulfur species via oxidation and minimize a cryptic sulfur cycle within the incubation bottles (Su et al., 2020). The sediment was diluted with sterile  $\text{SO}_4^{2-}$  free artificial seawater (ASW; for composition see Table S1) in a 1:4 ratio under a  $\text{N}_2$  atmosphere and carefully homogenized. Subsequently, 60 g of the slurry was transferred into a 120 ml serum bottle and the electron acceptors were added (see Table 1 for all treatments). The bottles were stoppered and capped, the headspace was replaced with a 100%  $\text{N}_2$  headspace, and the bottles were stored shaking 90 rpm at 4°C for one week.

After the pre-incubation, the artificial seawater was replaced with freshly prepared ASW, new electron acceptors were added to the bottles and molybdate and labelled acetate were added to obtain a concentration of 10 mmol  $\text{L}^{-1}$  and 2.5 mmol  $\text{L}^{-1}$ , respectively (for treatments, see Table 1), again under a  $\text{N}_2$  atmosphere. The headspace of the incubations with labelled  $\text{CH}_4$  was replaced by a mixture of 76%  $\text{N}_2$ , 4%  $\text{CO}_2$  and 20%  $^{13}\text{C}$ -labelled  $\text{CH}_4$ . For the incubations with labelled acetate, the headspace was replaced by a mixture of 96%  $\text{N}_2$  and 4%  $\text{CO}_2$ . The incubations from sites US5B and F26 were placed on a shaking table (90 rpm) at 4°C in the dark and incubated for 178 and 146 days, respectively.

### Supplement section 3. X-ray absorption spectroscopy procedures

Sediment samples were ground with an agate mortar and piston and pressed into a pellet (3 mm diameter) under an N<sub>2</sub> atmosphere. The pellets were placed in a sample holder within an airtight N<sub>2</sub> filled container equipped with Kapton windows to position the beam and analyzed on the Mn K-edge energy range (6500 – 6900 eV).

The spectra for analyzing X-ray absorption near edge structure XANES were normalized and extracted using the ATHENA software package (v0.8.056; Ravel & Newville, 2005). The ATHENA software package was also used to perform linear combination fitting to qualify and quantify the mineral phases of Mn.

The high amplitude of the pre-edge feature of the normalized XANES spectrum from the sample just above the fresh-brackish transition at US5B indicated self-absorption. The FLUO algorithm was used in ATHENA to correct for this (Haskel, 1999). As the exact composition at the measured spots was not known, the correction was made based on MnCO<sub>3</sub> \* (H<sub>2</sub>O)<sub>n</sub>. The number of water molecules (n) was adjusted until the magnitude of the pre-edge feature and the amplitude of the white line was similar to the XANES spectrum of rhodochrosite, showing strong resemblance with the spectra from the sample.

## Supplement Section 4. Specifications of the microbial analyses

### 16S rRNA gene amplicon sequencing

The DNA samples from the incubations with sediment from US5B amended with  $^{13}\text{C-CH}_4$  were sent for 16S rRNA gene amplification to analyze changes in the microbial community over the incubations. Amplification was performed using the primers Arch349F (5'-GYGCASCAGKCGMGAAW-3') and Arch806R (5' GGACTACVSGGGTATCTAAT-3'; Takai & Horikoshi, 2000), Bac341F (5'CCTACGGGNGGCWGCAG-3'; Herlemann et al., 2011) and Bbac806R (5'GGACTACHVGGGTWTCTAAT-3'; Caporaso et al., 2012). The amplicons were sequenced on the Illumina MiSeq Next Generation Sequencing platform by Macrogen (Seoul, South Korea) using Hercules II Fusion DNA Polymerase Nextera XT Index Kit V2, yielding 2x300 bp paired-end reads. The quality of the raw reads was verified with FastQC (v0.11.5; Andrews, 2010). Cutadapt (v1.15.8; Martin, 2011) was used to trim the paired-end reads to remove adapters. The DADA2 pipeline (v1.8; Callahan et al., 2016) was used to cluster the reads into amplicon sequence variants (ASVs), remove the chimera and determine the taxonomic classification with the SILVA 16S rRNA database (v138.1; Quast et al., 2013) using R. The Phyloseq package (v1.36.0; McMurdie & Holmes, 2013) was used to analyze the microbial community data.

### Metagenomic sequencing

The samples from the shotgun metagenomic sequencing were assembled and binned according to an adapted version of an in-house bioinformatics pipeline (In 't Zandt et al., 2019). BBDuk (v37.76; BBTools; Bushnell, 2014) package; was used for quality trimming and filtering of the raw sequencing reads, Tadpole (v39.06) was used for error correction and BBnorm (BBTools v37.76) was applied for normalization of the coverage of the reads. The trimmed and filtered reads were coassembled by metaSPAdes (v3.15.5; Nurk et al., 2017) with k-mer sizes 21, 33, 55, 77, 99 and 121, using the --only-assembler flag. For each sample, the reads were mapped back to the assembled contigs using BBmap (BBTools v37.76) and the mapping files were processed using SAMtools (v1.19.2; Li et al., 2009). The coassembled contigs were binned using CONCOCT (v1.1.0; Alneberg et al., 2014), MaxBin (v2.2.7; Wu et al., 2016), MetaBAT 2 (v2:2.15; Kang et al., 2019) and SemiBin2 (v2.0.2; Pan et al., 2023). Consensus bins were generated using DAS Tool (v1.1.2; Sieber et al., 2018). CheckM2 (v1.1.2; Chklovski et al., 2023) was used to check the quality of the consensus bins and GTDB-Tk v2 (v2.4.0; Chaumeil et al., 2022) was used for the taxonomic classification of the bins.

To obtain high quality bins for ANME's (completeness > 85%, contamination <5%, strain heterogeneity < 10%), the reads were filtered based on scaffold coverage. SingleM (Woodcroft et al., 2025) was used to find the coverage of ANME genera in the raw reads. The reads were filtered to remove the scaffolds with a coverage less than 12 or greater than or equal to 50 with the khmer package (Crusoe et al., 2015) in Python, using `filter_reads_by_coverage`. The reads were assembled and binned using the aviary pipeline (V0.11.0; Newell et al., 2025), including `fastp` (V0.23.x; Chen et al., 2018), `MEGAHIT` (V1.2.9; Li et al., 2015), `MetaBAT2` (V2.15; Kang et al., 2019), `CheckM` (V1.2.0; Parks et al., 2015) and `GTDB-Tk` (v2.4.0; Chaumeil et al., 2022). All bins obtained were dereplicated using the dRep tool (Olm et al., 2017).

One high quality bin (completeness 89.5%, contamination 1.3%, strain heterogeneity 0%) was identified as a methane-oxidizing organism (f\_Methanocomedenacea; g\_Kmv04) and was therefore selected for further analysis. Gene annotation of this bin was done with Metascan and FeGenie. Furthermore, putative multiheme c-type cytochromes (MHCs) were identified by searching open reading frames for  $\geq 3$  CXXCH + CXXXCH motifs using a custom Python script, the protein domains of these proteins were determined using InterPro (v105.0; Blum et al., 2025) and signal peptides were identified by SignalP v5.0 (Armenteros et al., 2019). The putative MHCs were analyzed using NCBI BlastP against the proteins reported for ANME that can couple CH<sub>4</sub> oxidation to Fe oxide reduction (*Ca. M. ferrireducens*; Cai et al., 2018) and to Mn oxide reduction (*Ca. M. manganireducens* and *Ca. M. manganicus*; Leu et al., 2020). The best blast hits were determined based on e-value, percentage identity and query coverage, where the hits were classified as a strong similarity (query coverage > 75; e-value < 1e-20), a likely similarity (30 < query coverage < 75; 1e-5 < e-value < 1e-20) and no similarity (query coverage < 30; e-value > 1e-5). An average amino acid identity (AAI) matrix of the different identified MHCs was created by Clustal2.1 using default settings (Larkin et al., 2007).

## Supplementary figures

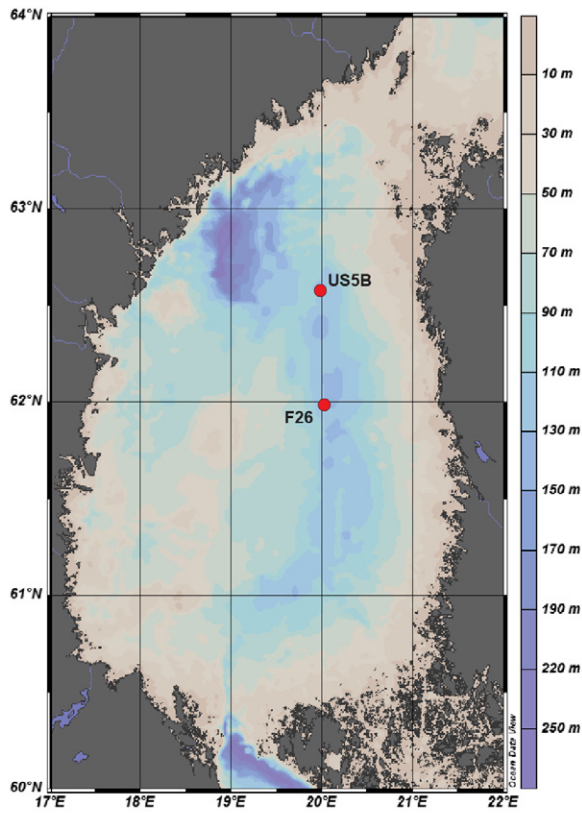


**Fig. S1** Bathymetric map of the Bothnian Sea, with the study sites, US5B and F26, indicated. Map generated using Ocean Data View (Schlitzer, 2023).

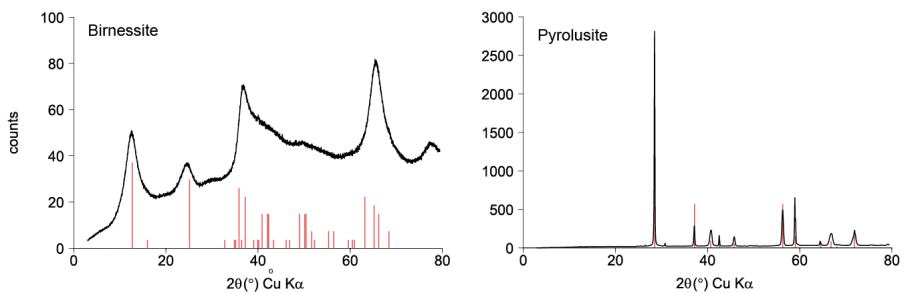


**Fig. S2** X-ray diffraction spectra of birnessite and pyrolusite added to the incubations. The red bars indicate the positions of the theoretical peaks in the spectrum (Lenstra et al., 2021b).

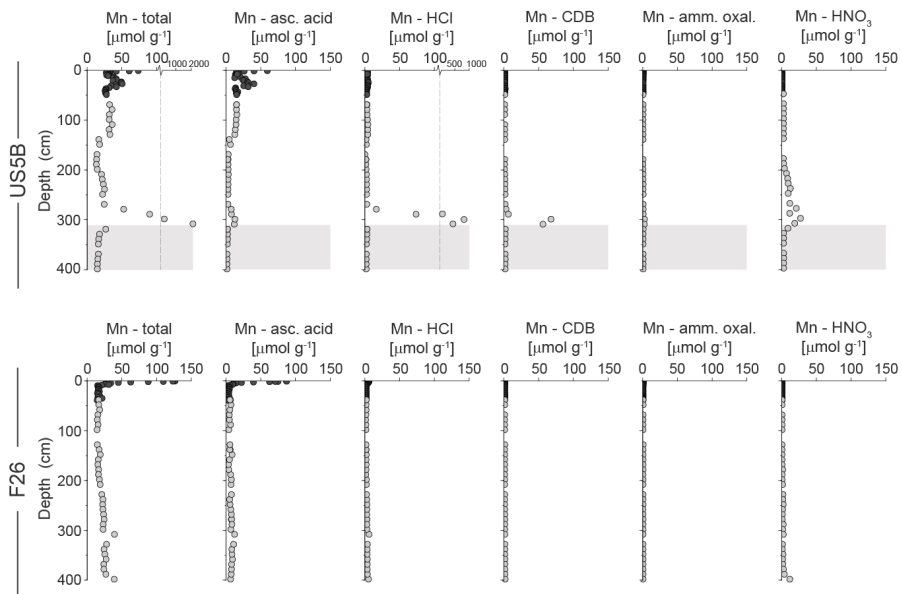


**Fig. S3** Overview of Mn extracted in the total destruction and all 5 extraction steps (ascorbic acid, HCl, sodium dithionite (CDB), ammonium oxalate and HNO<sub>3</sub>) for the Mn extraction for US5B and F26. Note the axis break in the graphs showing the total and HCl extracted Mn from site US5B. The shading in the panel for US5B indicates the freshwater sediments.

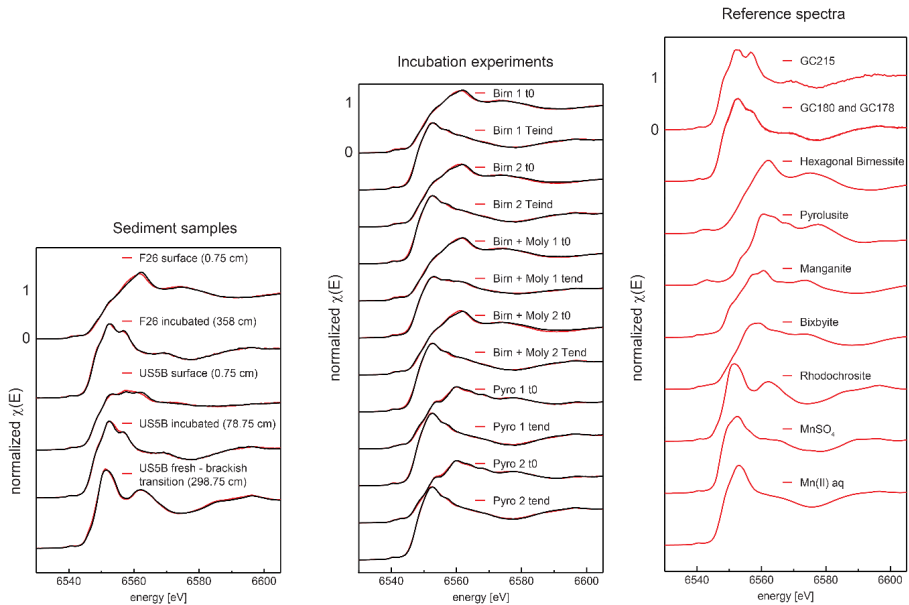


**Fig. S4** Mn-XANES spectra of the selected sediment samples, the samples from the start and end point of the incubations amended with birnessite, birnessite + molybdate and pyrolusite, for site US5B and the used reference spectra taken into consideration in the linear combination fitting of the spectra from samples of incubation experiments. For the linear combination fitting of the sediment samples, the XANES spectra from the analyzed sample with the lowest Mn content (GC215) is also included, assuming that this spectrum is reflecting the background signal of silicate-bound Mn phases. For incubation samples, the XANES spectra from the source sediment (GC180 and GC178) was included in the linear combination fitting, assuming that this spectrum reflects the background Mn phases. The red line is the collected spectrum, the black line shows the result of the linear combination fitting.

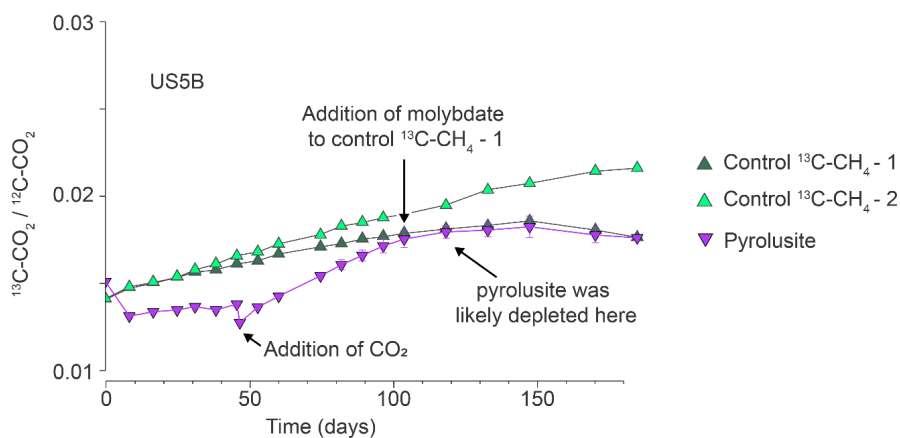


**Fig. S5** Headspace  $^{13}\text{C-CO}_2/^{12}\text{C-CO}_2$  for the control incubation with labelled methane and the incubation with pyrolusite. Error bars show the standard deviation for duplicate incubations with pyrolusite. The indicated points show where the AOM signal stops in the incubation with pyrolusite and thus likely the point where the pyrolusite was completely removed, the point where molybdate was added to one of the incubations with  $^{13}\text{C-CH}_4$  and the point where new  $\text{CO}_2$  was added to the incubation with pyrolusite.

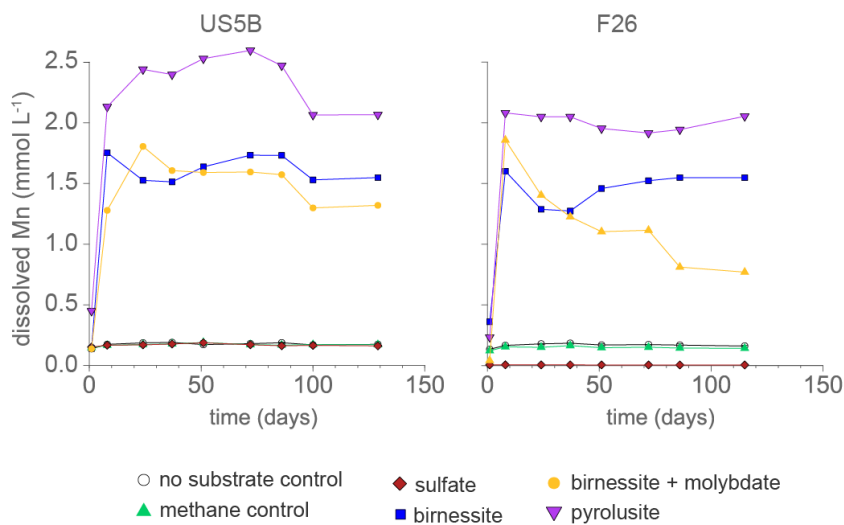


**Fig. S6** Concentrations of dissolved Mn in the incubations with sediment from US5B and F26. Error bars show the standard deviation for duplicate incubations.

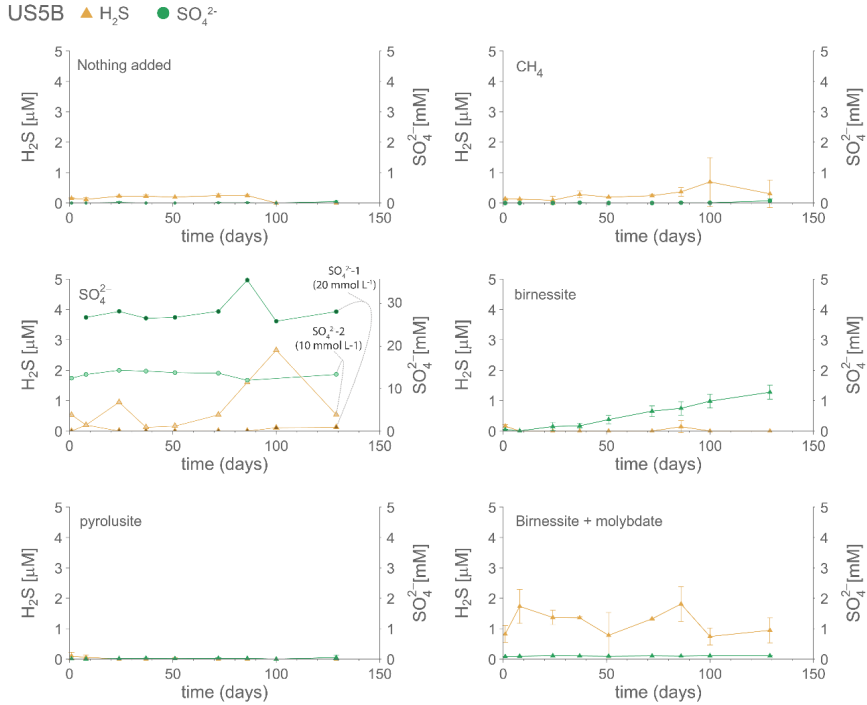


**Fig. S7** Concentrations of  $\text{SO}_4^{2-}$  and  $\text{H}_2\text{S}$  in the incubations with sediment from US5B. Error bars show the standard deviation for duplicate incubations. Interference of molybdate with the  $\text{H}_2\text{S}$  analysis likely results in an overestimation of  $\text{H}_2\text{S}$  concentrations in the incubations with birnessite + molybdate and after 100 days in the  $\text{CH}_4$  control and  $\text{SO}_4^{2-}$  incubations where molybdate was added. Note that in the incubations where  $\text{SO}_4^{2-}$  was added, two different concentrations were added and  $\text{SO}_4^{2-}$  and  $\text{H}_2\text{S}$  are shown for each bottle.

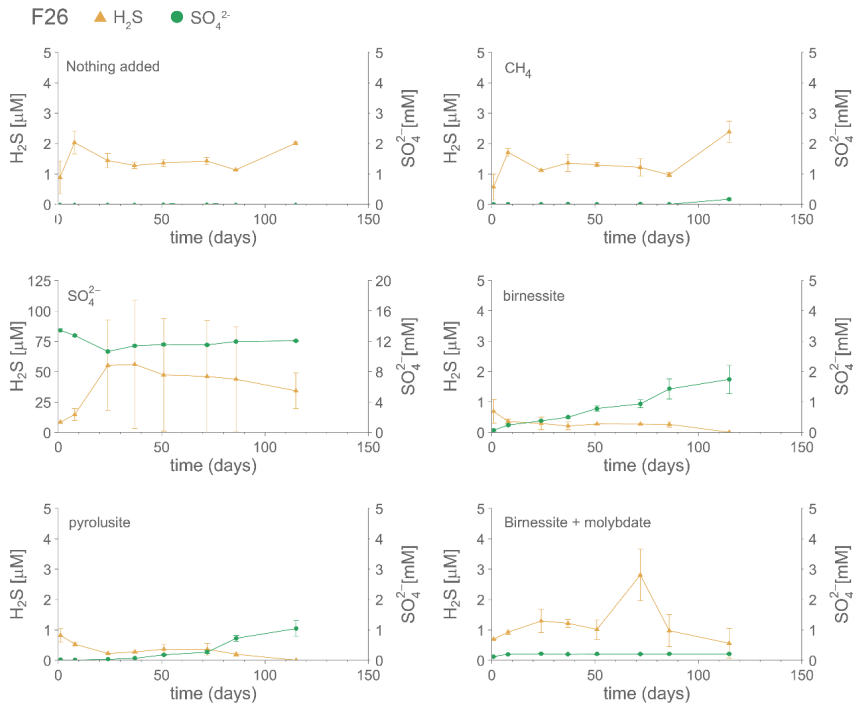


**Fig. S8** Concentrations of SO<sub>4</sub><sup>2-</sup> and H<sub>2</sub>S in the incubations with sediment from F26. Error bars show the standard deviation for duplicate incubations. Concentrations of H<sub>2</sub>S in the birnessite + molybdate incubations are likely overestimated, due to interference of molybdate with the H<sub>2</sub>S analysis.

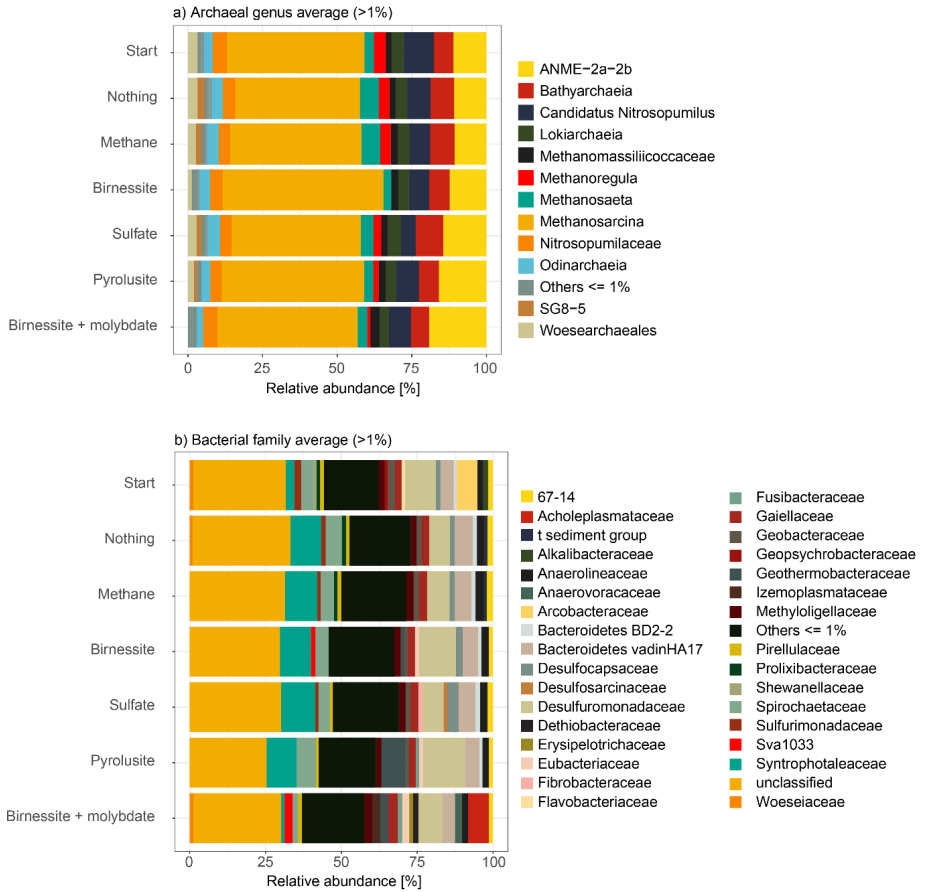


**Fig. S9** 16S rRNA amplicon sequencing results at the start of the incubations and at the end of all treatments with the sediment from US5B. The bar plots show the averages for (a) archaeal relative abundance on genus level and (b) bacterial relative abundance on family level.

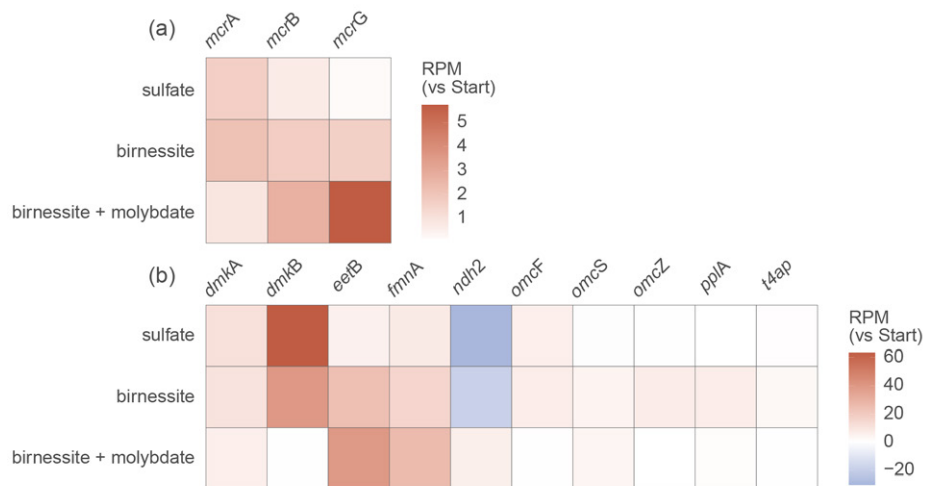


**Fig. S10** Change in reads per million (RPM) in the incubations with sulfate, birnessite and birnessite + molybdate relative to the start material for the *mcr* genes, that are involved in  $\text{CH}_4$  oxidation (a) and the genes that are involved in metal reduction (b).

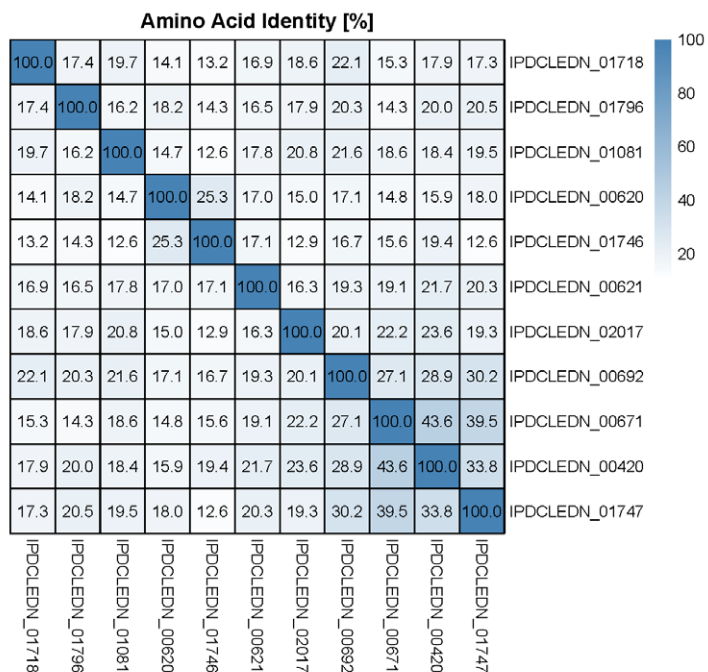


**Fig. S11** Average amino acid identity (AAI) matrix of the different identified MHCs.

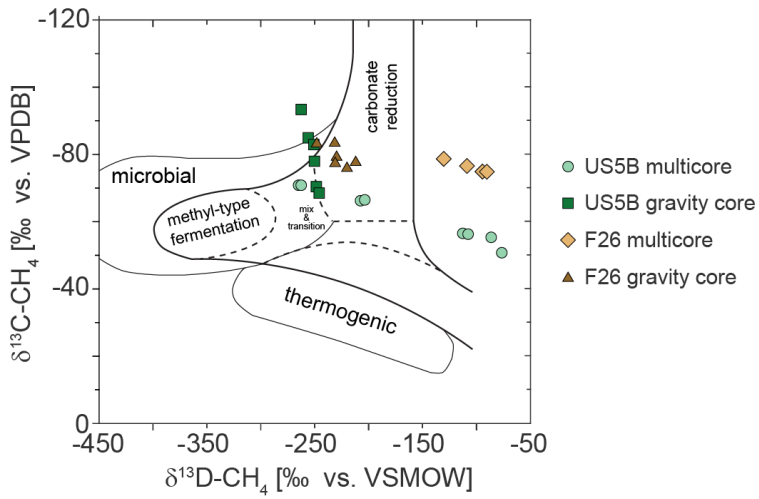


**Fig. S12**  $\text{CH}_4$  isotope classification diagram as presented by Whiticar (1999). The light green dots and dark green squares represent samples from the multicore and gravity core of US5B, respectively. Light brown diamonds and dark brown triangles represent samples from multicore and gravity core of F26, respectively. VPDB is Vienna Pee Dee Belemnite and V-SMOW is Vienna Standard Mean Ocean Water. Figure adapted from Egger et al. (2017).

## Supplementary tables

**Table S1** Composition of the artificial sulfate-free seawater (pH 7.5).

Compound	Concentration
NaCl	5.2 g L <sup>-1</sup>
MgCl <sub>2</sub> * 6 H <sub>2</sub> O	1 g L <sup>-1</sup>
CaCl <sub>2</sub> * 2 H <sub>2</sub> O	0.28 g L <sup>-1</sup>
KCl	0.1 g L <sup>-1</sup>
HEPES	20 mmol L <sup>-1</sup>

**Table S2** For the incubations, sediment used for the DNA extractions and the amount of DNA extracted per g sediment.

Incubation bottle	Sediment used (g)	DNA extracted (ng/g sed)
Start	0.316	11582
Control 1	0.312	11250
Control 2	0.269	10855
CH <sub>4</sub> 1	0.270	8015
CH <sub>4</sub> 2	0.275	12146
SO <sub>4</sub> <sup>2-</sup> 1	0.290	8483
SO <sub>4</sub> <sup>2-</sup> 2	0.267	13446
Birnessite 1	0.308	8506
Birnessite 2	0.256	12421
Birnessite + molybdate 1	0.310	8032
Birnessite + molybdate 2	0.308	6299
Pyrolusite 1	0.249	11526
Pyrolusite 2	0.255	10980

**Table S3** Molybdenum (Mo) concentrations after 114 days in the incubations with US5B sediment as measured with ICP-OES. Dissolved Mo is assumed to represent molybdate (MoO<sub>4</sub><sup>2-</sup>).

Incubation bottle	Mo (mmol L <sup>-1</sup> )
SO <sub>4</sub> <sup>2-</sup> - 1	10.7
Control with <sup>13</sup> C-CH <sub>4</sub> - 1	10.7
birnessite + molybdate - 1	7.2
birnessite + molybdate - 2	6.0

**Table S4** Overview of the high quality MAGs that were obtained with the metagenomic analysis.

<b>Highest taxonomic classification (GTDB-TK)</b>	<b>Completeness</b>	<b>Contamination</b>	<b>Strain heterogeneity</b>
f_JADFYW01	99.94	2.3	0
g_ <i>Syntrophotalea</i>	97.02	1.49	0
g_RPRC01	96.69	0.65	0
g_M0040	94.91	0.97	0
g_ <i>Methanosarcina</i>	93.95	0	0
g_ <i>Methanosarcina</i>	92.76	0	0
s_SPBP01 sp004525935	91.86	0.68	0
g_JAAXQD01	91.83	4.53	0
f_Anaerohalospaeraceae	90.34	3.74	0
g_Kmv04	89.49	1.31	0
g_Desulforhopalus	87.84	3.21	9.09

**Table S5** An overview of the genes in Kmv04 MAG for the reversed methanogenesis pathway (Leu et al., 2020). Furthermore, the table shows the encoded genes that are linked to metal reduction, using the FeGenie tool (Garber et al., 2020).

Genes reverse methanogenesis pathway	Mcr	Mer	Mtd	Mch	Ftr	Fwd	HdrDE	Mtr	ATPase	HdrABC	FrhB	Fpo
Genes encoded in Kmv04 MAG	McrA	Mer	Mtd	Mch	FtrC	FwdB	Hdr	MtrA	*subunit B	HdrA2	FrhB	FpoA
	McrB					FwdD		MtrB	*subunit C	HdrC2		FpoB
	McrC					FwdE		MtrD	*subunit E	HdrB2		FpoC
	McrG					FwdG		MtrE	*subunit F			FpoD
								MtrF	*subunit G/H			FpoH
								MtrG	*subunit I			FpoJ
								MtrH	*subunit K			FpoK
												FpoL
												FpoN
												FpoO

Genes linked to metal reduction	Dissimilatory metal reduction	Fe gene regulation
	**FmnB	PF02742
	**DmkB	

\**V/A*-type  $H^+/Na^+$ -transporting ATPase

\*\* Genes are linked to extracellular electron transfer in bacteria (Light et al., 2018), their function in archaea is unknown.

**Table S6** Proteins with MHCs encoded in the Kmv04 MAG, the amount of MHCs found (CXXCH and CXXXCH), the predicted domain where the protein is active and the signal peptide predictions. Results are shown of best hits when comparing the proteins o the Kmv04 MAG against those of Ca. Methanoperedens ferrireducens (Cai et al., 2018; ref. "a"), Ca. Methanoperedens manganireducens and Ca. Methanoperedens manganireducens (both from Leu et al., 2020; ref. "b").

Protein ID (Length)	CXX(X)CH	Domain*	SignalP	Best blast hit (acc. length)	Identity (%)	e-value	Query coverage (%)	Organism	Ref
IPDCLEDN_00420 (374)	16	a	SP	M.ferri_0002 (316)	25.6	4E-19	99	Ca. M. ferrireducens	a
IPDCLEDN_00620 (446)	9	a, b, c		M.ferri_1464 (3346)	48.4	1E-141	99	Ca. M. ferrireducens	a
				Mn-Methanoperedens-2_00838 (5412)	53.1	7E-163	99	Ca. M. manganireducens	b
IPDCLEDN_00621 (361)	7	a, c		M.ferri_1464 (3346)	53.0	3E-134	100	Ca. M. ferrireducens	a
				Mn-Methanoperedens-2_00838 (5412)	59.8	1E-150	100	Ca. M. manganireducens	b
IPDCLEDN_00671 (198)	6	a, c		M.ferri_1055 (311)	34.51	3E-10	53	Ca. M. ferrireducens	a
IPDCLEDN_00692 (297)	13	a, c	SP	Mn-Methanoperedens-2_00838 (5412)	22.02	9E-9	89	Ca. M. manganireducens	b
IPDCLEDN_01081 (476)	9	a, c, d	SP	M.ferri_0009 (1337)	24.06	7E-5	35	Ca. M. ferrireducens	a
IPDCLEDN_01718 (373)	8	a, c		Mn-Methanoperedens-1_01729 (2523)	44.39	3E-40	92	Ca. M. manganicus	b
IPDCLEDN_01746 (657)	7	a, 2x b, c		M.ferri_2246 (1180)	29.3	2E-83	97	Ca. M. ferrireducens	a
				Mn-Methanoperedens-2_02465 (5599)	32.8	1E-97	94	Ca. M. manganireducens	b
IPDCLEDN_01747 (236)	12	a, c		M.ferri_1681 (315)	27.8	7E-4	93	Ca. M. ferrireducens	a

Table S6 Continued

Protein ID (Length)	CXX(X)CH	Domain*	SignalP	Best blast hit (acc. length)	Identity (%)	e-value	Query coverage (%)	Organism	Ref
IPDCLEDN_01796 (418)	7	a, c, d, e	SP	Mn-Methanoperedens-2_01203 (1094)	26.9	2E-30	77	Ca. M. manganireducens	b
IPDCLEDN_02017 (171)	5	a		Mi.ferri_1463 (163)	52.8	2E-62	94	Ca. M. ferrireducens	a

\* a = MHCs (IPR036280), b = S-layer domain (IPR006457), c = Cytochrome C3, d = Cytochrome c554 and c-prime, e = Flavocytochrome C3; Chain A





## Chapter 8

# Synthesis and outlook

---

R. Klomp<sup>1</sup>

<sup>1</sup>Department of Microbiology, Radboud Institute for Biological and Environmental Sciences,  
Radboud University, Heyendaalseweg 135, 6525AJ Nijmegen, the Netherlands

Methane ( $\text{CH}_4$ ) is a greenhouse gas that is responsible for 16 - 23 % of the global warming since the start of industrialization around 1750 CE (Etminan et al., 2016; Meinshausen et al., 2017). The relatively short lifetime of  $\text{CH}_4$  in the atmosphere ( $\sim 9$  years; Prather et al., 2012), which contrasts with the long residence time of  $\text{CO}_2$  (thousands of years; Archer et al., 2009), implies that a reduction of  $\text{CH}_4$  emissions would enable a relatively rapid decrease in global warming (Ocko et al., 2021; Szopa et al., 2021). Currently, atmospheric  $\text{CH}_4$  concentrations are, however, still increasing (Dean et al., 2018). Hence, it is urgent to gain a better understanding of the sources and sinks of  $\text{CH}_4$  to mitigate climate warming (Saunois et al., 2025).

Marine sediments experience high rates of  $\text{CH}_4$  production and form a very large reservoir of  $\text{CH}_4$  (Regnier et al., 2011). Most of this  $\text{CH}_4$  is already removed in the sediment via aerobic and anaerobic oxidation (Knittel & Boetius, 2009). In coastal systems, however, a part of this  $\text{CH}_4$  can escape and reach the atmosphere (Weber et al., 2019). Sulfate ( $\text{SO}_4^{2-}$ ) is the major electron acceptor in anaerobic  $\text{CH}_4$  oxidation (AOM) in brackish and marine systems (Egger et al., 2018). However, other electron acceptors, such as nitrate/nitrite (Raghoebarsing et al., 2006), natural organic matter (Valenzuela et al., 2017; Pelsma et al., 2023), and metal oxides (Beal et al., 2009; Egger et al., 2015; Leu et al., 2020) can also be utilized. A coupling of AOM and manganese (Mn) oxide reduction (Mn-AOM) has been suggested for brackish and marine sediments based on results of incubations (Beal et al., 2009; Xu et al., 2021), the concomitant occurrence of maxima in dissolved Mn and  $\text{CH}_4$  in porewater (Soyol-Erdene & Huh, 2013; Riedinger et al., 2014) and reactive transport modelling (Lenstra et al., 2023; Xiao et al., 2023). Definitive proof for a direct coupling of  $\text{CH}_4$  oxidation and Mn reduction in these environments, as well as identification of the key microbes for this process and an understanding of its quantitative importance, are, however, still lacking (Wallenius et al., 2021; Xue et al., 2025).

In this thesis, we focus on the interaction between  $\text{CH}_4$  and Mn oxides in coastal sediments from both a geochemical and microbiological perspective. In **chapter 2**, we present a sequential extraction method to identify and quantify the different Mn mineral forms in coastal sediments. The research in **chapters 3-7** focuses on two study areas: a seasonally euxinic coastal marine basin in Lake Grevelingen and the brackish Bothnian Sea. In **chapter 3**, we show that dissolved Mn(III) is a key redox intermediate in manganese cycling in the sediment of the seasonally euxinic system. In **chapter 4** we observe that  $\text{H}_2\text{S}$  toxicity for ANME strongly controls the  $\text{CH}_4$  filter in the sediment. In **chapter 5** we demonstrate the possibility of Mn-AOM and identify ANME-2ab and ANME-3 as key microbial players in brackish sediments. We find potential for a variety of AOM pathways by ANME-2ab, which likely

contribute to the resilience of the microbial  $\text{CH}_4$  filter in **chapter 6**, and we present evidence for a direct coupling between  $\text{CH}_4$  oxidation and Mn oxide reduction by ANME-2ab in **chapter 7**. In the current chapter, the main implications of our findings are discussed, alongside key directions for further research

## Co-occurrence of Mn oxides and $\text{CH}_4$

An important prerequisite for Mn-AOM is the co-occurrence of  $\text{CH}_4$  and Mn oxides. In marine sediments, this co-occurrence is not expected under steady state conditions, as Mn oxides reductively dissolve in the upper part of the sediment and  $\text{CH}_4$  typically forms and is removed in deeper layers of the sediment (Froelich et al., 1979).

Under non-steady state conditions, Mn oxides can be buried into the methanic zone, creating an opportunity for  $\text{CH}_4$  and Mn oxides to interact and be biologically removed. This is observed at our study site in Lake Grevelingen, where  $\text{CH}_4$  production is so high that  $\text{CH}_4$  is present throughout the sediment (Egger et al., 2016; van Helmond et al., 2025; **chapter 3, 4, 5**). At this site, Mn oxides are mostly deposited in winter and spring and escape reduction because of rapid burial into a  $\text{H}_2\text{S}$ -free zone below the SMTZ. This shows that Mn oxides can be buried into methanic sediments even when these systems are strongly impacted by eutrophication.

Interactions between  $\text{CH}_4$  and Mn oxides can also be promoted in non-steady state systems where the SMTZ moves upwards upon increased eutrophication. Our study area in the Bothnian Sea provides an example of such a system (Slomp et al., 2013; Egger et al., 2015; Rooze et al., 2016; **chapter 6**). In this region, Mn oxides may be buried below the SMTZ (Slomp et al., 2013). Additionally, the high organic matter input stimulates methanogenesis (Egger et al., 2015). At site US2 (**chapter 6**), this results in the presence of  $\text{CH}_4$  all the way up to the sediment-water interface, which also enhances the contact between  $\text{CH}_4$  and Mn oxides.

## Manganese driven methane oxidation

In our experiments, we show that different Mn oxide minerals (birnessite, pyrolusite and manganite) can enhance  $\text{CH}_4$  oxidation (**chapter 5, 6, 7**). Oxidation of  $\text{CH}_4$  with Mn oxides can occur via two pathways. One pathway involves the production of  $\text{SO}_4^{2-}$  via the oxidation of reduced sulfur species such as FeS by Mn oxides, referred

to as a “cryptic sulfur cycling” (Holmkvist et al., 2011; Su et al., 2020), while the other is a direct biological coupling between  $\text{CH}_4$  oxidation and Mn oxide reduction (e.g. Leu et al., 2020). The accumulation of  $\text{SO}_4^{2-}$  in the incubations with birnessite and pyrolusite in **chapter 5** and **6** makes it impossible to distinguish AOM that is directly coupled to Mn oxide reduction from AOM via a cryptic sulfur cycle (Su et al., 2020). Hence, AOM via a cryptic sulfur cycle driven by Mn reduction may contribute to *in-situ*  $\text{CH}_4$  removal. The absence of  $\text{SO}_4^{2-}$  in the incubation with manganite in **chapter 5** implies that a cryptic sulfur cycle cannot take place, driven by manganite reduction. This might be because Mn(III) minerals are less efficient in oxidizing reduced sulfur species than Mn(IV) minerals (Aller & Rude, 1987). In **chapter 7**, we provide evidence for a direct coupling of  $\text{CH}_4$  oxidation to the reduction of birnessite in incubations where  $\text{SO}_4^{2-}$  reduction is inhibited by molybdate. We also show the possibility of a direct coupling between the reduction of pyrolusite and  $\text{CH}_4$  oxidation, because  $\text{SO}_4^{2-}$  is absent from the incubations. Hence, a coupling between Mn oxide reduction and  $\text{CH}_4$  oxidation is possible with various types of Mn oxides.

Dissolved Mn(III) was abundantly present in Scharendijke sediments, also in the methanic zone (**chapter 3**), however it did not enhance AOM in the incubations performed in **chapter 5**. It is remarkable that we found dissolved Mn(III) in porewater with such a high  $\text{H}_2\text{S}$  concentration. Possibly the organic ligands that stabilize dissolved Mn(III) kinetically hinder Mn(III) reduction by  $\text{H}_2\text{S}$  (Oldham et al., 2015). We speculate in **chapter 5** that the organic ligand could also shield Mn(III) from microbial reduction. Furthermore, the metabolic pathway required to utilize dissolved Mn for AOM might be different from the pathway for solid phase Mn, further explaining why dissolved Mn(III), in contrast to Mn oxides, is not used for AOM.

We identified ANME-2ab (family of *Methanocomedenaceae*; Chadwick et al., 2022) as a key microbe for Mn-AOM in brackish and marine sediments in **chapters 5, 6, and 7**. ANME-2ab are common in a wide range of brackish and marine environments, including continental margin sediments, brackish coastal sediments, deep-sea cold  $\text{CH}_4$  seeps, and shallow-water permeable sediments (e.g. Cambon-Bonavita et al., 2009; Mason et al., 2015; Ruff et al., 2016; Li et al., 2020; Rasigraf et al., 2020). Oxidation of  $\text{CH}_4$  coupled to Fe reduction has also been linked to ANME-2a based on sediment incubations (Aromokeye et al., 2020) and similar depth trends in total sediment Fe and ANME-2a in Bothnian Sea sediments, where Fe-AOM was demonstrated in incubations (Egger et al., 2015; Rasigraf et al., 2020). Furthermore, ANME-2ab were present in sediments where Mn-AOM activity was observed in sediment incubations (Xu et al., 2021). In our incubations in **chapter 5, 6 and 7**, ANME-2ab had a higher archaeal relative abundance compared to the start and

control when Mn oxides were added. This indicates that ANME-2ab are involved in Mn-AOM.

We find in **chapter 5** that ANME-3 (Ca. *Methanovorans*; Chadwick et al., 2022) may be more important than ANME-2ab when Mn-AOM involves a cryptic sulfur cycle. ANME-3 are typically found in deep water sediments, at sites with fluid flow such as cold seeps and mud volcanoes (Niemann et al., 2006; Vigneron et al., 2013). Lake Grevelingen has so far been the only coastal sediment where ANME-3 is observed (Bhattarai et al., 2017; Wallenius et al., 2025).

Strong counter gradients between the abundance of ANME and concentrations of  $H_2S$  in the sediment of Lake Grevelingen indicated that  $H_2S$  is toxic for ANME (**chapter 4**). ANME-2ab appear to be less sensitive to  $H_2S$  compared to ANME-3, as they are still present at higher  $H_2S$  concentrations. These results confirm previous work showing that  $H_2S$  hinders AOM by ANME, based on incubations with eutrophic coastal sediments (Dalcin Martins et al., 2024) and explain the absence of ANME in  $H_2S$  rich marine cold-seeps (Semler & Dekas, 2025). The  $H_2S$  toxicity narrows the zone where ANME can oxidize  $CH_4$  and therefore limits the efficiency of the sedimentary  $CH_4$  filter in Lake Grevelingen.

ANME can form a consortium with a bacterial partner, where the bacteria perform electron acceptor reduction and the ANME perform  $CH_4$  oxidation (Boetius et al., 2000). Bacteria that typically form a consortium with ANME belong to the *Desulfosarcina/Desulfococcus* clades and *Desulfobulbaceae* family (Boetius et al., 2000; Orphan et al., 2002; Lösekann et al., 2007). Bacterial partners may also be involved in metal AOM (Slobodkin et al., 2023). In **chapter 5** we identified *Desulfobulbaceae* as a potential bacterial partner for ANME-2ab in Mn-AOM. Some members of the *Desulfobulbaceae* showed the ability to reduce metal oxides in sediment incubations (Lovley et al., 1993; Müller et al., 2020), and hence could indeed reduce Mn oxides. When AOM was performed by ANME-3, which likely involves a cryptic sulfur cycle, *Desulfosarcinacea* and *Desulfovibrionaceae* were identified as potential bacterial partners for ANME-3 (**chapter 5**). Determination of the bacterial partners was based on a simultaneous increase in relative abundance of these bacteria and the ANME in the incubations and therefore remains speculative. Direct proof of a consortium of ANME and bacteria in Mn-AOM and the identification of the bacterial partners could be obtained via Fluorescent In Situ Hybridization (FISH; e.g. Boetius et al., 2000), at the end of Mn-AOM incubation experiments. It is also possible that ANME function independently of a bacterial

partner and perform both CH<sub>4</sub> oxidation and Mn reduction, most likely using extracellular electron transfer to the solid phase metal oxides (e.g. Leu et al., 2020).

In **chapter 7**, where CH<sub>4</sub> reduction is shown to be directly coupled to Mn reduction, we propose that ANME-2ab performs extracellular electron transfer to couple these processes. Extracellular electron transfer can occur via various mechanisms, and may involve different types of proteins (Zhao et al., 2021; Paquete et al., 2022). For *Candidatus Methanoperedens* (ANME-2d), multiheme c-type cytochromes are likely important for extracellular electron transfer to perform metal reduction (Cai et al., 2018; Leu et al., 2020; Zhang et al., 2023; Ouboter et al., 2024). We suggested extracellular electron transfer by ANME-2ab based on a comparison of multiheme c-type cytochrome proteins between the ANME-2ab from our experiment and those from *Ca. Methanoperedens* proposed to perform extracellular electron transfer (Cai et al., 2018; Leu et al., 2020; Ouboter et al., 2024). To verify extracellular electron transfer by ANME-2ab, further research can aim to identify or compare the protein structures that are potentially involved in this process (e.g. Edwards et al., 2014; Filman et al., 2019) and test these structures on electron transport properties in a biochemical assay (e.g. Vamshi Krishna & Venkata Mohan, 2019).

## The impact of Mn-AOM

Coastal sediments are hotspots for marine methane release (Weber et al., 2019). The input of Mn oxides to coastal sediments is also relatively high compared to the open ocean, given the proximity to the terrestrial sources of Mn oxides and the lateral Mn transfer and recycling that is typical for coastal environments (Adelson et al., 2001; Lenstra et al., 2022). Furthermore, ANME-2ab, the key microbes for Mn-AOM in brackish and marine sediments, are present in various coastal systems (e.g. Rasigraf et al., 2020; Ruff et al., 2016). The co-occurrence of ANME-2ab and Mn oxides in coastal sediments suggests a potential contribution of Mn-AOM to CH<sub>4</sub> removal. In the following section, the impact of Mn-AOM on both the carbon and manganese cycles will be explored.

We find Mn-AOM rates of 2.2 & 12.7 μmol cm<sup>-3</sup> yr<sup>-1</sup> in **chapter 6**. These rates compare well with experimentally determined Mn-AOM rates reported in literature, which range from 0.2 to 14 μmol cm<sup>-3</sup> yr<sup>-1</sup> (Beal et al., 2009; Segarra et al., 2013; Xu et al., 2021). The *in-situ* Mn-AOM rates predicted in reactive transport modelling are lower than those obtained in laboratory experiments (Lenstra et al., 2023; Xiao et al., 2023; **chapter 3**). This likely results from more beneficial conditions of, for example, temperature and Mn oxide content in the laboratory experiments compared to the

*in-situ* conditions. A future challenge would be to experimentally determine *in-situ* Mn-AOM rates as verification for the rates calculated in computer models. Experimental determination of *in-situ* Mn-AOM rates remains challenging with current techniques, however, because it is difficult to separate the different AOM pathways.

In brackish and marine sediments, aerobic methane oxidation and  $\text{SO}_4^{2-}$ -AOM are often considered the most important pathways for methane oxidation (Knittel & Boetius, 2009; Egger et al., 2018; Lenstra et al., 2023). Notably, AOM coupled to Mn oxide reduction is energetically much more favorable than  $\text{SO}_4^{2-}$ -AOM, with a Gibbs free energy of  $-790 \text{ kJ mol}^{-1} \text{ CH}_4$  for Mn oxides (Sturm et al., 2019) versus  $-17 \text{ kJ mol}^{-1} \text{ CH}_4$  for  $\text{SO}_4^{2-}$  (Meulepas et al., 2010). Nevertheless,  $\text{SO}_4^{2-}$ , which is present at 25 - 30  $\text{mmol L}^{-1}$  in marine environments, contributes more to AOM. A key reason is that solutes are more easily available to microbes compared to solid phase electron acceptors (Xue et al., 2025). Another reason is that the supply of  $\text{SO}_4^{2-}$  to the methanic zone of the sediment depends on diffusion and fluid transport and is therefore more rapid than that of Mn oxide, which depends on sediment accumulation rates. Furthermore, based on the reaction stoichiometry,  $\text{SO}_4^{2-}$  ( $\text{CH}_4:\text{SO}_4^{2-} = 1:1$ ) is more efficient per molecule in the conversion of  $\text{CH}_4$  compared to Mn oxides ( $\text{CH}_4:\text{Mn(IV)} = 1:4$ ). Nonetheless, it has been estimated that metal AOM could contribute up to 10% percentage of methane removal in metal-rich coastal systems (Lenstra et al., 2023; Xiao et al., 2023). It is therefore a sink that should be considered when investigating  $\text{CH}_4$  dynamics in coastal sediments.

Besides the effect on the carbon cycle, Mn-AOM also affects the Mn cycle. The reaction stoichiometry which requires 4 Mn(IV), and 8 Mn(III), per  $\text{CH}_4$  molecule oxidized, and results in high Mn oxide reduction rates in AOM. Reduction of Mn oxides deeper in the sediment leads to the accumulation of dissolved Mn (**chapter 6**). Furthermore, elements that are adsorbed onto Mn oxides, such as molybdenum (Phillips & Xu, 2021; Żygadłowska et al., 2024a) and vanadium (Cui et al., 2023; van Helmond et al., 2025), which are both used as redox proxies (van Helmond et al., 2025), are also released into the pore water upon Mn oxide reduction. Therefore, Mn-AOM can affect how these proxies should be interpreted.

## Mn-AOM in a changing world

Coastal seas are changing rapidly under the effect of anthropogenic stresses. An increase in seawater temperature upon climate change enhances water column stratification and reduces oxygen solubility (Breitburg et al., 2018). At the same

time, eutrophication amplifies primary productivity and therefore the organic matter supply to the sediment, which increases the oxygen demand in the sediment and bottom water and promotes methanogenesis (Wallenius et al., 2021). Higher oxygen demand in combination with a reduced oxygen supply promotes anoxia in the bottom water and increasingly leads to coastal dead zones (Diaz & Rosenberg, 2008). These changes will have an impact on Mn-AOM in brackish and marine sediments as discussed below.

When the organic matter input to the sediment increases due to eutrophication, the SMTZ might move upwards as we and others observed in the Bothnian Sea (Slomp et al., 2013; Egger et al., 2015; Rooze et al., 2016; **chapter 6**). The ANME cannot move upwards and will end up in  $\text{SO}_4^{2-}$  depleted conditions (**chapter 6**). Here, the microbial community may shift from  $\text{SO}_4^{2-}$ -AOM to other electron acceptors for AOM, such as Mn oxides if these are present (**chapter 6**). Our results show that the versatility of the microbial community can enable a relatively quick response to such changes in sediment chemistry (**chapter 6**) because the microbial biomass is not limiting. Hence, variations in the depth of the SMTZ may increase the importance of alternative electron acceptors, such as Mn oxides, in AOM.

In a system that experiences seasonal anoxia where sedimentation rates and the metal oxide supply to the sediment are high, Mn oxides may be buried into the methanic zone, as seen in Scharendijke basin (**chapter 3, 4, 5**). Here, the potential for Mn-AOM is present (**chapter 5**), however,  $\text{H}_2\text{S}$  toxicity restricts the ANME to a narrow zone in the sediment and prevents them from establishing an efficient methane filter (**chapter 6**). Furthermore, the Mn oxide content of the sediment is low, which also makes Mn-AOM less favorable (**chapter 3, 5**). A further increase in eutrophication is expected to lead to a higher organic matter supply to the sediment, which increases  $\text{SO}_4^{2-}$  reduction. As a result, euxinia may become more severe and the ANME niche in the sediment may become even more narrow, which will negatively impact AOM in the sediment. Under fully anoxic conditions, the supply of Mn oxides to the sediment diminishes (Slomp et al., 1997), and the availability of Mn oxides for AOM is limited.

These examples show that an increase in  $\text{CH}_4$  production upon eutrophication in some situations might be partially compensated by Mn-AOM. When conditions in the sediment become too reducing, however, the burial of Mn oxides into the sediment is negatively affected because Mn oxide reduction by processes other than Mn-AOM increase, which limits the possibility of Mn-AOM. Furthermore, accumulation of  $\text{H}_2\text{S}$  in the porewater likely increases, which has a toxic effect on the ANME performing Mn-AOM.

## Concluding remarks

With the work presented in this thesis, we show that Mn driven AOM is possible in brackish and marine sediments. In some settings, a cryptic sulfur cycle may be involved. We identify ANME-2ab as the key organism for Mn-AOM in such environments. These results emphasize the versatility of the methanotrophic community in brackish and marine coastal sediments, show the occurrence of an extra CH<sub>4</sub> sink in such environments and indicate that accumulation of dissolved Mn below the SMTZ can be the result of Mn-AOM.

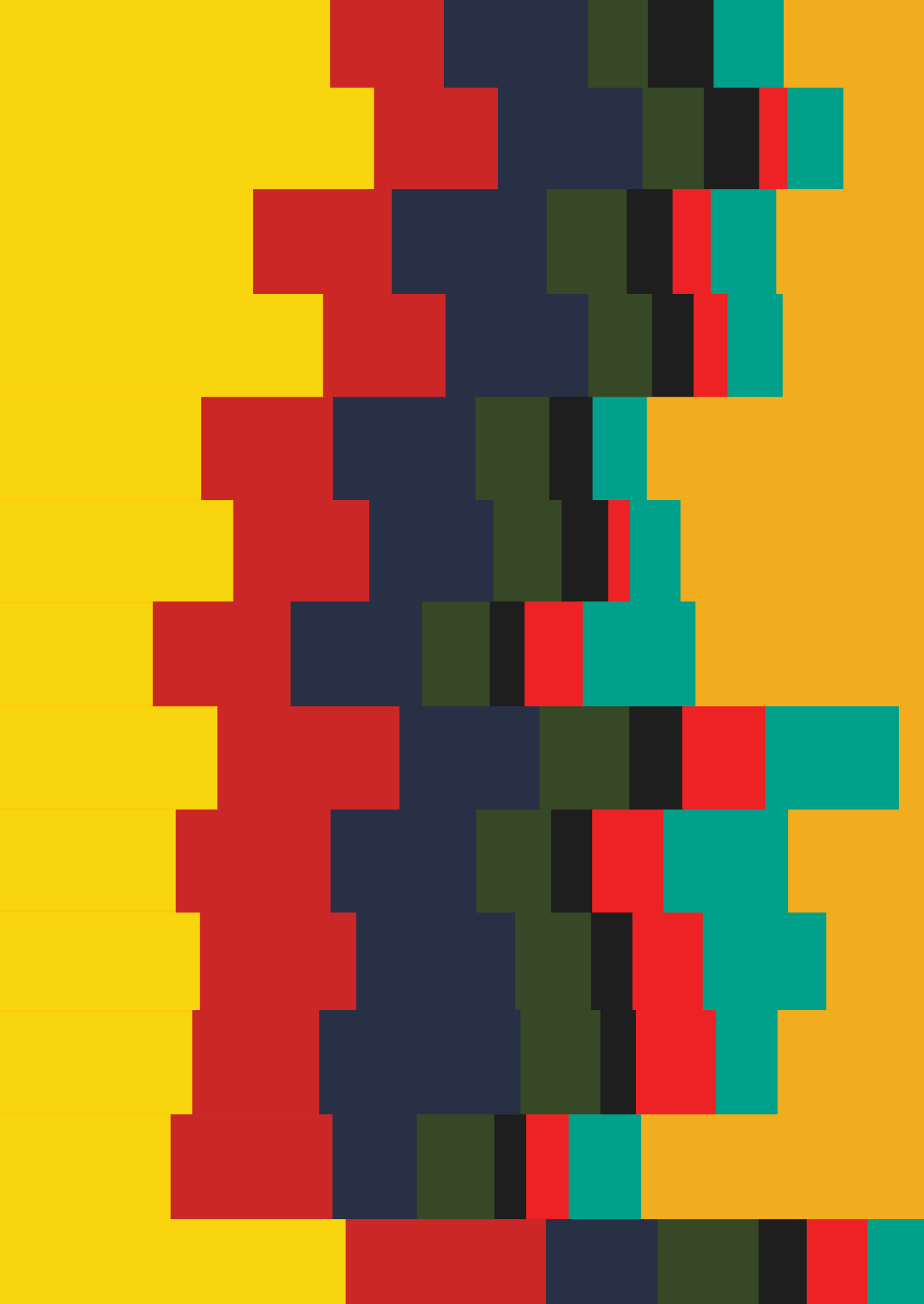
To fully understand the impact of Mn-AOM, more research should be carried out to quantify the contribution of Mn-AOM to CH<sub>4</sub> removal in various types of coastal sediments around the world. These contributions should focus both on the upper part of the sediment and deeper in the sediment if Mn oxides persist. Reactive transport models are a good tool to estimate *in-situ* Mn-AOM rates, as experimental determination of these *in-situ* rates remains challenging. Such models can also be used to predict the effect of anthropogenic impacts and climate change on Mn-AOM (e.g. Lenstra et al., 2023). Ideally, these reactive transport models include the dynamics of different types of ANME, and as such, a variety of pathways that specific clades can perform and the effects of the toxicity of sulfide.

Incorporation of the redox speciation of dissolved Mn into the reactive transport models also improves the estimates of Mn-AOM, as dissolved Mn(III) is a key component of Mn cycling (**chapter 3**). For this, more measurements of dissolved Mn(III) should be performed to obtain a better understanding of the dynamics of porewater Mn(II) and Mn(III). More insight into the different organic matter molecules that form a complex with Mn(III) can help understand the reactivity of dissolved Mn(III). It would be interesting to know which organic matter molecules stabilize dissolved Mn(III) in the light of organic matter-driven AOM, where certain reactive groups of organic matter facilitate CH<sub>4</sub> oxidation (Valenzuela et al., 2017).

The presence of Mn oxides in the sediment was based on the sequential extraction method tested in **chapter 2**. This method is a useful tool to obtain insight into the overall Mn mineral speciation, however, it does not provide very specific mineral information. We show in **chapters 5** and **7** that the type of Mn oxide affects the possibility for a cryptic sulfur cycle. It may also be possible that Mn-AOM rates are impacted by differences in Mn mineralogy, although we do not observe a clear difference in AOM signal between birnessite and pyrolusite in **chapter 7**. At depth in the sediment, Mn minerals often occur in low concentrations, which complicates

analysis via, for example, XRD or synchrotron-based X-ray spectroscopy. For further studies, it would be insightful to use a method that can determine the exact Mn mineralogy deeper in the sediment. This information is crucial to determine the potential for *in-situ* Mn-AOM and can therefore help to identify locations where this process can play a role in CH<sub>4</sub> removal.





Appendices

References

Data management

Acknowledgements/Dankwoord

List of publications

Curriculum Vitae

## References

- Adelson, J. M., Helz, G. R., & Miller, C. V. (2001). Reconstructing the rise of recent coastal anoxia; molybdenum in Chesapeake Bay sediments. *Geochimica et Cosmochimica Acta*, 65(2), 237–252. [https://doi.org/10.1016/S0016-7037\(00\)00539-1](https://doi.org/10.1016/S0016-7037(00)00539-1)
- Adnew, G. A., Röckmann, T., Blunier, T., Jørgensen, C. J., Sapper, S. E., van der Veen, C., Sivan, M., Popa, M. E., & Christiansen, J. R. (2025). Clumped isotope measurements reveal aerobic oxidation of methane below the Greenland ice sheet. *Geochimica et Cosmochimica Acta* 389, 249–264. doi: 10.1016/j.gca.2024.11.009
- Albertsen, M., Hugenholtz, P., Skarszewski, A., Nielsen, K. L., Tyson, G. W., & Nielsen, P. H. (2013). Genome sequences of rare, uncultured bacteria obtained by differential coverage binning of multiple metagenomes. *Nature Biotechnology*, 31(6), 533–538. <https://doi.org/10.1038/nbt.2579>
- Alcott, L.J., Krause, A. J., Hammarlund, E. U., Bjerrum, C. J., Scholz, F., Xiong, Y., Hobson, A. J., Neve, L., Mills, B. J. W., März, C., Schnetger, B., Bekker, A., & Poulton, S. W. (2020). Development of iron speciation reference materials for palaeoredox analysis. *Geostandards and Geoanalytical Research* 44, 581–591. <https://doi.org/10.1111/ggr.12342>
- Algesten, G., Brydsten, L., Jonsson, P., Kortelainen, P., Löfgren, S., Rahm, L., Räike, A., Sobek, S., Tranvik, L., Wikner, J., & Jansson, M. (2006). Organic carbon budget for the Gulf of Bothnia. *Journal of Marine Systems*, 63(3–4), 155–161. <https://doi.org/10.1016/j.jmarsys.2006.06.004>
- Aller, R. C. (1994). The sedimentary Mn cycle in Long Island Sound: Its role as intermediate oxidant and the influence of bioturbation, O<sub>2</sub>, and Corg flux on diagenetic reaction balances. *Journal of Marine Research*, 52(2), 259–295. <https://doi.org/10.1357/0022240943077091>, 1994.
- Aller, R. C., & Rude, P. D. (1987). Complete oxidation of solid phase sulfides by manganese and bacteria in anoxic marine sediments. *Geochimica et Cosmochimica Acta*, 52, 751–765. [https://doi.org/10.1016/0016-7037\(88\)90335-3](https://doi.org/10.1016/0016-7037(88)90335-3)
- Almagro Armenteros, J. J., Tsirigos, K. D., Sønderby, C. K., Petersen, T. N., Winther, O., Brunak, S., von Heijne, G., & Nielsen, H. (2019). SignalP 5.0 improves signal peptide predictions using deep neural networks. *Nature Biotechnology*, 37(4), 420–423. <https://doi.org/10.1038/s41587-019-0036-z>
- Alneberg, J., Bjarnason, B. S., De Bruijn, I., Schirmer, M., Quick, J., Ijaz, U. Z., Lahti, L., Loman, N. J., Andersson, A. F., & Quince, C. (2014). Binning metagenomic contigs by coverage and composition. *Nature Methods*, 11(11), 1144–1146. <https://doi.org/10.1038/nmeth.3103>
- Andrén, T., Björck, S., Andrén, E., Conley, D., Zillén, L., & Anjar, J. (2011). The Development of the Baltic Sea Basin During the Last 130 ka. In *The Baltic Sea Basin* (pp. 75–97). Berlin, Heidelberg: Springer Berlin Heidelberg. [https://doi.org/10.1007/978-3-642-17220-5\\_4](https://doi.org/10.1007/978-3-642-17220-5_4)
- Andrews, S. (2010). *FastQC*. <http://www.bioinformatics.babraham.ac.uk/projects/fastqc/>
- Anschutz, P., Dedieu, K., Desmazes, F., & Chaillou, G. (2005). Speciation, oxidation state, and reactivity of particulate manganese in marine sediments. *Chemical Geology*, 218(3–4), 265–279. <https://doi.org/10.1016/j.chemgeo.2005.01.008>
- APHA (2005). Standard Methods for the Examination of Water and Wastewater. American Public Health Association–American Water Works Association–Water Environment Federation.
- Archer, D., Eby, M., Brovkin, V., Ridgwell, A., Cao, L., Mikolajewicz, U., Caldeira, K., Matsumoto, K., Munhoven, G., Montenegro, A., & Tokos, K. (2009). Atmospheric lifetime of fossil fuel carbon dioxide. *Annual Review of Earth and Planetary Sciences*, 37, 117–134. <https://doi.org/10.1146/annurev.earth.031208.100206>

- Aromokeye, D. A., Kulkarni, A. C., Elvert, M., Wegener, G., Henkel, S., Coffinet, S., Eickhorst, T., Oni, O. E., Richter-Heitmann, T., Schnakenberg, A., Taubner, H., Wunder, L., Yin, X., Zhu, Q., Hinrichs, K. U., Kasten, S., & Friedrich, M. W. (2020). Rates and Microbial Players of Iron-Driven Anaerobic Oxidation of Methane in Methanic Marine Sediments. *Frontiers in Microbiology*, 10(January), 1–19. <https://doi.org/10.3389/fmicb.2019.03041>
- Aroney, S. T. N., Newell, R. J. P., Nissen, J. N., Camargo, A. P., Tyson, G. W., & Woodcroft, B. J. (2025). CoverM: read alignment statistics for metagenomics. *Bioinformatics* 41(4). doi: 10.1093/bioinformatics/btaf147
- Baas, E., Van Helmond, N. A. G. M., Van Erk, M. R., Żygadłowska, O. M., Klomp, R., Piso, L., Hennekam, R., Reichart, G.-J., Jetten, M. S. M., & Slomp, C. P. (2026). Geochemical records of Holocene environmental change in a high latitude coastal basin. *Chemical Geology*, 703, 123247, <https://doi.org/10.1016/j.chemgeo.2026.123247>.
- Bai, Y. N., Wang, X. N., Wu, J., Lu, Y. Z., Fu, L., Zhang, F., Lau, T. C., & Zeng, R. J. (2019). Humic substances as electron acceptors for anaerobic oxidation of methane driven by ANME-2d. *Water Research*, 164, 114935. <https://doi.org/10.1016/j.watres.2019.114935>
- Beal, E. J., House, C. H., & Orphan, V. J. (2009). Manganese- and iron-dependent marine methane oxidation. *Science*, 325(5937), 184–187. <https://doi.org/10.1126/science.1169984>
- Berelson, W., McManus, J., Coale, K., Johnson, K., Burdige, D., Kilgore, T., Colodner, D., Chavez, F., Kudela, R., & Boucher, J. (2003). A time series of benthic flux measurements from Monterey Bay, CA. *Continental Shelf Research*, 23(5), 457–481. [https://doi.org/10.1016/S0278-4343\(03\)00009-8](https://doi.org/10.1016/S0278-4343(03)00009-8)
- Berg, P., Rysgaard, S., & Thamdrup, B. O. (2003). Dynamic Modeling of Early Diagenesis and Nutrient Cycling. A Case Study in an Arctic Marine Sediment. *American Journal of Science*, 303, 905–955
- Bhattarai, S., Cassarini, C., Gonzalez-Gil, G., Egger, M., Slomp, C. P., Zhang, Y., Esposito, G., & Lens, P. N. L. (2017). Anaerobic Methane-Oxidizing Microbial Community in a Coastal Marine Sediment: Anaerobic Methanotrophy Dominated by ANME-3. *Microbial Ecology*, 74(3), 608–622. <https://doi.org/10.1007/s00248-017-0978-y>
- Bianchi, T.S., Lambert, C.D., Santschi, P.H., & Guo, L. (1997). Sources and transport of land-derived particulate and dissolved organic matter in the Gulf of Mexico (Texas shelf/ slope): the use of ligninphenols and loliolides as biomarkers. *Organic Geochemistry* 27, 65–78. [https://doi.org/10.1016/S0146-6380\(97\)00040-5](https://doi.org/10.1016/S0146-6380(97)00040-5)
- Biddle, J. F., Cardman, Z., Mendlovitz, H., Albert, D. B., Lloyd, K. G., Boetius, A., & Teske, A. (2012). Anaerobic oxidation of methane at different temperature regimes in Guaymas Basin hydrothermal sediments. *The ISME Journal* 6, 1018–1031. doi: 10.1038/ismej.2011.164
- Blum, M., Andreeva, A., Florentino, L. C., Chuguransky, S. R., Grego, T., Hobbs, E., Pinto, B. L., Orr, A., Paysan-Lafosse, T., Ponamareva, I., Salazar, G. A., Bordin, N., Bork, P., Bridge, A., Colwell, L., Gough, J., Haft, D. H., Letunic, I., Llinares-López, F., ... Bateman, A. (2025). InterPro: the protein sequence classification resource in 2025. *Nucleic Acids Research*, 53(D1), D444–D456. <https://doi.org/10.1093/nar/gkae1082>
- Boetius, A., Ravensschlag, K., Schubert, C. J., Rickert, D., Widdel, F., Gieseke, A., Amann, R., Jürgensen, B. B., Witte, U., & Pfannkuche, O. (2000). A marine microbial consortium apparently mediating anaerobic oxidation of methane. *Nature*, 407, 623–626. <https://doi.org/https://doi.org/10.1038/35036572>
- Boudreau, P. (1996) A Method-of-Lines Code For Carbon and Nutrient Diagenesis in Aquatic Sediments. *Computers and Geosciences*, 22(5), 479–496.

- Boudreau, B. P. (1996). The diffusive tortuosity of fine-grained unlithified sediments. *Geochimica et Cosmochimica Acta*, 60(16), 3139–3142. [https://doi.org/10.1016/0016-7037\(96\)00158-5](https://doi.org/10.1016/0016-7037(96)00158-5)
- Boudreau, B. P. (1997) Diagenetic models and their implementation : modelling transport and reactions in aquatic sediments. Springer Berlin Heidelberg. <https://doi.org/10.1007/978-3-642-60421-8>.
- Brass, M., & Röckmann, T. (2010). Continuous-flow isotope ratio mass spectrometry method for carbon and hydrogen isotope measurements on atmospheric methane. *Atmospheric Measurement Techniques*, 3(6), 1707–1721. <https://doi.org/10.5194/amt-3-1707-2010>
- Breitburg, D., Levin, L. A., Oschlies, A., Grégoire, M., Chavez, F. P., Conley, D. J., Garçon, V., Gilbert, D., Gutiérrez, D., Isensee, K., Jacinto, G. S., Limburg, K. E., Montes, I., Naqvi, S. W. A., Pitcher, G. C., Rabalais, N. N., Roman, M. R., Rose, K. A., Seibel, B. A., ... Zhang, J. (2018). Declining oxygen in the global ocean and coastal waters. *Science*, 359(6371). <https://doi.org/10.1126/science.aam7240>
- Brumsack, H.J. (2006). The trace metal content of recent organic carbon-rich sediments: implications for cretaceous black shale formation. *Palaeogeography, Palaeoclimatology Palaeoecology* 232, 344–361. <https://doi.org/10.1016/j.palaeo.2005.05.011>
- Burdige, D.J. (1993). The biogeochemistry of manganese and iron reduction in marine sediments. *Earth Science Reviews* 35, 249–284. [https://doi.org/10.1016/0012-8252\(93\)90040-E](https://doi.org/10.1016/0012-8252(93)90040-E)
- Burdige, D.J. (2006). *Geochemistry of Marine Sediments*. Princeton University Press.
- Burdige, D. J. (2007). Preservation of organic matter in marine sediments: Controls, mechanisms, and an imbalance in sediment organic carbon budgets? *Chemical Reviews*, 107(2), 467–485. <https://doi.org/10.1021/cr050347q>
- Burdige, D. J., Berelson, W. M., Coale, K. H., McManus, J., & Johnson, K. S. (1999). Fluxes of dissolved organic carbon from California continental margin sediments. *Geochimica et Cosmochimica Acta*, 63(10), 1507–1515. [https://doi.org/10.1016/S0016-7037\(99\)00066-6](https://doi.org/10.1016/S0016-7037(99)00066-6)
- Burdige, D. J., Dhakar, S. P., & Nealson, K. H. (1992). Effects of manganese oxide mineralogy on microbial and chemical manganese reduction. *Geomicrobiology Journal*, 10(1), 27–48. <https://doi.org/10.1080/01490459209377902>
- Burdige, D. J., Kline, S. W., & Chen, W. (2004). Fluorescent dissolved organic matter in marine sediment pore waters. *Marine Chemistry*, 89, 289–311. <https://doi.org/10.1016/j.marchem.2004.02.015>.
- Burdige, D.J., & Nealson, K.H. (1986). Chemical and microbiological studies of sulfide mediated manganese reduction. *Geomicrobiological Journal* 4, 361–387. <https://doi.org/10.1080/01490458609385944>
- Burton, E. D., Sullivan, L. A., Bush, R. T., Johnston, S. G., & Keene, A. F. (2008). A simple and inexpensive chromium-reducible sulfur method for acid-sulfate soils. *Applied Geochemistry*, 23(9), 2759–2766. <https://doi.org/10.1016/j.apgeochem.2008.07.007>
- Bushnell, B. (2014). BBMap: A Fast, Accurate, Splice-Aware Aligner. 1. <https://doi.org/10.1186/1471-2105-13-238>
- Cai, C., Leu, A. O., Jianhua, G. X., Yuexing, G., Zhao, F. J., & Tyson, G. W. (2018). A methanotrophic archaeon couples anaerobic oxidation of methane to Fe ( III ) reduction. *The ISME Journal*, 12, 1929–1939. <https://doi.org/10.1038/s41396-018-0109-x>
- Callahan, B. J., McMurdie, P. J., Rosen, M. J., Han, A. W., Johnson, A. J. A., & Holmes, S. P. (2016). DADA2: High-resolution sample inference from Illumina amplicon data. *Nature Methods* 2016 13:7 13, 581–583. doi: 10.1038/nmeth.3869
- Calvert, S., & Pedersen, T. F. (1993). Geochemistry of recent oxic and anoxic marine sediments: implications for the geological record. *Marine Geology* 113, 67–88. [https://doi.org/10.1016/0025-3227\(93\)90150-T](https://doi.org/10.1016/0025-3227(93)90150-T)
- Calvert, S. E., & Pedersen, T. F. (1996) Sedimentary Geochemistry of Manganese: Implications for the Environment of Formation of Manganiferous Black Shales. *Econ. Geol.*, 91(3), 36–47, 1996. <https://doi.org/10.2113/gsecongeo.91.1.36>

- Cambon-Bonavita, M. A., Nadalig, T., Roussel, E., Delage, E., Duperron, S., Caprais, J. C., Boetius, A., & Sibuet, M. (2009). Diversity and distribution of methane-oxidizing microbial communities associated with different faunal assemblages in a giant pockmark of the Gabon continental margin. *Deep-Sea Research Part II: Topical Studies in Oceanography*, 56(23), 2248–2258. <https://doi.org/10.1016/j.dsr2.2009.04.007>
- Canfield, D.E. (1988). Reactive iron in marine sediments. *Geochimica et Cosmochimica Acta* 53, 619–632. [https://doi.org/10.1016/0016-7037\(89\)90005-7](https://doi.org/10.1016/0016-7037(89)90005-7)
- Canfield, D. E., Kristenen, E., & Thamdrup, B. (2005). *The Sulfur Cycle* (Vol. 48). Academic Press.
- Canfield, D.E., Jørgensen, B.B., Fossing, H., Glud, R., Gundersen, J., Ramsing, N.B., Thamdrup, B., Hansen, J.W., Nielsen, L.P. & Hall, P.O.J. (1993). Pathways of organic carbon oxidation in three continental margin sediments. *Marine Geology* 133, 27–40. [https://doi.org/10.1016/0025-3227\(93\)90147-N](https://doi.org/10.1016/0025-3227(93)90147-N)
- Canfield, D. E., & Thamdrup, B. (2009). Towards a consistent classification scheme for geochemical environments, or, why we wish the term “suboxic” would go away: Editorial. In *Geobiology* (Vol. 7, Issue 4, pp. 385–392). <https://doi.org/10.1111/j.1472-4669.2009.00214.x>
- Canfield, D. E., Thamdrup, B., & Hansen, J. W. (1993). The anaerobic degradation of organic matter in Danish coastal sediments: Iron reduction, manganese reduction, and sulfate reduction. *Geochimica et Cosmochimica Acta*, 57(16), 3867–3883. [https://doi.org/10.1016/0016-7037\(93\)90340-3](https://doi.org/10.1016/0016-7037(93)90340-3)
- Canuel, E. A., Cammer, S. S., McIntosh, H. A., & Pondell, C. R. (2012). Climate change impacts on the organic carbon cycle at the land-ocean interface. *Annual Review of Earth and Planetary Sciences*, 40, 685–711. <https://doi.org/10.1146/annurev-earth-042711-105511>
- Capella-Gutiérrez, S., Silla-Martínez, J. M., & Gabaldón, T. (2009). trimAl: a tool for automated alignment trimming in large-scale phylogenetic analyses. *Bioinformatics* 25, 1972–1973. doi: 10.1093/bioinformatics/btp348
- Caporaso, J. G., Lauber, C. L., Walters, W. A., Berg-Lyons, D., Huntley, J., Fierer, N., Owens, S. M., Betley, J., Fraser, L., Bauer, M., Gormley, N., Gilbert, J. A., Smith, G., & Knight, R. (2012). Ultra-high-throughput microbial community analysis on the Illumina HiSeq and MiSeq platforms. *ISME Journal* 2012 6:8 6, 1621–1624. doi: 10.1038/ismej.2012.8
- Chadwick, G. L., Skennerton, C. T., Laso-Pérez, R., Leu, A. O., Speth, D. R., Yu, H., Morgan-Lang, C., Hatzenpichler, R., Goudeau, D., Malmstrom, R., Brazelton, W. J., Woyke, T., Hallam, S. J., Tyson, G. W., Wegener, G., Boetius, A., & Orphan, V. J. (2022). Comparative genomics reveals electron transfer and syntrophic mechanisms differentiating methanotrophic and methanogenic archaea. *PLoS Biology*, 20(1), 1–71. <https://doi.org/10.1371/journal.pbio.3001508>
- Chaumeil, P. A., Mussig, A. J., Hugenholtz, P., & Parks, D. H. (2022). GTDB-Tk v2: memory friendly classification with the genome taxonomy database. *Bioinformatics*, 38(23), 5315–5316. <https://doi.org/10.1093/bioinformatics/btac672>
- Chen, Q., Wang, N., Huang, D., Yuan, T., Wu, H., & Xu, Q. (2023). Enhancement of methane production from anaerobic digestion using different manganese species. *Biomass Conversion and Biorefinery*, 13(11), 9783–9793. <https://doi.org/10.1007/s13399-021-01839-6>
- Chen, S., Zhou, Y., Chen, Y., & Gu, J. (2018). Fastp: An ultra-fast all-in-one FASTQ preprocessor. *Bioinformatics*, 34(17), i884–i890. <https://doi.org/10.1093/bioinformatics/bty560>
- Ciais, P., Sabine, C., Bala, G., Bopp, L., Brovkin, V., Canadell, J., Chhabra, A., DeFries, R., Galloway, J., Heimann, M., Jones, C., Le Quéré, C., Myneni, R., Piao, S., Thornton, P., Qin, D., Plattner, G., Tignor, M., Allen, S., ... Brovkin Germany, V. (2013). *Carbon and Other Biogeochemical Cycles*. In: *Climate Change 2013: The Physical Science Basis. Contribution of Working Group I to the Fifth Assessment Report of the Intergovernmental Panel on Climate Change*.
- Claff, S.R., Sullivan, L.A., Burton, E.D., & Bush, R.T. (2010). A sequential extraction procedure for acid sulfate soils: partitioning of iron. *Geoderma* 155, 224–230.

- Chaumeil, P.-A., Mussig, A. J., Hugenholtz, P., & Parks, D. H. (2020). GTDB-Tk: a toolkit to classify genomes with the Genome Taxonomy Database. *Bioinformatics* 36, 1925–1927. doi: 10.1093/bioinformatics/btz848
- Chen, S. (2023). Ultrafast one-pass FASTQ data preprocessing, quality control, and deduplication using fastp. *iMeta* 2, e107. doi: 10.1002/imt2.107
- Chen, Y., Xu, C., Wu, N., Sun, Z., Liu, C., Zhen, Y., Xin, Y., Zhang, X., Geng, W., Cao, H., Zhai, B., Li, J., Qion, S., & Zhou, Y. (2022). Diversity of Anaerobic Methane Oxidizers in the Cold Seep Sediments of the Okinawa Trough. *Frontiers in Microbiology* 13. doi: 10.3389/fmicb.2022.819187
- Chklovski, A., Parks, D. H., Woodcroft, B. J., & Tyson, G. W. (2023). CheckM2: a rapid, scalable and accurate tool for assessing microbial genome quality using machine learning. *Nature Methods*, 20(8), 1203–1212. <https://doi.org/10.1038/s41592-023-01940-w>
- Cline, J. D. (1969). Spectrophotometric Determination of Hydrogen Sulfide in Natural Waters. *Limnology and Oceanography*, 14(3), 454–458. <https://doi.org/10.4319/lo.1969.14.3.0454>
- Cremers, G., Jetten, M. S. M., Op den Camp, H. J. M., & Lückner, S. (2022). Metascan: METabolic Analysis, SScreening and ANnotation of Metagenomes. *Frontiers in Bioinformatics*, 2. <https://doi.org/10.3389/fbinf.2022.861505>
- Crusoe, M. R., Alameldin, H. F., Awad, S., Boucher, E., Caldwell, A., Cartwright, R., Charbonneau, A., Constantinides, B., Edverson, G., Fay, S., Fenton, J., Fenzl, T., Fish, J., Garcia-Gutierrez, L., Garland, P., Gluck, J., González, I., Guermond, S., Guo, J., ... Brown, C. T. (2015). The khmer software package: Enabling efficient nucleotide sequence analysis. *F1000Research*, 4. <https://doi.org/10.12688/f1000research.6924.1>
- Cui, M., Luther, G. W., & Gomes, M. (2023). Constraining the major pathways of vanadium incorporation into sediments underlying natural sulfidic waters. *Geochimica et Cosmochimica Acta*, 359, 148–164. <https://doi.org/10.1016/j.gca.2023.08.008>
- Dalcin Martins, P., de Monleval, J. P. R. C., Echeveste Medrano, M. J., Lenstra, W. K., Wallenius, A. J., Hermans, M., Slomp, C. P., Welte, C. U., Jetten, M. S. M., & Van Helmond, N. A. G. M. (2024). Sulfide Toxicity as Key Control on Anaerobic Oxidation of Methane in Eutrophic Coastal Sediments. *Environmental Science and Technology*, 58(26), 11421–11435. <https://doi.org/10.1021/acs.est.3c10418>
- Dale, A. W., Regnier, P., & Van Cappellen, P. (2006). Bioenergetic Controls on Anaerobic Oxidation of Methane (AOM) in Coastal Marine Sediments: A Theoretical Analysis. *American Journal of Science*, 306, 246–294. <https://doi.org/10.2475/04.2006.02>
- Dean, J. F., Middelburg, J. J., Röckmann, T., Aerts, R., Blauw, L. G., Egger, M., Jetten, M. S. M., de Jong, A. E. E., Meisel, O. H., Rasigraf, O., Slomp, C. P., in't Zandt, M. H., & Dolman, A. J. (2018). Methane Feedbacks to the Global Climate System in a Warmer World. *Reviews of Geophysics*, 56(1), 207–250. <https://doi.org/10.1002/2017RG000559>
- Dellwig, O., Bosselmann, K., Kölsch, S., Hentscher, M., Hinrichs, J., Böttcher, M.E., Reuter, R., & Brumsack, H.-J. (2007). Sources and fate of manganese in a tidal basin of the German Wadden Sea. *Journal of Sea Research*, 57, 1–18. <https://doi.org/10.1016/j.seares.2006.07.006>
- Dellwig, O., Leipe, T., März, C., Glockzin, M., Pollehne, F., Schnetger, B., Yakushev, E.V., Böttcher, M.E., & Brumsack, H.J. (2010). A new particulate Mn-Fe-P-shuttle at the redoxcline of anoxic basins. *Geochimica et Cosmochimica Acta* 74, 7100–7115. <https://doi.org/10.1016/j.gca.2010.09.017>
- Dellwig, O., Schnetger, B., Meyer, D., Pollehne, F., Häusler, K., & Arz, H. W. (2018). Impact of the major Baltic inflow in 2014 on manganese cycling in the gotland deep (Baltic Sea). *Frontier in Marine Science*, 5(JUL), 1–20. <https://doi.org/10.3389/fmars.2018.00248>
- Deng, L., Bølsterli, D., Glombitza, C., Jørgensen, B. B., Røy, H., & Lever, M. A. (2025). Drivers of methane-cycling archaeal abundances, community structure, and catabolic pathways in continental margin sediments. *Frontiers in Microbiology* 16. doi: 10.3389/fmicb.2025.1550762

- Deng, L., Bölsterli, D., Kristensen, E., Meile, C., Su, C.-C., Bernasconi, S. M., Seidenkrantz, M.-S., Glombitza, C., Lagostina, L., Han, X., Jørgensen, B. B., Røy, H., & Lever, M. A. (2020). Macrofaunal control of microbial community structure in continental margin sediments. *Proceedings of the National Academy of Sciences*, 117(27). <https://doi.org/10.1073/pnas.1917494117/-/DCSupplemental>
- Diaz, R. J., & Rosenberg, R. (2008). Spreading dead zones and consequences for marine ecosystems. *Science*, 321(5891), 926–929. <https://doi.org/10.1126/science.1156401>.
- Dijkstra, N., Hagens, M., Egger, M., & Slomp, C. P. (2018a). Post-depositional formation of vivianite-type minerals alters sediment phosphorus records. *Biogeosciences* 15, 861–883.
- Dijkstra, N., Kraal, P., Séguret, M.J., Flores, M.R., Gonzalez, S., Rijkenberg, M. J., & Slomp, C. P. (2018b). Phosphorus dynamics in and below the redoxcline in the Black Sea and implications for phosphorus burial. *Geochimica et Cosmochimica Acta* 222, 685–703. <https://doi.org/10.1016/j.gca.2017.11.016>
- Dijkstra, N., Quintana Krupinski, N. B., Yamane, M., Obrochta, S. P., Miyairi, Y., Yokoyama, Y., & Slomp, C. P. (2018c). Holocene Refreshening and Reoxygenation of a Bothnian Sea Estuary Led to Enhanced Phosphorus Burial. *Estuaries and Coasts*, 41(1), 139–157. <https://doi.org/10.1007/s12237-017-0262-x>
- Dijkstra, N., Slomp, C. P., & Behrends, T. (2016). Vivianite is a key sink for phosphorus in sediments of the Landsort Deep, an intermittently anoxic deep basin in the Baltic Sea. *Chemical Geology*, 438, 58–72. <https://doi.org/10.1016/j.chemgeo.2016.05.025>
- Doney, S. C. (2010). The Growing Human Footprint on Coastal and Open-Ocean Biogeochemistry. *Science*, 328, 1512–1516. <https://doi.org/10.1126/science.1185198>
- Drits, V. A., Lanson, B., & Gaillot, A-C. (2007). Birnessite polytype systematics and identification by powder X-ray diffraction, *American mineralogist*, 92(5-6), 771–788. <https://doi.org/10.2138/am.2007.2207>
- Echeveste Medrano, M. J., Lee, S., de Graaf, R., Holohan, B. C., Sánchez-Andrea, I., Jetten, M. S. M., & Welte, C. U. (2025). Physiological Stress Response to Sulfide Exposure of Freshwater Anaerobic Methanotrophic Archaea. *Environmental Science and Technology* 59, 10262–10273. doi: 10.1021/acs.est.4c12489
- Echeveste Medrano, M. J., Su, G., Blattner, L. A., Leão, P., Sánchez-Andrea, I., Jetten, M. S. M., Welte, C. U., & Zopfi, J. (2025). Methanotrophic Flexibility of 'Ca. Methanoperedens' and Its Interactions With Sulphate-Reducing Bacteria in the Sediment of Meromictic Lake Cadagno. *Environmental Microbiology*, 27(7). <https://doi.org/10.1111/1462-2920.70133>
- Edgar, R. C. (2004). MUSCLE: multiple sequence alignment with high accuracy and high throughput. *Nucleic Acids Research* 32, 1792–1797. doi: 10.1093/nar/gkh340
- Egger, M., Hagens, M., Sapart, C. J., Dijkstra, N., van Helmond, N. A. G. M., Mogollón, J. M., Risgaard-Petersen, N., van der Veen, C., Kasten, S., Riedinger, N., Böttcher, M. E., Röckmann, T., Jørgensen, B. B., & Slomp, C. P. (2017). Iron oxide reduction in methane-rich deep Baltic Sea sediments. *Geochimica et Cosmochimica Acta*, 207, 256–276. <https://doi.org/10.1016/j.gca.2017.03.019>.
- Egger, M., Jilbert, T., Behrends, T., Rivard, C., & Slomp, C.P. (2015). Vivianite is a major sink for phosphorus in methanogenic coastal surface sediments. *Geochimica et Cosmochimica Acta* 169, 217–235. <https://doi.org/10.1016/j.gca.2015.09.012>
- Egger, M., Kraal, P., Jilbert, T., Sulu-gambari, F., Sapart, C. J., & Röckmann, T. (2016). Anaerobic oxidation of methane alters sediment records of sulfur, iron and phosphorus in the Black Sea. *Biogeosciences*, 5333–5355. <https://doi.org/10.5194/bg-13-5333-2016>
- Egger, M., Lenstra, W., Jong, D., Meysman, F. J. R., Sapart, C. J., Van Der Veen, C., Röckmann, T., Gonzalez, S., & Slomp, C. P. (2016). Rapid sediment accumulation results in high methane effluxes from coastal sediments. *PLoS ONE*, 11(8), 1–22. <https://doi.org/10.1371/journal.pone.0161609>

- Egger, M., Rasigraf, O., Sapart, C. J., Jilbert, T., Jetten, M. S. M., Röckmann, T., Van Der Veen, C., Bânda, N., Kartal, B., Ettwig, K. F., & Slomp, C. P. (2015). Iron-mediated anaerobic oxidation of methane in brackish coastal sediments. *Environmental Science and Technology*, *49*(1), 277–283. <https://doi.org/10.1021/es503663z>
- Egger, M., Riedinger, N., Mogollón, J. M., & Jørgensen, B. B. (2018). Global diffusive fluxes of methane in marine sediments. *Nature Geoscience*, *11*(6), 421–425. <https://doi.org/10.1038/s41561-018-0122-8>
- Eitel, E.M., Zhao, S., Tang, Y., & Taillefert, M. (2018). Effect of manganese oxide aging and structure transformation on the kinetics of thiol oxidation. *Environmental Science and Technology* *52*, 13202–13211. <https://doi.org/10.1021/acs.est.8b03993>
- Erickson, B. E., & Helz, G. R. (2000). Molybdenum(VI) speciation in sulfidic waters: Stability and lability of thiomolybdates. *Geochimica et Cosmochimica Acta* *64*, 1149–1158. doi: 10.1016/S0016-7037(99)00423-8
- Etheridge, D. M., Pearman, G. I., & Fraser, P. J. (1992). Changes in tropospheric methane between 1841 and 1978 from a high accumulation-rate Antarctic ice core. *Tellus*, *44*(4), 282–294. <https://doi.org/10.1034/j.1600-0889.1992.t01-3-00006.x>
- Etminan, M., Myhre, G., Highwood, E. J., & Shine, K. P. (2016). Radiative forcing of carbon dioxide, methane, and nitrous oxide: A significant revision of the methane radiative forcing. *Geophysical Research Letters*, *43*(24), 12,614–12,623. <https://doi.org/10.1002/2016GL071930>
- Ettwig, K. F., Zhu, B., Speth, D., Keltjens, J. T., Jetten, M. S. M., & Kartal, B. (2016). Archaea catalyze iron-dependent anaerobic oxidation of methane. *Proceedings of the National Academy of Sciences*, *113*(45), 2–6. <https://doi.org/10.1073/pnas.1609534113>
- Evans, P. N., Boyd, J. A., Leu, A. O., Woodcroft, B. J., Parks, D. H., Hugenholtz, P., & Tyson, G. W. (2019). An evolving view of methane metabolism in the Archaea. *Nature Reviews Microbiology* (Vol. 17, Issue 4, pp. 219–232). <https://doi.org/10.1038/s41579-018-0136-7>
- Ferry, J. G. (2020). Methanosarcina acetivorans: A Model for Mechanistic Understanding of Aceticlastic and Reverse Methanogenesis. *Frontiers in Microbiology* (Vol. 11). <https://doi.org/10.3389/fmicb.2020.01806>
- Findlay, A. J., Pellerin, A., Laufer, K., & Jørgensen, B. B. (2020). Quantification of sulphide oxidation rates in marine sediment. *Geochimica et Cosmochimica Acta* *280*, 441–452. doi: 10.1016/j.gca.2020.04.007
- Fossing, H., & Jørgensen, B. B. (1989). Measurement of bacterial sulfate reduction in sediments: Evaluation of a single-step chromium reduction method. *Biogeochemistry*, *8*, 205–222. <https://doi.org/https://doi.org/10.1007/BF00002889>
- Froelich, P. N., Klinkhammer, G. P., Bender, M. L., Luedtke, N. A., Heath, G. R., Cullen, D., Dauphin, P., Hammond, D., & Hartman, B. (1979). Early oxidation of organic matter in pelagic sediments of the eastern equatorial Atlantic : suboxic diagenesis. *Geochimica et Cosmochimica Acta*, *43*, 1075–1090. [https://doi.org/https://doi.org/10.1016/0016-7037\(79\)90095-4](https://doi.org/https://doi.org/10.1016/0016-7037(79)90095-4)
- Furukawa, K., & Takahashi, Y. (2008). Effect of complexation with humic substances on diffusion of metal ions in water. *Chemosphere*, *73*(8), 1272–1278. <https://doi.org/10.1016/j.chemosphere.2008.07.017>
- Garber, A. I., Nealson, K. H., Okamoto, A., McAllister, S. M., Chan, C. S., Barco, R. A., & Merino, N. (2020). FeGenie: A Comprehensive Tool for the Identification of Iron Genes and Iron Gene Neighborhoods in Genome and Metagenome Assemblies. *Frontiers in Microbiology*, *11*. <https://doi.org/10.3389/fmicb.2020.00037>
- Glasby, G. P. (1972) The mineralogy of manganese nodules from a range of marine environments, *Marine geology*, *13*(1), 57–72. [https://doi.org/10.1016/0025-3227\(72\)90071-0](https://doi.org/10.1016/0025-3227(72)90071-0)
- Goldberg, E.D. (1954). Marine Geochemistry 1. Chemical Scavengers of the Sea. *The Journal of Geology*, *62*, 249–265.

- Grasshof, K. M., & Chan, K. M. (1969). An automatic method for the determination of hydrogen sulphide in natural waters. *Analytica Chimica Acta*, 53(2), 442–445. [https://doi.org/https://doi.org/10.1016/S0003-2670\(01\)82105-X](https://doi.org/https://doi.org/10.1016/S0003-2670(01)82105-X)
- Green-Saxena, A., Dekas, A. E., Dalleska, N. F., & Orphan, V. J. (2014). Nitrate-based niche differentiation by distinct sulfate-reducing bacteria involved in the anaerobic oxidation of methane. *ISME Journal*, 8(1), 150–163. <https://doi.org/10.1038/ismej.2013.147>
- Grégoire, M., Garçon, V., Garcia, H., Breitburg, D., Isensee, K., Oschlies, A., Telszewski, M., Barth, A., Bittig, H. C., Carstensen, J., Carval, T., Chai, F., Chavez, F., Conley, D., Coppola, L., Crowe, S., Currie, K., Dai, M., Deflandre, B., ... Yasuhara, M. (2021). A Global Ocean Oxygen Database and Atlas for Assessing and Predicting Deoxygenation and Ocean Health in the Open and Coastal Ocean. *Frontiers in Marine Science*, 8(December), 1–29. <https://doi.org/10.3389/fmars.2021.724913>
- Gu, Y., Guberman-Pfeffer, M. J., Srikanth, V., Shen, C., Giska, F., Gupta, K., Londer, Y., Samatey, F. A., Batista, V. S., & Malvankar, N. S. (2023). Structure of Geobacter cytochrome OmcZ identifies mechanism of nanowire assembly and conductivity. *Nature Microbiology*, 8(2), 284–298. <https://doi.org/10.1038/s41564-022-01315-5>
- Hagens, M., Slomp, C. P., Meysman, F. J. R., Seitaj, D., Harlay, J., Borges, A. V., & Middelburg, J. J. (2015). Biogeochemical processes and buffering capacity concurrently affect acidification in a seasonally hypoxic coastal marine basin. *Biogeosciences* 12, 1561–1583. doi: 10.5194/bg-12-1561-2015
- Hamdan, L. J., & Wickland, K. P. (2016). Methane emissions from oceans, coasts, and freshwater habitats: New perspectives and feedbacks on climate. *Limnology and Oceanography*, 61, S3–S12. <https://doi.org/10.1002/lno.10449>
- Händel, M., Rennert, T., & Totsche, K. U. (2013). A simple method to synthesize birnessite at ambient pressure and temperature. *Geoderma*, 193–194, 117–121. <https://doi.org/10.1016/j.geoderma.2012.09.002>
- Häusler, K., Moros, M., Wacker, L., Hammerschmidt, L., Dellwig, O., Leipe, T., Kotilainen, A., & Arz, H. W. (2017). Mid- to late Holocene environmental separation of the northern and central Baltic Sea basins in response to differential land uplift. *Boreas*, 46(1), 111–128. <https://doi.org/10.1111/bor.12198>
- Haskel, D. (1999). FLUO: Correcting XANES for self-absorption in fluorescence measurements.
- Helder, W., & De Vries, R. T. P. (1979). An automatic phenol-hypochlorite method for the determination of ammonia in sea- and brackish waters. *Netherlands Journal of Sea Research*, 13(1), 154–160.
- Hem, J.D. & Lind, C.J. (1983). Nonequilibrium models for predicting forms of precipitated manganese oxides. *Geochimica et Cosmochimica Acta* 47, 2037–2046. [https://doi.org/10.1016/0016-7037\(83\)90219-3](https://doi.org/10.1016/0016-7037(83)90219-3)
- Helz, G. R., Miller, C. V., Charnock, J. M., Mosselmans, J. F. W., Patrick, R. A. D., Garner, C. D., & Vaughan, D. J. (1996). Mechanism of molybdenum removal from the sea and its concentration in black shales: EXAFS evidence. *Geochimica et Cosmochimica Acta*, 60, 3631–3642. doi: 10.1016/0016-7037(96)00195-0
- Herlemann, D. P. R., Labrenz, M., Jürgens, K., Bertilsson, S., Waniek, J. J., & Andersson, A. F. (2011). Transitions in bacterial communities along the 2000 km salinity gradient of the Baltic Sea. *The ISME Journal* 2011 5:10 5, 1571–1579. doi: 10.1038/ismej.2011.41
- Hermans, M., Lenstra, W.K., Hidalgo-Martinez, S., Van Helmond, N.A.G.M., Witbaard, R., Meysman, F.J., Gonzalez, S., & Slomp, C.P. (2019). Abundance and biogeochemical impact of cable bacteria in baltic sea sediments. *Environmental Science and Technology*, 53, 7494–7503. <https://doi.org/10.1021/acs.est.9b01665>
- Hermans, M., Lenstra, W. K., Van Helmond, N. A. G. M., Behrends, T., Egger, M., Séguret, M. J. M., Gustafsson, E., Gustafsson, B. G., & Slomp, C. P. (2019). Impact of natural re-oxygenation on the sediment dynamics of manganese, iron and phosphorus in a euxinic Baltic Sea basin. *Geochimica et Cosmochimica Acta*, 246, 174–196. <https://doi.org/10.1016/j.gca.2018.11.033>

- Hermans, M., Astudillo Pascual, M., Behrends, T., Lenstra, W.K., Conley, D.J., & Slomp, C. P. (2021). Coupled dynamics of iron, manganese, and phosphorus in brackish coastal sediments populated by cable bacteria. *Limnol. Oceanogr.* 1–21. <https://doi.org/10.1002/lno.11776>
- Howarth, R. W., & Jørgensen, B. B. (1984). Formation of 35S-labelled elemental sulfur and pyrite in coastal marine sediments (Limfjorden and Kysing Fjord, Denmark) during short-term 35SO42–reduction measurements. *Geochimica et Cosmochimica Acta* 48, 1807–1818. doi: 10.1016/0016-7037(84)90034-6
- Holmkvist, L., Ferdelman, T. G., & Jørgensen, B. B. (2011). A cryptic sulfur cycle driven by iron in the methane zone of marine sediment (Aarhus Bay, Denmark). *Geochimica et Cosmochimica Acta*, 75(12), 3581–3599. <https://doi.org/10.1016/j.gca.2011.03.033>
- Huang, L., Liu, X., Nealsen, K. H., & Rensing, C. (2021). Light-driven carbon dioxide reduction to methane by *Methanosarcina barkeri* in an electric syntrophic coculture. *The ISME Journal*, 16(February), 370–377. <https://doi.org/10.1038/s41396-021-01078-7>
- Huerta-Diaz, M.A., & Morse, J.W. (1990). A quantitative method for determination of trace metal concentrations in sedimentary pyrite. *Marine Chemistry* 29, 119–144. [https://doi.org/10.1016/0304-4203\(90\)90009-2](https://doi.org/10.1016/0304-4203(90)90009-2)
- Huerta-Diaz, M.A., & Morse, J.W. (1992). Pyritization of trace metals in anoxic marine sediments. *Geochimica et Cosmochimica Acta* 56, 2681–2702. [https://doi.org/10.1016/0016-7037\(92\)90353-K](https://doi.org/10.1016/0016-7037(92)90353-K)
- Hulth, S., Aller, R. C., & Gilbert, F. (1999). Coupled anoxic nitrification / manganese reduction in marine sediments. *Geochimica et Cosmochimica Acta*, 63(1), 49–66. [https://doi.org/10.1016/S0016-7037\(98\)00285-3](https://doi.org/10.1016/S0016-7037(98)00285-3)
- Hyacinthe, C., & Van Cappellen, P. (2004). An authigenic iron phosphate phase in estuarine sediments: composition, formation and chemical reactivity. *Marine Chemistry* 91, 227–251. <https://doi.org/10.1016/j.marchem.2004.04.006>
- Hyacinthe, C., Anschutz, P., Carbonel, P., Jouanneau, J.-M., & Jorissen, F.J. (2001). Early diagenetic processes in the muddy sediments of the Bay of Biscay. *Marine Geology* 177, 111–128. [https://doi.org/10.1016/S0025-3227\(01\)00127-X](https://doi.org/10.1016/S0025-3227(01)00127-X)
- Hyatt, D., Chen, G.-L., Locascio, P. F., Land, M. L., Larimer, F. W., & Hauser, L. J. (2010). Prodigal: prokaryotic gene recognition and translation initiation site identification. *BMC Bioinformatics*, 11(119). <https://doi.org/https://doi.org/10.1186/1471-2105-11-119>
- In 't Zandt, M. H., De Jong, A. E. E., Slomp, C. P., & Jetten, M. S. M. (2020). The hunt for the most-wanted chemolithoautotrophic spookmicrobes. *FEMS Microbiology Ecology* 94(6). <https://doi.org/10.1093/femsec/fiy064>
- In 't Zandt, M. H., Kip, N., Frank, J., Jansen, S., Van Veen, J. A., Jetten, M. S. M., & Welte, C. U. (2019). High-Level Abundances of Methanobacteriales and Syntrophobacteriales May Help To Prevent Corrosion of Metal Sheet Piles. *Environmental Microbiology*, 85(20). <https://doi.org/https://doi.org/10.1128/AEM.01369-19>
- Iversen, N., & Jørgensen, B. B. (1985). Anaerobic methane oxidation rates at the sulfate-methane transition in marine sediments from Kattegat and Skagerrak (Denmark). *Limnology and Oceanography*, 30(5), 944–955. <https://doi.org/10.4319/lo.1985.30.5.0944>
- Jilbert, T., Conley, D. J., Gustafsson, B. G., Funkey, C. P., & Slomp, C. P. (2015). Glacio-isostatic control on hypoxia in a high-latitude shelf basin. *Geology*, 43(5), 427–430. <https://doi.org/10.1130/G36454.1>
- Jilbert, T., & Slomp, C.P. (2013). Iron and manganese shuttles control the formation of authigenic phosphorus minerals in the euxinic basins of the Baltic Sea. *Geochimica et Cosmochimica Acta* 107, 155–169. <https://doi.org/10.1016/j.gca.2013.01.005>

- Johnson, E. F., & Mukhopadhyay, B. (2008). Coenzyme F420-Dependent Sulfite Reductase-Enabled Sulfite Detoxification and Use of Sulfite as a Sole Sulfur Source by *Methanococcus maripaludis*. *Applied and Environmental Microbiology* 74, 3591–3595. doi: 10.1128/AEM.00098-08
- Johnson, J.E., Webb, S.M., Ma, C., & Fischer, W.W. (2016). Manganese mineralogy and diagenesis in the sedimentary rock record. *Geochimica et Cosmochimica Acta* 173, 210–231. <https://doi.org/10.1016/j.gca.2015.10.027>
- Jørgensen, B. B., Beulig, F., Egger, M., Petro, C., Scholze, C., & Røy, H. (2019). Organoclastic sulfate reduction in the sulfate-methane transition of marine sediments. *Geochimica et Cosmochimica Acta*, 254, 231–245. <https://doi.org/10.1016/j.gca.2019.03.016>
- Jørgensen, B. B., & Fenchel, T. (1974). The sulfur cycle of a coastal marine sediment. *Marine Biology*, 24, 189–201. <https://doi.org/https://doi.org/10.1007/BF00391893>
- Jørgensen, B. B., Findlay, A. J., & Pellerin, A. (2019). The biogeochemical sulfur cycle of marine sediments. *Frontiers in Microbiology*, 10(APR), 1–27. <https://doi.org/10.3389/fmicb.2019.00849>
- Jørgensen, B. B., Weber, A., & Zop, J. (2001). Sulfate reduction and anaerobic methane oxidation in Black Sea sediments. *Deep-Sea Research I* (Vol. 48).
- Josefson, A. B., Norkko, J., & Norkko, A. (2012). Burial and decomposition of plant pigments in surface sediments of the Baltic Sea: Role of oxygen and benthic fauna. *Marine Ecology Progress Series*, 455, 33–49. <https://doi.org/10.3354/meps09661>
- Kalinichev, A. G., & Kirkpatrick, R. J. (2007). Molecular dynamics simulation of cationic complexation with natural organic matter. *Eur. J. Soil Sci.*, 58(4), 909–917. <https://doi.org/10.1111/j.1365-2389.2007.00929.x>.
- Kallmeyer, J., Ferdelman, T. G., Weber, A., Fossing, H., & Jørgensen, B. B. (2004). A cold chromium distillation procedure for radiolabeled sulfide applied to sulfate reduction measurements. *Limnology and Oceanography: Methods*, 2(6), 171–180. <https://doi.org/10.4319/lom.2004.2.171>
- Kamyshny, A., Sela, D., Klein, R., Turchyn, A. V., Antler, G., & Freund, H. (2024). Biogeochemical sulfur transformations in the cohesive and permeable tidal flat sediments of Jade Bay (North Sea). *Marine Chemistry* 267, 104464. doi: 10.1016/j.marchem.2024.104464
- Kang, D. D., Froula, J., Egan, R., & Wang, Z. (2015). MetaBAT, an efficient tool for accurately reconstructing single genomes from complex microbial communities. *PeerJ* 3, e1165. doi: 10.7717/peerj.1165
- Kang, D. D., Li, F., Kirton, E., Thomas, A., Egan, R., An, H., & Wang, Z. (2019). MetaBAT 2: an adaptive binning algorithm for robust and efficient genome reconstruction from metagenome assemblies. *PeerJ* 7, e7359. doi: 10.7717/peerj.7359
- Karolewski, J. S., Sutherland, K. M., Hansel, C. M., & Wankel, S. D. (2021) An isotopic study of abiotic nitrite oxidation by ligand-bound manganese (III). *Geochimica et Cosmochimica Acta*, 293, 365–378. <https://doi.org/10.1016/j.gca.2020.11.004>, 2021.
- Kasten, S., Freudenthal, T., Gingele, F. X., & Schulz, H. D. (1998). Simultaneous formation of iron-rich layers at different redox boundaries in sediments of the Amazon deep-sea fan. *Geochimica et Cosmochimica Acta*, 62(13), 2253–2264.
- Keeling, C. D. (1960). The Concentration and Isotopic Abundances of Carbon Dioxide in the Atmosphere. *Tellus A: Dynamic Meteorology and Oceanography*, 12(2), 200–203. <https://doi.org/10.3402/tellusa.v12i2.9366>
- Kester, D.R., Duedall, I.W., Connors, D.N., & Pytkowicz, R.M. (1967). Preparation of artificial seawater. *Limnology and Oceanography*, 12, 176–179.
- Kim, B., Lingappa, U. F., Magyar, J., Monteverde, D., Valentine, J. S., Cho, J., & Fischer, W. (2022). Challenges of measuring soluble Mn(III) species in natural samples. *Molecules*, 27(5), 1661. <https://doi.org/10.3390/molecules27051661>

- Klomp, R., Żygadłowska, O. M., Jetten, M. S. M., Oldham, V. E., van Helmond, N. A. G. M., Slomp, C. P., & Lenstra, W. K. (2025). Dissolved Mn(III) is a key redox intermediate in sediments of a seasonally euxinic coastal basin. *Biogeosciences* 22, 751–765. doi: 10.5194/bg-22-751-2025
- Knaack, D. R., Leybourne, M. I., Layton-Matthews, D., McDonald, A. M., Vuletich, A., Chipley, D., Silva L. G., & Pufahl, P. K. (2020). Manganese nodules NOD-A-1 and NOD-P-1: Implications of pre-treatment on oxygen isotopes and mineralogy, *Chemical Geology*, 558, 119,924. <https://doi.org/10.1016/j.chemgeo.2020.119924>
- Knittel, K., & Boetius, A. (2009). Anaerobic Oxidation of Methane: Progress with an Unknown Process. *Annual Review of Microbiology* 63, 311–334. doi: 10.1146/annurev.micro.61.080706.093130
- Koschinsky, A., & Hein, J.R. (2003). Uptake of elements from seawater by ferromanganese crusts: solid-phase associations and seawater speciation. *Marine Geology* 198, 331–351. [https://doi.org/10.1016/S0025-3227\(03\)00122-1](https://doi.org/10.1016/S0025-3227(03)00122-1)
- Koschinsky, A., Fritsche, U., & Winkler, A. (2001). Sequential leaching of Peru Basin surface sediment for the assessment of aged and fresh heavy metal associations and mobility. *Deep-Sea Research Part II: Topical Studies in Oceanography* 48, 3683–3699. [https://doi.org/10.1016/S0967-0645\(01\)00062-5](https://doi.org/10.1016/S0967-0645(01)00062-5)
- Kostka, J. E., Luther, G. W., & Nealson, K. H. (1995). Chemical and biological reduction of Mn (III)-pyrophosphate complexes: Potential importance of dissolved Mn (III) as an environmental oxidant. *Geochimica et Cosmochimica Acta*, 59(5), 885–894. [https://doi.org/10.1016/0016-7037\(95\)00007-0](https://doi.org/10.1016/0016-7037(95)00007-0)
- Kraal, P., Dijkstra, N., Behrends, T., & Slomp, C. P. (2017). Phosphorus burial in sediments of the sulfidic deep Black Sea: Key roles for adsorption by calcium carbonate and apatite authigenesis. *Geochimica et Cosmochimica Acta*, 204, 140–158. <https://doi.org/10.1016/j.gca.2017.01.042>
- Kubeneck, L.J., Lenstra, W.K., Malkin, S.Y., Conley, D.J., & Slomp, C.P. (2021). Phosphorus burial in vivianite-type minerals in methane-rich coastal sediments. *Marine Chemistry*, 231, 103948. <https://doi.org/10.1016/j.marchem.2021.103948>
- Kubeneck, J. L., ThomasArrigo, L. K., Rothwell, K. A., Kaegi, R., & Kretzschmar, R. (2023). Competitive incorporation of Mn and Mg in vivianite at varying salinity and effects on crystal structure and morphology. *Geochimica et Cosmochimica Acta*, 346, 231–244. <https://doi.org/10.1016/j.gca.2023.01.029>
- Kuliński, K., Rehder, G., Asmala, E., Bartosova, A., Carstensen, J., Gustafsson, B., Hall, P. O. J., Humborg, C., Jilbert, T., Jürgens, K., Meier, H. E. M., Müller-Karulis, B., Naumann, M., Olesen, J. E., Savchuk, O., Schramm, A., Slomp, C. P., Sofiev, M., Sobek, A., ... Undeman, E. (2022). Biogeochemical functioning of the Baltic Sea. *Earth System Dynamics* 13(1), 633–685. <https://doi.org/10.5194/esd-13-633-2022>
- Kurth, J. M., Huub, & Op Den Camp, J. M., & Welte, C. U. (2020). Several ways one goal-methanogenesis from unconventional substrates. *Applied Microbiology and Biotechnology*, 104, 6839–6854. <https://doi.org/10.1007/s00253-020-10724-7> Published
- Lacis, A. A., Schmidt, G. A., Rind, D., & Reudy, R. A. (2010). Atmospheric CO<sub>2</sub>: Principal Control Knob Governing Earth's Temperature. *Science*, 330(6002), 353–356. <https://doi.org/10.1126/science.1195475>
- Lam, P.J., Twining, B.S., Jeandel, C., Roychoudhury, A., Resing, J.A., Santschi, P.H., & Anderson, R.F. (2015). Methods for analyzing the concentration and speciation of major and trace elements in marine particles. *Progress in Oceanography*, 133, 32–42. <https://doi.org/10.1016/j.pocean.2015.01.005>
- Lan, X., Thoning, K. W., & Dlugokencky, E. J. (2025). Trends in globally-averaged CH<sub>4</sub>, N<sub>2</sub>O and SF<sub>6</sub> determined from NOAA Global Monitoring Laboratory measurements. Version 2025-09. <https://doi.org/10.15138/P8XG-AA10>

- Lapham, L. L., Lloyd, K. G., Fossing, H., Flury, S., Jensen, J. B., Alperin, M. J., Rehder, G., Holzhueter, W., Ferdelman, T., & Jørgensen, B. B. (2024). Methane leakage through the sulfate–methane transition zone of the Baltic seabed. *Nature Geoscience* 17, 1277–1283. doi: 10.1038/s41561-024-01594-z
- Lapham, L. L., Lloyd, K. G., Fossing, H., Flury, S., Jensen, J. B., Alperin, M. J., Rehder, G., Holzhueter, W., Ferdelman, T., & Jørgensen, B. B. (2024). Methane leakage through the sulfate–methane transition zone of the Baltic seabed. *Nature Geoscience*, 17(12), 1277–1283. <https://doi.org/10.1038/s41561-024-01594-z>
- Larkin, M. A., Blackshields, G., Brown, N. P., Chenna, R., Mcgettigan, P. A., McWilliam, H., Valentin, F., Wallace, I. M., Wilm, A., Lopez, R., Thompson, J. D., Gibson, T. J., & Higgins, D. G. (2007). Clustal W and Clustal X version 2.0. *Bioinformatics*, 23(21), 2947–2948. <https://doi.org/10.1093/bioinformatics/btm404>
- Learman, D.R., Wankel, S.D., Webb, S.M., Martinez, N., Madden, A.S., & Hansel, C.M. (2011). Coupled biotic-abiotic Mn(II) oxidation pathway mediates the formation and structural evolution of biogenic Mn oxides. *Geochimica et Cosmochimica Acta* 75, 6048–6063.
- Lee, J.-M., Lam, P. J., Vivancos, S. M., Pavia, F. J., Anderson, R. F., Lu, Y., Cheng, H., Zhang, P., Lawrence Edwards, R., Xiang, Y., & Webb, S. M. (2021). Changing chemistry of particulate manganese in the near-and far-field hydrothermal plumes from 15° S East Pacific rise and its influence on metal scavenging. *Geochimica et Cosmochimica Acta* 300, 95–118. <https://doi.org/10.1016/j.gca.2021.02.020>
- Lee, H., Calvin, K., Dasgupta, D., Krinner, G., Mukherji, A., Thorne, P. W., Trisos, C., Romero, J., Aldunce, P., Barrett, K., Blanco, G., Cheung, W. W. L., Connors, S. L., Denton, F., Diongue-Niang, A., Dodman, D., Garschagen, M., Geden, O., Hayward, B., ... Ha, M. (2023). *IPCC, 2023: Climate Change 2023: Synthesis Report. Contribution of Working Groups I, II and III to the Sixth Assessment Report of the Intergovernmental Panel on Climate Change* (P. Arias, M. Bustamante, I. Elgizouli, G. Flato, M. Howden, C. Méndez-Vallejo, J. J. Pereira, R. Pichs-Madruga, S. K. Rose, Y. Saheb, R. Sánchez Rodríguez, D. Ürge-Vorsatz, C. Xiao, N. Yassaa, J. Romero, J. Kim, E. F. Haites, Y. Jung, R. Stavins, ... C. Péan (eds.)). <https://doi.org/10.59327/IPCC/AR6-9789291691647>
- Leivuori, M., & Niemistö, L. (1995). Sedimentation of Trace Metals in the Gulf of Bothnia. *Chemosphere*, 31(8), 3839–3856. [https://doi.org/https://doi.org/10.1016/0045-6535\(95\)00257-9](https://doi.org/https://doi.org/10.1016/0045-6535(95)00257-9)
- Lenstra, W. K., Egger, M., Helmond, N. A. G. M. Van, Kritzberg, E., Conley, D. J., & Slomp, C.P. (2018). Large variations in iron input to an oligotrophic Baltic Sea estuary : impact on sedimentary phosphorus burial. *Biogeosciences*, 15, 6979–6996. <https://doi.org/10.5194/bg-15-6979-2018>
- Lenstra, W.K., Hermans, M, Séguret, M. J. M., Witbaard, R., Behrends, T., Dijkstra, N., Van Helmond, N. A. G. M., Kraal, P., Laan, P., Rijkjenberg, M. J. A., Severman, S., Teacă, A., & Slomp, C. P. (2019). The shelf-to-basin iron shuttle in the Black Sea revisited. *Chemical Geology*, 511, 314–341. <https://doi.org/10.1016/j.chemgeo.2018.10.024>
- Lenstra, W. K., Hermans, M., Séguret, M. J. M., Witbaard, R., Severmann, S., Behrends, T., & Slomp, C. P. (2021a) Coastal hypoxia and eutrophication as key controls on benthic release and water column dynamics of iron and manganese. *Limnology and Oceanography*, 66(3), 807–826. <https://doi.org/10.1002/lno.11644>
- Lenstra, W. K., Klomp, R., Molema, F., Behrends, T., & Slomp, C. P. (2021b) A sequential extraction procedure for particulate manganese and its application to coastal marine sediments. *Chemical Geology*, 584(June), 120538. <https://doi.org/10.1016/j.chemgeo.2021.120538>.
- Lenstra, W. K., Séguret, M. J. M., Behrends, T., Groeneveld, R. K., Hermans, M., Witbaard, R., & Slomp, C. P. (2020). Controls on the shuttling of manganese over the northwestern Black Sea shelf and its fate in the euxinic deep basin. *Geochimica et Cosmochimica Acta*, 273, 177–204. <https://doi.org/10.1016/j.gca.2020.01.031>.

- Lenstra, W. K., Van Helmond, N. A. G. M. van, Dalcin Martins, P., Wallenius, A. J., Jetten, M. S. M., & Slomp, C. P. (2023). Gene-Based Modeling of Methane Oxidation in Coastal Sediments: Constraints on the Efficiency of the Microbial Methane Filter. *Environmental Science & Technology* 57, 12722–12731. doi: 10.1021/ACS.EST.3C02023
- Lenstra, W. K., Van Helmond, N. A. G. M., Żygadłowska, O. M., van Zummeren, R., Witbaard, R., & Slomp, C. P. (2022). Sediments as a Source of Iron, Manganese, Cobalt and Nickel to Continental Shelf Waters (Louisiana, Gulf of Mexico). *Frontiers in Marine Science*, 9(January), 1–13. <https://doi.org/10.3389/fmars.2022.811953>
- Lenz, C., Behrends, T., Jilbert, T., Silveira, M., & Slomp, C.P. (2014). Redox-dependent changes in manganese speciation in Baltic Sea sediments from the holocene thermal maximum: an EXAFS, XANES and LA-ICP-MS study. *Chemical Geology* 370, 49–57. <https://doi.org/10.1016/j.chemgeo.2014.01.013>
- Lenz, C., Jilbert, T., Conley, D.J., & Slomp, C.P. (2015). Hypoxia-driven variations in iron and manganese shuttling in the Baltic Sea over the past 8 kyr. *Geochemistry, Geophysics, Geosystems* 16, 3754–3766. <https://doi.org/10.1002/2015GC005960>
- Lenz, C., Jilbert, T., Conley, D. J., Wolthers, M., & Slomp, C. P. (2015). Are recent changes in sediment manganese sequestration in the euxinic basins of the Baltic Sea linked to the expansion of hypoxia? *Biogeosciences*, 12(16), 4875–4894. <https://doi.org/10.5194/bg-12-4875-2015>
- Letunic, I., & Bork, P. (2021). Interactive Tree Of Life (iTOL) v5: an online tool for phylogenetic tree display and annotation. *Nucleic Acids Research* 49, W293–W296. doi: 10.1093/nar/gkab301
- Leu, A. O., Cai, C., McIlroy, S. J., Hu, S., Tyson, G. W., & Tyson, G. W. (2020). Anaerobic methane oxidation coupled to manganese reduction by members of the Methanoperedenaceae. *The ISME Journal*, 1030–1041. <https://doi.org/10.1038/s41396-020-0590-x>
- Lepland, A., & Stevens, R.L. (1998). Manganese authigenesis in the Landsort Deep, Baltic Sea. *Marine Geology* 151, 1–25. [https://doi.org/10.1016/S0025-3227\(98\)00046-2](https://doi.org/10.1016/S0025-3227(98)00046-2)
- Li, D., Liu, C. M., Luo, R., Sadakane, K., & Lam, T. W. (2015). MEGAHIT: An ultra-fast single-node solution for large and complex metagenomics assembly via succinct de Bruijn graph. *Bioinformatics*, 31(10), 1674–1676. <https://doi.org/10.1093/bioinformatics/btv033>
- Li, H., Handsaker, B., Wysoker, A., Fennell, T., Ruan, J., Homer, N., Marth, G., Abecasis, G., & Durbin, R. (2009). The Sequence Alignment/Map format and SAMtools. *Bioinformatics*, 25(16), 2078–2079. <https://doi.org/10.1093/bioinformatics/btp352>
- Li, W. L., Wu, Y. Z., Zhou, G. wei, Huang, H., & Wang, Y. (2020). Metabolic diversification of anaerobic methanotrophic archaea in a deep-sea cold seep. *Marine Life Science and Technology*, 2(4), 431–441. <https://doi.org/10.1007/s42995-020-00057-9>
- Light, S. H., Su, L., Rivera-Lugo, R., Cornejo, J. A., Louie, A., Iavarone, A. T., Ajo-Franklin, C. M., & Portnoy, D. A. (2018). A flavin-based extracellular electron transfer mechanism in diverse Gram-positive bacteria. *Nature*, 562(7725), 140–157. <https://doi.org/10.1038/s41586-018-0498-z>
- Liu, Y., Beer, L. L., & Whitman, W. B. (2012). Methanogens: a window into ancient sulfur metabolism. *Trends in Microbiology* 20, 251–258. doi: 10.1016/j.tim.2012.02.002
- Liu, Y., & Whitman, W. B. (2008). Metabolic, phylogenetic, and ecological diversity of the methanogenic archaea. *Annals of the New York Academy of Sciences*, 1125, 171–189. <https://doi.org/10.1196/annals.1419.019>
- Lord III, C.J. (1982). A selective and precise method for pyrite determination in sedimentary materials: research-method paper. *Journal of Sedimentological Research*, 52(2), 664 - 666.
- Lösekan, T., Knittel, K., Nadalig, T., Fuchs, B., Niemann, H., Boetius, A., & Amann, R. (2007). Diversity and Abundance of Aerobic and Anaerobic Methane Oxidizers at the Haakon Mosby Mud Volcano, Barents Sea. *Applied and Environmental Microbiology* 73, 3348–3362. doi: 10.1128/AEM.00016-07

- Love, M. I., Huber, W., & Anders, S. (2014). Moderated estimation of fold change and dispersion for RNA-seq data with DESeq2. *Genome Biology*, 15(12). <https://doi.org/10.1186/s13059-014-0550-8>
- Lovley, D. R., Roden, E. E., Phillips, E., & Woodward, J. (1993). Enzymatic iron and uranium reduction by sulfate-reducing bacteria. In *Marine Geology* (Vol. 113).
- Lowemark, L., März, C., O'Regan, M., & Gyllencreutz, R. (2014). Arctic Ocean Mn-stratigraphy: genesis, synthesis and inter-basin correlation. *Quaternary Science Reviews*, 92, 97–111. <https://doi.org/10.1016/j.quascirev.2013.11.018>
- Luther, G. W. (2005) Manganese(II) oxidation and Mn(IV) reduction in the environment - Two one-electron transfer steps versus a single two-electron step. *Geomicrobiol. J.*, 22(3–4), 195–203. <https://doi.org/10.1080/01490450590946022>
- Luther, G. W. (2010). The role of one- and two-electron transfer reactions in forming thermodynamically unstable intermediates as barriers in multi-electron redox reactions. *Aquatic Geochemistry*, 16(3), 395–420. <https://doi.org/10.1007/s10498-009-9082-3>
- Luther, G. W., Madison, A. S., Mucci, A., Sundby, B., & Oldham, V. E. (2015). A kinetic approach to assess the strengths of ligands bound to soluble Mn(III). *Marine Chemistry*, 173, 93–99. <https://doi.org/10.1016/j.marchem.2014.09.006>
- Luther, G.W., Sundby, B., Lewis, B.L., Brendel, P.J., & Silverberg, N. (1997). Interactions of manganese with the nitrogen cycle: alternative pathways to dinitrogen. *Geochimica et Cosmochimica Acta* 61, 4043–4052. [https://doi.org/10.1016/S0016-7037\(97\)00239-1](https://doi.org/10.1016/S0016-7037(97)00239-1)
- Luther, G. W., Thibault de Chanvalon, A., Oldham, V. E., Estes, E. R., Tebo, B. M., & Madison, A. S. (2018). Reduction of Manganese Oxides : Thermodynamic , Kinetic and Mechanistic Considerations for One - Versus Two - Electron Transfer Steps. *Aquat. Geochem.*, 24, 257–277. <https://doi.org/10.1007/s10498-018-9342-1>
- Luo, Y., Ding, J., Shen, Y., Tan, W., Liu, F., & Qiu, G. (2018). Interaction mechanism and kinetics of ferrous sulfide and manganese oxides in aqueous system. *Journal of Soils and Sediments*, 18(2), 564–575. <https://doi.org/10.1007/s11368-017-1774-5>
- Lyons, T.W., & Severmann, S. (2006). A critical look at iron paleoredox proxies: new insights from modern euxinic marine basins. *Geochimica et Cosmochimica Acta* 70, 5698–5722. <https://doi.org/10.1016/j.gca.2006.08.021>
- Madison, A. S., Tebo, B. M., & Luther, G. W. (2011). Simultaneous determination of soluble manganese(III), manganese(II) and total manganese in natural (pore)waters. *Talanta*, 84(2), 374–381. <https://doi.org/10.1016/j.talanta.2011.01.025>
- Madison, A. S., Tebo, B. M., Mucci, A., Sundby, B., & Luther, G. W. (2013). Abundant Porewater Mn(III) Is a Major Component of the Sedimentary Redox System. *Science*, 341(August), 875–878. <https://doi.org/10.5040/9780755621101.0007>
- Maltby, J., Sommer, S., Dale, A. W., & Treude, T. (2016). Microbial methanogenesis in the sulfate-reducing zone of surface sediments traversing the Peruvian margin. *Biogeosciences* 13, 283–299. doi: 10.5194/bg-13-283-2016
- Martin, J.H., & Knauer, G.A. (1980). Manganese cycling in northeast Pacific waters. *Earth and Planetary Science Letters* 51(2), 266–274. [https://doi.org/10.1016/0012-821X\(80\)90209-5](https://doi.org/10.1016/0012-821X(80)90209-5)
- Martin, M. (2011). Cutadapt removes adapter sequences from high-throughput sequencing reads. *EMBnet.Journal*, 17(1), 10–12. <http://www-huber.embl.de/users/an->
- März, C., Hoffmann, J., Bleil, U., De Lange, G. J., & Kasten, S. (2008). Diagenetic changes of magnetic and geochemical signals by anaerobic methane oxidation in sediments of the Zambezi deep-sea fan ( SW Indian Ocean ). *Marine Geology*, 255(3–4), 118–130. <https://doi.org/10.1016/j.margeo.2008.05.013>

- Mason, O. U., Case, D. H., Naehr, T. H., Lee, R. W., Thomas, R. B., Bailey, J. V., & Orphan, V. J. (2015). Comparison of Archaeal and Bacterial Diversity in Methane Seep Carbonate Nodules and Host Sediments, Eel River Basin and Hydrate Ridge, USA. *Microbial Ecology*, 70(3), 766–784. <https://doi.org/10.1007/s00248-015-0615-6>
- Mathon, O., Beteva, A., Borrel, J., Bugnazet, D., Gatla, S., Hino, R., Kantor, I., Mairs, T., Munoz, M., Pasternak, S., Perrin, F., & Pascarelli, S. (2015). The time-resolved and extreme conditions XAS (Texas) facility at the European Synchrotron Radiation Facility: The general-purpose EXAFS bending-magnet beamline BM23. *Journal of Synchrotron Radiation*, 22, 1548–1554. <https://doi.org/10.1107/S1600577515017786>
- Mattila, J., Kankaanpää, H., & Illus, E. (2006). Estimation of recent sediment accumulation rates in the Baltic Sea using artificial radionuclides  $^{137}\text{Cs}$  and  $^{239,240}\text{Pu}$  as time markers. *Boreal Environment Research*, 11: 95–107
- Meinshausen, M., Vogel, E., Nauels, A., Lorbacher, K., Meinshausen, N., Etheridge, D. M., Fraser, P. J., Montzka, S. A., Rayner, P. J., Trudinger, C. M., Krummel, P. B., Beyeler, U., Canadell, J. G., Daniel, J. S., Enting, I. G., Law, R. M., Lunder, C. R., O'Doherty, S., Prinn, R. G., ... Weiss, R. (2017). Historical greenhouse gas concentrations for climate modelling (CMIP6). *Geoscientific Model Development*, 10(5), 2057–2116. <https://doi.org/10.5194/gmd-10-2057-2017>
- Meulepas, R. J. W., Jagersma, C. G., Khadem, A. F., Stams, A. J. M., & Lens, P. N. L. (2010). Effect of methanogenic substrates on anaerobic oxidation of methane and sulfate reduction by an anaerobic methanotrophic enrichment. *Applied Microbiology and Biotechnology*, 87(4), 1499–1506. <https://doi.org/10.1007/s00253-010-2597-0>
- McGlynn, S. E., Chadwick, G. L., Kempes, C. P., & Orphan, V. J. (2015). Single cell activity reveals direct electron transfer in methanotrophic consortia. *Nature*, 526(7574), 531–535. <https://doi.org/10.1038/nature15512>
- McManus, J., Berelson, W. M., Severmann, S., Johnson, K. S., Hammond, D. E., Roy, M., & Coale, K. H. (2012). Benthic manganese fluxes along the Oregon-California continental shelf and slope. *Continental Shelf Research*, 43, 71–85. <https://doi.org/10.1016/j.csr.2012.04.016>
- McMurdie, P. J., & Holmes, S. (2013). Phyloseq: An R Package for Reproducible Interactive Analysis and Graphics of Microbiome Census Data. *PLoS ONE* 8. doi: 10.1371/JOURNAL.PONE.0061217
- Mercone, D., Thomson, J., Abu-Zied, R.H., Croudace, I.W. & Rohling, E.J. (2001). High-resolution geochemical and micropalaeontological profiling of the most recent Eastern Mediterranean sapropel. *Marine Geology* 177, 25–44. [https://doi.org/10.1016/S0025-3227\(01\)00122-0](https://doi.org/10.1016/S0025-3227(01)00122-0)
- Metcalfe, K. S., Murali, R., Mullin, S. W., Connon, S. A., & Orphan, V. J. (2021). Experimentally-validated correlation analysis reveals new anaerobic methane oxidation partnerships with consortium-level heterogeneity in diazotrophy. *The ISME Journal* 15, 377–396. doi: 10.1038/s41396-020-00757-1
- Meysman, F. J. R., Boudreau, B. P., & Middelburg, J. J. (2005). Modeling reactive transport in sediments subject to bioturbation and compaction. *Geochimica et Cosmochimica Acta*, 69(14), 3601–3617. <https://doi.org/10.1016/j.gca.2005.01.004>
- Michel, S. E., Lan, X., Miller, J., Tans, P., Clark, J. R., Schaefer, H., Sperlich, P., Brailsford, G., Morimoto, S., Moossen, H., & Li, J. (2024). Rapid shift in methane carbon isotopes suggests microbial emissions drove record high atmospheric methane growth in 2020–2022. *Proceedings of the National Academy of Sciences* 121, e2411212121. doi: 10.1073/pnas.2411212121
- Middelburg, J.J., De Lange, G.J., & Van der Weijden, C.H. (1987). Manganese solubility control in marine pore waters. *Geochimica et Cosmochimica Acta*, 51, 759–763. [https://doi.org/10.1016/0016-7037\(87\)90086-X9](https://doi.org/10.1016/0016-7037(87)90086-X9)
- Millero, F.J. (1974). Seawater as a multicomponent electrolyte solution. *The Sea, Volume 5, Marine Chemistry*, pp. 3–80.

- Moodley, L., Middelburg, J. J., Herman, P. M. J., Soetaert, K., & De Lange, G. J. (2005). Oxygenation and organic-matter preservation in marine sediments: Direct experimental evidence from ancient organic carbon-rich deposits. *Geology*, 11, 889–892. <https://doi.org/10.1130/G21731.1>
- Moore, C. M., Mills, M. M., Arrigo, K. R., Berman-Frank, I., Bopp, L., Boyd, P. W., Galbraith, E. D., Geider, R. J., Guieu, C., Jaccard, S. L., Jickells, T. D., La Roche, J., Lenton, T. M., Mahowald, N. M., Marañón, E., Marinov, I., Moore, J. K., Nakatsuka, T., Oschlies, A., Saito, M. A., Thingstad, T. F., Tsuda, A., & Ulloa, O. (2013). Processes and patterns of oceanic nutrient limitation. *Nature Geoscience*, 6, 701–710. <https://doi.org/10.1038/ngeo1765>
- Mouret, A., Anschutz, P., Lecroart, P., Chaillou, G., Hyacinthe, C., Deborde, J., Jorissen, F. J., Deflandre, B., Schmidt, S., & Jouanneau, J.-M. (2009). Benthic geochemistry of manganese in the Bay of Biscay, and sediment mass accumulation rate. *Geo-Marine Letters* 29, 133–149. <https://doi.org/10.1007/s00367-008-0130-6>
- Mucci, A. (1988). Manganese uptake during calcite precipitation from seawater: conditions leading to the formation of a pseudokutnahorite. *Geochimica et Cosmochimica Acta*, 52, 1859–1868. [https://doi.org/10.1016/0016-7037\(88\)90009-9](https://doi.org/10.1016/0016-7037(88)90009-9)
- Müller, H., Marozava, S., Probst, A. J., & Meckenstock, R. U. (2020). Groundwater cable bacteria conserve energy by sulfur disproportionation. *ISME Journal*, 14(2), 623–634. <https://doi.org/10.1038/s41396-019-0554-1>
- Murali, R., Yu, H., Speth, D. R., Wu, F., Metcalfe, K. S., Crémière, A., Laso-Pérez, R., Malmstrom, R. R., Goudeau, D., Woyke, T., Hatzenpichler, R., Chadwick, G. L., Connon, S. A., & Orphan, V. J. (2023). Physiological potential and evolutionary trajectories of syntrophic sulfate-reducing bacterial partners of anaerobic methanotrophic archaea. *PLoS Biology*, 21(9 September). <https://doi.org/10.1371/journal.pbio.3002292>
- Nakano, S. (1992). Manganooan vivianite in the bottom sediments of Lake Biwa, Japan. *Mineralogical Journal*, 16, 96–107.
- Nauhaus, K., Albrecht, M., Elvert, M., Boetius, A., & Widdel, F. (2007). In vitro cell growth of marine archaeal-bacterial consortia during anaerobic oxidation of methane with sulfate. *Environmental Microbiology* 9, 187–196. doi: 10.1111/j.1462-2920.2006.01127.x
- Neumann, T., Heiser, U., Leosson, M.A., & Kersten, M. (2002). Early diagenetic processes during Mn-carbonate formation: evidence from the isotopic composition of authigenic Ca-rhodochrosites of the Baltic Sea. *Geochimica et Cosmochimica Acta* 66, 867–879. [https://doi.org/10.1016/S0016-7037\(01\)00819-5](https://doi.org/10.1016/S0016-7037(01)00819-5)
- Neretin, L. N., Pohl, C., Leipe, T., & Pollehne, F. (2003). Manganese cycling in the Gotland Deep, Baltic Sea. *Marine Chemistry*, 82, 125–143. [https://doi.org/10.1016/S0304-4203\(03\)00048-3](https://doi.org/10.1016/S0304-4203(03)00048-3)
- Newell, R. J. P., Aroney, S. T. N., Zaugg, J., Sternes, P., Tyson, G. W., & Woodcroft, B. J. (2024). Aviary: Hybrid assembly and genome recovery from metagenomes with Aviary. doi: 10.5281/zenodo.10806928
- Niemann, H., Lösekann, T., de Beer, D., Elvert, M., Nadalig, T., Knittel, K., Amann, R., Sauter, E. J., Schlütler, M., Klages, M., Foucher, J. P., & Boetius, A. (2006). Novel microbial communities of the Haakon Mosby mud volcano and their role as a methane sink. *Nature*, 443, 854–858.
- Nissen, J. N., Johansen, J., Allesøe, R. L., Sønderby, C. K., Armenteros, J. J. A., Grønbech, C. H., Jensen, L. J., Nielsen, H. B., Nordahl Petersen, T., Winther, O., & Rasmussen, S. (2021). Improved metagenome binning and assembly using deep variational autoencoders. *Nature Biotechnology*, 39, 555–560. doi: 10.1038/s41587-020-00777-4
- Norði, K. Á., Thamdrup, B., & Schubert, C. J. (2013). Anaerobic oxidation of methane in an iron-rich Danish freshwater lake sediment. *Limnology and Oceanography*, 58(2), 546–554. <https://doi.org/10.4319/lo.2013.58.2.0546>

- Nurk, S., Meleshko, D., Korobeynikov, A., & Pevzner, P. A. (2017). metaSPAdes: a new versatile metagenomic assembler. *Genome Research*, 27, 824–834. doi: 10.1101/gr.213959.116
- Ocko, I. B., Sun, T., Shindell, D., Oppenheimer, M., Hristov, A. N., Pacala, S. W., Mauzerall, D. L., Xu, Y., & Hamburg, S. P. (2021). Acting rapidly to deploy readily available methane mitigation measures by sector can immediately slow global warming. *Environmental Research Letters*, 16(5). <https://doi.org/10.1088/1748-9326/abf9c8>
- Oldham, V. E., Chmiel, R., Hansel, C. M., DiTullio, G. R., Rao, D., & Saito, M. (2021). Inhibited Manganese Oxide Formation Hinders Cobalt Scavenging in the Ross Sea. *Global Biogeochemical Cycles*, 35(5), 1–14. <https://doi.org/10.1029/2020GB006706>.
- Oldham, V. E., Miller, M. T., Jensen, L. T., & Luther, G. W. (2017a). Revisiting Mn and Fe removal in humic rich estuaries. *Geochimica et Cosmochimica Acta*, 209, 267–283. <https://doi.org/10.1016/j.gca.2017.04.001>.
- Oldham, V. E., Mucci, A., Tebo, B. M., & Luther, G. W. (2017b). Soluble Mn(III)–L complexes are abundant in oxygenated waters and stabilized by humic ligands. *Geochimica et Cosmochimica Acta*, 199, 238–246. <https://doi.org/10.1016/j.gca.2016.11.043>.
- Oldham, V. E., Owings, S. M., Jones, M. R., Tebo, B. M., & Luther, G. W. (2015). Evidence for the presence of strong Mn(III)-binding ligands in the water column of the Chesapeake Bay. *Marine Chemistry*, 171, 58–66. <https://doi.org/10.1016/j.marchem.2015.02.008>.
- Oldham, V. E., Siebecker, M. G., Jones, M. R., Mucci, A., Tebo, B. M., & Luther, G. W. (2019). The Speciation and Mobility of Mn and Fe in Estuarine Sediments. *Aquatic Geochemistry*, 25(1–2), 3–26. <https://doi.org/10.1007/s10498-019-09351-0>
- Olm, M. R., Brown, C. T., Brooks, B., & Banfield, J. F. (2017). DRep: A tool for fast and accurate genomic comparisons that enables improved genome recovery from metagenomes through de-replication. *ISME Journal*, 11(12), 2864–2868. <https://doi.org/10.1038/ismej.2017.126>
- Orphan, V. J., House, C. H., Hinrichs, K.-U., Mckeegan, K. D., & Delong, E. F. (2002). Multiple archaeal groups mediate methane oxidation in anoxic cold seep sediments. *Proceedings of the National Academy of Sciences*, 99(11), 7663–7668. <https://doi.org/10.1073/pnas.072210299>
- Orphan, V. J., Turk, K. A., Green, A. M., & House, C. H. (2009). Patterns of 15N assimilation and growth of methanotrophic ANME-2 archaea and sulfate-reducing bacteria within structured syntrophic consortia revealed by FISH-SIMS. *Environmental Microbiology* 11, 1777–1791. doi: 10.1111/j.1462-2920.2009.01903.x
- Ostrander, C.M., Nielsen, S.G., Owens, J.D., Kendall, B., Gordon, G.W., Romaniello, S.J., & Anbar, A.D. (2019). Fully oxygenated water columns over continental shelves before the Great Oxidation Event. *Nature Geoscience* 12, 186–191. <https://doi.org/10.1038/s41561-019-0309-7>
- Ouboter, H. T., Mesman, R., Sleutels, T., Postma, J., Wissink, M., Jetten, M. S. M., Ter Heijne, A., Berben, T., & Welte, C. U. (2024). Mechanisms of extracellular electron transfer in anaerobic methanotrophic archaea. *Nature Communications*, 15(1). <https://doi.org/10.1038/s41467-024-45758-2>
- Owings, S.M., Bréthous, L., Eitel, E. M., Fields, B. P., Boever, A., Beckler, J. S., Bombled, B., Lansard, B., Metzger, E., Rabouille, C., & Taillefert, M. (2021). Differential manganese and iron recycling and transport in continental margin sediments of the Northern Gulf of Mexico. *Marine Chemistry* 229, 103908. <https://doi.org/10.1016/j.marchem.2020.103908>
- Pakhomova, S. V., Hall, P. O. J., Kononets, M. Y., Rozanov, A. G., Tengberg, A., & Vershinin, A. V. (2007). Fluxes of iron and manganese across the sediment-water interface under various redox conditions. *Marine Chemistry*, 107(3), 319–331. <https://doi.org/10.1016/j.marchem.2007.06.001>.
- Pan, S., Zhao, X. M., & Coelho, L. P. (2023). SemiBin2: self-supervised contrastive learning leads to better MAGs for short- and long-read sequencing. *Bioinformatics*, 39, 121–129. <https://doi.org/10.1093/bioinformatics/btad209>

- Pan, S., Zhu, C., Zhao, X.-M., & Coelho, L. P. (2022). A deep siamese neural network improves metagenome-assembled genomes in microbiome datasets across different environments. *Nature Communications* 13, 2326. doi: 10.1038/s41467-022-29843-y
- Paquete, C. M., Morgado, L., Salgueiro, C. A., & Louro, R. O. (2022). Molecular Mechanisms of Microbial Extracellular Electron Transfer: The Importance of Multiheme Cytochromes. *Frontiers in Bioscience-Landmark*, 27(6). <https://doi.org/10.31083/j.fbl2706174>
- Parks, D. H., Imelfort, M., Skennerton, C. T., Hugenholtz, P., & Tyson, G. W. (2015). CheckM: Assessing the quality of microbial genomes recovered from isolates, single cells, and metagenomes. *Genome Research*, 25(7), 1043–1055. <https://doi.org/10.1101/gr.186072.114>
- Pelsma, K. A. J., Van Helmond, N. A. G. M. Van, Lenstra, W. K., Röckmann, T., Jetten, M. S. M., Slomp, C. P., & Welte, C. U. (2023). Anaerobic methanotrophy is stimulated by graphene oxide in a brackish urban canal sediment. *Environmental Microbiology*, April, 3104–3115. <https://doi.org/10.1111/1462-2920.16501>
- Phillips, R., & Xu, J. (2021). A critical review of molybdenum sequestration mechanisms under euxinic conditions: Implications for the precision of molybdenum paleoredox proxies. In *Earth-Science Reviews* (Vol. 221). <https://doi.org/10.1016/j.earscirev.2021.103799>
- Polyakov, I. V., Tikka, K., Haapala, J., Alkire, M. B., Alenius, P., & Kuosa, H. (2022). Depletion of Oxygen in the Bothnian Sea Since the Mid-1950s. *Frontiers in Marine Science*, 9. <https://doi.org/10.3389/fmars.2022.917879>
- Post, J. E. (1999). Manganese oxide minerals: Crystal structures and economic and environmental significance. *Proceedings of the National Academy of Sciences*, 96, 3447–3454. [www.pnas.org](http://www.pnas.org).
- Postma, D., 1985. Concentration of Mn and separation from Fe in sediments-I. Kinetics and stoichiometry of the reaction between birnessite and dissolved Fe(II) at 10 degrees C. *Geochimica et Cosmochimica Acta* 49, 1023–1033. [https://doi.org/10.1016/0016-7037\(85\)90316-3](https://doi.org/10.1016/0016-7037(85)90316-3)
- Poulton, S.W., & Canfield, D.E. (2005). Development of a sequential extraction procedure for iron: implications for iron partitioning in continentally derived particulates. *Chemical Geology* 214, 209–221. <https://doi.org/10.1016/j.chemgeo.2004.09.003>
- Prather, M. J., Holmes, C. D., & Hsu, J. (2012). Reactive greenhouse gas scenarios: Systematic exploration of uncertainties and the role of atmospheric chemistry. *Geophysical Research Letters*, 39(9). <https://doi.org/10.1029/2012GL051440>
- Price, M. N., Dehal, P. S., & Arkin, A. P. (2010). FastTree 2 – Approximately Maximum-Likelihood Trees for Large Alignments. *PLOS ONE* 5, e9490. doi: 10.1371/journal.pone.0009490
- Quast, C., Pruesse, E., Yilmaz, P., Gerken, J., Schweer, T., Yarza, P., Peplies, J., & Oliver Glöckner, F. (2013). The SILVA ribosomal RNA gene database project: improved data processing and web-based tools. *Nucleic Acids Research* 41, D590–D596. doi: 10.1093/NAR/GKS1219
- Raghoebarsing, A. A., Pol, A., Van De Pas-Schoonen, K. T., Smolders, A. J. P., Ettwig, K. F., Rijpstra, W. I. C., Schouten, S., Sinninghe Damsté, J. S., Op Den Camp, H. J. M., Jetten, M. S. M., & Strous, M. (2006). A microbial consortium couples anaerobic methane oxidation to denitrification. *Nature*, 440(7086), 918–921. <https://doi.org/10.1038/nature04617>
- Raiswell, R., & Canfield, D. E. (2012). The Iron Biogeochemical Cycle Past and Present. *Geochemical Perspectives*, 1(1), 1 - 220. <https://doi.org/10.7185/geochempersp.1.1>
- Raiswell, R., Hardisty, D.S., Lyons, T.W., Canfield, D.E., Owens, J.D., Planavsky, N.J., Poulton, S.W., & Reinhard, C.T. (2018). The iron paleoredox proxies: a guide to the pitfalls, problems and proper practice. *American Journal of Science*, 318 (5), 491 – 526. <https://doi.org/10.2475/05.2018.03>
- Raiswell, R., Vu, H.P., Brinza, L., & Benning, L.G. (2010). The determination of labile Fe in ferrihydrite by ascorbic acid extraction: methodology, dissolution kinetics and loss of solubility with age and de-watering. *Chemical Geology* 278, 70–79. <https://doi.org/10.1016/j.chemgeo.2010.09.002>

- Rasigraf, O., Van Helmond, N. A. G. M., Frank, J., Lenstra, W. K., Egger, M., Slomp, C. P., & Jetten, M. S. M. (2020). Microbial community composition and functional potential in Bothnian Sea sediments is linked to Fe and S dynamics and the quality of organic matter. *Limnology and Oceanography*, 65(S1), S113–S133. <https://doi.org/10.1002/lno.11371>
- Ravel, B., & Newville, M. (2005). ATHENA, ARTEMIS, HEPHAESTUS: Data analysis for X-ray absorption spectroscopy using IFEFFIT. *Journal of Synchrotron Radiation*, 12(4), 537–541. <https://doi.org/10.1107/S0909049505012719>
- Raven, J. A. (1990). Predictions of Mn and Fe use efficiencies of phototrophic growth as a function of light availability for growth and of C assimilation pathway. *New Phytologist*, 116(1), 1–18. <https://doi.org/10.1111/j.1469-8137.1990.tb00505.x>
- Raven, K. P., Jain, A., & Loeppert, R. H. (1998). Arsenite and Arsenate Adsorption on Ferrihydrite: Kinetics, Equilibrium, and Adsorption Envelopes. *Environmental Science and Technology*, 32(3), 344–349. <https://doi.org/10.1021/es970421p>
- Reeburgh, W. S. (2007). Oceanic Methane Biogeochemistry. *Chemical Reviews* 107, 486–513. doi: 10.1021/cr050362v
- Reed, D. C., Gustafsson, B. G., & Slomp, C. P. (2016). Shelf-to-basin iron shuttling enhances vivianite formation in deep Baltic Sea sediments. *Earth and Planetary Science Letters*, 434, 241–251. <https://doi.org/10.1016/j.epsl.2015.11.033>.
- Reed, D. C., Slomp, C. P., & De Lange, G. J. (2011a) A quantitative reconstruction of organic matter and nutrient diagenesis in Mediterranean Sea sediments over the Holocene. *Geochimica et Cosmochimica Acta*, 75(19), 5540–5558. <https://doi.org/10.1016/j.gca.2011.07.002>.
- Reed, D. C., Slomp, C. P., & Gustafsson, B. G. (2011b) Sedimentary phosphorus dynamics and the evolution of bottom-water hypoxia: A coupled benthic-pelagic model of a coastal system. *Limnology and Oceanography*, 56(3), 1075–1092. <https://doi.org/10.4319/lno.2011.56.3.1075>
- Regnier, P., Dale, A. W., Arndt, S., LaRowe, D. E., Mogollón, J., & Van Cappellen, P. (2011). Quantitative analysis of anaerobic oxidation of methane (AOM) in marine sediments: A modeling perspective. *Earth-Science Reviews* 106(1–2), 105–130. <https://doi.org/10.1016/j.earscirev.2011.01.002>
- Rickard, D. (1997). Kinetics of pyrite formation by the H<sub>2</sub>S oxidation of iron (II) monosulfide in aqueous solutions between 25 and 125 °C: The rate equation. *Geochimica et Cosmochimica Acta*, 61(1), 115–134, 1997. [https://doi.org/10.1016/S0016-7037\(96\)00321-3](https://doi.org/10.1016/S0016-7037(96)00321-3)
- Rickard, D., & Luther, G. W. (2007). Chemistry of Iron Sulfides. *Chemical Reviews* 107, 514–562. doi: 10.1021/cr0503658
- Riedinger, N., Formolo, M. J., Lyons, T. W., Henkel, S., Beck, A., & Kasten, S. (2014). An inorganic geochemical argument for coupled anaerobic oxidation of methane and iron reduction in marine sediments. *Geobiology*, 12(2), 172–181. <https://doi.org/10.1111/gbi.12077>
- Rigutto, I. M. L., Sburban, Ş. C., de Bont, L. W. P., Berben, T., de Graaf, R. M., Slomp, C. P., & Jetten, M. S. M. (2025). Sediments From a Seasonally Euxinic Coastal Ecosystem Show High Nitrogen Cycling Potential. *Environmental Microbiology*, 27(7). <https://doi.org/10.1111/1462-2920.70139>
- Rooze, J., Egger, M., Tsandev, I., & Slomp, C. P. (2016). Iron-dependent anaerobic oxidation of methane in coastal surface sediments: Potential controls and impact. *Limnology and Oceanography*, 61(1), S267–S282. <https://doi.org/10.1002/lno.10275>
- Rotaru, A.-E., Shrestha, P. M., Liu, F., Shrestha, M., Shrestha, D., Embree, M., Zengler, K., Wardman, C., Nevin, K. P., & Lovley, D. R. (2014). A new model for electron flow during anaerobic digestion: direct interspecies electron transfer to Methanosaeta for the reduction of carbon dioxide to methane. *Energy & Environmental Science*, 7, 408–415. <https://doi.org/10.1039/c3ee42189a>
- Rouzies, D., & Millet, J.M. (1993). Mössbauer study of synthetic oxidized vivianite at room temperature. *Hyperfine Interactions*, 77, 19–28. <https://doi.org/10.1007/BF02320295>

- Rosentreter, J. A., Borges, A. V., Deemer, B. R., Holgerson, M. A., Liu, S., Song, C., Melack, J., Raymond, P. A., Duarte, C. M., Allen, G. H., Olefeldt, D., Poulter, B., Battin, T. I., & Eyre, B. D. (2021). Half of global methane emissions come from highly variable aquatic ecosystem sources. *Nature Geoscience*, 1–6. doi: 10.1038/s41561-021-00715-2
- Ruff, S. E., Felden, J., Gruber-Vodicka, H. R., Marcon, Y., Knittel, K., Ramette, A., & Boetius, A. (2019). In situ development of a methanotrophic microbiome in deep-sea sediments. *ISME Journal* 13, 197–213. doi: 10.1038/s41396-018-0263-1
- Ruff, S. E., Kuhfuss, H., Wegener, G., Lott, C., Ramette, A., Wiedling, J., Knittel, K., & Weber, M. (2016). Methane seep in shallow-water permeable sediment harbors high diversity of anaerobic methanotrophic communities, Elba, Italy. *Frontiers in Microbiology*, 7(MAR). <https://doi.org/10.3389/fmicb.2016.00374>
- Sander, S. G., & Koschinsky, A. (2011) Metal flux from hydrothermal vents increased by organic complexation. *Nature Geoscience*, 4(3), 145–150. <https://doi.org/10.1038/ngeo1088>.
- Sapart, C. J., Van Der Veen, C., Vigano, I., Brass, M., Van De Wal, R. S. W., Bock, M., Fischer, H., Sowers, T., Buizert, C., Sperlich, P., Blunier, T., Behrens, M., Schmitt, J., Seth, B., & Röckmann, T. (2011). Simultaneous stable isotope analysis of methane and nitrous oxide on ice core samples. *Atmospheric Measurement Techniques*, 4(12), 2607–2618. <https://doi.org/10.5194/amt-4-2607-2011>
- Sarno, N., Montgomery, A., Zhuang, G.-C., Martinez, B. R., Anda, V. D., Joye, S. B., & Baker, B. J. (2024). Methane production from hydrocarbons by consortia dominated by ANME archaea. *BioRxiv*. 2024.10.30.621140.
- Saunois, M., R. Stavert, A., Poulter, B., Bousquet, P., G. Canadell, J., B. Jackson, R., A. Raymond, P., J. Dlugokencky, E., Houweling, S., K. Patra, P., Ciais, P., K. Arora, V., Bastviken, D., Bergamaschi, P., R. Blake, D., Brailsford, G., Bruhwiler, L., M. Carlson, K., Carrol, M., ... Zhuang, Q. (2020). The global methane budget 2000-2017. *Earth System Science Data*, 12(3), 1561–1623. <https://doi.org/10.5194/essd-12-1561-2020>
- Saunois, M., Martinez, A., Poulter, B., Zhang, Z., Raymond, P. A., Regnier, P., Canadell, J. G., Jackson, R. B., Patra, P. K., Bousquet, P., Ciais, P., Dlugokencky, E. J., Lan, X., Allen, G. H., Bastviken, D., Beerling, D. J., Belikov, D. A., Blake, D. R., Castaldi, S., ... Zhuang, Q. (2025). Global Methane Budget 2000-2020. *Earth System Science Data*, 17(5), 1873–1958. <https://doi.org/10.5194/essd-17-1873-2025>
- Scheller, S., Yu, H., Chadwick, G. L., McGlynn, S. E., & Orphan, V. J. (2016). Sulfate Reduction. *Science*, 351(6274), 703–4707. <https://doi.org/10.1016/b978-0-12-114860-7.50024-7>
- Schlitzer, R. (2023). Ocean Data View.
- Schreiber, L., Holler, T., Knittel, K., Meyerdierks, A., & Amann, R. (2010). Identification of the dominant sulfate-reducing bacterial partner of anaerobic methanotrophs of the ANME-2 clade. *Environmental Microbiology* 12, 2327–2340. doi: 10.1111/j.1462-2920.2010.02275.x
- Segarra, K. E. A., Comerford, C., Slaughter, J., & Joye, S. B. (2013). Impact of electron acceptor availability on the anaerobic oxidation of methane in coastal freshwater and brackish wetland sediments. *Geochimica et Cosmochimica Acta*, 115, 15–30. <https://doi.org/10.1016/j.gca.2013.03.029>
- Semler, A. C., & Dekas, A. E. (2025). Unexpected scarcity of ANME archaea in hydrocarbon seeps within Monterey Bay. *Biogeosciences*, 22(2), 385–403. <https://doi.org/10.5194/bg-22-385-2025>
- Seifert, R., Nauhaus, K., Blumenberg, M., Krüger, M., & Michaelis, W. (2006). Methane dynamics in a microbial community of the Black Sea traced by stable carbon isotopes in vitro. *Organic Geochemistry*, 37(10), 1411–1419. <https://doi.org/10.1016/j.orggeochem.2006.03.007>
- Sela-Adler, M., Ronen, Z., Herut, B., Antler, G., Vigderovich, H., Eckert, W., Sivan, O. (2017). Co-existence of Methanogenesis and Sulfate Reduction with Common Substrates in Sulfate-Rich Estuarine Sediments. *Frontiers in Microbiology* 8, 766. doi: 10.3389/fmicb.2017.00766
- Semler, A. C., & Dekas, A. E. (2025). Unexpected scarcity of ANME archaea in hydrocarbon seeps within Monterey Bay. *Biogeosciences* 22, 385–403. doi: 10.5194/bg-22-385-2025

- Shaffer, M., Borton, M. A., McGivern, B. B., Zayed, A. A., La Rosa, S. L., Solden, L. M., Liu, P., Narrowe, A. B., Rodríguez-Ramos, J., Bolduc, B., Consuelo Gazitúa, M., Daly, R. A., Smith, G. J., Vik, D. R., Pope, P. B., Sullian, M. B., Roux, S., & Wrighton, K. C. (2020). DRAM for distilling microbial metabolism to automate the curation of microbiome function. *Nucleic Acids Research* 48, 8883–8900. doi: 10.1093/nar/gkaa621
- Sieber, C. M. K., Probst, A. J., Sharrar, A., Thomas, B. C., Hess, M., Tringe, S. G., & Banfield, J. F. (2018). Recovery of genomes from metagenomes via a dereplication, aggregation and scoring strategy. *Nature Microbiology*, 3, 836–843. doi: 10.1038/s41564-018-0171-1
- Silburn, B., Kröger, S., Parker, E. R., Sivyer, D. B., Hicks, N., Powell, C. F., Johnson, M., & Greenwood, N. (2017). Benthic pH gradients across a range of shelf sea sediment types linked to sediment characteristics and seasonal variability. *Biogeochemistry*, 135(1–2), 69–88. <https://doi.org/10.1007/s10533-017-0323-z>
- Sivan, M., Röckmann, T., van der Veen, C., & Popa, M. E. (2024). Extraction, purification, and clumped isotope analysis of methane ( $\Delta^{13}\text{CDH}_3$  and  $\Delta^{13}\text{CD}_2\text{H}_2$ ) from sources and the atmosphere. *Atmospheric Measurement Techniques* 17, 2687–2705. doi: 10.5194/amt-17-2687-2024
- Slobodkin, A. I., Ratnikova, N. M., Slobodkina, G. B., Klyukina, A. A., Chernyh, N. A., & Merkel, A. Y. (2023). Composition and Metabolic Potential of Fe(III)-Reducing Enrichment Cultures of Methanotrophic ANME-2a Archaea and Associated Bacteria. *Microorganisms*, 11(3). <https://doi.org/10.3390/microorganisms11030555>
- Slomp, C. P., Malschaert, J. F. P., Lohse, L., & Van Raaphorst, W. (1997). Iron and manganese cycling in different sedimentary environments on the North Sea continental margin. *Science*, 17(9), 1083–1117. [https://doi.org/10.1016/S0278-4343\(97\)00005-8](https://doi.org/10.1016/S0278-4343(97)00005-8)
- Slomp, C. P., Mort, H. P., Jilbert, T., Reed, D. C., Gustafsson, B. G., & Wolthers, M. (2013). Coupled Dynamics of Iron and Phosphorus in Sediments of an Oligotrophic Coastal Basin and the Impact of Anaerobic Oxidation of Methane. *PLOS ONE*, 8(4). <https://doi.org/10.1371/journal.pone.0062386>
- Soetaert, K., & Meysman, F. (2012). Environmental Modelling & Software Reactive transport in aquatic ecosystems: Rapid model prototyping in the open source software R. *Environmental Model Software*, 32, 49–60. <https://doi.org/10.1016/j.envsoft.2011.08.011>
- Soetaert, K., Petzoldt, T., & Meysman, F. (2010) marelac: Tools for Aquatic Sciences.
- Solórzano, L. (1968) Determination of Ammonia in Natural Waters by the Phenolhypochlorite Method. *Limnology and Oceanography*, 14(September), 799–801. <https://doi.org/10.4319/lo.1969.14.5.0799>
- Soyol-Erdene, T. O., & Huh, Y. (2013). Rare earth element cycling in the pore waters of the Bering Sea Slope (IODP Exp. 323). *Chemical Geology*, 358, 75–89. <https://doi.org/10.1016/j.chemgeo.2013.08.047>
- Stoeva, M. K., & Coates, J. D. (2019). Specific inhibitors of respiratory sulfate reduction: Towards a mechanistic understanding. *Microbiology*, 165(3), 254–269. <https://doi.org/10.1099/mic.0.000750>
- Stoll, M. H. C., Bakker, K., Nobbe, G. H., & Haese, R. R. (2001). Continuous-flow analysis of dissolved inorganic carbon content in seawater. *Analytical Chemistry*, 73(17), 4111–4116. <https://doi.org/10.1021/ac010303r>
- Sturm, A., Fowle, D. A., Jones, C. A., Leslie, K., Nomosatryo, S., Henny, C., Canfield, D. E., & Crowe, S. A. (2019). Rates and pathways of CH<sub>4</sub> oxidation in ferruginous Lake Matano, Indonesia. *Geobiology*, 17(3), 294–307. <https://doi.org/10.1111/gbi.12325>
- Su, G., Zopfi, J., Yao, H., Steinle, L., Niemann, H., & Lehmann, M. F. (2020). Manganese/iron-supported sulfate-dependent anaerobic oxidation of methane by archaea in lake sediments. *Limnology and Oceanography*, 65(4), 863–875. <https://doi.org/10.1002/lno.11354>

- Suess, E. (1979). Mineral phases formed in anoxic sediments by microbial decomposition of organic matter. *Geochimica et Cosmochimica Acta* 43, 399–352. [https://doi.org/10.1016/0016-7037\(79\)90199-6](https://doi.org/10.1016/0016-7037(79)90199-6)
- Sulu-Gambari, F., Roepert, A., Jilbert, T., Hagens, M., Meysman, F. J. R., & Slomp, C. P. (2017). Molybdenum dynamics in sediments of a seasonally-hypoxic coastal marine basin. *Chemical Geology*, 466(April), 627–640. <https://doi.org/10.1016/j.chemgeo.2017.07.015>
- Sulu-Gambari, F., Seitaj, D., Behrends, T., Banerjee, D., Meysman, F. J. R., & Slomp, C. P. (2016). Impact of cable bacteria on sedimentary iron and manganese dynamics in a seasonally-hypoxic marine basin. *Geochimica et Cosmochimica Acta*, 192, 49–69. <https://doi.org/10.1016/j.gca.2016.07.028>
- Sundby, B., & Silverberg, N. (1985). Manganese fluxes in the benthic boundary layer. *Limnology and Oceanography* 30, 372–381. <https://doi.org/10.4319/lo.1985.30.2.0372>
- Szeinbaum, N., Nunn, B. L., Cavazos, A. R., Crowe, S. A., Stewart, F. J., Dichristina, T. J., Reinhard, C. T., & Glass, J. B. (2020). Brief Report Novel insights into the taxonomic diversity and molecular mechanisms of bacterial Mn (III) reduction. *Environmental Microbiology Reports*, 12(5), 583–593. <https://doi.org/10.1111/1758-2229.12867>
- Szopa, S., Naik, V., Adhikary, B., Artaxo, P., Berntsen, T., Collins, W. D., Fuzzi, S., Gardallo, L., Kiendler-Scharr, A., Klimont, Z., Liao, H., Unger, N., & Zanis, P. (2021). Short-lived Climate Forcers. In *Climate Change 2021 – The Physical Science Basis Contribution of Working Group I to the Sixth Assessment Report of the Intergovernmental Panel on Climate Change* (pp. 817–922). Cambridge University Press. <https://doi.org/10.1017/9781009157896.008>
- Takai, K., & Horikoshi, K. (2000). Rapid detection and quantification of members of the archaeal community by quantitative PCR using fluorogenic probes. *Applied and Environmental Microbiology* 66, 5066–5072. doi: 10.1128/AEM.66.11.5066-5072.2000
- Tessier, A., Campbell, P.G., & Bisson, M. (1979). Sequential Extraction Procedure for the Speciation of Particulate Trace Metals. *Analytical Chemistry*, 51(7)
- Thamdrup, B., & Dalsgaard, T. (2000). The fate of ammonium in anoxic manganese oxide-rich marine sediment. *Geochimica et Cosmochimica Acta*, 64(24), 4157–4164. [https://doi.org/10.1016/S0016-7037\(00\)00496-8](https://doi.org/10.1016/S0016-7037(00)00496-8)
- Thamdrup, B., Fossing, H., & Jørgensen, B. B. (1994). Manganese, iron and sulfur cycling in a coastal marine sediment, Aarhus bay, Denmark. *Geochimica et Cosmochimica Acta* 58, 5115–5129. doi: 10.1016/0016-7037(94)90298-4
- Thibault de Chanvalon, A., & Luther, G. W. (2019). Mn speciation at nanomolar concentrations with a porphyrin competitive ligand and UV-vis measurements. *Talanta*, 200, 15-21. <https://doi.org/10.1016/j.talanta.2019.02.069>
- Tian, T., Qiao, S., Yu, C., Tian, Y., Yang, Y., & Zhou, J. (2017). Distinct and diverse anaerobic respiration of methanogenic community in response to MnO<sub>2</sub> nanoparticles in anaerobic digester sludge. *Water Research*, 123, 206–215. <https://doi.org/10.1016/j.watres.2017.06.066>
- Timmers, P. H. A., Gieteling, J., Widjaja-Greefkes, H. C. A., Plugge, C. M., Stams, A. J. M., Lens, P. N. L., & Meulepas, R. J. W. (2015). Growth of anaerobic methane-oxidizing archaea and sulfate-reducing bacteria in a high-pressure membrane capsule bioreactor. *Applied and Environmental Microbiology* 81, 1286–1296. doi: 10.1128/AEM.03255-14
- Trouwborst, R. E., Clement, B. G., Tebo, B. M., Glazer, B. T., & Luther, G. W. (2006). Soluble Mn(III) in suboxic zones. *Science*, 313(5795), 1955–1957. <https://doi.org/10.1126/science.1132876>
- Tu, T. H., Wu, L. W., Lin, Y. S., Imachi, H., Lin, L. H., & Wang, P. L. (2017). Microbial community composition and functional capacity in a terrestrial ferruginous, sulfate-depleted mud volcano. *Frontiers in Microbiology*, 8(NOV), 1–15. <https://doi.org/10.3389/fmicb.2017.02137>

- Valenzuela, E. I., Avendaño, K. A., Balagurusamy, N., Arriaga, S., Nieto-Delgado, C., Thalasso, F., & Cervantes, F. J. (2019). Electron shuttling mediated by humic substances fuels anaerobic methane oxidation and carbon burial in wetland sediments. *Science of the Total Environment*, 650, 2674–2684. <https://doi.org/10.1016/j.scitotenv.2018.09.388>
- Valenzuela, E. I., Bryce, C., Forberg, J., Planer-Friedrich, B., Kappler, A., & Cervantes, F. J. (2022). Unraveling the role of sulfide-natural organic matter interplay on methane cycling in anoxic environments. *Biogeochemistry*, 161(2), 193–206. <https://doi.org/10.1007/s10533-022-00977-x>
- Valenzuela, E. I., Prieto-davó, A., López-lozano, N. E., García-gonzález, A. S., López, M. G., & Cervantes, J. (2017). Anaerobic Methane Oxidation Driven by Microbial Reduction of Natural Organic Matter in a Tropical Wetland. *Applied and Environmental Microbiology*, 83(11). <https://doi.org/https://doi.org/10.1128/AEM.00645-17>
- Van Cappellen, P., & Wang, Y. (1996). Cycling of iron and manganese in surface sediments: a general theory for the coupled transport and reaction of carbon, oxygen, nitrogen, sulfur, iron and manganese. *American Journal of Science*, 296(March), 197–243.
- Van der Zee, C., van Raaphorst, W., & Epping, E. (2001). Absorbed Mn<sup>2+</sup> and Mn redox cycling in Iberian continental margin sediments (northeast Atlantic Ocean). *Journal of Marine Research*, 59, 133–166.
- Van Grinsven, S., Sinninghe Damsté, J. S., & Villanueva, L. (2020). Assessing the effect of humic substances and Fe(III) as potential electron acceptors for anaerobic methane oxidation in a marine anoxic system. *Microorganisms*, 8(9), 1–15. <https://doi.org/10.3390/microorganisms8091288>
- Van Helmond, N. A. G. M., Żygadłowska, O. M., Lenstra, W. K., Klomp, R., Humborg, C., Conley, D. J., Jetten, M. S. M., & Slomp, C. P. (2025). Sedimentary vanadium depletion under sulfidic conditions: Implications for (paleo)redox proxy applications. *Geochimica et Cosmochimica Acta*. <https://doi.org/10.1016/j.gca.2025.01.022>
- Van Santvoort, P. J. M., De Lange, G. J., Thomson, J., Colley, S., Meysman, F. J. R., & Slomp, C. P. (2002). Oxidation and origin of organic matter in surficial Eastern Mediterranean hemipelagic sediments. *Aquat. Geochem.*, 8(3), 153–175. <https://doi.org/10.1023/A:1024271706896>, 2002.
- Venetz, J., Żygadłowska, O. M., Dotsios, N., Wallenius, A. J., van Helmond, N. A. G. M., Lenstra, W. K., Klomp, R., Slomp, C. P., Jetten, M. S. M., & Veraart, A. J. (2024). Seasonal dynamics of the microbial methane filter in the water column of a eutrophic coastal basin. *FEMS Microbiology Ecology* 100, fae007. doi: 10.1093/femsec/fiae007
- Vigneron, A., Cruaud, P., Pignet, P., Caprais, J. C., Cambon-Bonavita, M. A., Godfroy, A., & Toffin, L. (2013). Archaeal and anaerobic methane oxidizer communities in the Sonora Margin cold seeps, Guaymas Basin (Gulf of California). *ISME Journal*, 7(8), 1595–1608. <https://doi.org/10.1038/ismej.2013.18>
- Virtasalo, J. J., Endler, M., Moros, M., Jokinen, S. A., Hämäläinen, J., & Kotilainen, A. T. (2016). Base of brackish-water mud as key regional stratigraphic marker of mid-Holocene marine flooding of the Baltic Sea Basin. *Geo-Marine Letters*, 36(6), 445–456. <https://doi.org/10.1007/s00367-016-0464-4>
- Wallenius, A. J., Dalcin Martins, P., Slomp, C. P., & Jetten, M. S. M. (2021). Anthropogenic and Environmental Constraints on the Microbial Methane Cycle in Coastal Sediments. *Frontiers in Microbiology*, 12(February). <https://doi.org/10.3389/fmicb.2021.631621>
- Wallenius, A. J., Venetz, J., Żygadłowska, O. M., Lenstra, W. K., van Helmond, N. A. G. M., Martins, P. D., Slomp, C. P., Jetten, M. S. M. (2025). A ubiquitous and diverse methanogenic community drives microbial methane cycling in eutrophic coastal sediments. *FEMS Microbiology Ecology*, faf075. doi: 10.1093/femsec/faf075
- Wallheimer, R. N., Halevy, I., & Sivan, O. (2025). Modeling the controls on microbial iron and manganese reduction in methanogenic sediments. *Geochimica et Cosmochimica Acta*. <https://doi.org/10.1016/j.gca.2025.05.026>

- Weber, T., Wiseman, N. A., & Kock, A. (2019). Global ocean methane emissions dominated by shallow coastal waters. *Nature Communications*, 10(1). <https://doi.org/10.1038/s41467-019-12541-7>
- Weinstein, M. M., Prem, A., Jin, M., Tang, S., & Bhasin, J. M. (2019). FIGARO: An efficient and objective tool for optimizing microbiome rRNA gene trimming parameters. *BioRxiv*. <https://doi.org/10.1101/610394>
- Whiticar, M. J. (1999). Carbon and hydrogen isotope systematics of bacterial formation and oxidation of methane. *Chemical Geology*, 161(1), 291–314. [https://doi.org/10.1016/S0009-2541\(99\)00092-3](https://doi.org/10.1016/S0009-2541(99)00092-3)
- Wickham, H. (2016). *ggplot2: Elegant Graphics for Data Analysis*. Springer New York. doi: 10.1007/978-0-387-98141-3
- Wilson, L. G., & Bandurski, R. S. (1958). Enzymatic reactions involving sulfate, sulfite, selenate, and molybdate. *The Journal of Biological Chemistry*, 233(4), 975–981. [https://doi.org/10.1016/s0021-9258\(18\)64689-7](https://doi.org/10.1016/s0021-9258(18)64689-7)
- Woodcroft, B. J., Aroney, S. T. N., Zhao, R., Cunningham, M., Mitchell, J. A. M., Blackall, L., & Tyson, G. W. (2024). SingleM and Sandpiper: Robust microbial taxonomic profiles from metagenomic data. *BioRxiv*. doi: 10.1101/2024.01.30.578060
- Woods, P. H., Speth, D. R., Laso-Pérez, R., Utter, D. R., Ruff, S. E., & Orphan, V. J. (2024). Convergence and horizontal gene transfer drive the evolution of anaerobic methanotrophy in archaea. *bioRxiv*, 2024.05.23.595608. doi: 10.1101/2024.05.23.595608
- Wu, Y. W., Simmons, B. A., & Singer, S. W. (2016). MaxBin 2.0: An automated binning algorithm to recover genomes from multiple metagenomic datasets. *Bioinformatics*, 32(4), 605–607. <https://doi.org/10.1093/bioinformatics/btv638>
- Xiao, X., Luo, M., Zhang, C., Zhang, T., Yin, X., Wu, X., Zhao, J., Tao, J., Chen, Z., Liang, Q., & Dong, X. (2023). Metal-Driven Anaerobic Oxidation of Methane as an Important Methane Sink in Methanic Cold Seep Sediments. *Microbiology Spectrum*, 11(2). <https://doi.org/10.1128/spectrum.05337-22>
- Xu, L., Zhuang, G. C., Montgomery, A., Liang, Q., Joye, S. B., & Wang, F. (2021). Methyl-compounds driven benthic carbon cycling in the sulfate-reducing sediments of South China Sea. *Environmental Microbiology*, 23(2), 641–651. <https://doi.org/10.1111/1462-2920.15110>
- Xue, Y., Lu, H., Li, Y., Yang, H., Tang, Y., & Lu, Y. (2025). Anaerobic oxidation of methane by manganese oxides in marine sediments: a review. *Frontiers in Marine Science*, 12. <https://doi.org/10.3389/fmars.2025.1609892>
- Yakushev, E. V., Pollehne, F., Jost, G., Kuznetsov, I., Schneider, B., & Umlauf, L. (2007). Analysis of the water column oxic/anoxic interface in the Black and Baltic seas with a numerical model. *Mar. Chem.*, 107(3), 388–410. <https://doi.org/10.1016/j.marchem.2007.06.003>
- Yang, Z., & Lu, Y. (2022). Coupling methanogenesis with iron reduction by acetotrophic Methanosarcina mazei zm-15. *Environmental Microbiology Reports*, 14(5), 804–811. <https://doi.org/10.1111/1758-2229.13098>
- Young, E. D., Kohl, I. E., Lollar, B. S., Etiope, G., Rumble, D., Li (李姝宁), S., Haghnegahdar, M.A., Schauble, E. A., McCain, K. A., Foustoukos D. I., Sutcliffe, C., Warr, O., Ballentine, C. J., Onstott, T. C., Hosgormez, H., Neubeck, Marques, J. M., Pérez-Rodríguez, I., Rowe, A. R., LaRowe, D. E., & Bryndzia, L. T. (2017). The relative abundances of resolved  $^{12}\text{CH}_2\text{D}_2$  and  $^{13}\text{CH}_3\text{D}$  and mechanisms controlling isotopic bond ordering in abiotic and biotic methane gases. *Geochimica et Cosmochimica Acta* 203, 235–264. doi: 10.1016/j.gca.2016.12.041
- Yu, H., Susanti, D., McGlynn, S. E., Skennerton, C. T., Chourey, K., Iyer, R., Scheller, S., Tavormina, P. L., Hettich, R. L., Mukhopadhyay, B., & Orphan, V. J. (2018). Comparative genomics and proteomic analysis of assimilatory sulfate reduction pathways in anaerobic methanotrophic archaea. *Frontiers in Microbiology* 9, 422729. doi: 10.3389/fmicb.2018.02917

- Zhang, X., Joyce, G. H., Leu, A. O., Zhao, J., Rabiee, H., Viridis, B., Tyson, G. W., Yuan, Z., Mcllroy, S. J., & Hu, S. (2023). Multi-heme cytochrome-mediated extracellular electron transfer by the anaerobic methanotroph 'Candidatus Methanoperedens nitroreducens.' *Nature Communications*, 14(1). <https://doi.org/10.1038/s41467-023-41847-w>
- Zhang, T., Xiao, X., Chen, S., Zhao, J., Chen, Z., Feng, J., Liang, Q., Phelps, T. J., & Zhang, C. (2020). Active Anaerobic Archaeal Methanotrophs in Recently Emerged Cold Seeps of Northern South China Sea. *Frontiers in Microbiology*, 11. <https://doi.org/10.3389/fmicb.2020.612135>
- Zhao, J., Li, F., Cao, Y., Zhang, X., Chen, T., Song, H., & Wang, Z. (2021). Microbial extracellular electron transfer and strategies for engineering electroactive microorganisms. In *Biotechnology Advances* (Vol. 53). Elsevier Inc. <https://doi.org/10.1016/j.biotechadv.2020.107682>
- Zhao, Y., Liu, Y., Cao, S., Hao, Q., Liu, C., & Li, Y. (2024). Anaerobic oxidation of methane driven by different electron acceptors: A review. *Science of the Total Environment* 946 <https://doi.org/10.1016/j.scitotenv.2024.174287>
- Zillén, L., Lenz, C., & Jilbert, T. (2012). Stable lead (Pb) isotopes and concentrations - A useful independent dating tool for Baltic Sea sediments. *Quaternary Geochronology*, 8(1), 41–45. <https://doi.org/10.1016/j.quageo.2011.11.001>
- Żygadłowska, O. M., Venetz, J., Klomp, R., Lenstra, W. K., Van Helmond, N. A. G. M., Röckmann, T., Wallenius, A. J., Dalcin Martins, P., Veraart, A. J., Jetten, M. S. M., & Slomp, C. P. (2023). Pathways of methane removal in the sediment and water column of a seasonally anoxic eutrophic marine basin. *Frontiers in Marine Science*, January, 1–15. <https://doi.org/10.3389/fmars.2023.1085728>
- Żygadłowska, O. M., van Helmond, N. A. G. M., Lenstra, W. K., Klomp, R., Accou, R., Puyk, R., Dickson, A. J., Jetten, M. S. M., & Slomp, C. P. (2024a). Seasonal euxinia in a coastal basin: Impact on sedimentary molybdenum enrichments and isotope signatures. *Chemical Geology*, 670(September), 122297. <https://doi.org/10.1016/j.chemgeo.2024.122297>
- Żygadłowska, O. M., Roth, F., van Helmond, N. A. G. M., Lenstra, W. K., Venetz, J., Dotsios, N., Röckmann, T., Veraart, A. J., Stranne, C., Humborg, C., Jetten, M. S. M., & Slomp, C. P. (2024b). Eutrophication and Deoxygenation Drive High Methane Emissions from a Brackish Coastal System. *Environmental Science and Technology*, 58(24), 10582–10590. <https://doi.org/10.1021/acs.est.4c00702>
- Żygadłowska, O. M., Venetz, J., Klomp, R., Lenstra, W. K., Van Helmond, N. A. G. M., Röckmann, T., Wallenius, A. J., Dalcin Martins, P., Veraart, A. J., Jetten, M. S. M., & Slomp, C. P. (2023). Pathways of methane removal in the sediment and water column of a seasonally anoxic eutrophic marine basin. *Frontiers in Marine Science*, January, 1–15. <https://doi.org/10.3389/fmars.2023.1085728>
- Żygadłowska, O. M., Venetz, J., Lenstra, W. K., Van Helmond, N. A. G. M., Klomp, R., Röckmann, T., & Slomp, C. P. (2024). Ebullition drives high methane emissions from a eutrophic coastal basin. *Geochimica et Cosmochimica Acta*, 384, 1–13. <https://doi.org/10.1016/j.gca.2024.08.028>

## Data management

The research in this dissertation has been carried out according to the Research Data Management policy of the Radboud Institute for Biological and Environmental Sciences (RIBES, version 1-Dec-2022 accessed at [www.ru.nl/ribes](http://www.ru.nl/ribes))

- Chapter 1** No original data was gathered for this chapter.
- Chapter 2** The data presented in this study are published and available at <https://doi.org/10.1016/j.chemgeo.2021.120538>
- Chapter 3** The data presented in this chapter are published and available in the Zenodo repository at <https://doi.org/10.5281/zenodo.14509408>
- Chapter 4** The data presented in this study are deposited in the Zenodo repository and available via <https://doi.org/10.5281/zenodo.16913015>. The raw sequencing data of the 16S rRNA gene amplicon sequencing is accessible on the National Center for Biotechnology Information (NCBI) website under the BioProject accession number PRJNA1257658, metagenome data is uploaded to NCBI under the BioProject accession number PRJNA1167897.
- Chapter 5** The data presented in this paper are deposited in the Zenodo database at <https://doi.org/10.5281/zenodo.16909310>. The raw sequencing data of the 16S rRNA gene amplicon sequencing can be accessed in the NCBI database under Bioproject number PRJNA1268434.
- Chapter 6** The dataset for this study is available through Zenodo at <https://doi.org/10.5281/zenodo.16920164>. Sequencing data is available at the NCBI website under the accession number PRJNA1306556.
- Chapter 7** All data presented in this paper and the code used for the MHC motif search are deposited on Zenodo and available at [10.5281/zenodo.17174800](https://doi.org/10.5281/zenodo.17174800). The raw sequencing data can be accessed in the European Nucleotide Archive under the accession number PRJNA1314788.
- Chapter 8** No original data was gathered for this chapter

## Acknowledgements/Dankwoord

The past four years I worked very hard to get this thesis together. Luckily, I did not have to do this work alone. Therefore, I would like to thank some people who have been especially valuable for me along the way.

I am really grateful towards my supervisory team, without whom all of this would not have been possible. **Caroline**, thank you for always making time for a good discussion, to answer my questions or to help me with texts I struggled to write. It is inspiring to see your drive for science and your passion to transfer this enthusiasm to others. I feel really fortunate that I was under your supervision. **Mike**, you have been great for the MARIX team spirit. I greatly appreciate the insights you provided based on your experience and learned a lot from your advice. **Wytze**, already since my bachelor thesis, you were the first to go to with for example struggles during lab analyses, freshly written text or bugs in a computer model. Thank you for your patience while answering all of my questions and while reading and commenting a lot of my texts.

It has been wonderful to be a part of the MARIX team. It was great to see how everyone contributed to the team in her or his own way. I don't think I will ever be part again of such an efficient and well streamered team as we were on all the fieldworks! **Niels** and **Olga**, thank you for teaching me the ins and outs of geochemical sampling and analysis both on board and in the lab. **Anna**, you are to thank for teaching me very patiently the ins and outs of anaerobic environmental microbiology and for all the fun hours in the lab and on the boat singing along with our favourite ABBA tunes. **Jessica**, you were the best room buddy during the conference and thank you for appreciating my jokes. **Evalien**, **Lina** and **Marit**, I was very happy to get some colleagues in Nijmegen that were (at least) as much fascinated by geology as I am! **Isabel** and **Peter**, thanks a lot for all the good times on the boat filled with hard work, great views and a lot of karaoke. And of course our adopted 'MARIX' geochemist, **Signe**, I really appreciate your never ending enthusiasm!

I started my PhD at Utrecht University. I would like to thank the Geochemistry group for the fun breaks, interesting discussions and good atmosphere in the lab and office. Also thanks to everybody at the GeoLab for all the help with sample analyses.

After one year, I continued my PhD at Radboud University. I really enjoyed the welcoming atmosphere and the space to be the odd geologist who spread dirt all

over the labs (yes, there is a difference between minerals and rocks...). You have all been kind and open, which lead to many good conversations and a lot of laughter over a warm cup of Green tea Lemon, or a (cold) beer in the coffee corner. Thanks to everybody: permanent staff, postdocs, PhD's, lab analysts and students for creating such a great working atmosphere in the Microbiology department during the years that I was a part of it.

A special thanks goes to my office buddies 4 ever: **Rob, Ida** and **Nicky**. I really appreciated the safe space in our office and the fun we had together. It was great to get to know you all better over the past three years.

Ik wil ook mijn familie bedanken voor de steun de afgelopen vier jaar. Het is heel fijn om te weten dat er mensen zijn waar je altijd op terug kunt vallen en waar een warm kop thee altijd zal worden bijgevuld.

Ten slotte wil ik **Robin** bedanken dat je me dwong regelmatig mijn gedachten te verzetten en te realiseren dat er meer is dan alleen promotieonderzoek. Bedankt dat je me de afgelopen jaren onvoorwaardelijk hebt gesteund. Ik ben heel erg blij dat wij al zo lang samen zijn en kijk uit naar een mooie toekomst met elkaar.

## List of publications

Lenstra, W. K., **Klomp, R.**, Molema, F., Behrends, T., & Slomp, C. P. (2021) A sequential extraction procedure for particulate manganese and its application to coastal marine sediments. *Chemical Geology*, 584(June), 120538. <https://doi.org/10.1016/j.chemgeo.2021.120538>.

**Klomp, R.**, Żygadłowska, O. M., Jetten, M. S. M., Oldham, V. E., van Helmond, N. A. G. M., Slomp, C. P., & Lenstra, W. K. (2025). Dissolved Mn(III) is a key redox intermediate in sediments of a seasonally euxinic coastal basin. *Biogeosciences* 22, 751–765. doi: 10.5194/bg-22-751-2025

Żygadłowska, O. M., Venetz, J., **Klomp, R.**, Lenstra, W. K., van Helmond, N. A. G. M., Röckmann, T., Wallenius, A. J., Dalcin Martins, P., Veraart, A. J., Jetten, M. S. M. & Slomp, C. P. (2023). Pathways of methane removal in the sediment and water column of a seasonally anoxic eutrophic marine basin. *Frontiers in Marine Science*, 10, 1085728. <https://doi.org/10.3389/fmars.2023.1085728>

Venez, J., Żygadłowska, O. M., Dotsios, N., Wallenius, A. J., van Helmond, N. A. G. M., Lenstra, W. K., **Klomp, R.**, Slomp, C. P., Jetten, M. S. M. & Veraart, A. J. (2024). Seasonal dynamics of the microbial methane filter in the water column of a eutrophic coastal basin. *FEMS Microbiology Ecology*, 100(3), fae007. <https://doi.org/10.1093/femsec/fae007>

Żygadłowska, O. M., Venetz, J., Lenstra, W. K., van Helmond, N. A. G. M., **Klomp, R.**, Röckmann, T., Veraart, A. J., Jetten, M. S. M. & Slomp, C. P. (2024). Ebullition drives high methane emissions from a eutrophic coastal basin. *Geochimica et Cosmochimica Acta*, 384, 1-13. <https://doi.org/10.1016/j.gca.2024.08.028>

Żygadłowska, O. M., van Helmond, N. A. G. M., Lenstra, W. K., **Klomp, R.**, Accou, R., Puyk, R., Dickson, A. J., Jetten, M. S. M. & Slomp, C. P. (2024). Seasonal euxinia in a coastal basin: Impact on sedimentary molybdenum enrichments and isotope signatures. *Chemical Geology*, 670, 122430. <https://doi.org/10.1016/j.chemgeo.2024.122430>

van Helmond, N. A. G. M., Żygadłowska, O. M., Lenstra, W. K., **Klomp, R.**, Humborg, C., Conley, D. J., Jetten, M. S. M. & Slomp, C. P. (2025). Sedimentary vanadium depletion under sulfidic conditions: Implications for (paleo) redox proxy applications. *Geochimica et Cosmochimica Acta*, 393, 238-253. <https://doi.org/10.1016/j.gca.2025.01.022>

Baas, E., van Helmond, N. A. G. M., van Erk, M. R., Żygadłowska, O. M., **Klomp, R.**, Piso, L., Hennekam, R., Reichart, G-J, Jetten, M. S. M. & Slomp, C. P. (2026). Geochemical records of Holocene environmental change in a high latitude coastal basin. *Chemical Geology*, 123247. <https://doi.org/10.1016/j.chemgeo.2026.123247>

### **Accepted manuscripts**

**Klomp, R.**, Wallenius, A. J., van Helmond, N. A. G. M., Lenstra, W. K., Żygadłowska, O. M., Jetten, M. S. M., Slomp, C. P., Potential for manganese oxide driven anaerobic methane oxidation in sediments of a seasonally euxinic coastal basin. *Estuaries and Coasts*

## Curriculum Vitae



Robin Klomp was born on the 29<sup>th</sup> of December in Arnhem, The Netherlands. Already at a young age he was interested in nature, resulting amongst others in a large collection of rocks. During geography lessons in high school at the Overbetuwe College in Bommel he became fascinated by the geological processes that shape the natural world around us. Driven by this fascination, he enrolled in the bachelor Earth Sciences at Utrecht University. During the bachelor his interest was mostly drawn to sedimentology and geochemistry. He continued with the master Earth Life and Climate, with a focus on biogeochemistry. As a part of his master program he did an internship at the wastewater treatment plant in Amersfoort, where he helped optimizing the recovery of fertilizers from wastewater in the form of struvite ( $\text{Mg}(\text{NH}_4)\text{PO}_4 \cdot 6 \text{H}_2\text{O}$ ) minerals. For his MSc thesis, he adapted a reactive transport model to describe Mn cycling in sediments of a seasonally euxinic basin, under the supervision of Wytze Lenstra and Caroline Slomp. A curiosity to further unravel natural processes made Robin start his PhD under the supervision of Caroline Slomp, Mike Jetten and Wytze Lenstra at Utrecht University into methane removal in coastal sediments. After one year of his PhD, the research group Robin was part of moved to the Microbiology department of the Radboud University of Nijmegen, where he had the chance to learn a lot about microbiology. After finishing his PhD, he started working as a soil consultant for TAUW Netherlands, to apply his knowledge of chemistry and microbiology to help cleaning polluted soils in the Netherlands.



Radboud Universiteit

